EPFL

Thèse n° 9207

New tools for phase segmentation and denoising of analytical STEM data for enhanced chemical sensitivity, applied to Earth mantle research

Présentée le 26 juin 2023

Faculté des sciences de base
Laboratoire de spectrométrie et microscopie électronique
Programme doctoral en science et génie des matériaux

pour l'obtention du grade de Docteur ès Sciences

par

Hui CHEN

Acceptée sur proposition du jury

Dr J. C. Plummer, président du jury
Prof. C. Hébert, directrice de thèse
Prof. W. Grogger, rapporteur
Dr Z. Saghi, rapporteuse
Dr A. Hessler-Wyser, rapporteuse

École polytechnique fédérale de Lausanne

2023

The journey of a thousand miles
begins with a single step.
— Lao Tzu

To 寿玉, 汉秋 and 洪举

Acknowledgements

I begin by expressing my utmost gratitude to my advisor, Prof. Cécile Hébert, for her unwavering support and guidance throughout this remarkable journey. Thank you for always being there for me through the ups and downs, and thank you for being the kind of advisor who trusts her students and gives them the space to experiment, make mistakes, and learn from them. Your willingness to provide me with the freedom to explore new avenues of research has been truly invaluable. It has broadened my academic horizons and allowed me to grow both personally and professionally. Moreover, I am grateful for the scientific discussions we have had, where you have always provided insightful feedback and constructive criticism. These discussions have helped me sharpen my analytical skills and have been invaluable to the success of this project.

I am also deeply grateful for the contributions of Dr. Duncan T.L. Alexander. Not only did he provide me with world-class electron microscopy training, but he also never hesitated to engage in scientific discussions about my research. And let's not forget about his proofreading skills! Duncan literally proofread everything I wrote, from presentations to posters to publications, and helped me sound like a true scholar. And, of course, I can't forget to mention his charming British sarcasm, which always kept things interesting. But all joking aside, Duncan has taught me so much about what it means to be a competitive scholar and the commitment required to see a project through to the end. His mentorship has been instrumental in my growth as a researcher. Thank you, Duncan, for being a constant source of support and guidance throughout my PhD journey. Additionally, I would like to extend a special thanks to Dr. J. Badro for suggesting the cutting-edge geochemistry problem that became the focus of my PhD thesis. I also appreciate the fact that he synthesized samples for me and provided assistance throughout the project.

I would like to express a heartfelt thank you to the entire CIME team for their constant support throughout my PhD study. Special thanks to Marco, who provided me with invaluable help and guidance whenever I faced software or hardware microscopy issues. Thank you,

Lucie, my office mate for over two years. Your kindness, warmth, and positive attitude have been a constant source of inspiration and joy to me. Thank you, Rita and Victor, for your excellent assistance with microscopy and pleasant company during our conversations. Your willingness to help and your cheerful dispositions have made every day at CIME a joyous one. Lastly, I want to thank Thomas, Nadine, Emad, Barbora, Grégoire, and Fabienne for being an integral part of my PhD experience. Thank you all.

I would like to express my appreciation to my lab mates, both old and new, for their camaraderie, support, and helpful discussions. Their friendship has made my PhD journey more enjoyable and rewarding. Farhang, you are the wittiest person I have ever met. Everything becomes fun when you are around. Thanks for your help from the very beginning. Without your assistance, my project would have been much more difficult. Adrien, you are always generous in providing any kind of assistance. I appreciate the invaluable discussions we had on EDXS. Your developed EDXS data synthesis code played a significant role in completing my thesis. Gulnaz, you are an angel who brings joy to everyone around you. And it is always a pleasure to visit your home for dinner. Stéphane, your culinary skills have made everyone's day. Winter brings pancakes, and summer brings BBQs. Federica, sharing the office with you for a span of two years has been an incredible experience filled with interesting discussions and mutual encouragement. Héloïse, thank you for always bringing me the best macarons from Pierre Hermé and Ladurée. It has been a joy getting to know you and working with you. Diane, you are undoubtedly the best secretary in the world. Thank you for all of the invaluable support you have provided me over the years. And last but not least, I would like to thank Teresa, Bernat, Anastasiia, Sebastian, and Chih-Ying. I have enjoyed spending time with all of you.

I would like to extend my sincere gratitude to my friends Yao, Suiyang, Tzu-Hsien, Miao, Yanfei, Xingyu, Shuxuan, Kaicheng, Jingyue, Shuhui, Ting and Jing for the wonderful moments we have shared together. I especially want to thank Yao for the countless adventures we went on together. Having you by my side is something I will always be grateful for. And my sincere thanks go to my friend Zhiping, whom I have known since high school and whom I will cherish for life as a trustworthy friend.

Lastly, but most importantly, I want to express my deepest gratitude to my family for their unconditional love and support. You have never demanded anything of me, yet you have given me everything. I want to extend special thanks to my uncle, 义发, and my aunt, 华平, for their steadfast believe in me, which has fueled many crucial decisions in my life. And to dear dang dang, thank you for being my rock through it all.

Lausanne, 17 February 2023 HUI CHEN

Abstract

This thesis is dedicated to developing innovative methodologies that improve elemental quantification in scanning transmission electron microscopy (STEM) using energy-dispersive X-ray spectroscopy (EDXS). The primary motivation stems from a geochemistry problem concerning Si deficiency in the Earth's upper mantle. To address this, mantle melting experiments were conducted on pyrolite composition under lower mantle conditions, followed by the characterization of the synthesized mineral phases using STEM-EDXS. The results reveal that within the investigated lower mantle pressure range, bridgmanite, a silicate mineral, is the first phase to crystallize during mantle solidification, supporting the hypothesis of a Si-rich lower mantle that could account for the Si depletion in the upper mantle.

The mineral specimens exhibiting complex phase features provide opportunities for the development of advanced data processing techniques, including classical machine learning and deep learning approaches. These techniques have been employed to overcome challenges in phase segmentation and improve elemental quantification, particularly for trace elements. Two novel methodologies, non-negative matrix factorization (NMF) aided and pan-sharpening fused non-negative matrix factorization (PSNMF), have been developed. These methodologies effectively unmix overlapping phases, enhance chemical sensitivity, and improve the precision of STEM-EDXS quantification. Additionally, this thesis combines the complementary techniques of EDXS and EELS (electron energy-loss spectroscopy) using a deep learning approach to enhance elemental analysis. The preliminary results of this methodology show promising potential.

In summary, this thesis significantly advances the analytical capabilities of STEM-EDXS and deepens our understanding of the Earth's mantle. The proposed methodologies are applicable to the analysis of various materials that exhibit complex volumetric phase relationships, low signal-to-noise ratios (SNR), or contain vital trace constituents.

Key words: scanning transmission electron microscopy (STEM), energy-dispersive X-ray (EDX) spectroscopy, phase segmentation, denoising, elemental quantification, machine

learning, lower mantle, melting relations, mantle differentiation

Résumé

Cette thèse est consacrée au développement de méthodologies innovantes visant à améliorer la quantification des éléments dans la microscopie électronique à transmission en balayage (STEM) utilisant la spectroscopie des rayons X à dispersion d'énergie (EDXS). La motivation principale provient d'un problème de géochimie concernant la déficience en Si du manteau supérieur de la Terre. Des expériences de fusion du manteau sur une composition de pyrolite dans les conditions du manteau inférieur ont été réalisées, suivies de la caractérisation des phases minérales synthétisées à l'aide de STEM-EDXS. Les résultats révèlent que la bridgmanite, un minéral silicaté, est la première phase à cristalliser lors de la solidification du manteau dans la plage de pression du manteau inférieur étudiée, soutenant la possibilité d'un manteau inférieur riche en silicium qui pourrait expliquer la déplétion en Si du manteau supérieur.

Les échantillons minéraux présentant des caractéristiques de phase complexes offrent des opportunités pour le développement de techniques avancées de traitement de données, notamment des approches d'apprentissage de type "machine learning" classique et de "deep learning", pour surmonter les défis de segmentation de phase et améliorer la quantification des éléments, en particulier pour les éléments traces. Deux méthodologies novatrices, la factorisation matricielle non négative (NMF) simple et assistée par la fusion de données (pan-sharpening ou aussi PSNMF), ont été développées, permettant de séparer efficacement les phases superposées, d'améliorer la sensibilité chimique et d'accroître la précision de la quantification de STEM-EDXS. De plus, cette thèse aborde la combinaison les techniques complémentaires de EDXS et EELS (spectroscopie de perte d'énergie électronique) en utilisant une approche d'apprentissage profond pour améliorer l'analyse élémentaire. Les résultats préliminaires de cette méthodologie montrent un potentiel prometteur.

En résumé, cette thèse améliore considérablement les capacités analytiques de STEM-EDXS et approfondit notre compréhension du manteau terrestre. Les méthodologies proposées sont applicables à l'analyse d'une large gamme de matériaux présentant des relations de

phase volumétriques complexes, des rapports signal-bruit (SNR) faibles ou des constituants traces essentiels.

Mots clés : microscopie électronique en transmission à balayage (STEM), spectroscopie de dispersion d'énergie des rayons X (EDXS), segmentation de phase, débruitage, quantification élémentaire, apprentissage automatique, manteau inférieur, relations de fusion, différenciation du manteau

Preface

Motivations and Objectives

Energy-dispersive X-ray spectroscopy (EDXS) and electron energy-loss spectroscopy (EELS) are widely used techniques in (scanning) transmission electron microscopy ((S)TEM) for elemental quantification across diverse fields such as materials science, physics, chemistry, and biology. Despite their extensive applications, each technique possesses distinct strengths and limitations. Therefore, the initial objective of this project was to develop innovative methodologies that leverage either EDXS or EELS, or both, to achieve more accurate, precise, and comprehensive elemental quantification compared to conventional quantification methods used in the electron microscopy community.

The laboratory where I conducted my doctoral studies has had a longstanding research partnership with Dr. J. Badro from the Institut de Physique du Globe de Paris (IPGP). At the outset of my doctoral study, Dr. Badro proposed a research endeavor focusing on a state-of-the-art geochemistry problem—the Si deficiency in the Earth's upper mantle. One hypothesis postulates that the 'missing' Si might be sequestered in the Earth's lower mantle, owing to the fractionation of Si-rich mineral(s) during the early solidification of the Earth's mantle [1, 2].

To explore this possibility, Dr. J. Badro led mantle melting experiments using pyrolite, a composition model representing the average Earth mantle, in laser-heated diamond anvil cells (LHDAC). These experiments aim to simulate the solidification process of the Earth's mantle and determine the crystallization sequence of mineral phase(s) during solidification.

Since the synthesized mineral phases are nanometric in size, their characterization necessitates high-resolution techniques such as ((S)TEM). For this purpose, Dr. F. Nabiei prepared four TEM lamellae using the focused ion beam (FIB) technique. My role in the project involves employing STEM-EDXS to characterize these samples. Once the liquidus phase(s) is (are) identified and quantified, Dr. Badro could assess the partitioning of trace elements between the liquidus phase(s) and the coexisting residual silicate melt, providing

vital geochemical insights into the existence of 'hidden' reservoirs in the lower mantle. Addressing this geochemical issue was one of the primary objectives of the project and held great significance in understanding the Earth's mantle.
The mineral specimens under investigation exhibit complex and diverse phase features, which pose analytical challenges for STEM characterization while simultaneously creating opportunities for the development of innovative quantification methodologies. These relevant phases contain both heavy and light elements, as well as major, minor, and trace elements. Moreover, these phases share common elements that result in spectral similarities, and they overlap spatially along the thickness direction, leading to mixed compositions in relevant pixels. Additionally, the mineral assemblages are susceptible to beam damage, limiting the signal-to-noise ratio (SNR) of the acquired dataset and increasing the uncertainties in elemental quantification. Another significant objective of this thesis was to develop advanced data processing techniques that address the aforementioned challenges and improve quantification, thus enhancing the analytical capabilities of STEM.
As mentioned earlier, one of the initial propositions of this research was to integrate the complementary techniques of EDXS and EELS to achieve a more comprehensive elemental quantification. In the final part of this thesis, the feasibility of this proposition was explored utilizing a deep learning approach on simultaneously acquired EDXS and EELS data.
To summarize, this thesis is dedicated to developing innovative methodologies that enhance chemical analysis in analytical STEM, with a primary focus on STEM-EDXS technique; this research also seeks to address the geochemical problem of Si deficiency in the Earth's upper mantle through mantle melting experiments conducted under lower mantle conditions. The chemical analyses of the synthesized mineral specimens have spurred the development of advanced data processing methodologies to address challenges in phase segmentation and elemental quantification inherent in STEM-EDXS. Lastly, the thesis explores the integration of EDXS and EELS techniques to improve elemental analysis. The preliminary results suggest considerable promise in this approach.

Thesis Structure

The first three chapters of this thesis offer a comprehensive literature review. In **Chapter 1**, the essential Earth science background information is presented to understand the geochemical problem under scrutiny. **Chapter 2** outlines the fundamentals of analytical STEM, including the theories of EDXS and EELS quantification, as well as recent methodologies developed for the synergistic analysis of EDXS and EELS. **Chapter 3** reviews classical machine learning methods and deep learning methods, discussing their principles, advantages, disadvantages, recent developments, and their applications in analytical STEM data analysis.

In **Chapter 4**, we conducted mantle melting experiments on pyrolite at pressures of 47, 55, 71, and 88 GPa, and characterized the resulting melt pocket and solidus mineral assemblages using STEM-EDXS and the traditional Cliff-Lorimer ratio method. Our findings indicate that bridgmanite, a silicate, is the first mineral phase to crystallize within the investigated lower mantle pressure range. This implies that the fractionated crystallization of bridgmanite during the solidification of Earth's mantle can result in a Si-rich lower mantle. We also observed the preferential accumulation of Fe in the residual melt, which provides experimental support for the basal magma ocean theory [3]. Additionally, we investigated the partitioning behavior of Fe between solidus ferropericlase and bridgmanite. It is postulated that variations in Fe content in bridgmanite could be responsible for the observed rheological variations in the lower mantle.

The objective of **Chapter 5** is to enhance the quantification of solidus mineral assemblages using STEM-EDXS, which plays a crucial role in understanding the mineralogy of Earth's lower mantle. This chapter introduces a non-negative matrix factorization (NMF) aided phase analysis method that effectively unmixes phases with significant spatial and spectral overlap, and improves the sensitivity and precision of STEM-EDXS quantification. Applying this method to analyze beam-sensitive solidus mineral assemblages enables retrieving the true EDX spectra of the constituent phases and their corresponding phase abundance maps. Furthermore, this method allows for reliable quantification of trace elements at concentration levels of ~100 ppm.

Building upon the success of the NMF-aided method and acknowledging its limitations, such as the requirement for a feasible SNR and reliance on phase size, **Chapter 6** proposes the pan-sharpening fused non-negative matrix factorization (PSNMF) method for a more resilient and effective STEM-EDXS analysis. This approach enables simultaneous phase unmixing and dataset denoising. We assess its effectiveness using a variety of STEM-EDXS datasets, including synthetic datasets with moderate and extremely low SNR, as well as an experimentally acquired dataset with medium SNR. Our results demonstrate the ability of PSNMF to accurately extract phase abundance maps and spectra even in the presence of high levels of noise. Moreover, PSNMF exhibits superior denoising capabilities compared to the classical principal component analysis (PCA) method. It enables precise quantification of minor and trace elements, even in datasets with extremely low SNR (i.e., containing an average of only 15 X-ray counts per pixel).

As stated in the beginning, one of the initial propositions of this research was to integrate the complementary techniques of EDXS and EELS in order to improve elemental quantification. **Chapter 7** introduces a novel methodology that utilizes a deep learning method, implicit neural representation (INR), to establish a correlation between simultaneously obtained

EDXS and EELS datasets. The preliminary results show that by utilizing INR on EELS data with a suitable SNR and EDXS data with poor statistics, a significant improvement in the quality of the final output EDXS data can be achieved. This preliminary study, therefore, raises a number of promising prospects for enhanced elemental analysis via correlative analytical STEM.

Chapter 8 concludes with insights into the solidification process of the Earth's mantle, advanced data processing techniques for STEM-EDXS analysis, and the potential of INR for improved chemical characterization via analytical STEM data.

Contents

List of Figures

List of Tables

1 Introduction to Earth Science

The history of Earth is long and complex that can be traced back to 4.5 billion years ago when the planet was first formed from a swirling cloud of dust and gas known as a solar nebula [4]. Advances in geophysical and geochemical techniques have led to significant discoveries of Earth's interior. Today, Earth is still evolving and changing with many open questions. Where we stand in this process of planetary differentiation is not entirely clear. Many aspects of Earth's mantle, including its composition, structure, and dynamics, have yet to be profoundly understood.

1.1 How to Probe Earth's interior?

There are a number of methods for exploring the interior of Earth across various disciplines, and we briefly introduce five general approaches in this section.

1.1.1 Seismic Observation

Seismology could be seen as the geophysical equivalent of medical radiography. Instead of using X-rays as the probe, seismology uses elastic waves generated by earthquakes and studies their propagation through the globe. The propagation velocities are determined by the density and elasticity of the medium that seismic waves travel through. Geophysicists have therefore established Earth's seismic wave velocity and density profiles–the Preliminary Reference Earth Model (PREM) [5]. As illustrated in Figure 1.1, Earth has a layered structure: the solid inner core, the liquid outer core, the mantle, and the crust. Indeed, little was known about Earth's internal structure, but numerous theories until the advent of seismology.

With the expansion of networks of broadband seismometers and open-access availability of seismic data, global-scale seismology and seismic tomography have made steady progress

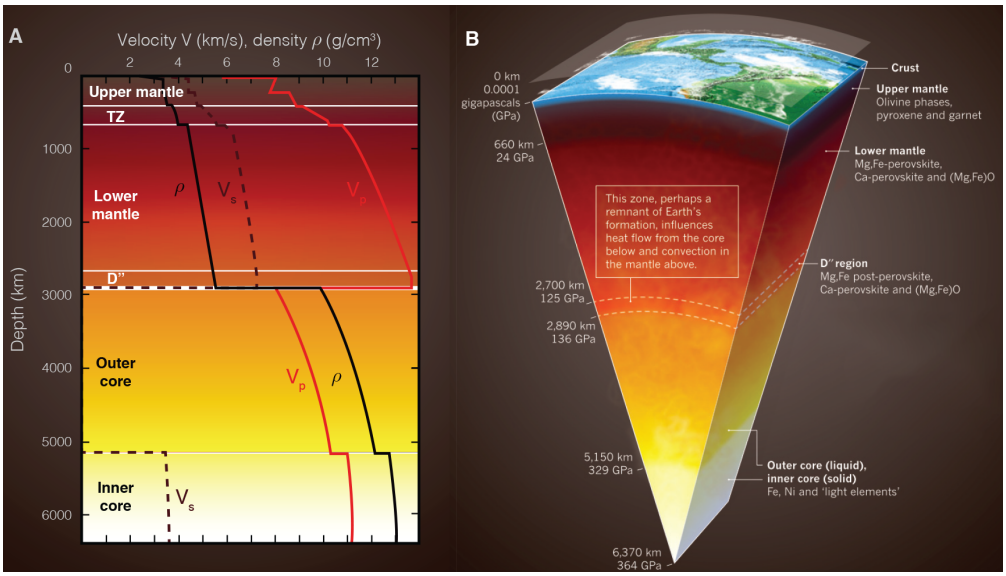

Figure 1.1: a) Preliminary Reference Earth Model (PREM) of the structure of Earth. b) Corresponding cross-section of Earth and mineral composition. Image from [6].

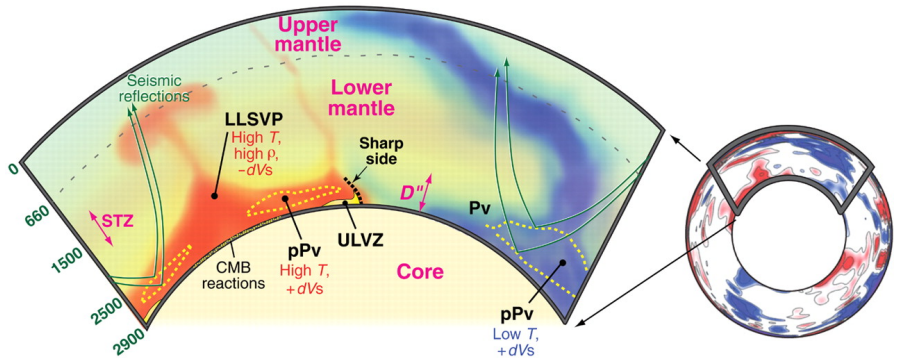

Figure 1.2: Seismic tomography of the lower mantle. Image from [8].

in the recent two decades to reveal Earth's interior at a finer scale. For instance, the lower mantle had suggested to being homogeneous from the PREM model; however, seismic tomography has permitted to imaging of heterogeneities of the lower mantle, such as large low-shear-velocity provinces (LLSVPs) and ultra-low velocity zones (ULVZs) (Figure 1.2) that play crucial roles in Earth's mantle convection as well as surface plate tectonics [7].

Seismological studies give a global picture of the current Earth and raises many new questions. For instance, how has the layered structure formed? What is the origin of the heterogeneities in its structure? Geophysics and geochemistry studies will together contribute to answering all these pending questions.

1.1.2 Characterization of Terrestrial Rocks

A direct approach to studying Earth is to characterize the terrestrial rocks coming from Earth's interior. Unfortunately, our ability to directly sample Earth's interior is limited to drilling, which reaches, at best, just a few kilometers into the crust. Meanwhile, Earth has provided some chances of exposing the upper mantle to the surface via tectonic processes or explosive volcanic eruptions.

Tectonically emplaced mantle rocks include subcontinental, suboceanic, and subarc mantle rocks that were exhumed from the upper mantle and occur as massif peridotites [9], ophiolite bodies[10], and abyssal peridotites [11]. They give geologists a window through which to study the upper mantle's properties and composition as well as the processes that have shaped it. However, their provenances easily fall into debates due to the uncertainties of original geodynamic settings and complicated deformation and metamorphism during emplacement into the crust. This limits the ability of the tectonically exposed mantle rocks to represent the composition of the upper mantle.

Rocks and mineral inclusions of mantle derivation that are transported to the surface via volcanism are termed 'mantle xenoliths' or 'mantle nodules'. In contrast to the tectonically exposed mantle rocks, xenoliths are erupted rapidly and freeze the mineralogical signatures of their depth of origin, and provide direct evidence of the nature of the mantle beneath; in addition, many xenolith suites, particularly those erupted by kimberlites, provide samples from a considerably greater depth range. However, the small size of many xenoliths makes the accurate estimation of bulk mantle compositions difficult and accentuates modal heterogeneities. Xenoliths derived from depths of 100-200 km indicate that the upper mantle is predominate of peridotitic composition [12], which contains more than 50% olivine, variable amounts of orthopyroxene (opx) and clinopyroxene (cpx), plus an aluminous phase whose identity depends on the pressure (i.e., depth) at which the peridotite equilibrated—plagioclase at low pressures, spinel at intermediate pressures, and garnet at high pressures.

Besides xenoliths, diamonds that occur in kimberlite alongside xenoliths, often contain pristine inclusions of mantle minerals and they are an important source for probing the mantle. Some diamonds are discovered to originate from Earth's transition zone and the top of the lower mantle [13], which makes them the deepest natural geochemical probes of the mantle.

In summary, aside from a few inclusions in diamonds that may have a deeper origin, most mantle rock samples come from depths less than 200 km (~ 6 GPa). Therefore studies on natural terrestrial samples can constrain only the composition of the upper mantle.

1.1.3 Cosmochemical Estimation

Meteorites are believed to be fragments of the planetesimals that formed Earth. They are classified into three broad categories: achondrites, stony meteorites, and chondrites. Among them, the chondrites were from undifferentiated parent bodies; hence their composition would be more representative of the primordial composition of the solar system than the differentiated bodies. Chondrites fall into three groups: enstatite chondrites, ordinary chondrites, and carbonaceous chondrites. Carbonaceous chondrites are the most primitive in composition; in particular, CI carbonaceous chondrites have a composition that closely matches that of the solar photosphere [14] (Figure 1.3) and hence that of the solar nebula. Due to their assumed primordial nature, the composition of CI carbonaceous chondrites is frequently used to reflect the composition of the bulk Earth (BE, core + mantle + crust). As a result, the composition models of Earth's core are built on comparative studies between extraterrestrial meteoritic samples and terrestrial samples of bulk silicate Earth (BSE, mantle + crust).

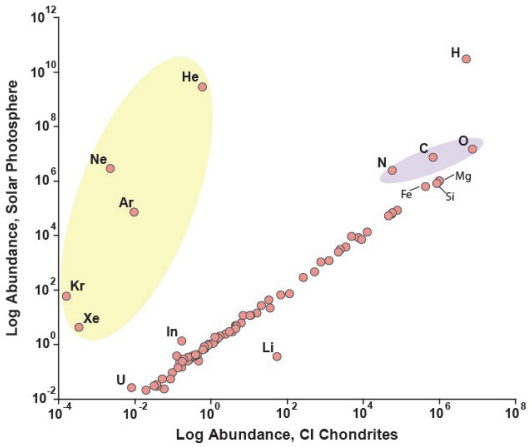

Figure 1.3: Solar vs. CI chondrites element abundances. Image from [15].

Meanwhile, the chemical study of primitive upper mantle rocks shows that many ratios of refractory lithophile elements (RLEs, e.g., rare earth elements, Be, Al, Ca, Sc, Ti, Sr, Y, Zr, Nb, Ba, Hf, Th, U) are very similar to those observed in CI carbonaceous chondrites [12, 17, 18]. Figure 1.4 displays the abundances of elements ratioed to those in CI carbonaceous chondrites and normalized to Mg. They are plotted against the temperature by which 50% of the element would have condensed from a gas of solar composition. This observation has also indicated that Earth was created from CI carbonaceous chondrites. However, there is an important exception to the pattern described above. The Mg/Si ratio of the upper mantle is substantially lower than the 'primordial' Mg/Si ratio of CI carbonaceous chondrites. The

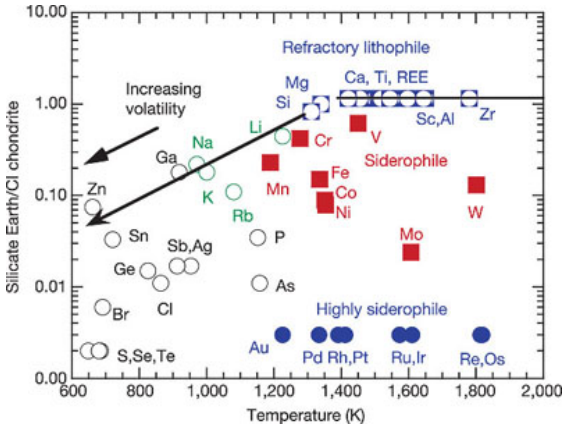

Figure 1.4: Elemental abundances between Earth and CI chondrites normalized with respect to Mg ratio. Image from [16].

deficiency of Si in the upper mantle relative to other refractory lithophile elements implies additional reservoirs of Si that might exist in either the core or lower mantle. The lower mantle is speculated to be chemically different from the upper mantle, which is a complex and controversial issue.

1.1.4 Experimental Petrology and Mineral Physics

Earth has a layered structure, and it is indeed largely unsampled. Experimental petrology therefore uses laboratory experiments to study the physical and chemical processes that occur in Earth's interior. It involves creating high pressures and temperatures that are similar to Earth's interior to study the physical and chemical behavior of relevant rocks and minerals. Through the development of novel instruments capable of creating greater pressures and temperatures, our understanding of Earth has continuously evolved. With the invention of diamond anvil cell (DAC), we are allowed to conduct high-pressure experiments from few GPa up to ~ 400 GPa which exceeds the pressure at the center of Earth [19]. This field of study can provide important insights into the petrological processes that lead to the formation of distinct mineralogy in each layer of Earth, and the evolution of Earth.

1.1.5 Numerical Calculation

The numerical calculation primarily aims to simulate the stability of terrestrial materials under the conditions relevant to Earth's interior. Significant computational advancements have enabled calculations performed at the atomistic level, giving access to the electronic structure and the energetics of minerals and rocks. It can produce valuable data on possible mineral phase transitions and the physical properties of mineral phases when the experi-

mental conditions are too challenging. It helps not only explain the observed transitions but also predict new phase transitions prior to the experimental studies sometimes [20]. Meanwhile, numerical simulation can be very demanding in computing power and requires the use of computer clusters.

The methods mentioned above all shed light on the internal structure and composition of Earth. Earth is essentially composed of a central metallic core that is further divided into an outer liquid layer and an inner solid part; a silicate mantle surrounds the core and is divided into several layers, including the upper mantle, the transition zone, the lower mantle, and the D" layer (Figure 1.1). The boundaries of these layers are defined by discontinuities in seismic velocities, which correspond to major compositional and structural phase changes of the minerals and rocks composing them. On top of the silicate mantle lies the crust.

1.2 Lower Mantle

The mantle constitutes 82% of Earth's volume and 65% of its mass [21], extending from the base of the crust to the top of the metallic core. Within the mantle, three distinct changes in seismic wave velocity have been revealed at depths of about 410, 660, and 2700 km (Figure 1.1). The 660 km discontinuity separates the lower mantle from the upper mantle. We will focus on the lower mantle and its mineralogy which is the most relevant background for this thesis.

1.2.1 Bulk Composition and Mantle Minerals

Without access to natural samples, the composition of the lower mantle is mainly determined by melt-residue relations. Ringwood [22] first proposed the concept of a pyrolitic composition (i.e., pyrolite) representing the composition of the primitive upper mantle (PUM) before the extraction of magmas that formed the crust (the melt) and left a peridotite residue (the residue after melting), and is thought to represent the composition of the lower mantle. Pyrolite was constructed by mixing mantle-derived magma (basaltic or komatiitic) with refractory residue (peridotites) in proportions [23, 24]. The broad range of chemical compositions of sampled peridotites led to further refinements of the pyrolite composition. Moreover, the density of pyrolitic mantle matches that of PREM for the mantle. Pyrolite composition, therefore, represents a fair average of the bulk composition of the mantle. Mineral proportions in a pyrolitic mantle [25] are shown in Figure 1.5.

In pyrolitic composition, bridgmanite (Brg), ferropericlase (Fp), and calcium silicate perovskite (CaPv) have been known as the major phases in the lower mantle. Ferropericlase has a cubic 'rock-salt' structure (NaCl-type) with the chemical formula (Mg, Fe) O. Its Fe composition determines the name of the mineral: ferropericlase for Mg-rich minerals and

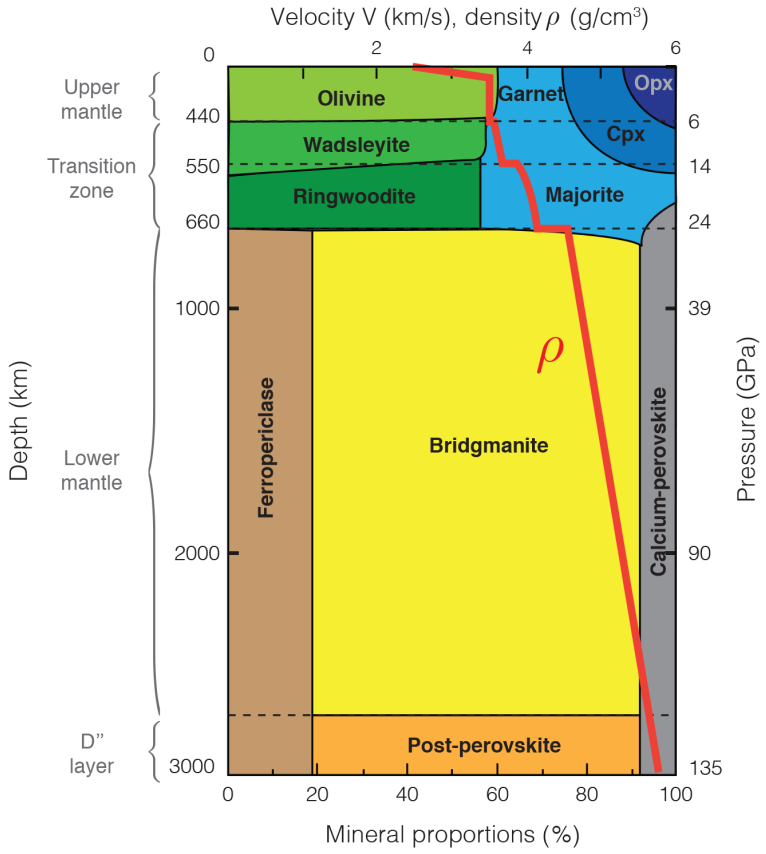

Figure 1.5: Mineral proportions in a pyrolitic mantle. Image from [6].

magnesiowüstite for Fe-rich minerals. Ferropericlase has been shown to incorporate almost exclusively Fe^{2+} [26]. Bridgmanite, which was previously called magnesium silicate perovskite, was renamed 'Bridgmanite' in honour to Percy Bridgman, an eminent researcher in high-pressure mineralogy. It has an orthorhombic structure in the lower mantle condition with the octahedral and dodecahedral sites occupied by Si^{4+} and Mg^{2+} (or Fe^{2+}) respectively. Bridgmanite incorporates Fe^{2+} but also Fe^{3+} in the presence of Al in the chemical system [26]. Calcium silicate perovskite is proportionally minor but is likely the predominant host for numerous trace elements that record chemical differentiation events [27]. It exhibits cubic symmetry at the temperature range of the lower mantle (>1900 K) but is possibly distorted in subducted cold materials [28].

1.2.2 Seismic Heterogeneities

Large Low Shear Velocity Provinces (LLSVPs)

The Large Low Shear Velocity Provinces (LLSVPs) are two anomalously large structures detected at the bottom of the mantle with a few percent of the shear velocity reduction [8,

29], and are hotter and denser than the surrounding mantle [8]. The origin of the LLSVPs has been much debated for many years between purely thermal models [30, 31] and thermo-chemical models [29, 32]. The locations of LLSVPs are also shown to be correlated with hotspot volcanoes on Earth [33].

Ultra-low Velocity Zones (ULVZs)
Ultralow velocity zones (ULVZs) [34, 35] are small-scale (with thicknesses of about 5-50 km) seismic anomalies detected adjacent to the core-mantle boundary (CMB) with significant velocity reductions up to 25% and 50% for P wave and S wave. The origin of ULVZs is highly controversial. A number of models have been suggested: the presence of dense Fe-enriched mantle minerals [36, 37]; chemical reactions between the mantle and core [38]; partial melts of the lowermost mantle [39, 40]; melt derived by subducting slabs [41, 42]; and recent observations of the locations of the ULVZs point to an independent origin of the ULVZs from the LLSVPs [43].

To understand the seismic heterogeneities in the lower mantle, it is crucial to understand the melting relationships in the lower mantle, and this will be one of the focuses of Chapter 4 of this thesis.

1.3 Magma Ocean Crystallization and Mantle Differentiation

Planets progressively grow from the aggregation of matter in the protoplanetary disk is called accretion. Earth itself has formed from the accretion of several proto-planets following their impacts. Indeed, it is believed that the Moon was formed by a giant impact between Earth and a Mars-sized body in Hadean [44]. The energy transferred to Earth completely (or extensively) melted the planet, formed a magma ocean, and induced an efficient differentiation of Earth. The layered structure of Earth was shaped through the crystallization of this melt.

Although no rock samples from the Hadean are preserved, radiogenic isotope analysis on Archean rocks (3.8-2.5 Ga) supports the early mantle differentiation during the Hadean [46, 47] It is possible that early mantle differentiation events were related to magma ocean processes. Liebske et al. [45] proposed that the deep magma ocean may have led to significant chemical differentiation and possibly stratification of the mantle by crystal fractionation, as depicted in Figure 1.6.

Suppose a magma ocean extended well to the present-day lower mantle or possibly to the core-mantle boundary (Figure 1.6); the most likely candidates for crystal fractionation are the lower mantle phases Brg, Fp, and CaPv. Thus, understanding the melting relations in this pressure range is crucial for investigating the effects of deep magma ocean crystallization

on mantle differentiation. Furthermore, once the most likely liquidus phase(s) is(are) determined, the partitioning of trace elements between crystallizing phases and the residual silicate melt provides significant geochemical constraints on how much of a crystal reservoir may exist in the chemically distinct reservoir in the lower mantle [27], without violating the chondritic pattern of RLEs of the upper mantle. Particularly, the fractionation of Brg would produce a Si-enriching lower mantle and help explain the upper mantle's elevated Mg/Si ratio.

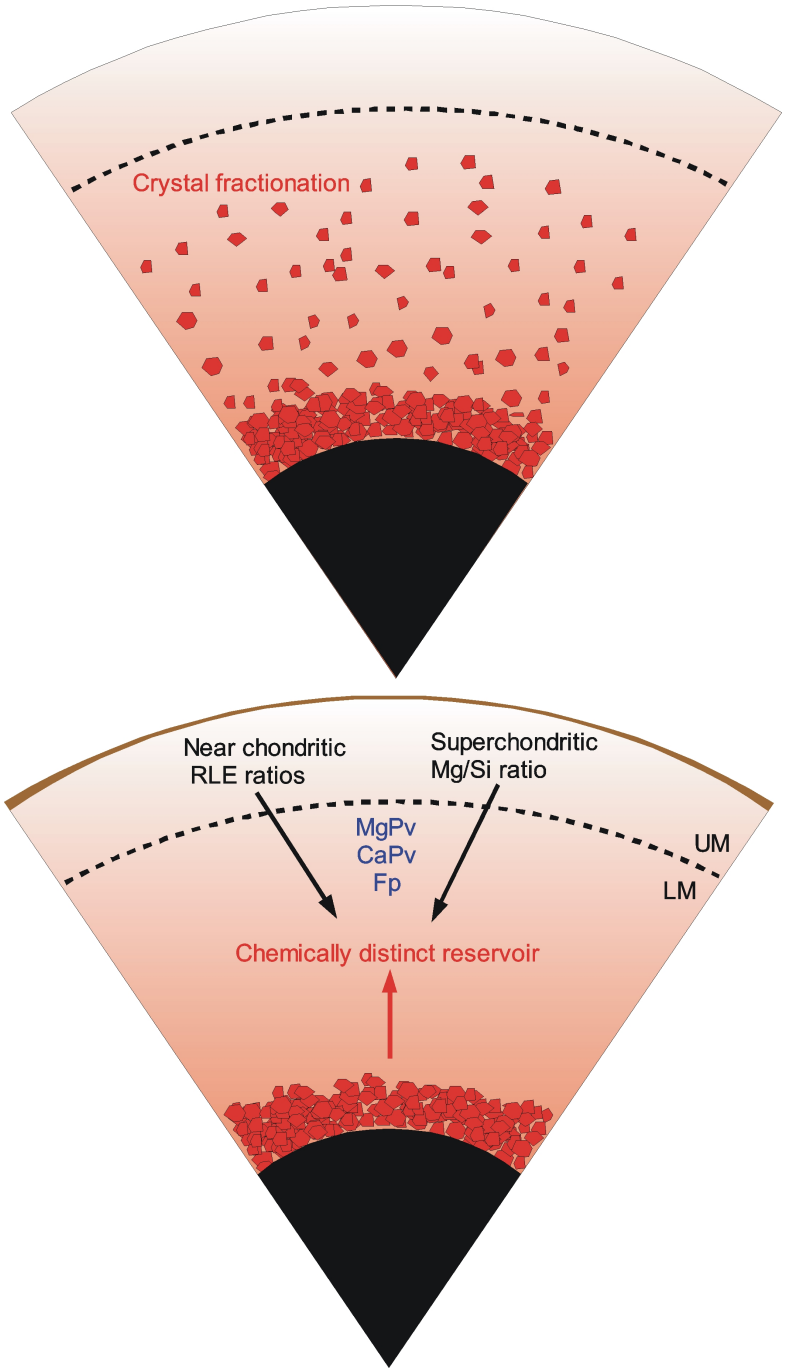

Figure 1.6: Possible process during magma ocean crystallisation. Crystal fractionation at lower mantle pressure took place and resulted in the formation of a chemically distinct reservoir in the lower mantle. Image from [45].

2 Chemical Quantification in STEM

2.1 Scanning Transmission Electron Microscopy

Since its invention in the 1930s [48], transmission electron microscopy (TEM) has become one of the most important techniques for analyzing various materials [49–51]. As was first proposed by Rayleigh [52], the minimum resolvable distance between two objects is proportional to the wavelength of the illuminating source. The smallest wavelength of light that we can reach using optical systems is about 400 nm, leading to the resolution limit of traditional visible light microscopes being about 200 nm. By contrast, electron wavelengths are typically on the order of 1×10^{-3} nm for typical transmission electron microscope energies (100-300 keV) and therefore have the potential to resolve not only nanometre-size features but further down to the atomic level.

Two modes of operation are commonly used in TEM: conventional TEM (CTEM) and scanning (STEM). CTEM is similar to a traditional light microscope, for they both use a broad parallel illumination. In STEM, a focused probe is scanned across a sample in a pixel-by-pixel manner (Figure 2.1(a)). The two modes are indeed interrelated by the principle of reciprocity. A significant advantage of STEM is that, at each point of the scan, multiple signals can be collected simultaneously by different detectors. The raster-scanned approach is particularly useful in spectroscopy, where a single spectrum can be collected at each pixel using spectrum imaging (SI).

2.1.1 Electron-matter Interactions

Practically all of the detected signals in TEM stem from how the fast incident electrons that pass through the sample interact with the nuclei and shell electrons of the atoms constituting the sample. The interactions can be broadly classified as elastic or inelastic scattering,

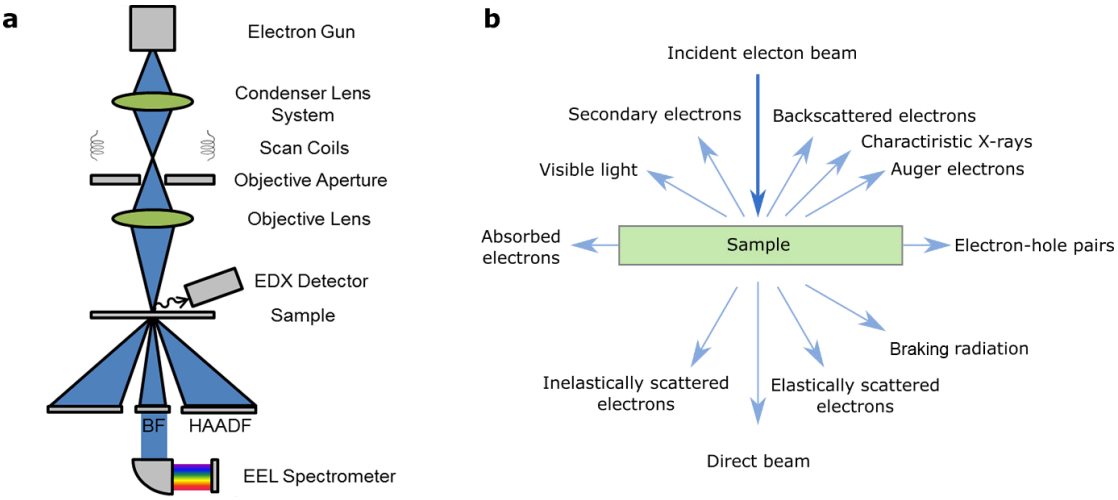

Figure 2.1: a) Illustration of the components of a scanning transmission electron microscope and the associated signals. b) A range of signals generated by interaction of the high-energy electron beam with the sample.

depending on whether energy is transferred during the scattering process. In inelastic scattering, the incident electrons lose a significant amount of energy, whereas in elastic scattering, they are deflected without energy loss. In reality, elastic scattering also results in a transfer of energy, but this energy is negligible in comparison to the energy of the incident electrons (< 1 eV vs. 100-300 keV) [53]. Figure 2.1(b) summarizes the most important signals that arise from electron-matter interactions in TEM.

Elastic Scattering

Electrons that are elastically scattered interact with atoms through Coulomb forces, which include electron-electron interactions and electron-nucleus interactions. Generally, electron-electron interactions lead to relatively small scattering angles and coherent scattering. In contrast, electron-nucleus interactions dominate for larger scattering angles and are known as Rutherford scattering. Its differential cross-section—the probability of scattering into a small solid angle dΩ at an angle θ, is defined by

$$\frac{d\sigma(\theta)}{d\Omega} = \frac{e^4 Z^2}{16(E_0)^2(\sin\frac{\theta}{2})^4} \tag{2.1}$$

where e is the unit electric charge, Z is the atomic number of the nucleus and E_0 is the incident electron beam energy [54]. It can be seen that the scattering cross-section is proportional to Z^2 of the nucleus at a fixed beam energy E_0. This is the fundamental principle behind high-angle annular dark-field (HAADF) imaging in STEM, also known as Z-contrast imaging. In practice, the screening effect of the electron cloud modifies the scattering cross-section to some degree and itself also exhibits a dependency on Z.

Inelastic Scattering

Incident electrons experience energy loss in inelastic scattering events due to electron-electron collisions or a collective excitation with outer-shell electrons. As displayed in Figure 2.1(b), such collisions result in the transfer of energy from the incident electron to the sample, which subsequently produces a variety of observable signals such as x-rays, secondary electrons, visible light, etc. The lost energies of incident electrons and the probability of these events contain information about the properties of the studied sample, such as its chemical composition, electronic structure, etc. Furthermore, improvements in TEM instruments over the past few decades have made it possible to (near)-simultaneously record the energy-loss spectrum of the incident electrons that pass through the sample and the spectrum of the secondary signals, providing an excellent opportunity for a thorough investigation of the materials.

2.2 High-angle Annular Dark-field Imaging

As the name suggests, HAADF imaging uses an annular detector to collect scattered electrons over a threshold scattering angle (Figure 2.1(a)). As we mentioned, the primary interaction between the incident electrons and the specimen is Rutherford scattering at high scattering angles. For a single nucleus, the probability of scattering is proportional to its atomic number $Z^{1.6-2}$, which underlies the elemental sensitivity of this imaging technique. However, for the sample as a whole, the total scattered intensity scales with the total number of atoms in the interaction volume and, therefore, with the density and projected thickness of the sample. That is often referred to as the ”mass-thickness contrast”.

Although HAADF imaging is frequently used to study the elemental distribution in bimetallic nanoparticles [55–57] due to the intensity dependence on the atomic number, in many other cases, it is insufficient. The main issue arises from the sensitivity of HAADF to both mass-density as well as the projected thickness of the sample. We cannot determine *a priori* from an observed bright area whether it is made of a heavy substance or simply has a high thickness. Also, it is challenging to distinguish between materials with similar densities Z.

For these reasons, HAADF imaging is not always sufficient to conduct a chemical analysis of materials. In a nutshell, HAADF is primarily used for answering qualitative questions—for example, to confirm the presence of a core-shell nanostructure or to identify elements on atomic resolution images. To unambiguously determine and quantify elements present within a sample, spectroscopic techniques, such as energy-dispersive X-ray spectroscopy (EDXS) or electron energy-loss spectroscopy (EELS), are more appropriate.

2.3 Energy-dispersive X-ray Spectroscopy

2.3.1 X-ray Generation

Characteristic X-rays

High-energy incident electrons in TEM can ionize the atoms in the sample by displacing their inner-shell electrons (Figure 2.2(a)). The electron vacancies created in this manner are energetically unfavorable. Three atom de-excitation processes can occur after the inner-shell ionization: X-ray emission, Auger electron emission, and Coster-Kronig transition (Figure 2.3). When an outer-shell electron fills the inner-shell vacancy, a characteristic X-ray photon is released with an energy equal to the energy difference between the inner and outer electron shells.

Alternatively, it is possible that the energy will be transferred into another atomic electron, resulting in the ejection of that electron (i.e., the Auger electron). This process becomes a Coster-Kronig transition if the ejected electron and the outer-shell electron that fills the vacancy are in the same shell. The probability of X-ray versus Auger emission is described by the fluorescence yield, ω, which is the ratio of X-ray emissions to inner-shell ionizations. The ω is a strong function of atomic number and decreases at a rate proportional to Z^4 as Z decreases [54]. For carbon ($Z = 6$), ω is $\sim 10^{-3}$; it hence requires ionizations of 1000 carbon atoms to produce a single C Ka X-ray. Therefore, EDXS is not suitable for analyzing light elements. Instead, EELS could be used because we can always detect the energy-loss electron whether or not it has generated an X-ray.

Different types of characteristic X-rays may be generated for a given vacancy depending on which subshell the filling electron is from. Figure 2.2(b) gives a diagram of the possible electron transitions in the atom with associated X-rays labeled. Since each chemical element has a unique set of characteristic X-ray energies, they can be used to identify the atoms comprising the materials unambiguously. Moreover, the total intensity of the generated X-rays is proportional to the number of atoms interacting with the electron beam, which allows for quantifying the elemental composition of the studied materials.

Bremsstrahlung X-rays

Another type of X-ray is bremsstrahlung, which can be translated as "braking radiation." When the incident electron interacts with the Coulomb field of the nucleus, it experiences a substantial change in momentum, and during this process, it may emit an X-ray. The incident electron may lose any amount of energy, depending on the strength of the interaction, and release X-rays with continuous energy up to the beam energy.

It is common to use the Kramers cross-section [59] to predict the bremsstrahlung production

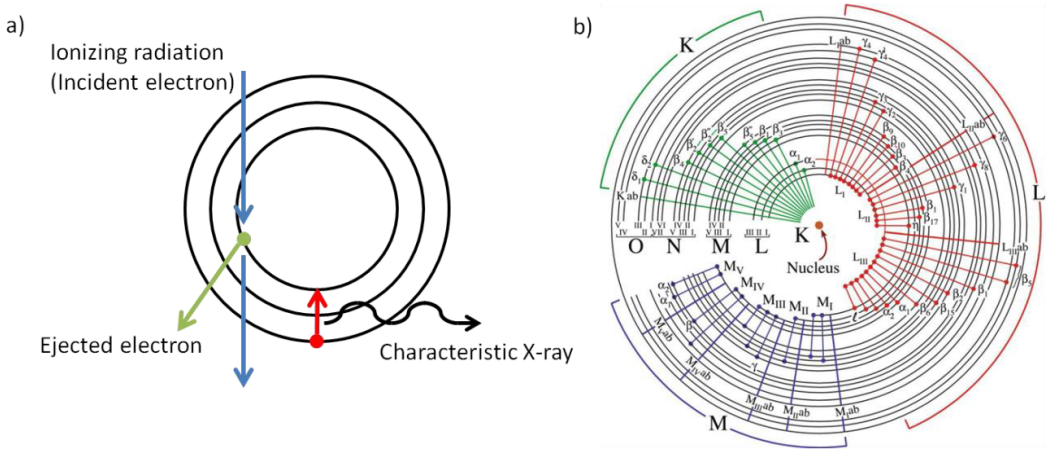

Figure 2.2: a) Diagram of the process in which an incident electron causes a characteristic X-ray to be emitted from an atom. b) Diagram of the possible electron transitions in the atom with associated X-rays labelled. Image from [54].

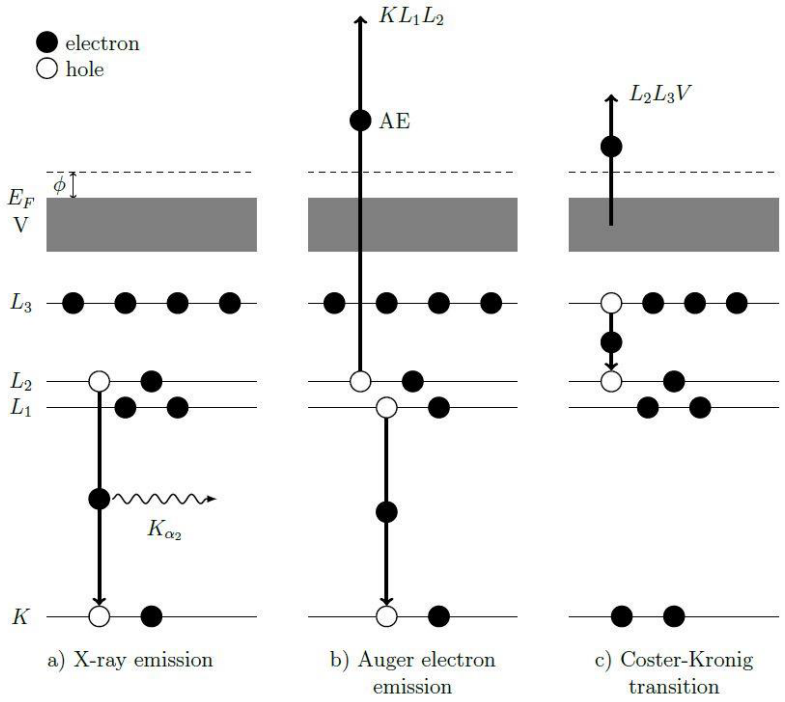

Figure 2.3: a) X-ray emission, b) Auger electron emission, c) Coster-Kronig transition as possible de-excitation processes after the K- or L-shell ionization. Image from [58].

rather than the probability of interaction. The approximate expression used is

$$N(E) = \frac{KZ(E_0 - E)}{E} \tag{2.2}$$

where $N(E)$ is the number of bremsstrahlung photons of energy E (i.e., the intensity) produced by electrons of energy E_0, K is Kramers' constant, and Z is the atomic number of the ionized atom.

The bremsstrahlung is continuous, on which the characteristic X-rays are always superimposed. In contrast to the isotropic emission of the characteristic X-rays, the bremsstrahlung is highly anisotropic and shows strong forward scattering. X-ray spectrometers are, therefore, generally placed at large scattering angles to collect many more useful characteristic X-rays than relatively useless bremsstrahlung X-rays.

The bremsstrahlung intensity depends on the average Z of the sample, which is useful to biologists or polymer scientists who are interested in this aspect of their samples. However, materials scientists are often troubled by this signal as it may obscure characteristic X-ray lines that offer more accurate quantitate chemical information.

Spurious X-rays and Common Artifacts
Many different artifacts are introduced to the spectrum due to the scattering of X-rays after their initial creation, the signal processing of electronics, or the characteristics of the detector. Some of these are automatically corrected by the acquisition software, while some need to be examined and corrected manually. The most common artifacts are summarized in Table 2.1.

Common system X-rays may come from the support grid and sample holder (Cu), the pole piece (Fe and Co), the detector (Si and Pb), and, counterproductively, the X-ray collimator (Zr in the case of the Super-X detector system). It is possible to avoid the production of some of these system X-rays by using holders and grids manufactured from Be, which only produce low-energy X-rays that neither can be resolved by the EDX detector nor fluoresce higher-energy X-rays elsewhere.

2.3.2 X-ray Absorption

When characterizing thin TEM samples, X-ray absorption effects are usually ignored as they are considered small. However, this is not the case for all specimens. The absorption effects can be pronounced for light elements with the energy of X-ray lines being less than 2 keV, such as O. The absorption of X-rays in matter follows the exponential attenuation law

Table 2.1: Common artifacts in EDXS.

Spurious X-rays	X-rays come from the specimen but are not generated by the electron probe in the chosen analysis region.
System X-rays	X-rays that come from parts of TEM other than the specimen.
Coherent bremsstrahlung	A bremsstrahlung spectrum that contains small, Gaussian-shaped peaks due to the coulomb interaction between the electron beam and the periodically spaced nuclei in the crystal specimen.
Sum peak	Two X-rays enter the detector at exactly the same time. The analyzer then registers an energy corresponding to the sum of the two X-rays.
Escape peak	An incoming X-ray of energy E fluoresces a Si Kα X-ray which escapes from the intrinsic region of the detector. The detector then registers an apparent X-ray energy of $(E-1.74)$ keV
Internal fluorescence peak	Si Kα X-rays generated in the dead layer of the detector

proposed by Beer and Lambert for light, where X-ray intensity is given by

$$I = I_0 \exp[-(\frac{\mu}{\rho})\rho l] \tag{2.3}$$

where I is the X-ray intensity after absorption, I_0 is the incident X-ray intensity, $\frac{\mu}{\rho}$ is the mass absorption coefficient, ρ is the density of the sample and l refers to the absorption path length. The density and mass attenuation coefficient both strongly depend on the atomic number, so materials with a higher atomic number typically absorb X-rays more strongly. The mass attenuation coefficient also depends on the energy of the X-ray. Lower-energy X-rays, therefore, are more easily absorbed and attenuated than those of higher energy.

In a thin film, the X-ray path length is given by $l = z\csc\alpha$ [60], where z is the depth of the X-ray produced in the sample and α is the take-off angle. Under the assumption that the X-rays are generated uniformly through the depth of the thin film, the absorption correction factor (ACF) becomes

$$A_i = \frac{(\mu/\rho)^i_{comp}\rho t \csc\alpha}{1-\exp[-(\mu/\rho)^i_{comp}\rho t \csc\alpha]} \tag{2.4}$$

where $(\mu/\rho)^i_{comp}$ is the mass absorption coefficient of X-ray i in a compound, and ρt is the mass-thickness of the sample. The ACF term (Equation 2.4) can be incorporated into the

ζ-factor method for elemental quantification, which we will introduce later.

X-ray Fluorescence
As a result of photoelectric absorption, the atom will undergo a de-excitation process. If the energy of the electron-induced X-ray is greater than the excitation energy of a certain shell of the targeted atom, a secondary X-ray will be produced, which is termed X-ray fluorescence. Generally, fluorescence corrections are negligible, except in the rare case where they are crucial for accurate specimen analysis.

2.3.3 X-ray Detection

The proportion of generated X-rays that are ultimately collected is determined by several factors: the solid angle that the detector subtends, the absorption of X-rays in the sample, and the detector characteristics. Many studies have been conducted to increase this X-ray "collection efficiency."

Detector Development
Most commercial X-ray detectors for TEM are silicon semiconductors. When X-rays traverse the detector, a number of electron-hole pairs proportional to the X-ray energy are generated. They create a current signal (electron cloud), which is amplified by a field-effect transistor, and then digitally encoded and stored in the proper energy channel. Noise, whether electronic or thermal, is also detected as small changes in voltage in the same manner as characteristic X-rays. The noise may be isolated and assigned to channels with energies around 0 eV, causing a large peak at this value, or it may be detected on top of a step of a characteristic X-ray, leading to the broadening of the characteristic X-ray peak and hence limiting the energy resolution of the technique (typically 125-135 eV). The detector may also contribute to the spectrum's artifacts, as summarized in Table 2.1. In addition, detectors may also suffer from incomplete charge collection, resulting in a shoulder on the low-energy side of characteristic peaks.

Most modern TEMs use silicon-drift detectors (SDDs), as opposed to Lithium-drifted silicon detectors (Si(Li)) that are commonly used for older generations of microscopes. The SDD features a large n-doped silicon crystal with concentric p-doped rings embedded on the back side of the detector. This design shortens discharge times, leading to faster processing and a higher X-ray count rate and hence better counting statistics than that of the Si(Li) detector. One disadvantage of SDD is that it is typically thinner than Si(Li) detectors, implying that they do not detect all incident X-rays above a certain energy level. As a result, the detection efficiency of SDD decreases as X-ray energy increases.

Detector Geometry

Traditional EDXS detector geometry in STEM consists of a single detector with a solid angle of 0.1-0.3 sr, implying that only 0.8-2.4% of the emitted X-rays are collected. The poor collection efficiency makes EDXS a very inefficient method. Therefore, an important portion of the EDXS methodology development has been centered on extending the solid angle of detectors to boost the collection efficiency.

The debut of SDD has allowed for larger detector sizes and enabled the detector to be placed closer to the sample, both extending the solid angle of detectors. Meanwhile, novel detector geometries have also been proposed, including a dual detector setup [61], an annular detector placed above the sample [62], and a π steradian detector placed after the sample [63]. The Super-X detector, which is a component of FEI's ChemiSTEM technology, has unquestionably achieved the most commercial success and is the one that is used in this thesis [64]. In this setup, four separate SDDs are positioned symmetrically within the polepiece of the STEM, which increases the solid angle up to 0.9 sr [64].

More recently, the electron microscopy community has witnessed a significant improvement in collection efficiency utilizing novel configurations of X-ray detectors. Notably, the X-ray Perimeter Array Detector (XPAD) [65], developed by the distinguished researcher N. Zaluzec, demonstrates an impressive collection solid angle of 4.5 sr. Based on this concept, Thermo Fisher Scientific has introduced a state-of-the-art commercial detector, Ultra-X, which provides a solid angle of 4.45 sr in un-shadowed condition and 4.04 Sr with a double tilt analytical holder. These developments open up new capabilities in STEM-EDXS analysis of beam-sensitive materials and faster mapping for more stable specimens.

2.3.4 X-ray Shadowing

In EDXS, X-ray signals can be prevented from being detected by the penumbra of the specimen holder, which is known as X-ray shadowing and is illustrated in Figure 2.4(a). The shadow cast onto a detector leads to a loss of X-ray signals, resulting in systematic errors in EDXS quantification. The extent of detector shadowing depends on the geometry of the sample holder and the EDXS detector, and varies with the sample tilt angle. Tilting the sample is therefore desirable for some detector-holder setups in order to minimize the X-ray shadowing, as illustrated in Figure 2.4(b).

In EDXS tomography, X-ray shadowing has been shown to introduce artefacts into the reconstruction of a tilt series in a manner similar to the missing wedge effect [66]. Various efforts have been made to address this issue, such as using a needle-shaped sample to avoid missing projections due to X-ray detector shadowing [67, 68] and using a sample

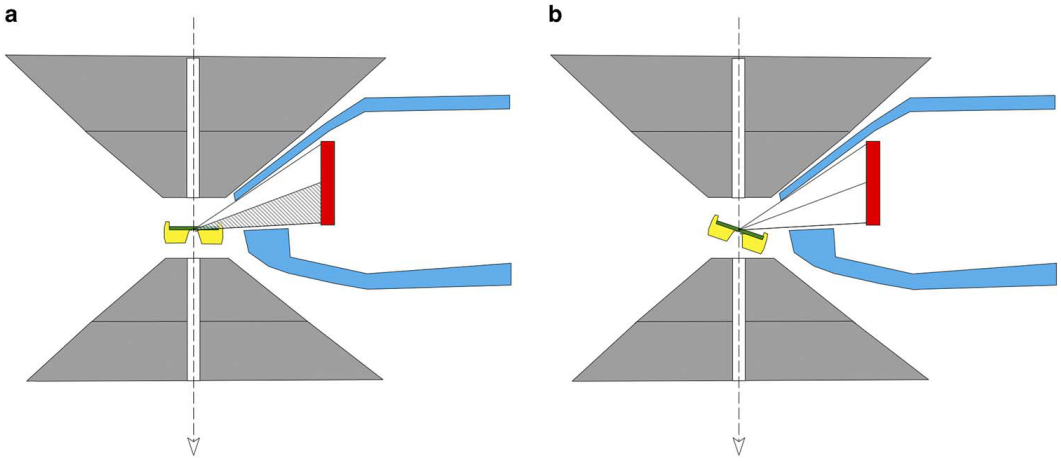

Figure 2.4: a) Cross-section of a STEM-EDXS geometry illustrating the X-ray shadowing of a side mounted X-ray detector by the penumbra of the holder. b) Tilting of the specimen holder to mitigate shadowing of the detector by the holder body allowing the full collection angle to be realized. Image from [54].

holder that minimizes or eliminates detector shadowing [69, 70]. When needle specimens or low-profile EDXS holders are not available, it is desirable to correct for shadowing-induced intensity variations either during acquisition or through post-processing methods. Yeoh et al. [71] proposed a simple model to predict and correct for X-ray shadowing, which requires two shadow angle inputs (an upper and lower shadow angle) to define the limits of the shadow. These parameters, combined with the knowledge of detector geometry, are used to characterize the shadowing of an EDX detector over a full sample tilt range, assuming a circular detector geometry in the model. This approach can also be applied to other types of detectors and associated geometries.

2.3.5 Quantification Methods

Cliff-Lorimer Method

The approach established by Cliff and Lorimer [72] has traditionally been used for the elemental quantification of EDXS. This method uses a sensitivity factor (k_{AB}) to relate the intensity of a pair of X-ray peaks (I_A and I_B) to their weight fraction (C_A and C_B).

$$\frac{C_A}{C_B} = k_{AB}\frac{I_A}{I_B} \tag{2.5}$$

The composition can easily be determined in a binary system combining $C_A + C_B = 100\%$ (i.e., the sum-to-one rule) with Equation 2.5. For more complicated material systems, this can easily be expanded by adding extra equations in the same form as Equation 2.5 and

combined with the sum-to-one rule.

The k-factor can be calculated using Equation 2.6 [73], where Q is the ionization cross-section, ω is the fluorescence yield, a is the line weight (relative transition probability), ϵ is the detector quantum efficiency, and A is the atomic weight of the element that emitted the X-ray line.

$$k_{AB} = \frac{(Q\omega a)_A A_B \epsilon_A}{(Q\omega a)_B A_A \epsilon_B} \tag{2.6}$$

However, the uncertainties of the ionization cross-section calculation result in large errors in the k-factor calculation (15-20%) [54]. A more accurate method is to experimentally measure the k-factors using standard samples of known composition [74]. Unfortunately, the experimental procedure is extremely time-consuming and tedious. Moreover, the procedure must be redone if anything changes in the instrumental setup. Also, multi-component thin film standards required may not always be available.

ζ-factor Method

A relatively recent technique for EDXS quantification in TEM is the ζ-factor method. It was first introduced by Watanabe et al. in 1996 [75] and later modified in 2006 [76]. It proposes utilizing thin films of pure-element as standards. Additionally, the mass-thickness and composition are determined simultaneously in the ζ-method, allowing absorption effects to be corrected using EDXS data alone.

The ζ-factor method is based on the assumption that the intensity of an X-ray line from an element A in a thin film sample is proportional to the mass-thickness and composition and can be expressed as

$$I_A = \frac{N_v Q_A \omega_A a_A}{M_A} C_A \rho t (\Omega/4\pi) \epsilon_A D_e \tag{2.7}$$

Where Q_A, ω_A, a_A, ϵ_A are the ionization cross-section, fluorescence yield, transition probability, and detector quantum efficiency of the X-ray line, N_v is Avogadro ' s number, M_A is the atomic weight of the element A, C_A represents the weight percent of the element A, ρ is the density of the sample, $(\Omega/4\pi)$ is the fraction of characteristic X-rays that reach the detector with Ω as the collection solid angle. D_e is the total electron dose that is expressed as

$$D_e = \frac{I_p \tau}{e} \tag{2.8}$$

where I_p is the in-situ beam current, τ is the acquisition time and e is the electron chagre. When we define the ζ-factor as

$$\zeta_A = \frac{M_A}{N_v Q_A \omega_A a_A (\Omega/4\pi) \epsilon_A} \tag{2.9}$$

we obtain

$$\rho t = \zeta_A \frac{I_A}{C_A D_e} \tag{2.10}$$

By combining Equation 2.10 and the sum-to-one rule for total concentration, the composition and mass-thickness of all the elements are given as

$$\rho t = \sum_j^N \frac{\zeta_j I_j}{D_e}, \quad C_A = \frac{\zeta_A I_A}{\sum_j^N \zeta_j I_j}, \quad \ldots, \quad C_N = \frac{\zeta_N I_N}{\sum_j^N \zeta_j I_j}, \tag{2.11}$$

As mentioned earlier, the ACF term can be incorporated into Equation 2.11 to achieve an easier absorption correction than the Cliff-Lorimer method.

Although this approach necessitates thickness calibration and beam current measurements, it is more accurate than the Cliff-Lorimer method. In addition, it allows benchmarking the analytical capabilities of different microscopes.

Partial Scattering Cross-section Method

In theory, the measured intensities from HAADF, EDXS, and EELS can be interpreted as appropriate partial scattering cross-sections [77–80]. Similar to the estimation of HAADF scattering cross-section [78], it is possible to determine the partial scattering cross-sections for EDXS [79] and EELS [53, 81]. The scattering cross-section approach has been shown to simplify the quantification procedure in HAADF, demonstrating robustness to a wide range of imaging parameters, including tilt, defocus, the field of view, source size, and astigmatism [78]

For thin samples, where absorption, fluorescence, multiple scattering, and channeling [82] can be neglected, the EDXS partial scattering cross-section for a single atom of element A is given by

$$\sigma_A^{EDXS} = \frac{I_A e}{i \tau n_A t} \tag{2.12}$$

where I_A is the X-ray counts detected from the sample, e is the electron charge, i is the probe current, τ is the exposure time, n_A is the volumetric number density of the elements being detected, t is the sample thickness.

The partial cross-section method is similar to the ζ-factor method, and it can be mathematically transformed as

$$\sigma_A^{EDXS} = \frac{M_A}{N_v \zeta_A} \tag{2.13}$$

where M_A is the atomic mass of element A, and N_v is Avogadro ' s constant. Thus, the partial cross-section method gives the composition in number of atoms rather than weight percent.

This method requires the parameters of the microscope to be meticulously characterized

in order to reach a good agreement with the theory, yet discrepancies still exist [83, 84]. Importantly, representing EDXS signals using a partial scattering cross-section gives us a chance to use HAADF, EDXS, and EELS signals in a correlative way to quantify challenging samples accurately.

2.4 Electron Energy-loss Spectroscopy

EELS is a technique for collecting and analyzing electrons that have lost energy due to inelastic scattering processes that occurred during the electron-matter interaction. The EEL spectrometer operates similarly to a light prism, using a magnetic prism to disperse electrons of different energy spatially onto an array of detectors—for example, a CCD camera (Figure 2.1(a)).

Figure 2.5 gives an example of a typical EELS spectrum. The spectrum is generally divided into two main regions: the low-loss region, which contains energy losses associated with phonons and plasmons, and the core-loss region, which contains energy losses associated with ionization events.

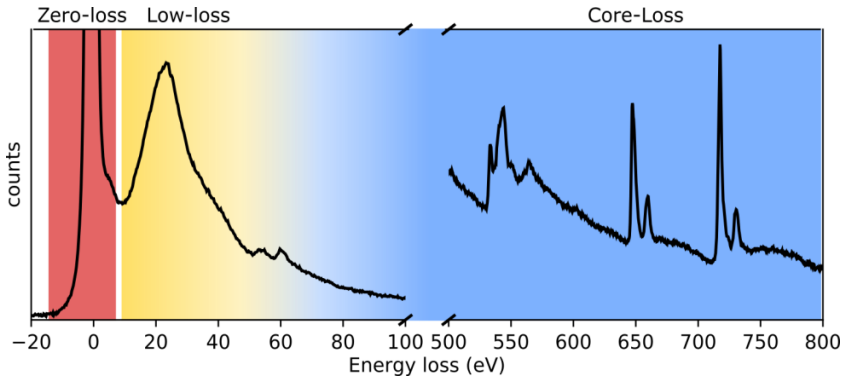

Figure 2.5: (Fe, Mg)O spectrum. Zero loss (red), low-loss (yellow) and core-loss (blue) regions are highlighted. Image from [85].

2.4.1 The Zero-loss Peak

The first feature of a EELS spectrum is the zero-loss peak (ZLP), which contains all of the unscattered and elastically scattered electrons. ZLP has an extremely high intensity compared to all other features of the spectrum, and its width gives an estimation of the energy resolution of the system.

Additionally, its intensity (I_{ZLP}) can be related to the thickness of the specimen (t).

$$\frac{t}{\lambda} = ln(\frac{I_T}{I_ZLP}) \tag{2.14}$$

where λ is the mean free path of electrons in the sample and I_T is the intensity of the whole spectrum. On the other hand, the position of ZLP is frequently used to calibrate any offsets of the system.

2.4.2 The Low-loss Spectrum

The low-loss region is typically defined from 0-50 eV, and Table 2.2 lists the interactions exhibited in this region along with their energy ranges. The dominating features are plasmon peaks. These and other features of the low-loss region are excited by the interactions between fast-moving electrons and weakly bound outer-shell electrons.

Table 2.2: Spectral features in the low-loss spectrum.

Transition	Energy loss (eV)
Vibrational excitations	0.05-0.5
Surface Plasmon	1-5
Band Gap	0-10
Bulk Plasmon peak	7-50

Bulk plasmonic excitations appear as a broad and intense peak or series of peaks. The feature helps determine composition as its position can be inferred from the number of valence band electrons and other composition-related parameters [53]. Also, the plasmon peak's width correlates with the excitation's lifetime. Furthermore, the whole low-loss is related to the imaginary part of the dielectric function. As a result, the relationship can be utilized to study the material's dielectric property in the framework of Kramers-Kronig transformations [53].

In addition to the collective plasmon excitation, valence electrons can also be excited individually by a fast electron and be lifted to a higher energy state. In semiconductors, these excitations can be, in principle, used to obtain information about their band structures [86]. The surface plasmon is created by surface charge oscillation in the material influenced by the incident electrons. A nanostructure's surface plasmon distribution can be attributed to the effects of size and quantum confinement and some of its optical characteristics [87, 88]. Several transitions, such as phonon generation and other vibration excitations on crystalline lattices, give rise to small energy losses at a few meV. It was until just recently that these

features were resolved due to the energy resolution improvement of EELS [89].

2.4.3 The Core-loss Spectrum

The core-loss regime is typically defined as energy losses above 100 eV. These transitions often result via atom ionizations. Since the energy loss of incident electrons in these ionizations is distinctive for a specific element and shell type, they can be used to identify elements. The ionization edges are usually denoted by the atomic shells, such as K, L_1, $L_{2,3}$, or $M_{4,5}$ edges.

Depending on the shape, ionization edges can be grouped into three categories (Figure 2.6): white lines, hydrogenic edges, and delayed edges. The shape relates to not only the type of elements and the shell of excitation but also the density of states in the initial and final energy levels of the ionized atomic electron. Analysis of the shape of ionization edges is known as energy-loss near-edge structure (ELNES). It can probe the electronic structure and, thereby, the structural and chemical environment of atoms [82]. For example, the oxidation state of many transition metals can be determined by the relative intensity or the position of their white line peaks [90, 91]. However, in the core-loss regime, the measured chemical signals of interest are often superimposed on a background dominated by single and collective low-loss electron excitations, rendering the target spectral features obscured.

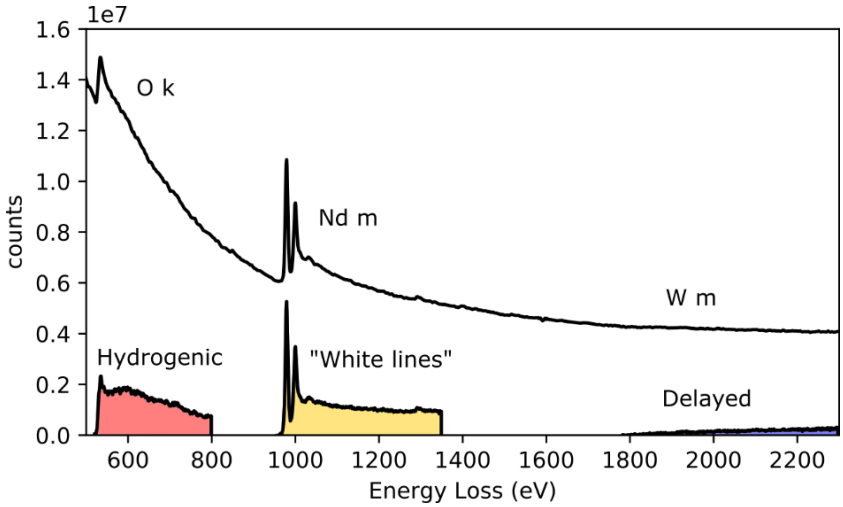

Figure 2.6: EELS spectrum of WNdO, showing a hydrogenic O K edge, Nd M edge white lines and a delayed w M edge. Image from [85].

2.4.4 Dual EELS

Dual EELS is an acquisition mode that was developed recently. As the name implies, it enables the low-loss and core-loss parts of the spectrum to be recorded at each pixel separately [92,

93]. A fast beam switch (i.e., fast shutter) was integrated into the system to record the dual-spectrum separately with individual time ratios, thus overcoming the limited dynamic range of the CCD detectors [92, 94]. The fast shutter has a microsecond response time, enabling rapid deflection of the beam and allowing a wide range of exposure times for data acquisition. A core-loss spectrum at each pixel will be recorded after a low-loss spectrum with the same electron optical conditions but in a different area of the CCD detector. The two spectra can later be spliced to give a full loss spectrum, including ZLP. The ZLP can be used to normalize the core edge intensities, allowing an absolute quantification [95], which is one of the most important advantages of Dual EELS over classic EELS. It is also possible to apply Fourier logarithmic deconvolution [96], which gives the single scattering distribution of all core loss edges.

2.4.5 Quantification Methods

The Integration Method

R. Egerton first proposed this method for EELS elemental quantification in 1978 [97]. More than forty years later, it is still the method of choice for most EELS elemental analysis. The integration method adopts a practical approach: instead of constructing a detailed model of the acquired EELS signal, which may be cumbersome in many cases, the method performs an edge-by-edge simplified analysis to obtain the quantitative elemental information.

The elemental concentration is calculated from the intensity of relevant ionization edges. Background subtraction is required in order to extract the net intensity caused by the specified transition. In general, this background is fitted with a power law function (AE^{-r}) where the fitting region is a window before the core-loss edge. The function is then extrapolated to the region above the ionization edge to model the background of the ionization edge. After background subtraction, the areal density of an element can be approximated as

$$I_{CL}(\beta,\Delta) \approx N I_{LL}(\beta,\Delta)\sigma(\beta,\Delta) \tag{2.15}$$

if acquired with a collection angle β and integrated over an energy window Δ. $\sigma(\beta,\Delta)$ is a partial cross-section for a specific element and edge, which can be either calculated from simulations or measured experimentally. $NI_{LL}(\beta,\Delta)$ is the integral over the low-loss spectrum up to an energy range Δ including the ZLP. $I_{CL}(\beta,\Delta)$ is the integral over the same energy range of the ionization edge after background subtraction. The concentration of a specific element can be calculated if the thickness of the sample t is known as $n = N/t$.

While Equation 2.15 provides absolute quantification, relative quantification comparing the ratio between elements is also useful. The ratio of the concentration of two different

elements C_A/C_B can be calculated as

$$\frac{C_A}{C_B} = \frac{I_{CL,A}(\beta,\Delta)\sigma_B(\beta,\Delta)}{I_{CL,B}(\beta,\Delta)\sigma_A(\beta,\Delta)} \tag{2.16}$$

Despite the popularity of the method, it suffers from several drawbacks that preclude or limit its usage in many practical situations:

- This method usually performs well for thin samples where the ionization edge is above 100 eV with a high SNR and no overlap with other edges [98]. However, these conditions are generally not met all the time.
- The cross-sections for ionization excitations are usually determined from atomic calculations; therefore, they do not consider solid-state effects like ELNES. Using energy windows greater than 100 eV is advised to reduce the effect of the ELNES on quantification; however, this is often not feasible due to the presence of other ionization edges in the same energy range.
- It can be exhaustive to manually perform the "integration approach" pixel by pixel while analyzing SIs. If we do it lazily and use the same windows to analyze the entire SI data "easily", the compositional differences may result in artifacts that are challenging to identify. Meanwhile, the analysis is user-dependent, and the reliability of the results will strongly depend on the user's skills.

The Model Fitting Method

To overcome some of the drawbacks of the integration method, Steele et al. [99] proposed to build a parametric model of the full core-loss spectrum without considering the multiple scattering and use curve fitting to determine the unknown parameters. A number of model fitting methods have been used to measure trace quantities [100] and quantify overlapping edges [101]. However, this method can be complex for routine use, as the model is either experimentally obtained, requiring the acquisition of reference spectra under the same experimental conditions, or is theoretically computed that needs intensive statistical modeling [64, 102–104].

2.5 EDXS-EELS Synergistic Analysis

EDXS and EELS are indeed complementary techniques. When the probability of characteristic X-rays generation is reduced for lighter elements, EELS instead contains intense and sharp edges even for elements located at the beginning of the periodic table, such as Be and B, making it a suitable technique for characterizing materials containing light elements.

While EELS is always complicated by an intense background resulting from the long tails of the low-loss signals, EDXS usually has a low background intensity and a high peak-to-background ratio. As a result, EDXS is preferred when the concentration of the element of interest is low and the elemental ionization edge energy is high, both of which make it challenging to separate the signal from the background in EELS.

2.5.1 Partial Scattering Cross-section Method

With recent developments in hardware and software in TEM, it is now possible to acquire the EDXS and EELS signals (near)-simultaneously at high speed for accurate elemental quantification. The first attempt at linking EDXS and EELS signals was made by Kothleitner et al. [105], where the ζ-factor of EDXS and the partial scattering cross-section of EELS were linked to their respective measured intensities as follows:

$$\zeta \times \sigma^{EELS} = \frac{I_{CL}^{EELS}}{I_{LL}^{EELS} I^{EDXS}} \times \frac{M_A}{N_v} \times D_e \tag{2.17}$$

For a compound of two elements A and B, the expression comes down to

$$\frac{\zeta_A}{\zeta_B} \times \frac{\sigma_A^{EELS}}{\sigma_B^{EELS}} = \frac{I_B^{EDXS}}{I_A^{EDXS}} \times \frac{M_A}{M_B} \times \frac{I_A^{EELS}}{I_B^{EELS}} \times \frac{A_B}{A_A} \tag{2.18}$$

where A_B and A_A are X-ray absorption terms.

In Equation 2.17, the expression is rather cumbersome to deal with, as a density conversion from kg/m^3 to $atoms/m^3$ is required. Writing the EDXS signal in partial scattering cross-section notation would result in

$$\sigma^{EELS} = \frac{I_{CL}^{EELS}}{I_{LL}^{EELS}} \times \frac{D^e}{I^{EDXS}} \times \sigma^{EDXS} \tag{2.19}$$

For thin samples, if I_{LL}^{EELS} and D_e are expressed by the same total number of electrons interacting with the sample (derived from the full beam current), I_{LL}^{EELS} and D_e cancel out. As a result, the relationship of the partial scattering cross-section of EDXS and EELS is obtained:

$$\frac{\sigma^{EELS}}{\sigma^{EDXS}} = \frac{I^{EELS}}{I^{EDXS}} \tag{2.20}$$

For thin samples with thickness less than 10 nm, Equation 2.20 provides an easy conversion between the intensities of EDXS and EELS signals and their partial scattering cross-sections [106].

Combining EDXS and EELS in this manner provides an efficient and accurate chemical

analysis. Therefore, it is potentially helpful for the chemical characterization of thin samples such as nanoparticles. For example, in the case of bimetallic Pt-Co nanoparticles [107], the Co $L_{2,3}$ edge has well-defined white lines and is easier to acquire. In contrast, the Pt $M_{4,5}$ edge of higher energy is difficult to measure; instead, Pt L and M peaks are measured by EDXS for quantification.

2.5.2 Coincidence Spectroscopy

The concept to measure the time coincidence between X-rays and inelastic electrons has been applied by Kruit et al. [108] in 1984 where a gating circuit was developed which only collects electrons/X-rays when an X-ray/electron is detected within a short time interval. Recent developments in electron and X-ray detector technology have made it possible to identify single events whose time of arrival could be determined within nanosecond accuracy [109]. This better facilitates us to observe time correlations related to the excitation and de-excitation of atoms in a material, thus providing extra information than the individual EELS or EDXS spectra.

Figure 2.7 gives an example setup of the coincidence experiment [109]. It uses an SDD detector and a digital pulse processor [110, 111] to measure X-rays events, and a delay line detector [112, 113] (a Timepix detector [114, 115] alternatively can be used) mounted on the back of the EELS spectrometer to record electron events. This method provides EELS with a significantly suppressed background, overcoming many difficulties that exist in the conventional parametric background fitting, as it makes no assumptions about the shape of the background, requires no user input, and does not suffer from counting noise originating from the background signal. Coincidence spectroscopy has proven to improve the sensitivity for detecting trace elements compared to conventional EELS and EDXS [109].

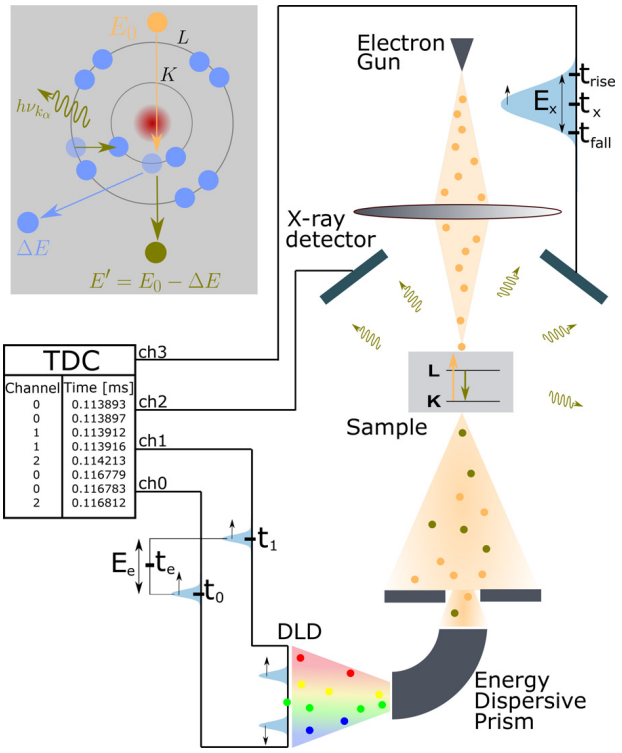

Figure 2.7: A sketch of a coincidence detection setup. Image from [109].

2.5.3 Multimodal Data Fusion

Coincidence spectroscopy explores the time correlation between EDXS and EELS, while 'data fusion' [116] opens another opportunity to link the two complementary spectroscopies in STEM. Data fusion refers to a category of established techniques of coupling multiple datasets via shared factors to uncover correlations between them. It is commonly used in various scientific fields [117–119] but has only been sparingly applied to multimodal hyperspectral TEM datasets [120, 121].

Thersleff et al. [122] propose a low-level data fusion method to jointly analyze simultaneously-acquired EELS and EDXS datasets (Figure 2.8). The framework that links EDXS and EELS data blocks is similar to that of Smilde et al. [123]. It consists of an asymmetrical block-weighted matrix concatenation that extends the spectral dimension of the fused dataset. Maximizing the explanatory power of the joint experiment can be achieved via appropriate data block weighting to maximize the explained variance of the fused dataset. The method has proven to give a rich descriptive model for estimating both transition metal valency and full chemical composition for core-shell nanoparticles [122]. Moreover, multimodal data fusion can also be complemented with other statistical methods, such as blind source separation (BSS) techniques [124], to permit the dissection of complex functional materials

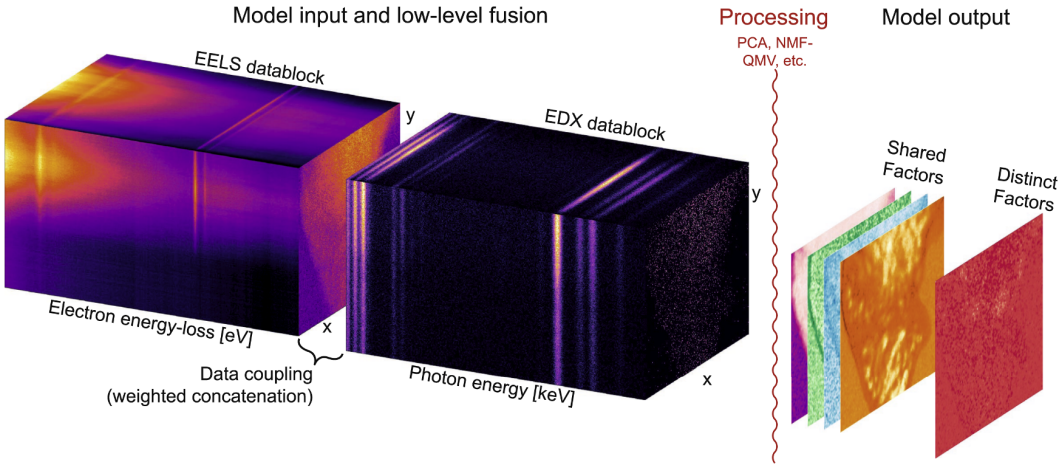

Figure 2.8: Schematic of a low-level data fusion approach to couple EELS and EDX datacubes via their shared spatial dimensions. Image from [122].

into their constituent morphological, compositional, and electronic components [125].

3 Machine Learning and Its Application to Analytical STEM Data

Electron microscopy is a powerful imaging and analytical technique that has revolutionized our understanding of the natural world at nanoscale and atomic levels. However, with the increasing complexity of data generated by electron microscopy, it has become difficult for human analysts to extract meaningful information from the collected data in a timely manner. Machine learning, a branch of artificial intelligence, has emerged as a promising tool for not only automating but also enhancing the analysis of electron microscopy data. In this chapter, I will introduce the fundamentals of machine learning and review its applications to analytical STEM data STEM, i.e., EDXS and EELS.

The effective application of most machine learning methods to analytical STEM data requires certain conditions to be met. One of the key requirements is that the data must be linearly dependent on the sample's properties and have noise that can be modeled as Gaussian or Poissonian. While EDXS data is more likely to meet this requirement than EELS data, the use of a direct electron detector can help EELS data to meet it. If the data diverges from this requirement, the results of the analysis are more likely to suffer from artifacts.

3.1 Introduction to Machine Learning

Machine learning is a rapidly growing field of artificial intelligence that focuses on developing algorithms and statistical models to learn patterns and relationships from data, and make predictions or decisions without being explicitly programmed [126]. The field has experienced tremendous growth in recent years due to the explosion of data, and the development of powerful computing hardware and open-source software tools.

There are several types of machine learning [127], including supervised learning, unsupervised learning, and reinforcement learning. In supervised learning, the algorithm learns

from labeled data, i.e., data that has already been categorized or classified. The goal of the algorithm is to learn a mapping function from the input data to the output data. A common example of supervised learning is image classification, where an algorithm is trained on a dataset of images labeled with their corresponding categories. The algorithm then uses this training data to predict the category of new, unseen images. In contrast, the unsupervised learning learns from unlabeled data. It aims to find patterns in the data without any prior knowledge of what the data represents. A common example of unsupervised learning is clustering, where an algorithm groups similar data points together based on their features. In reinforcement learning, the algorithm learns through trial and error, receiving feedback in the form of rewards or penalties based on its actions. The algorithm learns to make decisions that maximize its reward over time, and it is widely used on tasks such as game playing [128] and autonomous driving [129].

Alternatively, machine learning can be divided into classical and deep learning methods because the field of machine learning has been evolving rapidly over the past decade, with new techniques and algorithms constantly being created. Classical machine learning methods [130] are well-established techniques that have a solid theoretical foundation and are based on statistical principles. Linear regression [131], logistic regression [132], principal component analysis [133], support vector machines [134], and k-means clustering [135] are all examples of classical machine learning methods. These methods are generally simpler and easier to implement than deep learning methods, and they can be effective in a wide range of applications. Deep learning methods [136], on the other hand, have emerged in recent years, driven by advances in computing power and the availability of large amounts of data. These methods involve training deep neural networks with multiple layers to perform a given task, such as image or speech recognition. Common examples of deep learning methods include convolutional neural networks (CNNs) [137], recurrent neural networks (RNNs) [138], generative adversarial networks (GANs) [139], and autoencoders [140]. These methods are more computationally intensive than classical methods and require significantly more data to train, but they have proven to be effective in handling complex and diverse data [141–144]. Overall, both classical and deep learning methods have their advantages and disadvantages, and the choice of method depends on the specific problem being tackled. In the subsequent sections, I will delve deeper into some of these methods and discuss their applications to analytical STEM data.

3.2 Classical Machine Learning Methods and Their Applications

3.2.1 Principal Component Analysis

Principal Component Analysis (PCA) is a widely used unsupervised learning method in the field of data analysis [133, 145]. It is a dimensionality reduction technique used to transform high-dimensional data into a lower-dimensional space. PCA works by finding the principal components of the data, which account for the majority variance of the dataset and are orthogonal to each other. These principal components can be thought of as new axes in the lower-dimensional space, and the data can be projected onto these axes to create a lower-dimensional representation. Furthermore, the obtained reduced-dimensional data is often used as input to other machine learning algorithms, such as clustering, classification, and regression. Another advantage of PCA is that it is a relatively fast and computationally efficient algorithm, making it suitable for large datasets and real-time applications.

PCA was first demonstrated for aiding EELS analysis in the 1990s and, a decade after, it started to be widely used in the electron microscopy community [146–148]. An EDXS or EELS SI dataset can be written as a matrix D composed of m pixels and n energy channels and is decomposed by PCA as follows:

$$D = TP^T \tag{3.1}$$

where T is the score matrix (i.e., the distribution maps), and P^T is the transpose of the loading matrix (i.e., the spectra). In particular, D here needs to be weighted before the decomposition to account for the Poisson noise of counting events [149].

From Equation 3.1, D is represented as a linear combination of T and P. Components (T+P) are sorted according to their eigenvalues, representing the amount of variance expressed by a component. Ideally, most information contained in the dataset is represented by a small number of principal components, with the rest regarded as noise for their insignificant contributions to the variance. Thus, the dataset can be reconstructed using only the 'meaningful' components, leaving apart the noise.

PCA is used for two main aims: 1) as a noise filter to improve quantitative analysis of EDXS and EELS via the dataset reconstruction of the principal components [150–153]; and 2) as a data mining technique by interpreting the principal components in a qualitative manner [154]. For the first application, components for the reconstruction need to be carefully selected, relying on an empirical scree plot of principal components; notably, this reconstruction can introduce artifacts [155, 156]. For the latter, a main drawback is that loadings and scores can include negative values, and moreover have no intrinsic physical meaning [157]. Note that

some methods, such as factor rotation [158, 159], have been attempted to overcome this drawback in order to recover components with physical meaning.

3.2.2 Independent Component Analysis

Independent component analysis (ICA) [160] is a special case of the blind source separation technique [161], in which a linear mixture of signals is separated under the assumption that they are mutually statistically independent. It is also an unsupervised learning, as it find patterns and relationships in data without any labeled examples. One of the primary applications of ICA is in the field of signal processing. For example, in audio signal processing, ICA can be used to separate different sources of sound that are mixed together, such as different instruments in a musical recording [162].

While ICA is a powerful technique for separating multivariate signals into independent components, its performance can suffer when the underlying assumptions of the data change. To address this issue, various methods have been proposed, such as Robust ICA, Nonlinear ICA, and Kernel ICA. Robust ICA [163] aims to minimize the impact of noise or outliers on the estimation of the independent components. Nonlinear ICA [164] can handle situations where the independent components are not necessarily linear. Kernel ICA [165] uses kernel methods to transform the data into a higher dimensional space where the independent components can be more easily separated, making it particularly useful when the independent components are highly non-linear.

ICA was first proposed for EELS analysis by N Bonnet et al. in 2004 [166, 167], and afterward became greatly popularized in the electron microscopy community by its inclusion in the HyperSpy program package [168]. The method has been used on a wide variety of EELS measurements from samples ranging from perovskite-based solar cells [169] to III-V semiconductor nanostructures [170] or to relate ICA components to surface plasmon resonance modes in nanocubes [171]. It has been noticed that the performance of ICA on EELS data is greatly enhanced by working with the derivative of the signal instead of the signal itself [172], due to the derivative acting as a high-pass filter and diminishing the effect of the slowly varying features in the EELS signal (e.g., the background of core-loss signals). However, the success of this enhancement is limited to cases without overlapping fine structures [120]. ICA has also been applied to EDXS to determine the chemical composition of many materials, such as core–shell nanoparticles [173] and precipitates in a superalloy [174].

3.2.3 Non-negative Matrix Factorization

Non-negative matrix factorization (NMF) is a technique that decomposes one non-negative matrix into two non-negative matrices [175]. The goal of NMF is to find a low-dimensional representation of the original matrix that captures the underlying structure and patterns of the data. In NMF, the original matrix is factorized into two matrices: a matrix of basis vectors and a matrix of associated coefficients. The basis matrix represents the underlying features or components of the data, and the coefficient matrix represents the weighting of each component for each data point. The NMF problem is often solved using iterative optimization techniques, such as the alternating least squares algorithm or gradient descent. These algorithms update the basis and coefficient matrices iteratively, thus minimizing the difference between the original matrix and the approximation.

For EELS and EDXS data, the non-negative requirement is valid. Due to this, NMF has been successfully applied to many EDXS and EELS cases [176–178]. For example, NMF differentiated signals from three source components in a SEM-EDXS case [176]: supported metal nanostructures, a bulk semiconductor signal, and a carbon background.

However, compared to PCA, NMF is generally more computationally expensive and requires guessing the number of components to reach a subjectively good result. Additionally, NMF is sensitive to noise in the data, which can lead to inaccurate basis and coefficient matrices, as well as spurious basis vectors or coefficients that do not represent meaningful features of the data. This can be especially problematic for EDXS data analysis, where low counting statistics is common. To mitigate the impact of noise, algorithms such as robust NMF [179] have been developed using $L_{2,1}$-norm as loss function. This approach has been shown to handle noise and outliers effectively, resulting in more faithful basis factors and consistently better outcomes as compared to standard NMF.

Moreover, the non-uniqueness of NMF solutions can also be a challenge. In some cases, the algorithm may converge to a local minimum, rather than the global minimum of the loss function, leading to a non-unique outcome. To improve the uniqueness and accuracy of the decomposition, one can perform an exhaustive search over local minima or apply additional constraints (e.g., orthogonality [180], sparsity [181] of components, or minimum volume constraints [182]) to customize NMF for improved uniqueness and better decomposition.

In addition, NMF is a linear method and may not be optimal for non-linear EELS data. While it is still possible to utilize NMF for EELS analysis, it may not deliver the most precise decomposition. To cope with the non-linearity of data, Zhang et al. [183] proposed kernel NMF (KNMF), which can extract more useful features hidden within the original data than regular NMF, through kernel-induced non-linear mappings. Aternatively, Dobigeon et al. [184]

have extended the NMF model by introducing an additional term that accounts for possible non-linear effects. These solutions for non-linearity are certainly worth trying to improve EELS analysis.

3.2.4 Cluster Analysis

Cluster analysis is a method aimed at grouping similar objects or observations into clusters. Its purpose is to identify groups of objects or observations that are alike to each other but distinct from those in other clusters. Cluster analysis has a wide range of applications, including market research [185], image processing [186], and bio-informatics [187]. For example, in bio-informatics, cluster analysis was used to identify subgroups of cells based on gene expression data [188].

There are several types of cluster analysis, including hierarchical clustering and k-means clustering. Hierarchical clustering [189] is a method that involves recursively dividing the data into smaller and smaller clusters until a stopping criterion is met. k-means clustering [135] is a method that involves randomly assigning the data to k clusters and then iteratively optimizing the assignment to minimize the distance between each point and its assigned cluster centroid. The choice of cluster analysis method depends on the specific problem and the characteristics of the data. In general, hierarchical clustering is useful when the number of clusters is not known in advance, while k-means clustering is useful when the number of clusters is known or can be estimated.

Several cases have proven that cluster analysis improves the analysis of EELS data. For instance, k-means clustering was used to extract the representative spectral endmembers of an EELS SI dataset, which were later used in a multiple-linear least-squares (MLLS) fitting process to improve the accuracy of the obtained results [190]. Also, combiningng clustering with non-linear least-squares (NLLS) fitting has been proven as a promising solution to improve the stability of the latter [191], which facilitates an in-depth ELNES analysis for materials with changing oxidation states. Furthermore, Blanco-Portals et al. [192] developed an entirely data-driven methodology for ELNES analysis using state-of-the-art clustering algorithms (i.e., Hierarchical density-based spatial clustering of applications with noise (HDBSCAN) and uniform manifold approximation and projection (UMAP)).

3.3 Deep Learning Methods and Their Applications

Having briefly introduced several classical machine learning methods and their applications to analytical STEM data, now I turn my attention to deep learning methods, which have gained increasing attention and popularity in recent years.

3.3.1 Neural Networks and Deep Learning

Neural Networks

A neural network (NN) is a machine learning model that is designed to recognize patterns in data. It is modeled after the structure and function of the human brain, consisting of interconnected nodes (neurons) that process information in a parallel and distributed manner. A NN can be formulated as:

$$y = f_{NN}(\mathbf{x}) \tag{3.2}$$

f_{NN} is a nested function. For example, for a 3-layer neural network that returns a scalar output, f_{NN} can be expressed as follows:

$$y = f_{NN}(\mathbf{x}) = f_3(f_2(f_1(\mathbf{x}))) \tag{3.3}$$

where f_1 and f_2 are vector functions of the following form:

$$f_n(\mathbf{z}) = g_n(\mathbf{W_n}\mathbf{z} + \mathbf{b_n}) \tag{3.4}$$

where n is the layer index, and $\mathbf{z}$ is the input vector to the nth layer of the neural network. g_n is called an activate function that introduces non-linearity into a neural network, allowing the network to model complex relationships between the input and output data. $\mathbf{W_n}$ is the weight matrix and $\mathbf{b_n}$ is the bias vector. The function f_3 here is a scalar function, but can also be a vector function depending on the problem concerned.

An optimizer is needed to adjust the values of the $\mathbf{W_n}$ and $\mathbf{b_n}$ of each layer during training, in a way that minimizes the defined loss function. The loss function measures the discrepancy between the predicted and true output values for a given set of input data. Common examples of loss function include mean squared error (MSE) [193] that measures the average squared difference between the predicted and true output values, and Kullback-Leibler Divergence (KL divergence) [194] that measures the difference between the probability distributions of the predicted and true output values. The choice of loss function depends on various factors, such as dataset characteristics (e.g., distribution, dimensionality, sparsity, and noise type), task type (e.g., regression, classification, and segmentation), and the architecture of the neural network. The choice of optimizer is also important and can affect the performance and speed of the network. Some optimizers, such as stochastic gradient descent (SGD) [195], can converge to a suboptimal solution if the learning rate is set too high or too low, while other optimizers, such as Adam [196], are less sensitive to the choice of learning rate.

Deep Learning

Deep learning refers to training neural networks with multiple hidden layers (more than two),

which allows them to learn representations of data with multiple levels of abstraction. These methods have dramatically improved the state-of-the-art in speech recognition [197], image recognition [137], and many other domains such as drug discovery [198] and genomics [199].

The ability of deep learning to learn intricate nonlinear relationships between inputs and outputs is regarded as one of its principal advantages, thereby enabling the modeling of highly complex phenomena. In addition to this, deep learning facilitates automated feature engineering, which diminishes or eliminates the need for manual feature extraction. This considerably reduces the time and effort involved in the model development process, making it an appealing option for large scale datasets. Moreover, the pre-training of deep learning models on large datasets allows for efficient transfer of knowledge to smaller, domain-specific datasets.

Despite its numerous advantages, deep learning presents several challenges. One of the main challenges is the need for large amounts of labeled data, which can be expensive and time-consuming to acquire. Another challenge is the high computational requirements, which can limit the scale of deep learning applications. Additionally, deep learning models can be difficult to interpret, and their internal workings may not be transparent or easily understood. Notwithstanding the challenges that deep learning poses, its potential advantages make it an influential technique for addressing intricate problems across numerous domains. In the next section, a selection of applications of deep learning techniques on analytical STEM data will be presented.

3.3.2 Deep Learning Applied to Analytical STEM Data

Over the past decade, deep learning has been actively applied to the analysis of various electron microscopy data. These applications include diffraction pattern characterization [200–203], phase retrieval [204–206], and the denoising [207, 208], inpainting [209], and semantic segmentation [210–213] of TEM/STEM images.

Compared to the electron microscopy techniques stated above, the application of deep learning methods in EDXS and EELS analysis is not as prevalent. To facilitate EELS analysis, Chatzidakis and Botton [214] implemented a deep learning method for calibration-invariant EELS spectrum analysis, which enabled the identification of spectral peaks based on their shape while maintaining translation invariance. There are several cases of deep learning improved EDXS, with a particular focus on improving STEM-EDXS tomography. These include denoising of 2D elemental maps before performing a classical 3D reconstruction [215–217], and denoising of 3D data after the classical reconstruction [216]. An additional advantage of the former approach is that 2D image deep learning-based denoising has already been exten-

sively studied in other fields, which can serve as a foundation for the development of novel methodologies. Given deep learning's aptitude for processing intricate, high-dimensional, and nonlinear data, it therefore holds promise as a means of developing new analysis methodologies for EDXS and EELS. In this thesis, I test such an approach with the correlative analysis of simultaneously acquired EDXS and EELS data in Chapter 7.

4 Melting Experiments in Lower Mantle Conditions

This chapter is the result of a collaborative effort led by J. Badro and C. Hébert. J. Badro conceptualized the ideas for this research project based on the state-of-the-art geochemistry problem, while C. Hébert offered technical guidance throughout the project. J. Badro and F. Nabiei worked together to synthesize the samples in the laser-heated diamond anvil cell. F. Nabiei also prepared the TEM lamellae using the focused ion beam. H. Chen conducted the electron microscopy characterization of the samples and analyzed the resulting data.

4.1 Introduction

Similar to other terrestrial planets, the Earth experienced giant impacts during its growth [218]. Previous studies have shown that the mantle was extensively molten due to a giant impact which also created Moon [44]. The solidification and fractionated crystallization of the resulting magma ocean (i.e., primitive molten silicate mantle) play a significant role in the differentiation of the Earth [219]. Many present-day seismic and geochemical observations could be linked to this process which produced phases of distinct composition and density that are prone to gravitational segregation and geochemical isolation [220, 221]. For example, the ultra-low velocity zones (ULVZs), a seismic structure above the core-mantle boundary (CMB), have been considered remnants of the primitive magma ocean [3].

In order to advance our understanding of the observations of the Earth's mantle, it is essential to conduct melting experiments that serve as an analog to the magma ocean solidification process. There have been significant efforts to study mineral-melt phase relations and trace element partitioning in mantle rocks to pressure up to 26 GPa (i.e., a depth of 700 km in the mantle) [2, 27, 222, 223]. However, modeling shows that the putative conditions of magma ocean crystallization on Earth are significantly deeper [224], which goes from ~1500 km depth all the way to the core-mantle boundary where rare experiments on phase relations have been carried out.

The present limitation of these experiments corresponds to the pressure limit of the multi-anvil press using tungsten carbide anvils, which is the standard tool to investigate phase relations at high pressures and temperatures [225]. Typically in those experiments, a bulk starting composition is chosen, compressed and melted, and then cooled down to crystallize, and finally quenched, recovered, and analyzed chemically and mineralogically using standard analytical tools such as the electron microprobe or scanning electron microscope [226]. The mineral-melt phase relations and melting phase diagram of the chosen starting composition are derived from the chemical characterization.

Besides the routine experimental protocol using large-volume presses, another emerging methodology for conducting such an experiment is the laser-heated diamond anvil cell (LH-DAC) which provides higher pressures and temperatures that covers all plausible conditions of magma ocean crystallization on Earth. However, the melting experiments in LHDAC are challenging due to: 1) the inability to accurately control the temperature required to slowly crystallize the melt and attain controlled degrees of crystallization (e.g., fractions of residual melt); 2) the size of the phases produced is nanometric, whose characterization requires high-resolution analytical techniques.

Here, we employ the LHDAC approach and STEM-EDXS to study the melting relations of a

pyrolite composition [12], which is a fair estimation of the average composition of the Earth's mantle. We unambiguously determined the mineralogy and composition of the liquidus phase (i.e., the first mineral phase to crystallize in a cooling magma ocean at considered pressures) and probed a Fe-enriching phenomenon in the residual liquid. In addition, the chemical analysis of solidus phases produced from the experiment supports the idea that variation of affiliation of Fe in mineral phases is responsible for rheological variations observed in the Earth mantle.

4.2 Materials and Methods

Four melting experiments (i.e., partial crystallization experiments) were performed in LH-DAC at 46, 55, 71, and 88 GPa, using pyrolite that was doped with a trace amount of Nd, Sm, and U as starting materials (Table 4.1). Pyrolitic glass was produced in a gas-mixing aerodynamic levitation laser furnace at 2050 °C. All samples were compressed to the targeted pressure, then heated and molten using double-sided laser heating. The samples were then allowed to cool down at a rate of 90 K/s over a course of several seconds. The samples are then quenched by shutting off laser power and decompressed, unloaded from the LHDAC, and transferred to a focused ion beam (FIB) instrument for sample recovery. A thin slice of the center of the heated spot was prepared using the FIB lift-out technique with a Zeiss NVision 40 dual-beam instrument and finally transferred to a copper TEM grid. The STEM imaging and EDXS measurements were performed on a FEI Tecnai Osiris microscope operated at 200 kV. This microscope is equipped with four windowless Super-X SDD EDXS detectors and Esprit 1.9 acquisition software from Bruker.

Atomic %	Mg	Si	Al	Ca	Fe	Nd (ppm)	Sm (ppm)	U (ppm)	O
average	19.30	16.65	1.75	0.83	2.44	477	455	130	58.83
std dev	0.83	0.51	0.16	0.03	0.05	19	15	14	0.27

Table 4.1: The nominal composition of the starting material with standard deviation.

4.3 Results and Discussion

A representative FIB lamella synthesized at 88 GPa is displayed in Figure 4.1. As the figure shows, the lamella has rich phase features and is divided into five zones. The part of the sample that was molten and recrystallized is called the ‘melt pocket’, and consists of mineralogically differentiated concentric ensembles (i.e., liquidus phase (LP), equilibrium solids (ES)), and residual melt (RM). The outermost part is unheated and untransformed glassy material of the starting composition (i.e., untransformed area (UA)), and the glass is crystallized into nanometer-scale mineral assemblages (i.e., subsolidus phases (SP)) when it

approaches the edge of the melt pocket with increasing temperature. The HAADF overviews of the rest three samples are attached to the Appendix 1, 2, 3.

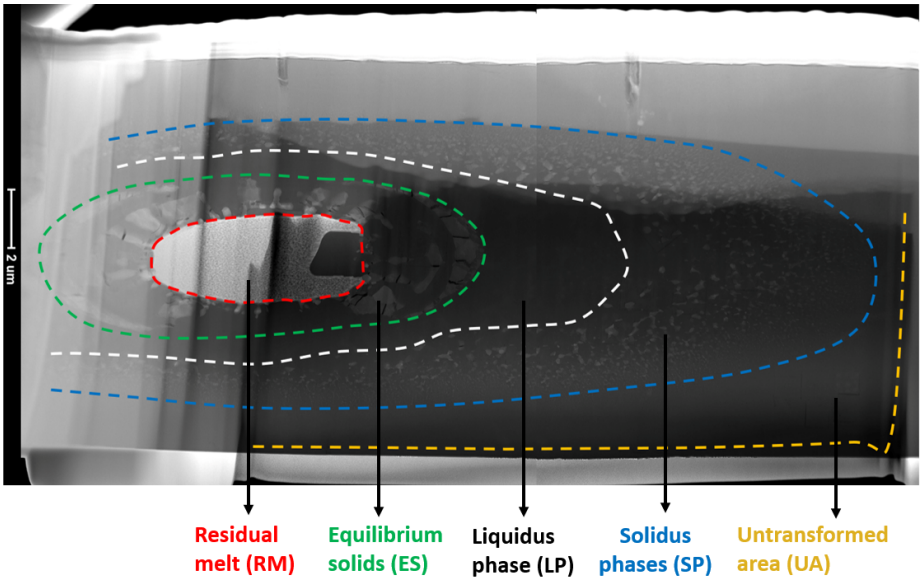

Figure 4.1: The overview (HAADF image) of the sample produced at 88 GPa.

Before performing a thorough study of the samples, we performed an "integrity" check on all four samples. By comparing the composition of mineral assemblages of the SP area to that of the UA area (i.e., the two parts should share the same composition in a closed system), we identified a degree of Fe loss in the sample synthesized at 71 GPa. Thus, this particular sample is of limited geochemical interest and will be discarded from further analysis in this chapter. Appendix 5a, 6a, 7a contains an index and compilation of all the STEM-EDXS maps acquired for the three geochemically significant samples. Meanwhile, we utilized the data acquired from the excluded sample to some extent, using it as a playground to develop innovative data processing techniques, which will be discussed in the upcoming chapter.

4.3.1 Evolution of Melt Pocket

Liquidus Phase and Compositional Gradient of Equilibrium Solids

Three samples were successfully synthesized at 46, 55, and 88 GPa, which correspond to conditions in the middle-to-lower mantle. Figure 4.2 illustrates the STEM-EDXS elemental maps of the equilibrium solids that crystallized from the melt. Textural and chemical analyses were conducted on them to understand the solidification of the liquid melt, which is an analog to the crystallization of the magma ocean.

Here, we take the 55 GPa sample as an example to demonstrate the chemical evolution of

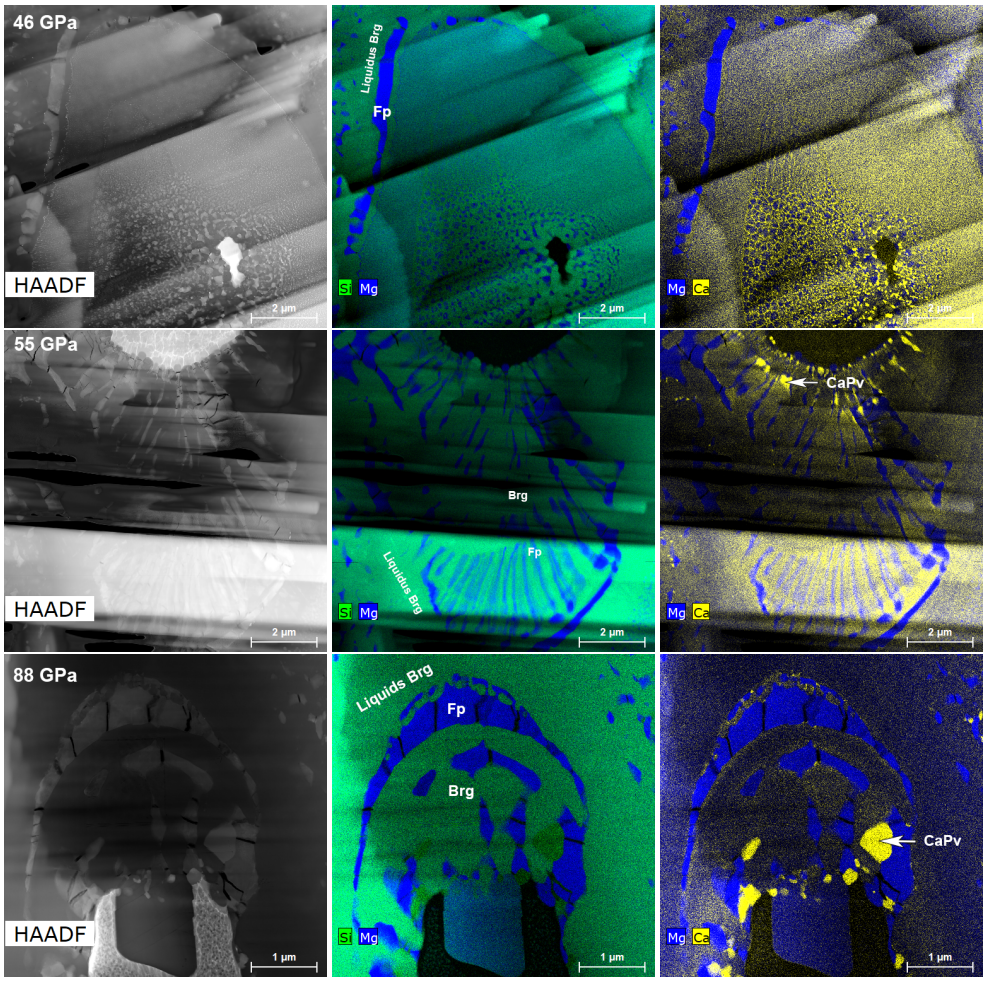

Figure 4.2: Representative views (HAADF image and EDXS maps) of the equilibrium solids of samples produced at 46, 55, and 88 GPa.

melt pocket from the rim to the center. The rim of the molten region has a distinct and constant composition in comparison to the rest of the melt pocket areas (Figure 4.3). This is identified to be the liquidus phase, which initially crystallized from the melt and is analyzed to be Brg in the case of 55 GPa sample. Adjacent to the liquidus phase, there exist equilibrium solids. They start with a ferropericlase (Fp) shell, followed by cotectic solids comprised of Fp and Brg, and then Ca-perovskite (CaPv) appears when further approaching the residual melt (Figure 4.2).

The liquidus Brg, and the Brg and Fp in the equilibrium solids are quantified using the traditional Cliff-Lorimer ratio method, and the k-factors from Esprit are used. It is found that the molar ratio of Fe/Fe+Mg of Fp, as depicted in Figure 4.3, increases monotonically when approaching the center. The outermost Fp shell exhibites a value of approximately 0.13-0.14, whereas that of the innermost Fp precipitates reaches as high as 0.30-0.35. This suggests

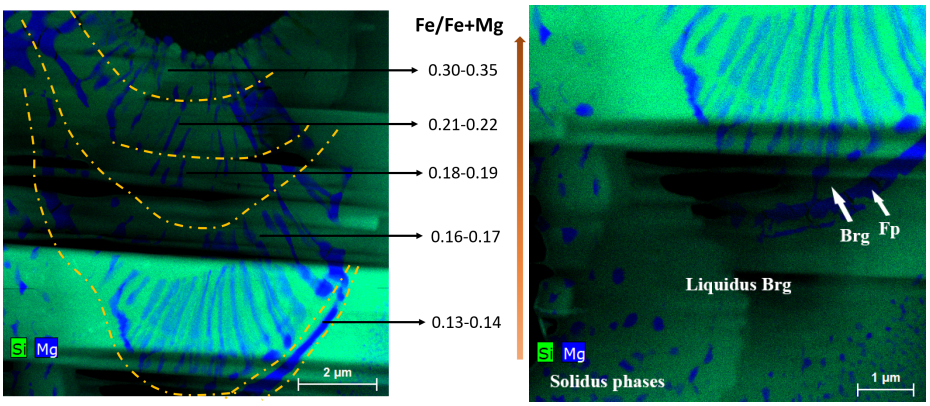

Figure 4.3: Compositional gradient of Fp in the equilibrium solids, and the liquidus phase is identified to be bridgmanite in the sample synthesized at 55 GPa.

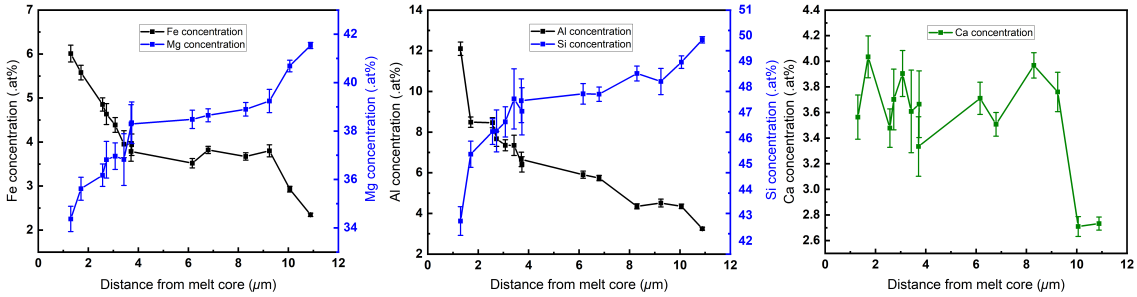

Figure 4.4: Compositional gradient of Brg in equilibrium solids of the sample synthesized at 55 GPa.

a Fe-enrichment phenomenon towards the residual melt, which will be further discussed later. Based on the results of quantification, it is observed that the chemical evolution trend of Brg in the equilibrium solids is similar to that of Fp. The Brg compositions around the long axis of the elliptic molten volume, starting from the Brg reaches the residual melt and ending with the liquidus Brg, are depicted in Figure 4.4. It is observed that the closer the Brg is located to the residual melt, the higher the Fe and Al content and the lower the Mg and Si content in its composition. Notably, for the sample synthesized at 46 GPa, CaPv is absent in the ES area; instead, Brg becomes more Ca-enriched when approaching the residual melt.

In all three samples, the liquidus phase is consistently identified as Brg (as shown in Appendix 5e, 6d, 7c). The compositions of these liquidus Brg are listed in Table 4.2. It is worth noting that trace amounts of Nd and Sm are present in the Brg. The reliability of their quantifications is attributed to the integration of X-ray signals over large areas. The reported error corresponds to the standard deviation of quantifications conducted on multiple regions.

Previous studies have shown that many ratios of refractory lithophile elements (RLEs, e.g., rare Earth elements, Be, Al, Ca, Sc, Ti, Sr, Y, Zr, Nb, Ba, Hf, Th, U) in the primitive upper mantle

rocks are very similar to those observed in CI chondrite meteorites [12, 17, 18]. However, the Mg/Si ratio of the upper mantle is significantly higher than that of chondritic meteorites, with a value of 1.12 compared to 1.0 [227]. Therefore, it has been suggested that the lower mantle may be enriched in Si relative to the upper mantle, possibly due to the crystal fractionation of lower mantle phases during magma ocean solidification. Meanwhile, any fractionation occurred in a crystallizing magma ocean should not cause the ratio of RLEs of the upper mantle to shift outside their chondritic bounds within a 10% uncertainty. If the fractionation of the liquidus phase (i.e., Brg in our case) formed a chemically distinct reservoir that may still exist in the lower mantle today without violating the chondritic pattern of RLEs in the upper mantle, it could contribute to the enrichment of Si in the lower mantle. Our collaborator Dr. J. Badro, will perform mass-balance calculations [228] to determine the extent of Brg fractionation based on the compositions of the liquidus Brg and coexisting melt.

Liquidus Brg	B-C2-46 GPa		C-C5-55 GPa		C-C4-88 Gpa	
	Atomic %	Error	Atomic %	Error	Atomic %	Error
Mg	40.45	0.440	41.79	0.519	42.07	0.557
Al	3.94	0.131	3.72	0.238	3.59	0.115
Si	51.07	0.590	49.61	0.256	50.77	0.656
Ca	1.98	0.174	2.33	0.248	1.98	0.190
Fe	2.27	0.175	2.28	0.251	1.38	0.119
Nd	0.059	0.017	0.062	0.016	0.033	0.014
Sm	0.079	0.017	0.094	0.017	0.052	0.015
U	0.007	0.010	0.003	0.010	0.001	0.007

Table 4.2: Chemial compositions of the liquidus phase Brg.

Fe Enrichment in Residual Melt

Having observed that Fp and Brg of equilibrium solids exhibit a tendency of Fe enrichment towards the residual melt core across all three samples, we now characterize the residual melt. Figure 4.5 illustrates the EDXS elemental maps of the residual melt and implies a heavily Fe-enrichment effect in the RM. Since the lamella represents a slice of the reaction volume, the composition quantified from the RM area may not be identical to but can be indicative of that of the RM itself. When the pressure increases, the Fe concentration of the RM undergoes a substantial rise, from roughly 10 at.% in the 46 GPa sample to over 70 at.% in the 55 and 88 GPa samples. The observation of a strong Fe enrichment in the residual melt lends support to the concept of gravitational stability of the melt at the bottom of the mantle. This finding additionally reinforces the proposal of the basal magma ocean theory as presented by by Labrosse et.al. [3].

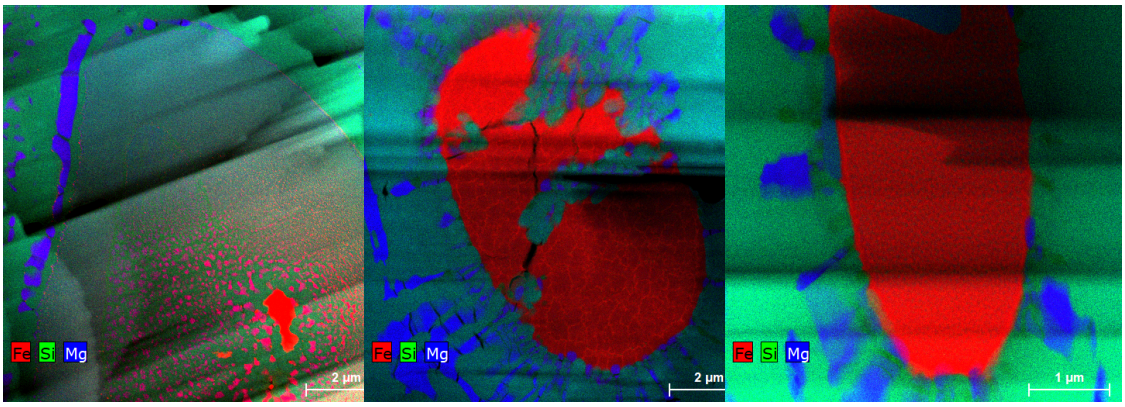

Figure 4.5: Representative views (HAADF image and EDXS map) of the melt residual of samples produced at 46, 55, and 88 GPa, respectively.

4.3.2 Fe Partition in Solidus Phases

We now shift our attention to the solidus mineral assemblages, which bear resemblance to the mineral assemblages in the lower mantle. Figure 4.6 illustrates the EDXS elemental maps of solidus assemblages formed from 46 GPa to 88 GPa. Quantitative analysis of the STEM-EDXS data reveals the evolution of the lower mantle mineralogy with increasing mantle depths (i.e., pressures). Throughout the pressure range, Fp and Brg are found, whereas Ca perovskite (CaPv) only emerges at higher pressures. Table 4.3 summarizes the quantification of the mineral phases, with the concentration of O being deconvolved. The quantifications are based on the STEM-EDXS data, as demonstrated in Appendix 5h, 6e, 7d . The reported error is the standard deviation of quantifications that were performed on multiple maps. It is observed that the solidus Brg also contains trace amounts of Nd and Sm. Nevertheless, the reliability of their concentrations is reduced as a result of their significantly reduced size compared to the liquidus Brg. Moreover, the acquisition parameters of STEM-EDXS data, in our cases, are considerably restricted due to the sensitivity of these minerals to long beam exposure.

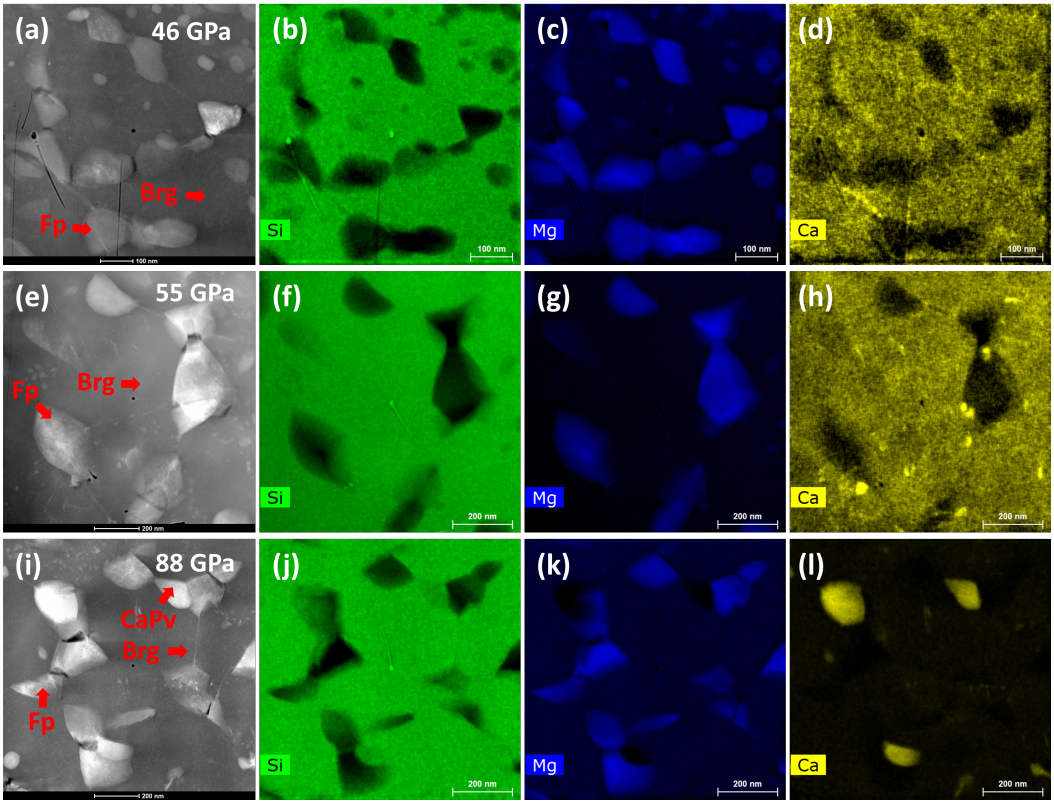

Figure 4.6: (a),(e),(i) the HAADF image; (b),(f),(j) the Si Kα; (c),(g),(k) the Mg Kα ; (d),(h),(l) the Ca Kα map of the subsolidus assemblages synthesized at 46 GPa, 55 GPa, and 88 GPa, respectively. Each elemental map's intensity scale is self-referential, with a linear scaling from 0 fractional intensity for the pixel spectrum with the lowest integrated peak counts to a value of 1 for the pixel spectrum with the highest integrated counts. As a result, the Brg appears dark in the Mg map despite its richness in Mg, as the Fp is even richer in Mg.

P (GPa)	46				55				88					
T (K)	~3000				~3200-3500				~3500-3700					
Phase	Fp		Brg		Fp		Brg		Fp		Brg		Ca-Pv	
	Mean	Error	Mean	Error	Mean	Error	Mean	Error	Mean	Error	Mean	Error	Mean	Error
Mg	82.83	1.27	39.32	0.77	83.35	1.03	40.46	0.85	84.44	1.43	40.96	0.48	-	-
Al	1.15	0.28	4.86	0.15	1.04	0.18	4.76	0.21	0.91	0.26	4.95	0.19	8.87	0.62
Si	-	-	49.04	0.61	-	-	48.38	0.39	-	-	48.9	0.26	37.7	1.42
Ca	-	-	2.33	0.1	-	-	2.4	0.14	-	-	1.87	0.23	39.95	0.81
Fe	16.04	1.2	4.03	0.19	15.51	1.18	3.63	0.51	14.33	1.35	3.08	0.44	0.47	0.4
Nd	-	-	0.137	0.026	-	-	0.122	0.025	-	-	0.052	0.016	6.78	0.41
Sm	-	-	0.138	0.025	-	-	0.129	0.026	-	-	0.068	0.019	5.14	0.27
U	-	-	0.018	0.022	-	-	0.009	0.014	-	-	0.001	0.008	0.51	0.18
K_{eff}	0.53				0.52				0.45					

Table 4.3: Synthesis conditions of samples and quantification results of solidus mineral assemblages.

In the lower mantle, Fe is the sole transition element entering the major composition of Brg

and Fp, which are the most and the second most abundant minerals, respectively. The partitioning of Fe between these minerals is a crucial factor in controlling the physical properties of the lower mantle, such as density, elasticity, and viscosity. As such, extensive research has been undertaken to determine the distribution of Fe between mantle minerals [229–233]. In this study, we evaluated the partitioning of Fe between Fp and Brg under conditions of lower mantle. We found that Fe prefers partitioning into Fp over Brg. This partitioning behavior was assessed by computing the effective equilibrium constant (K_{eff}), which represents the molar concentration ratio of Fe to Mg in Brg relative to that in Fp: K_{eff} ($K_{eff} = X_{Fe}^{Brg} X_{Mg}^{Fp} / X_{Fe}^{Fp} X_{Mg}^{Brg}$). Higher values of K_{eff} imply Fe-rich Brg, while lower values indicate Fe-rich Fp. Notably, the values of K_{eff} remain constant at 46 and 55 GPa (0.53 and 0.52, respectively), but drops to 0.45 at 88 GPa. Moreover, the trend of the K_{eff} with respect to pressure is observed to be anti-correlated with the radial viscosity profile reported previously [234]. Previous experiments conducted on olivine and Fp have shown an inverse correlation between Fe content and the measured viscosity [235, 236], with higher Fe concentrations being less viscous. Given that Brg is the dominant mineral in the lower mantle, variations in Fe content in Brg are likely to be responsible for the observed rheological variations in the lower mantle.

In addition to analyzing the partitioning behavior of Fe, investigating the interphase partitioning behavior of trace elements such as La, Nd, Sm, Gd, Lu, and U in the Earth's mantle minerals is of great interest to geochemists, as it offers insights into different chemical differentiation events in the mantle [27, 237]. However, conventional quantification methods have proven inadequate in precisely determining trace element concentrations in Brg, such as Nd and Sm. In fact, the quantification of mineral phases in solidus areas is a highly intricate process, given the spatial overlap of these phases in the thickness direction and their similarities in composition. Overcoming these challenges in STEM-EDXS quantification therefore represents a significant aspect of my Ph.D. project. As such, the subsequent two chapters will focus on the development of novel data processing techniques to address these issues.

4.4 Conclusion and Outlook

In this study, pyrolite samples were subjected to partial melting at pressures of 47, 55, and 88 GPa, and the resulting melt pocket and solidus mineral assemblages were characterized using STEM-EDXS. Our findings indicate that bridgmanite is the first mineral phase to crystallize from the melt within the investigated lower mantle pressure range. Therefore, the fractionated crystallization of Brg during the solidification of the magma ocean can result in a Si-rich lower mantle (i.e., an observed Si-depleted upper mantle). To further validate this hypothesis, mass balance calculations will be conducted in future studies to determine the

extent of this crystal fractionation.

Additionally, we observed the preferential accumulation of Fe in the residual melt, which provides experimental support for the basal magma ocean theory. We further investigated the partitioning behavior of Fe between solidus ferropericlase and bridgmanite, and postulated that variations in Fe content in Brg may be responsible for the observed rheological variations in the lower mantle.

5 NMF Aided Phase Unmixing and Quantification with STEM-EDXS

This chapter is a pre-submission version of a manuscript entitled ”Non-negative matrix factorization aided phase unmixing and trace element quantification with STEM-EDXS” authored by H. Chen, F. Nabiei, J. Badro, D.T.L. Alexander, and C. Hébert.

H. Chen developed the project ideas with C. Hébert. J. Badro developed the idea for the sample based on state-of-the-art geochemical knowledge. J. Badro and F. Nabiei synthesized the sample in the laser-heated diamond anvil cell. F. Nabiei prepared the TEM lamella in the focused ion beam. H. Chen characterized the sample using electron microscopy, developed the python code for data processing, and wrote the manuscript. C. Hébert and D.T.L. Alexander participated in discussing the results and the scientific output and provided writing advice throughout the project.

Abstract

Energy-dispersive X-ray spectroscopy (EDXS) mapping with a scanning transmission electron microscope (STEM) is commonly used for chemical characterization of materials. However, STEM-EDXS quantification becomes complicated or even problematic when the constituent phases share common elements and overlap spatially. In this paper, we present a methodology to identify, segment, and unmix phases which have a substantial spectral and spatial overlap in an automated fashion, which combines non-negative matrix factorization with *a priori* knowledge of the sample. We illustrate the methodology using a sample of electron beam-sensitive mineral assemblages that represent the deep Earth mantle. With it, we retrieve the true EDX spectra of the constituent phases and their corresponding phase abundance maps. It further enables us to achieve a reliable quantification for trace elements with concentration levels of ~ 100 ppm. Our approach can be adapted to aid the analysis of many materials systems that produce STEM-EDXS datasets having phase overlap and/or limited signal-to-noise ratio in spatially-integrated spectra.

5.1 Introduction

A scanning transmission electron microscope (STEM) equipped with a silicon drift X-ray detector (SDD) is a fast, robust and widely-used tool for the chemical analysis of materials from microscale to nanoscale. With the spectrum imaging (SI) technique, an energy-dispersive X-ray (EDX) spectrum is acquired at each scanned point and stored to enable chemical analysis to be performed for every pixel in the SI dataset. The comprehensive chemical information contained in a STEM-EDXS SI dataset allows a detailed chemical analysis of materials [238–240]. However, if the sample is made of several phases overlapping in the thickness of the specimen, the technique cannot deliver an individual quantification of each phase upon analyzing relevant pixels, but only an average composition of a mixture of phases. This is even more problematic when the phases share some elements. For example, identifying chemically similar multiphase nanoprecipitates in complex fission products remains difficult when characterizing irradiated nuclear fuels using EDXS mapping inside a STEM [241].

Another drawback of STEM-EDXS is the low counting statistics due to the limited thickness of samples used for STEM characterization, which is typically around or less than 100 nm. It is a key factor limiting the precision of STEM-EDXS when quantifying minor elements and makes the trace element quantification incredibly challenging. Technically, using large electron probes with a strong beam current or counting for a long time can help reduce quantification errors. However, there is then an increased risk of specimen drift, contamina-

tion, or damage. Furthermore, if the material of interest is highly sensitive to electron doses, such as macromolecules and polymers [242, 243], metal-organic frameworks [244, 245], and low-dimensional materials [246, 247] etc., STEM-EDXS measurement would hardly attain sufficient signal-to-noise ratio (SNR) for an accurate and precise quantification.

In the past decade, machine learning (ML) algorithms, such as principal component analysis (PCA) [155, 248, 249], independent component analysis (ICA) [172–174], and non-negative matrix factorization (NMF) [176, 177, 181] etc., have been exploited to aid analyzing various electron microscopy datasets. PCA is widely used for denoising. However, its bias can induce artifacts into the reconstructed data [152, 156]. NMF stands as a promising technique to separate different components of a complex sample because it assumes a non-negativity for all the collected signals that is physically sound, and the returned results are more easily interpretable [181]. Nonetheless, the components extracted by NMF are not identical to the characteristics of the true physical phases, and the component spectra cannot directly be used for the quantification of phases [176]. Also, the abundance maps are not equal to the true quantitative distributions of phases, the revealing of which is helpful for understanding multiple properties of materials, such as mechanical properties [250, 251], transport properties [252, 253], or magnetic properties [254, 255].

In this paper, we propose a new method that combines NMF with *a priori* knowledge of the sample, to retrieve the physical EDX spectra of phases as well as their quantitative distribution maps under significant spatial and spectral superimposition of phases. Furthermore, the signals of trace elements contained in the relevant phase spectrum are remarkably increased; allowing us to quantify trace elements at the concentration level of ~ 100 ppm.

5.2 Experiment Procedures

5.2.1 Sample Synthesis and Preparation

The material studied in this paper is Earth mantle mineral assemblages synthesized in a laser-heated diamond anvil cell (LHDAC) [Institut de Physique du Globe de Paris (IPGP)], an experimentation tool for investigating the phase behavior of materials at thermodynamic conditions comparable to the deep interior of the Earth. The starting material was a pyrolite glass [24], with a composition chosen to represent the typical composition of the average Earth mantle in terms of major elements. Additionally, a trace amount of Nd, Sm, and U (0.3 wt.% for each) was added to the starting material. The nominal composition of the starting material was measured by EDXS in a scanning electron microscope and is listed in Table 5.1.

The specimen was first compressed to 71 GPa, then heated to ~ 4500 K and held in a molten

state for 2 minutes using double-sided laser-heating, followed by fast cooling to ~ 3900 K at a rate of around 90 K/s. The specimen was then quenched by switching off the laser power, and slowly decompressed, unloaded from the LHDAC and transferred to a focused ion beam (FIB) instrument for sample preparation. A thin slice of the center of the heated spot was prepared using the FIB lift-out technique with a Zeiss NVision 40 dual beam instrument [Centre Interdisciplinaire de Microscopie Électronique (CIME), École Polytechnique Fédérale de Lausanne (EPFL)].

Atomic %	Mg	Si	Al	Ca	Fe	Nd (ppm)	Sm (ppm)	U (ppm)	O
average	19.30	16.65	1.75	0.83	2.44	477	455	130	58.83
std dev	0.83	0.51	0.16	0.03	0.05	19	15	14	0.27

Table 5.1: The nominal composition of the starting material with standard deviation.

5.2.2 STEM-EDXS SI Acquisition

The STEM imaging and EDXS measurements were performed on an FEI Tecnai Osiris microscope (CIME, EPFL) operated at 200 kV. This microscope is equipped with four windowless Super-X SDD EDXS detectors and Esprit 1.9 acquisition software from Bruker. The EDXS SI data of 512 ×512 pixels were acquired with a nominal beam current of 750 pA, a pixel dwell time of 60 μs, and frame counts of 46, leading to a total time of 12 minutes per SI map. The EDXS acquisition parameters yield ~ 160 counts per pixel for all X-rays, which ensures an appropriate SNR for characterizing the minor elements (i.e. Al Kα, Fe Kα, Ca Kα) without causing severe damage to the specimen.

5.3 Results and Discussion

5.3.1 Conventional STEM-EDXS Analysis

At first, we conducted a conventional STEM-EDXS analysis on the FIB sample. Figure 5.1 illustrates the high-angle annular dark-field (HAADF) image and EDXS elemental maps of a representative solidus mineral assemblage synthesized at the set-up condition. We identify three mineral phases from the qualitative analysis of the elemental maps, which are bridgmanite ($MgSiO_3$ with minor amount of Fe, Al, and Ca, $abbr.$ Brg), ferropericlase ((Mg,Fe)O, $abbr.$ Fp), and Ca-perovskite ($CaSiO_3$ with minor amount of Al, Nd, Sm, and U, $abbr.$ CaPv). Three regions of interest (i.e., ROI_1, ROI_2, ROI_3) are selected to study the three phases as indicated in Figure 5.2(a), and their spectra are displayed in Figure 5.2(b)-(d).

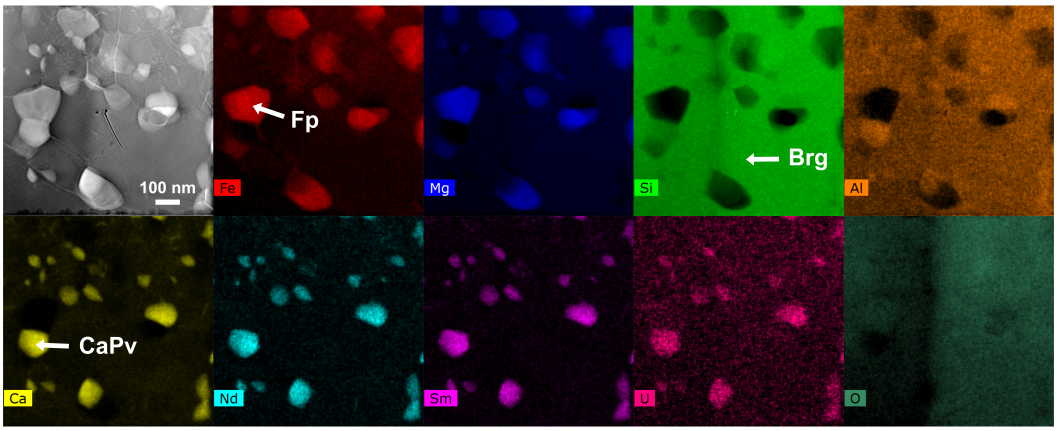

Figure 5.1: HAADF image and EDXS elemental intensity maps of integrated peak counts of a representative mineral assemblage of the pyrolite specimen. Each elemental map's intensity scale is self-referential, with a linear scaling from 0 fractional intensity for the pixel spectrum with the lowest integrated peak counts to a value of 1 for the pixel spectrum with the highest integrated counts. As a result, the Brg appears dark in the Mg map despite its richness in Mg, as the Fp is even richer in Mg.

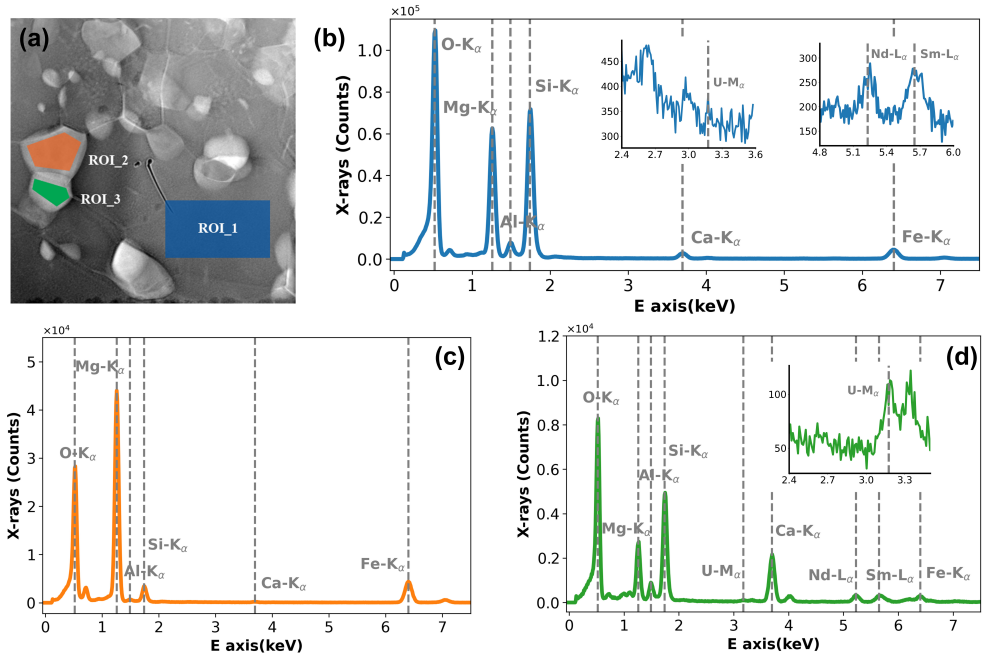

Figure 5.2: ROIs of Brg, Fp, and CaPv (i.e., ROI_1, ROI_2 and ROI_3, respectively) are selected and indicated in (a), the corresponding spectra are presented in (b), (c), and (d), respectively. The two insets of (b) show the X-ray signals of U Mα, Nd Lα and Sm Lα in the ROI of Brg (i.e., ROI_1). The inset of (a) shows the X-ray signals of U Mα in the ROI of CaPv (i.e., ROI_3).

A vital geochemical interest for geoscientists is to investigate the interphase partitioning behavior of trace elements in the Earth's mantle, such as La, Nd, Sm, Gd, Lu, U, and others, which evidences different chemical differentiation events in the mantle [27, 237]. CaPv is proportionally a minor phase but is the predominant host for trace elements [256], as illustrated by the Nd Lα, Sm Lα, and U Mα in the spectrum of ROI_3. Meanwhile, Mg Kα is found in the same spectrum. Since Mg cannot exist in CaPv [256], this signal must come from Brg that is superimposed with the CaPv in the electron beam path. Similarly, we observe the Si Kα peak in the spectrum of ROI_2, which indicates that Fp and Brg also overlap [256]. In fact, the two precipitates were identified to co-overlap with Brg in general after selecting more ROIs and inspecting their spectra.

Quantifying each relevant phase is essential for studying the interphase chemical partitioning behavior. The chemical composition of Brg can be directly quantified from the spectrum of ROI_1 if given sufficient SNR. Regarding the compositions of Fp and CaPv, they cannot be straightforwardly quantified from ROI_2 and ROI_3 since both of them share many elements with Brg and always spatially overlap with Brg. Geochemists usually follow a three-step procedure to obtain the compositions of precipitates in the overlapping scenario, which relies on the unique element in each pair of precipitate-matrix, namely Si in the Fp-Brg pair and Mg in the CaPv-Brg pair. Once the composition of Brg and the phase-mixture are characterized, the overlapping coefficient between each precipitate-matrix pair can be calculated, and the composition of the precipitate is then attained by subtracting the proportion of Brg in the phase-mixture. Therefore, we employed the Cliff-Lorimer ratio method to obtain the three phases' compositions from ROI_1, ROI_2, and ROI_3. To accomplish this, we utilized k-factors that were derived from X-ray emission cross-sections generated through state-of-the-art calculations with 'emtables' (Electron Microscopy Tables) library [257]. The quantification results are presented in Table 5.2 and Table 5.4.

However, given the complicated overlap between phases, selecting ROIs of Fp, CaPv, and Brg is an exacting process. On the one hand, we want to make large ROIs of the phases to gain a sufficient SNR for a precise quantification; on the other hand, we have to avoid the troublesome two-precipitate-overlapping areas (i.e., the three-phase-overlapping areas) where no distinct element is available to differentiate the phases. Another difficulty is the trace element measurements in Brg, which are usually conducted by inductively coupled plasma mass spectrometry (ICP-MS). While this offers phenomenal elemental sensitivity with detection limits in the low parts-per-trillion (ppt, 10^{-12}) for many elements [258], its spatial resolution is limited to several micrometers [259]. In comparison, the superior spatial resolution of STEM-EDXS enables a detailed analysis of the mineral phases towards this goal. We inspected the X-ray signals of Nd Lα, Sm Lα, and U Mα in a relatively large area of Brg, (i.e., ROI_1). Unfortunately, as depicted in the insets of Figure 5.2(b), the U Mα is hardly

discernible, and the Nd Lα and Sm Lα are rather noisy for reliable quantification.

In order to address these challenges and limitations, in the next section we will present a method for segmenting overlapped phases in an automated manner. This is used to generate high SNR spectra for improved phase quantification, particularly for detecting and quantifying trace elements included in relevant phases.

5.3.2 NMF Decomposition and NMF Aided Phase Unmixing

Our segmentation method is based upon NMF. The EDXS signal in each pixel of a STEM-EDXS SI dataset can be regarded as a linear combination of a number of individual phase spectra. Under this assumption, unmixing the phases is defined as the problem of determining a) the individual spectrum of each phase and b) the abundance map which indicates the local weighting of each phase spectrum. While matrix factorization [260] is a popular linear unmixing technique that matches the proposed assumption, its non-negative variant—NMF, applies a further non-negativity constraint that particularly suits EDXS data. Therefore, we started with NMF for phase unmixing and performed NMF on the mineral assemblage using Hyperspy [168].

Before conducting NMF decomposition, PCA was first applied to the dataset to guide us about the number of outputted components that must be specified in the NMF decomposition. According to the PCA scree plot (Figure 5.3(a)), the first three components account for the vast majority of variances of the dataset. Also, conventional EDXS analysis identifies three physical phases. Based on this consistency, we decomposed the assemblage into three components using NMF. Figure 5.3(b)-(c) shows the resultant component spectra and corresponding abundance maps. All the spectra are normalized by their maximum peak intensity. Figure 5.3(b) exhibits that the three component spectra correctly capture the chemical features of the three phases. The spectrum of NMF#0 contains all the essential elements comprising Brg; and peaks such as Si Kα and Ca Kα disappear in the spectrum of NMF#1, and the Mg Kα peak is absent in the spectrum of NMF#2, which are consistent with the true spectrum of Fp and CaPv, respectively. Besides, Figure 5.3(d) demonstrates that the spatial distribution of NMF#0 is similar to that of the matrix phase, Brg, and the spatial distribution of NMF#1 and NMF#2 is concentrated on Fp and CaPv precipitates, respectively. At first glance, the three NMF components therefore chemically represent the three mineral phases in the assemblage.

However, a closer examination of the spectra of the components reveals that they do not completely coincide with the true spectra of the physical phases. As depicted in Figure 5.3(c), we first notice ditches approaching zero intensity around the Si Kα and Ca Kα energy range in

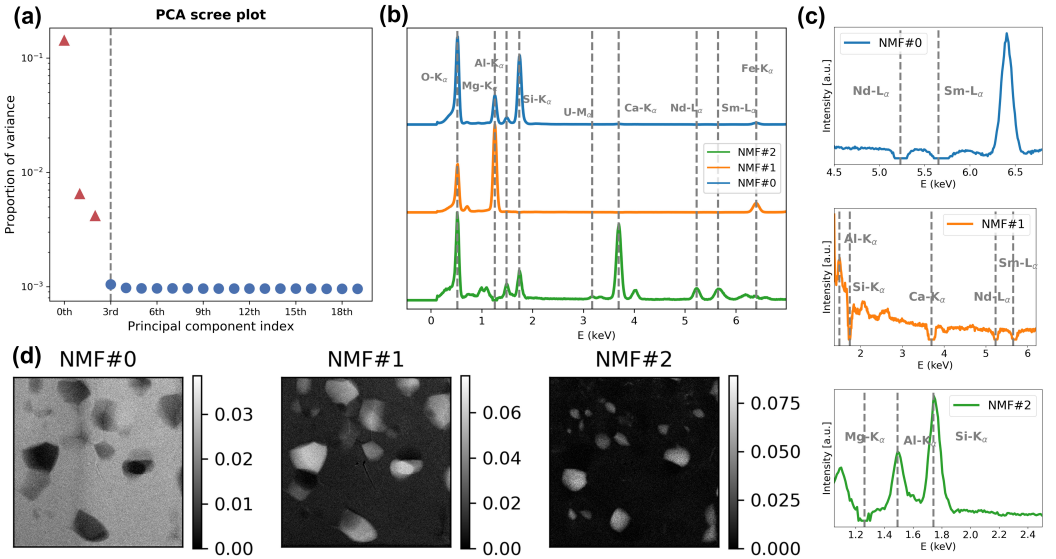

Figure 5.3: (a) The scree plot of PCA decomposition; (b) the three component spectra of NMF decomposition; and (c) their regional zoom-in spectral features; (d) the abundance maps of NMF decomposition.

the spectrum of NMF#1, and a ditch present around the Mg Kα energy range in the spectrum of NMF#2. A similar phenomenon from NMF decomposition was observed previously [177]. Physically, we understand that EDXS is composed of a continuum X-ray spectrum (i.e., bremsstrahlung background) and characteristic X-ray peaks. However, without additional constrains, a mathematical decomposition via NMF fails to account for the bremsstrahlung background, and returns zero when it assigns no element in a given energy range. We further notice that the spectrum of NMF#0 fails to recover signals of trace elements such as Nd Lα and Sm Lα that are proven to be in Brg (Figure 5.2(b)). After quantifying the three spectral components using the Cliff-Lorimer ratio method, we also find that their compositions do not match the compositions of phases. For example, NMF#0 has a significantly lower concentration ratio of Mg to O than that of Brg (from ROI_1), and NMF#1 has an inversely enhanced ratio compared to that of Fp (from ROI_2); also, NMF#2 is excessively enriched in Ca and deficient in Si when compared to the composition of CaPv (from ROI_3). This is not surprising: the mathematical formulation of NMF cannot guarantee an accurate decomposition when the multiple relevant phases overlap spatially and share many common elements at the same time.

While the NMF-derived component spectra show these inaccuracies compared to the actual phase spectra, the spatial loading maps are similar to the true phase distributions to some extent, as inferred from the elemental maps in Figure 5.1. Here, we exploit this resemblance for unmixing phases spatially. Demonstrated in Figure 5.4, two binary masks covering two precipitates, mask#1 and mask#2 (Figure 5.4(c)-(d)), are generated from the abundance

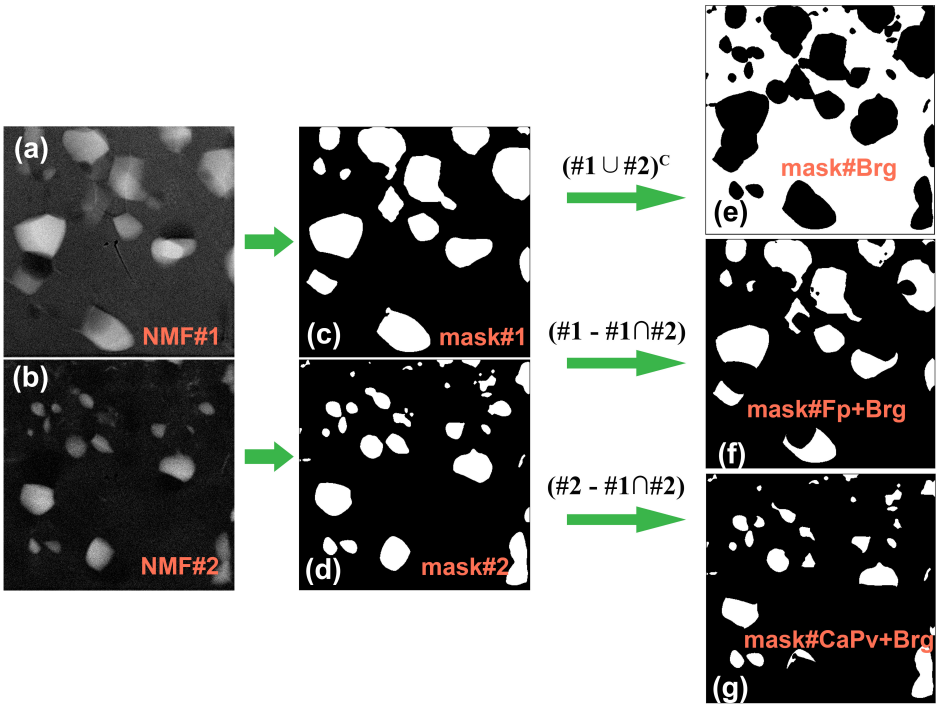

Figure 5.4: Abundance maps of the second and third NMF components; (c)-(d) binary masks generated from (a) and (b), respectively; the binary mask of (e) Brg, (f) the mixture of Fp and Brg, (g) the mixture of CaPv and Brg.

maps of NMF#1 and NMF#2 (Figure 5.4(a)-(b)), respectively. The union of the two masks covers all the precipitates. Consequently, the complement of the union is mask#Brg (Figure 5.4(e)), which covers all the available pure Brg areas. The intersection of mask#1 and mask#2 represents the problematic three-phase-overlapping areas; then, mask#Fp+Brg and mask#CaPv+Brg (Fig. 4(f)-(g)) are attained by subtracting the three-phase-overlapping areas from mask#1 and mask#2. We thus obtain a pure Brg mask and two masks represent the mixtures of Fp+Brg and CaPv+Brg. It is impossible to spatially segment Fp or CaPv from Brg since it is a matrix phase that distributes everywhere.

It is a critical step to create mask#1 and mask#2 that cover precipitates, and we adapted a graph-based algorithm (GrabCut) [261] to perform the segmentation task in a fast and accurate manner. Traditional algorithms such as histogram thresholding [262], edge-based segmentation [263], and region-based method such as watershed transform [264] not only require careful human superintendence, they further do not return a satisfying segmentation in our case, which does not always have a good background-to-foreground contrast ratio. In contrast, GrabCut views an image as a graph: every pixel is a vertex, and constraints between neighboring pixels are viewed as edges. Each edge is weighted by the computed affinity or similarity between two vertices. Pairs of vertices (pixels) within a subgraph have high affinity,

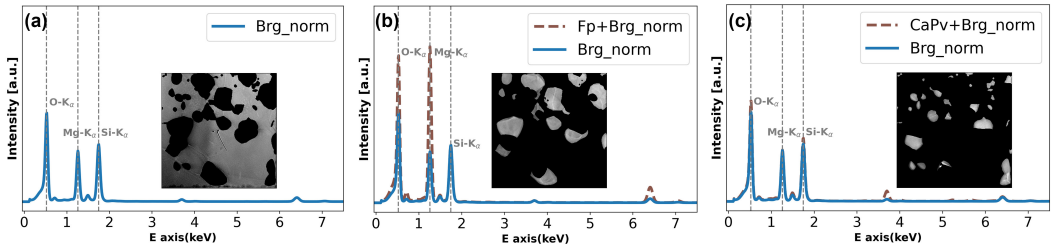

Figure 5.5: (a) The normalized spectrum of Brg (solid curve), (b) the normalized spectrum of Fp+Brg mixture (dashed curve), and (c) the normalized spectrum of CaPv+Brg mixture (dashed curve); the insets are the map of Brg, Fp+Brg mixture, and CaPv+Brg mixture, respectively.

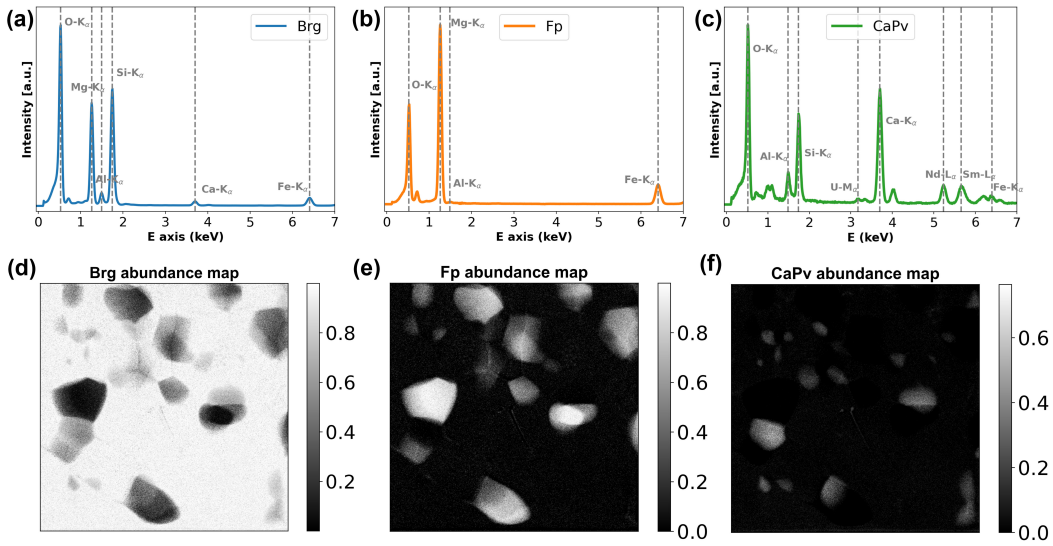

Figure 5.6: Phase spectrum of Brg (a), Fp (b), and CaPv (c), and the distribution maps of Brg (d), Fp (e), and CaPv (f).

while those from different subgraphs have low affinity. The partition of vertices into different subsets is therefore conducted by minimizing the cost of cutting edges [265, 266]. Each subgraph is then an image segment. The method does not solely utilize boundary or regional information but both to achieve optimal global segmentation. Moreover, it simply requires a user-specified rectangle drawn loosely around the object of interest as the input to realize a satisfying segmentation. As a result, we found that it produces a good segmentation.

Applying the GrabCut generated mask#Brg, mask#Fp+Brg, and mask#CaPv+Brg to the original EDXS SI dataset produces a map of pure Brg, a map of Fp+Brg mixture, and a map of CaPv+Brg mixture, as shown in the insets in Figure 5.5(a)-(c). The spectrum of Brg is readily obtained in Figure 5.5(a), and the spectra of Fp+Brg mixture and CaPv+Brg mixture are displayed as dashed curves in Figure 5.5(b)-(c). As mentioned earlier, the *a priori* knowledge

that Brg is a silicate while Fp is an oxide without Si enables us to separate the spectrum of Fp from the spectrum of Fp+Brg mixture. To do this, we normalized the spectrum of Brg and Fp+Brg mixture by their Si Kα intensity, as shown by Brg_norm and Fp+Brg_norm in Figure 5.5(b); next, we obtained the spectrum of Fp by subtracting the portion of Brg from the spectrum of Fp+Brg mixture. Then, in view of the fact that CaPv is a Ca-enriched silicate tolerating zero Mg in its crystal structure, an analogous routine is applied to extract the CaPv spectrum from that of the CaPv+Brg mixture, now based on normalization by the Mg Kα intensity.

Having obtained the true spectra of all the three phases (Figure 5.6(a)-(c)), we leverage them to identify their spatial abundances. Calculating the abundances of phases can be considered as a problem of linear spectral mixture analysis (LSMA) with predefined endmembers. The LSMA is often solved based on a least-squares criterion. In order to produce meaningful abundances of materials, we choose a fully constrained least squares LSMA (FCLS-LSMA) [267] that imposes two constraints on the weights of endmembers in each pixel: the abundance sum-to-one constraint and the abundance nonnegativity constraint. The obtained abundance maps of Brg, Fp, and CaPv are displayed in Figure 5.6(d)-(f).

5.3.3 Quantification of Trace Elements: Reduced Uncertainties and Enhanced Sensitivity

In Section 3.1, we quantified Brg from ROI_1. Its composition is listed in Table 5.2. However, the Nd signal and Sm signal are noisy and the U signal is undetected. When integrating over the masked pure Brg areas (Figure 5.7(b)), the U Mα peak becomes visible, and the Nd Lα peak and Sm Lα peak are smoother and well distinguished from the background, as illustrated by the blue spectrum in Figure 5.7(c). We hence calculated the composition of Brg from the masked Brg area using the Cliff-Lorimer ratio method and show the results in Table 5.2.

Atomic %	Mg	Si	Al	Ca	Fe	Nd (ppm)	Sm (ppm)	U (ppm)	O
Brg of ROI_1	18.30	21.33	2.20	0.87	1.81	285	334	-	55.30
Brg of map 1	18.30	21.12	2.21	0.83	2.05	252	314	101	55.32

Table 5.2: Compositions of Brg obtained by selecting a ROI and by using NMF aided method.

To demonstrate the improvement of SNRs of trace elements with increasing signal (i.e., the number of summed pixels), we additionally selected another three ROIs of Brg (Figure 5.7(a)). Figure 5.7c) visually proves that the SNR of U Mα, Nd Lα, and Sm Lα are substantially enhanced comparing their spectra and also sum spectrum with that of Brg mask 1. To further improve the SNR of U signal, we applied the NMF-aided phase unmixing method to another

two maps (Figure 5.8(a)-(b)) located in neighboring areas and containing the same mineral assemblages. Figure 5.8(c)-(d) are the two segmented pure Brg maps, and Figure 5.8(e) displays the U signal summed from the three respective masks as well as their summation. When integrating over the masked Brg areas of the three maps, U Mβ differentiates itself from the background, as illustrated by the brown spectrum in Figure 5.8(e).

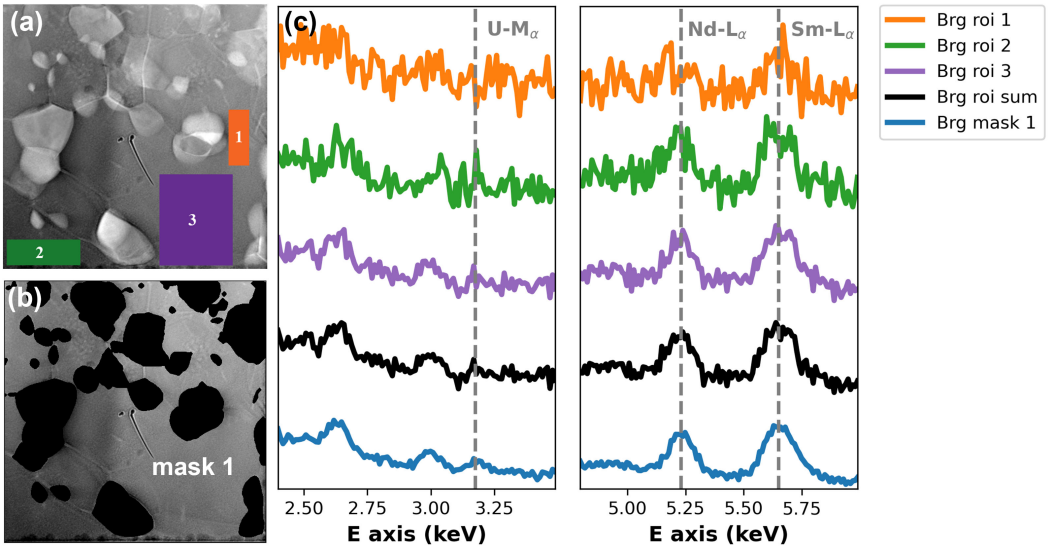

Figure 5.7: (a) 3 Brg ROIs; (b) the masked Brg map; (c) the spectral comparison between the masked Brg and 3 Brg ROIs.

We now calculate the SNRs of U Mα, Nd Lα, and Sm Lα of all the Brg ROIs and list them in Table 5.3, in order to quantitatively evaluate the SNR improvement with the increasing signals (i.e., number of pixels). Specifically, we define the net elemental signal (S) as the area of the peak above the background and take the noise (N) as the standard deviation (σ) of the background close to the actual or expected peak [268], which therefore yields: SNR $= \frac{S}{N} = \frac{S}{\sigma}$. When comparing X-ray peak signals of Brg mask 1 with that of Brg roi 1, the SNR of Nd Lα and Sm Lα is improved by 10.2 times and 8.3 times, respectively. As for the SNR of U Mα, it increases by a factor of 5.5 from the signal of Brg roi 3 to that of Brg mask sum. Figure 5.9 exhibits that the SNRs of trace elements approximately follow a square root relationship with the number of summed pixels. Phenomenologically, the SNRs of trace elements should approach around 10 in order to distinguish their signals from the background. The SNR of Nd Lα increases from 3.9 in Brg roi 1 (orange curve in Figure 5.7(c)) to 9.8 in Brg roi 2 (green curve in Figure 5.7(c)), resulting in the Nd Lα peak emerging from the background. Similarly, the SNR of Sm Lα increases from 7.1 in Brg roi 1 (orange curve in Figure 5.7(c)) to 12.9 in Brg roi 2 (green curve in Figure 5.7(c)), leading to a more identifiable Sm Lα peak. Also, the SNR of U Mα jumps from 2.2 in Brg roi 3 (purple curve in Figure 5.7(c)) to 9.7 in Brg mask 1 (blue curve in Figure 5.7(c)), differentiating the U Mα peak from the background.

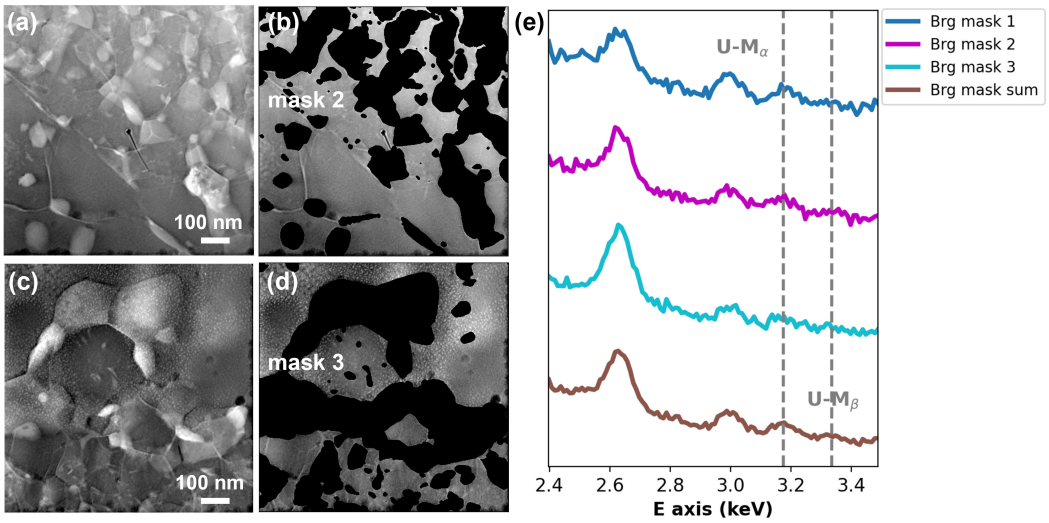

Figure 5.8: (a), (c) The HAADF images; (b), (d) the masked Brg maps of two neighboring mineral assemblages; (e) the spectral comparison of the masked Brg areas.

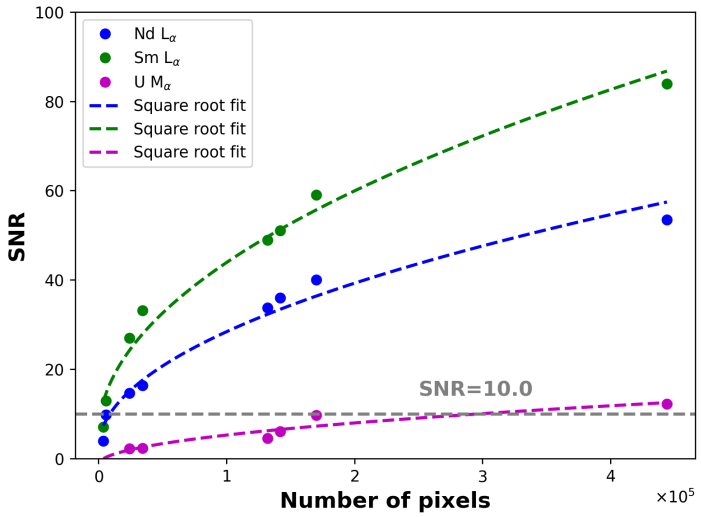

Figure 5.9: The SNRs of Nd Lα, Sm Lα, and U Mα and their square root fit with the number of summed Brg pixels.

Areas		roi 1	roi 2	roi 3	roi sum	mask 1	mask 2	mask 3	mask sum
Number of pixels		3,922	5,980	24,360	34,262	170,081	142,030	132,096	444,207
SNR	Nd Lα	3.9	9.8	14.6	16.4	40	36	33.8	53.5
	Sm Lα	7.1	12.9	27	33.1	59	51	48.9	83.9
	U Mα	-	-	2.2	2.3	9.7	6	4.5	12.2

Table 5.3: The SNRs of trace elements in Brg when integrating over different number of pixels.

By improving the SNRs of trace elements signals, two aspects of uncertainties for the quantification are reduced. First and foremost, we have a better spectrum fitting with reduced fitting error. Figures 5.10(a)-(c) illustrate the spectrum fitting of U Mα of Brg roi 3, Brg mask 1, and Brg mask sum, using Gaussians to model X-ray peaks and taking the variance of error as Poissonian. Reduced chi-squared (χ^2_{red}) is a general method for assessing the goodness of fitting. If a model is fitted to data and the resulting χ^2_{red} is larger than one, it is considered a "bad" fit; whereas if $\chi^2_{red} < 1$, it is considered an overfit. The 'best' fitting is the one whose value of χ^2_{red} is closest to one. The χ^2_{red} of Brg roi 3 is 1.24, and the value improves to 0.95 when integrating over the areas of Brg mask 1. Furthermore, the χ^2_{red} of Brg mask sum is 0.97 that is the closest to one, indicating a satisfying fitting. Since the emission and subsequent detection of a characteristic X-ray can be regarded as statistically independent events, the number of x-rays detected during any finite time interval is governed by the Poisson law. Under this approximation, we calculated quantification errors of the trace elements using the Cliff-Lorimer ratio method and show them in Figure 5.10(d)-(e). By increasing the signal intensities of the trace elements, the Poisson error of Nd concentration and Sm concentration has reduced from ±25 ppm and ±19 ppm in Brg roi 3 to ±3 ppm in Brg mask 1. Similarly, the Poisson error of U concentration has decreased from ±3.4 ppm in Brg mask 1 to ±2.0 ppm in Brg mask sum.

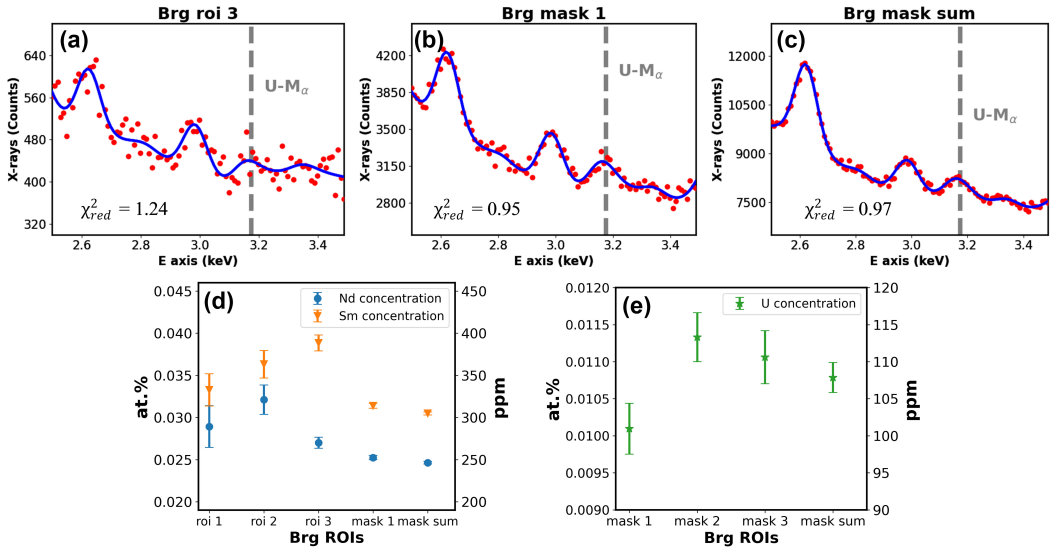

Figure 5.10: Spectrum fitting of (a) Brg roi 3, (b) Brg mask 1, and (c) Brg mask sum; concentration with Poisson errors of (d) Nd and Sm, (e) U.

The proposed NMF aided phase quantification not only reduces the quantification uncertainties of trace elements, but also pushes further the limit of detection (LOD) (i.e., sensitivity) of EDXS. In this part, we will take the spectra of Fp as an example to discuss the LOD improvement. The LOD, as defined by American Chemical Society [269, 270], is the lowest

concentration of an analyte that can be determined to be statistically distinct from a blank. In other words, LOD is equal to the concentration of an analyte at which the SNR equals three. We normalized the spectra of Fp subtracted from an ROI in map 1 (i.e., ROI_2 in Figure 5.2(a)), all of the Fp areas in map 1, and all of the Fp areas in three maps, respectively, by their maximal intensities. Figure 5.11 presents the spectrum signal from 4.8 keV to 6.0 keV which covers the energy range of Nd Lα and Sm Lα. No elemental signal is detected which fits the fact that neither Nd nor Sm can be incorporated into the crystal structure of Fp. Notably, the noise level is significantly reduced for the spectrum of Fp obtained from the NMF aided phase unmixing. If we take the concentration of Mg (45.48 $\pm$ 0.13 at. %) as a reference and use the Cliff-Lorimer ratio method, the LOD of Sm (calculated on Sm Lα position ranging from 5.45 keV to 5.90 keV) could be converted from units of counts to units of concentration. The LOD of Sm in Fp (if Sm were in Fp) decreases from 176 ppm to 106 ppm, and further to 65 ppm when we obtain Fp by applying NMF aided quantification to the three maps.

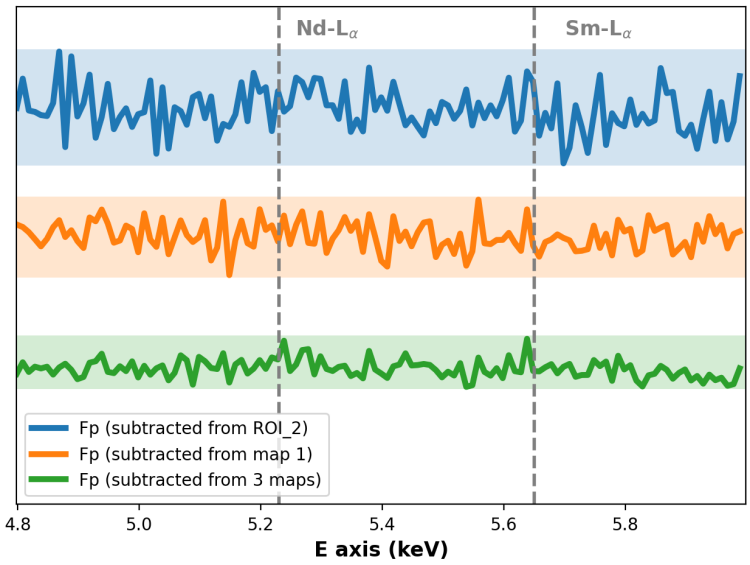

Figure 5.11: Comparison of the noise levels of Fp when subtracting from ROI_2, map 1, and all three relevant maps.

5.3.4 Quantification of Overlapped Phases

As we mentioned earlier, the traditional method for quantifying chemically similar and spatially overlapped phases requires at least one distinctive element between a pair of overlapped phases. This is also the prerequisite for NMF to unmix overlapped phases. NMF decomposition will fail if the concerned phases contain identical elements. Furthermore, in order to generate a true phase spectrum that provides the basis for unmixing the other

phases, the proposed NMF aided method needs that at least one of the overlapped phases has several pure pixels. Compared with the traditional method that demands meticulous ROI selections, the proposed method unmixes overlapped phases in an automated manner, which boosts the data processing efficiency. Another significant advantage of the method for phase quantification, as demonstrated in the previous section, is that it offers improved precision as well as enhanced sensitivity. It is more pronounced for the quantification of trace elements, and also improves the quantification of minor elements included in each phase with increasing SNRs. In Table 5.4, we compare the compositions of Fp and CaPv obtained from the ROI selections and the NMF aided method. The two methods output similar quantifications, but with more precise Al concentration in Fp and U as well as Fe concentration in CaPv for the NMF aided method.

Atomic %	Mg	Si	Al	Ca	Fe	Nd	Sm	U	O
Fp of ROI_2	44.81	-	0.20	-	6.54	-	-	-	48.44
Fp of map 1	45.31	-	0.42	-	7.11	-	-	-	47.14
CaPv of ROI_3	-	17.55	3.85	20.21	0.86	2.73	1.53	0.50	52.40
CaPv of map 1	-	18.12	4.05	21.00	0.55	3.00	1.69	0.63	51.20

Table 5.4: Compositions of Fp and CaPv obtained by selecting a ROI and by using NMF aided method.

5.4 Conclusion

In this paper, we introduced an NMF aided phase analysis method that successfully unmixes phases with substantial spatial and spectra overlap, and increases the sensitivity and precision of STEM-EDXS quantification. We have applied the method to studying Earth mantle phases (i.e., Brg, Fp, and CaPv) in beam-sensitive mineral assemblages. Despite having many elements in common and experiencing significant spatial overlap, the physical phase spectra and phase abundance maps were obtained. Using the developed method, we revealed and quantified the trace element signature, Nd, Sm, and U in Brg. STEM-EDXS combined with the proposed method is suitable to analyze a wide variety of materials that have complex volumetric phase relationships, restricted SNR and beam sensitivity, or vital trace constituents. Moreover, the presented strategy should also be applicable to other spectroscopic mapping techniques, such as electron energy-loss spectroscopy.

6 Beyond NMF: Enhancing STEM-EDXS Analysis with Pan-sharpening

This chapter presents the results of a research work in collaboration with D.T.L. Alexander and C. Hébert, and is meant to be submitted for a publication. Author contributions: H. Chen conceived the idea, performed the experimental data acquisition and the synthetic data simulation, developed the python code for data processing and wrote the manuscript. D.T.L. Alexander and C. Hébert participated in discussing the results and provided constructive advice throughout the course of this project. The samples utilized in this chapter were synthesized and prepared by J. Badro and F. Nabiei.

6.1 Introduction

In this chapter, we continue to explore advanced methods for enhancing the analytical capabilities of STEM-EDXS, building upon the success of the NMF aided method discussed in the previous chapter. Although the NMF aided method proved to be effective, its performance relies on an initial decomposition with NMF to obtain the masks required for integrating counts. Such a process is only feasible if the signal-to-noise ratio (SNR) of the data meet an appropriate threshold. Furthermore, the NMF aided method improves trace element quantification by summing more signal to boost the SNR of the target phases. The effectiveness of the method is, therefore, heavily influenced by the size of the target phase, potentially rendering it insufficient for target phases with limited size. To overcome these constraints and to minimize the dependence on phase size, in this chapter we propose a robust and effective method for unmixing overlapped phases and quantifying trace elements, by incorporating a data fusion technique known as pan-sharpening (PS) [271].

Originally developed for satellite imaging, PS combines datasets with complementary properties, producing a single dataset that retains the benefits of both. It is a typical approach for fusing the spatial information of a high-resolution panchromatic (pan) image and the spectral information of a low-resolution multispectral image to generate a high-resolution multispectra image. The recent work of Borodinov et al. [272] applied PS to hyperspectral EELS analysis, generating an enhanced dataset with improved SNR and without sacrificing spatial resolution. As related to the characteristics of their EELS detector, their implementation made use of two hyperspectral dataset recordings: first, a high spatial resolution (HSR) dataset, recorded with a large number of pixels but a short acquisition time per pixel; second, a high spectral fidelity (HSF) dataset, recorded with a few pixels but a long acquisition time per pixel. Inspired by this approach, we here introduce the PSNMF method, which fuses PS with NMF. Unlike the EELS method of Borodinov et al., owing to the Poissonian noise characteristics of EDXS detection, it requires only a single HSR STEM-EDXS dataset. The HSF dataset is obtained from the HSR one by a binning operation. With it, we simultaneously achieve phase unmixing, quantification improvement, and denoising.

We evaluate the performance of the proposed PSNMF method using both simulated and experimental STEM-EDXS datasets. The experimental data were obtained from the solidus mineral assemblages synthesized at 88 GPa, as detailed in Chapter 4. The acquisition parameters for the experimental dataset remain consistent with those employed in the previous chapter, giving an average of 120 X-ray counts per pixel. In addition to the experimental data, we make use of synthetic datasets based on the characteristics of the experimental data. These incorporate various SNRs to comprehensively assess the effectiveness of the PSNMF method. Indeed, these synthetic datasets with a known ground truth allow us to sys-

tematically investigate the performance of the proposed method under different conditions, thereby providing a more robust evaluation of its capabilities in addressing the challenges associated with overlapped phase unmixing and trace element quantification in STEM-EDXS analysis. The results and discussions of these evaluations are presented in the subsequent sections of this chapter.

6.2 Simulation of STEM-EDXS Data

In order to simulate STEM-EDXS datasets, we employ a Python library called 'espm' (Electron Spectro-Microscopy) [257], developed in our group by Dr. A. Teurtrie. espm is an open-source tool developed for generating synthetic STEM-EDXS datasets based on user-defined chemical compositions and spatial abundance maps of the constituent phases. The simulation process relies on X-ray emission cross-sections generated using state-of-the-art calculations with the accompanying 'emtables' (Electron Microscopy Tables) library [257]. emtables is an open source and user editable library of EDXS cross-sections for STEM-EDXS. To simulate the Bremsstrahlung background, a semi-empirical model is incorporated. Considering our phases of interest are composed of lower mantle minerals, we simulate the three phases, Fp, CaPv, and Brg with compositions as listed in Table 6.1. While Cu was not included in the starting experimental composition, we add 1.0 at.% Cu to the composition of Fp due to its importance in influencing the electrical conductivity of the Earth's mantle. The CaPv is designed to contain minor amounts of Fe, Nd, Sm, U (1.0 at.% for each), and Al (2.5 at.%). Finally, the Brg includes 1.0 at.% Fe and Ca, as well as 1.5 at.% Al, and trace amounts of Nd and Sm (0.1 at.% for each). The composition design was based on the results obtained from the NMF aided decomposition presented in the previous chapter. In terms of the spatial distribution, both Fp and CaPv phases always overlap with the matrix phase Brg in the simulated dataset. Furthermore, there exist areas where Fp and CaPv phases overlap with each other.

The simulation process can be summarized in several steps. Initially, pure spectra for each phase are created with the desired chemical composition and Bremsstrahlung parameters. Subsequently, an abundance map is generated for each phase. The two quantities are combined using a tensorial product, resulting in a noiseless datacube, which also serves as the ground truth. Figure 6.1 depicts these ground truth abundance maps and noiseless spectra utilized to generate noisy datasets. Brg acts as a matrix phase that overlaps with the Fp and CaPv precipitates; the Fp and CaPv also share some spatial common areas. Noisy datacubes are then constructed by designating an average number of counts per pixel and sampling from the noiseless data. Specifically, noisy pixel spectra are created by randomly sampling X-ray events from each normalized spectrum of the noiseless dataset according to a Poisson

distribution. For further details, the reader is referred to [257]. Herein, two datasets were simulated, one with a medium SNR averaging 147 counts per pixel (i.e., C147 dataset) and the other with a low SNR averaging 15 counts per pixel (i.e., C15 dataset), as displayed in Figure 6.2. The C147 dataset has a statistical profile that is comparable to that of the experimental dataset, while the C15 dataset exhibits an extremely low number of counts. Both simulated datasets have a spatial size of 180 by 180 pixels (1 nm pixel size) and an energy scale ranging from 0.3 keV to 10 keV (100 eV per energy channel). The electron beam energy is set to 200 keV, with the simulated sample thickness and density set at 100 nm and 4.5 g/cm^3, respectively.

Atomic %	Mg	Fe	O	Ca	Cu	Si	Al	Sm	U	Nd
Fp	39.00	10.00	50.00	-	1.00	-	-	-	-	-
CaPv	-	1.00	60.00	16.20	-	17.50	2.50	1.00	1.00	1.00
Brg	18.50	1.00	60.00	1.00	-	18.20	1.50	0.10	-	0.10

Table 6.1: Compositions of the three simulated phases used for generating the synthetic datasets.

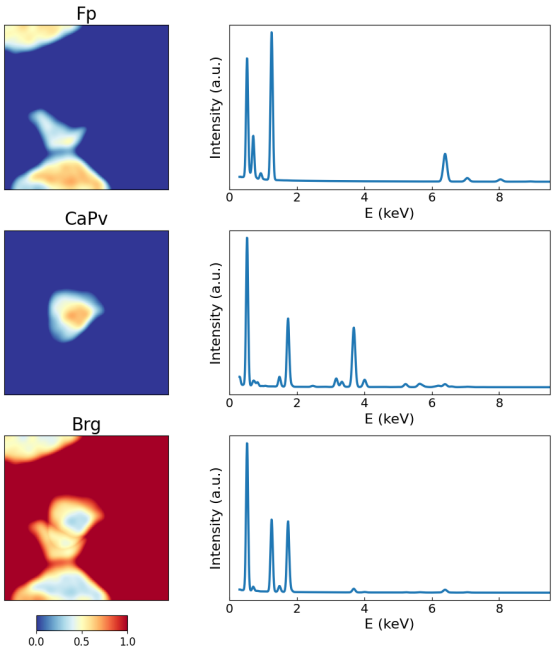

Figure 6.1: The first column: ground truth abundance maps; and the second column: noiseless spectra of the three simulated phases Fp, CaPv and Brg, respectively, derived with the compositions shown in Table 6.1.

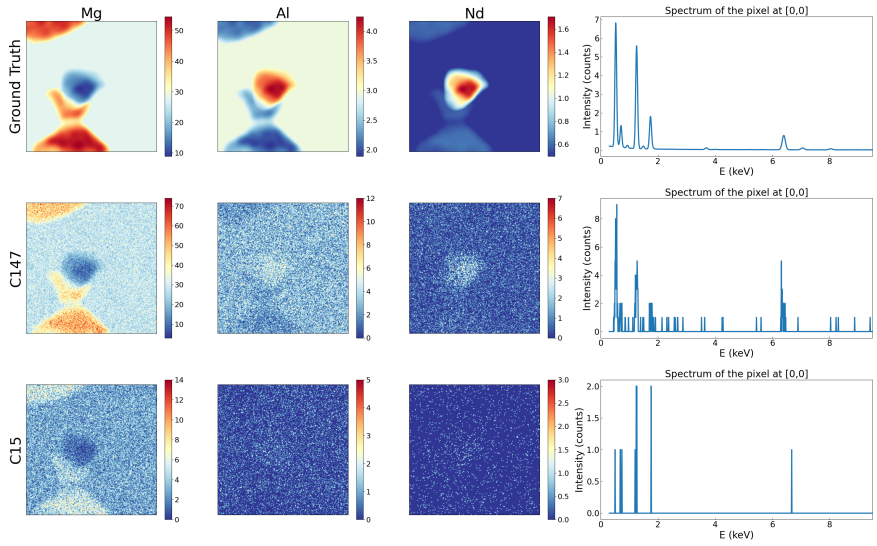

Figure 6.2: Mg Kα, Al Kα and Nd Lα maps, and pixel spectra at [0,0] of the simulated datasets: noiseless ground truth, C147 dataset, and C15 dataset.

6.3 PSNMF

6.3.1 Methodology

The potential of NMF to unmix signals is affected by a variety of factors, including noise levels, initial values, loss functions, and, critically, the signals themselves. Before exploring a range of algorithmic parameter tuning strategies, it is essential to establish the limits of NMF's ability to unmix spatially overlapping and spectrally similar signals under ideal conditions. By utilizing noiseless simulated data, we were able to address this question in a series of simulations not presented in this thesis. Specifically, we simulated a pair of phases, where $MgSiO_3$ acted as the matrix phase, and a spherical precipitate overlapped spatially with the matrix. We tested the effectiveness of NMF decomposition in cases where the spherical precipitate was composed of FeO, MgO, $CaSiO_3$, and $Ca_{0.9}Mg_{0.1}SiO_3$, respectively. Based on our findings, we concluded that NMF can effectively unmix a pair of spatially overlapped phases, provided that they possess at least one distinct element and sufficient SNR. This is in contrast to real-world scenarios, particularly in the context of STEM-EDXS datasets with low count rates. For such cases, we find that NMF often fails to retrieve components accurately. This is due to the fact that the loss function of NMF has multiple local minima in the presence of noise, producing suboptimal decomposition results [273]. As the noise level increases, the task of NMF to converge to the global minimum becomes more arduous, leading to greater difficulty in accurately identifying the underlying component vectors. We

also conducted more tests on NMF decomposition using the same phase settings mentioned above but adding different levels of noise. We found that NMF decomposition on high SNR datasets yields more accurate NMF spectral components than on low SNR ones. Moreover, we discovered that, when the SNR of the dataset meets an appropriate threshold, it results in NMF spectral components that are as accurate as those obtained from noiseless datasets. Although these results are not presented in the thesis, they provide valuable insights for our following research.

Given the above discussion, it is clear that improving the SNR of a dataset can improve the effectiveness of NMF decomposition. Starting from a fixed STEM-EDXS dataset, binning pixels in the spatial dimension is a possible strategy to enhance the SNR of its spectra. Specifically, if we have one single noisy dataset with a large number of pixels but a short acquisition time per pixel (i.e., a HSR dataset), spatial binning can produce a dataset with fewer pixels but an improved SNR per binned pixel (i.e., a HSF dataset). Clearly, spatial binning will reduce the spatial dimension of the original dataset. Therefore, our concept is to use the PS approach to ally the improved NMF spectral decomposition of a binned dataset with the high spatial resolution of the original dataset. The strategy involves several steps. First, NMF is applied to the binned HSF dataset, producing more accurate spectral components and corresponding spatial abundance maps with reduced spatial dimensionality. To recover the high spatial resolution of the abundance maps, a second NMF decomposition is performed on the HSR dataset, using the higher quality spectral components and their abundance maps obtained from the previous step as initialization values. Prior to the decomposition, these spatial abundance maps are upsampled to match the dimensions of the HSR dataset. Because NMF is a heuristic algorithm sensitive to initial values, the improved initialization significantly enhances the quality of the decomposition results compared to random initialization on the HSR dataset. However, the spectral components from the second NMF decomposition are not necessarily superior to those from the first decomposition, as it is influenced more by the SNR of the HSR dataset. The fundamental aim of the second NMF decomposition is to recover the the high spatial resolution abundance maps. We, therefore, obtain the high quality component spectra that are representative of the underlying phases' spectral signatures in the dataset from the first NMF decomposition, and recover the high spatial resolution abundance maps that indicate the spatial distribution of these spectral signatures from the second NMF decomposition. By combining these two sets, it is possible to reconstruct a high quality dataset with improved SNR. Through NMF decomposition, we thereby fuse the advantages of the two datasets (HSR and HSF) into a single dataset with the benefits of both. As explained earlier, we name this method PSNMF. Its corresponding flowchart is illustrated in Figure 6.3, and a detailed mathematical explanation is presented next, as based on the papers by Borodinov et al. [272] and Loncan et al. [274].

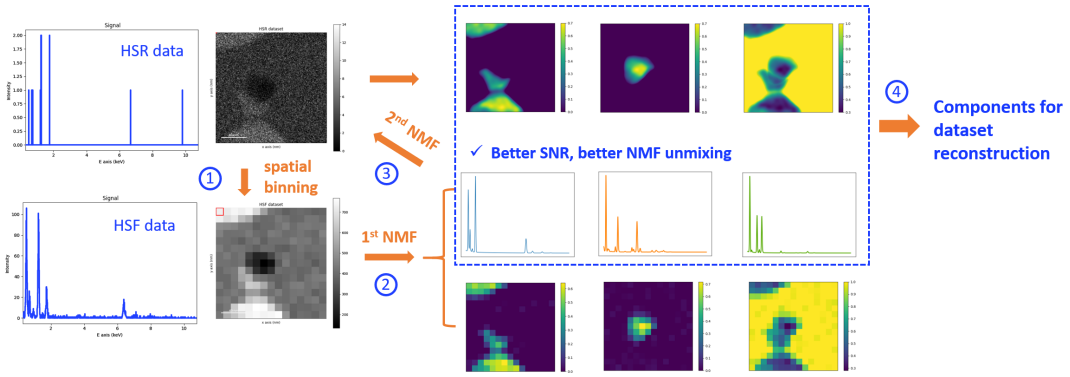

Figure 6.3: PSNMF method: a graphical overview of the workflow.

We begin with the original noisy HSR dataset (Y) of size (y, e), where e is the number of energy channels (spectral features) and y is the number of pixels (spatial dimensions). Through spatial binning, we create the HSF dataset (X) of size (x, e), where x is the number of pixels and is calculated as $x = \frac{y}{n^2}$, with n being the bin size (e.g. a bin size of 5 results in $x = \frac{y}{25}$). Our aim is to combine the beneficial properties of Y and X into a new dataset Z. Z is a matrix of size (y,e) that possesses improved SNR while maintaining high spatial resolution. The relationships between the datasets X, Y, and Z are described as follows:

$$X = ZS + E_s \tag{6.1}$$

$$Y = RZ + E_r \tag{6.2}$$

where S and R are transformation matrices, S is a spatial transformation matrix dictating the transformation of spatial features in Z for the low dimension dataset, and R is a spectral transformation matrix converting the spectral features in Z to match those in the lower spectral fidelity dataset. E_s and E_r are residuals. The data fusion problem is to estimate Z, which can be done via NMF:

$$Z = WH + \epsilon \tag{6.3}$$

where W denotes spectral components, and H represents corresponding abundance maps; ϵ is the residual (error) that is assumed to be zero if W and H are accurately obtained.

The X and Y can be approximated similarly as follows:

$$X \approx WH_h \tag{6.4}$$

$$Y \approx W_m H \tag{6.5}$$

where H_h is the spatially reduced abundance matrix, and W_m is the spectrally deteriorated component matrix.

We first unmix the HSF dataset to retrieve an estimate for W and H_h; then we initialize the decomposition of the HSR dataset using W and upsampled H_h to obtain H. The two matrices W and H can be multiplied to obatin the fused dataset, Z. To implement this, we utilize the NMF from scikit-learn library. Note that, compared with the standard NMF (also employed in Hyperspy [168]), we impose a 'sum-to-one' constraint on the abundance matrix; a constraint which is appropriate for the nature of STEM-EDXS data.

6.3.2 Performance Measure

When testing the PSNMF methodology, it is crucial to be able to properly assess its effectiveness. While a visual inspection of the spectra and abundance maps produced by the decomposition may be useful for this, a metric is also necessary to quantitatively compare the decomposition results with the ground truth. Here, two metrics are used to measure the quality of the decomposed spectra and abundances.

For spectra, the angle between the decomposition result and the ground truth is calculated as:

$$\theta = \arccos\left(\frac{v_1 \cdot v_2}{\|v_1\| \times \|v_2\|}\right) \tag{6.6}$$

where v_1 and v_2 are two spectral vectors of the same dimension. An angle of 0° represents a perfect agreement between the two spectra, and an angle of 90° means two fully different spectra.

For abundance maps, the mean squared error (MSE) between the decomposed maps and the true maps is calculated as:

$$MSE = \frac{\|m_1 - m_2\|^2}{P_x P_y} \tag{6.7}$$

where m_1 and m_2 are two maps of dimension $P_x \times P_y$. The MSE takes values between 0 and 1, and 0 represents a perfect agreement between the two maps.

To assess the effectiveness of the dataset denoising, the average map spectral angle metric is utilized. This metric compares the spectral similarity between the reconstructed dataset and the noiseless dataset on a pixel-by-pixel basis, and calculates the average spectral angle of

the reconstructed dataset. The calculation is performed as follows:

$$\theta_{\text{avg}} = \frac{1}{P_x \times P_y} \sum_{i=1}^{P_x \times P_y} \theta(i) \tag{6.8}$$

where $\theta(i)$ denotes the spectral angle between the pixel spectral vectors at position i, and θ_{avg} is the mean value of the spectral angles between all pixel pairs of the reconstructed dataset and the noiseless dataset.

6.4 Evaluation of PSNMF on Simulated Data

6.4.1 Medium SNR Dataset: C147

Overlapped Phase Unmixing

In this section, we test our PSNMF method on the synthetic dataset, starting with the C147 dataset with moderate counts. Before applying PSNMF, we first conduct a 'classical' NMF decomposition such that we can benchmark its capability. Figure 6.4 presents the outcomes of applying NMF directly to this C147 dataset. We specified the number of decomposition components to be three, and we observe that the first two components closely resemble Brg and Fp, respectively. Quantifying this resemblance, the first NMF spectral component has a spectral angle of 5.80° when compared with the Brg ground truth spectrum, and the second NMF spectral component has a spectral angle of 4.30° when compared with the Fp ground truth spectrum. In comparison, the spectrum and spatial abundance map for the third component are strongly different from the ground truths of CaPv. This discrepancy shows that the extraction of the CaPv phase was unsuccessful, likely due to inadequate SNR in the raw dataset.

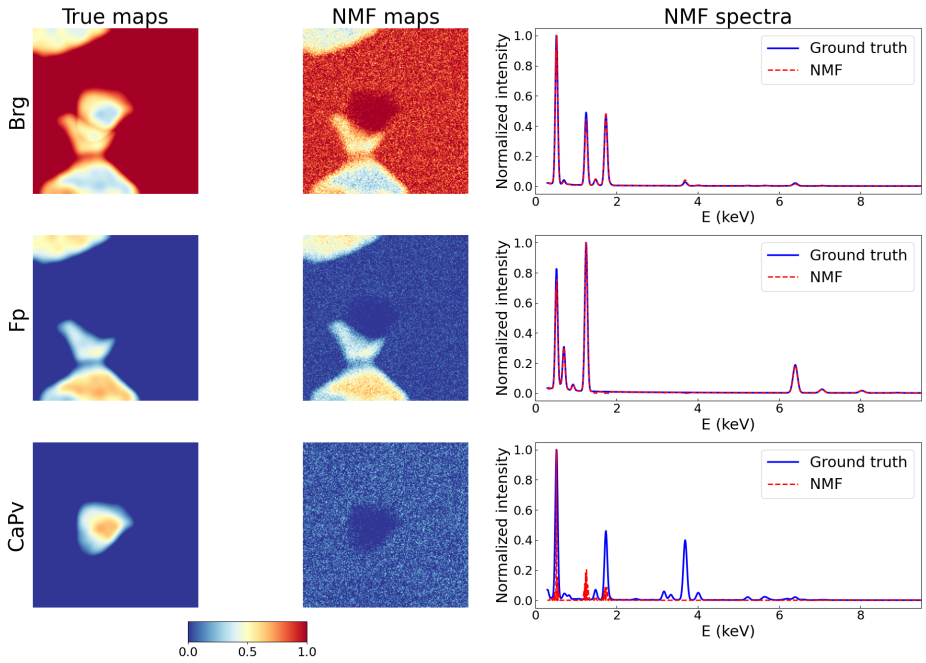

Figure 6.4: Abundance maps and spectra of NMF decomposition compared to ground truths on C147 dataset.

Having identified this failing of the direct NMF decomposition, we now conduct a series of binning experiments on the C147 dataset to generate HSF datasets, and apply the proposed PSNMF to them to assess the effect of increasing binning numbers on the accuracy of the decomposition results. Specifically, we performed binning numbers of 2 by 2, 4 by 4, 12 by 12, 15 by 15, and 30 by 30. We then analyzed the corresponding spectral angle and MSE of each component as well as the average spectral angle and the average MSE of the three components, with increasing binning numbers. These results are presented in Figure 6.5. Upon applying 4 by 4 binning, we now successfully extract the CaPv phase, with a spectral angle of 1.78°, which shows that the decomposed spectrum closely approximates the ground truth spectrum of CaPv. Also, the spectral angles for Brg and Fp decrease to 0.27° and 2.08°, respectively, indicating an improvement in the accuracy of the decomposition results. Therefore, consistent with our expectation, the increase in bin size lead to a more accurate decomposition. When the binning number increases to 12, the spectral angles of Brg, Fp, and CaPv further decrease to 0.25°, 1.52°, and 1.73°, respectively. Their corresponding spectra closely approximate the ground truth spectra, as depicted in Figure 6.6. Similarly, a binning number of 15 produces comparable results, with spectral angles of 0.25°, 1.59°, and 1.76° for Brg, Fp, and CaPv, respectively.

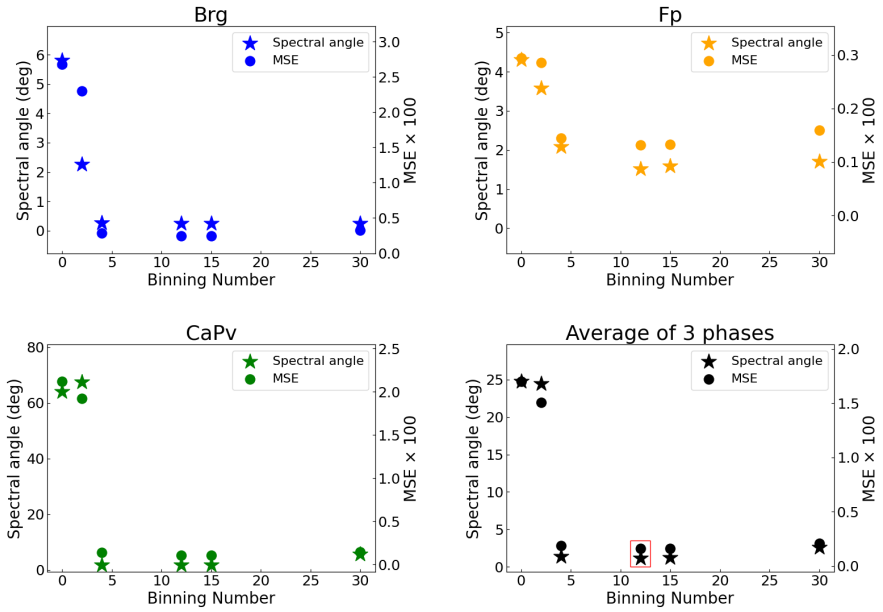

Figure 6.5: Spectral angles and MSEs of Brg, Fp, and CaPv components and their averages with increasing bin size for the C147 dataset.

Upon further increasing the binning number to 30, while we observe a stable spectral angle of 0.25° for Brg, the spectral angles for Fp and CaPv increase notably to 1.71° and 5.70°, respectively. This suggests that, beyond a certain binning number, further increases in bin size has a negative impact on the unmixing of phases with smaller spatial sizes. This is due to the fact that, as the bin size increases, the smaller phases become less distinct in the relevant pixels, thereby making it more challenging to accurately unmix them. Conversely, for larger phases, the noise mitigation effect of binning becomes more pronounced as the bin size increases. Notably, the spectral angle always remains larger than 0. This is due to the fact that, as discussed in the previous chapter, when NMF assigns no signal in a particular peak position, it produces a ditch approaching zero in that energy range rather than following a physical bremsstrahlung background.

From Figure 6.5, we also observe that MSE values of the PSNMF decomposed abundance maps follow a similar trend to the values of spectral angle, as the bin size increases. Notably, at the bin size of 12, the MSE values of the Brg, Fp, and CaPv components reduce to 0.0024, 0.0013, and 0.0011, respectively. These values indicate a remarkable match to the truth phase abundances, highlighting the effectiveness of PSNMF in retrieving phase distributions. Supplementary results of PSNMF decomposition on the HSF2, HSF4, HSF15, and HSF30 datasets are provided in the Appendix 8.

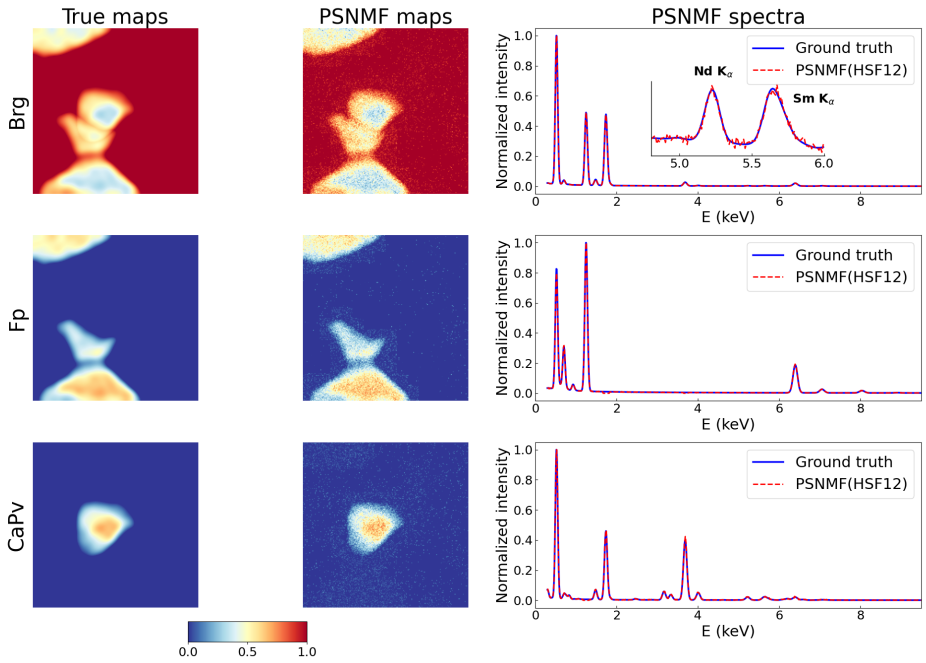

Figure 6.6: Abundance maps and spectra of PSNMF decomposition (12x bin) compared to ground truths on C147 dataset. The inset figure shows a localized magnification of trace elements Nd and Sm in the Brg component, proving accurate phase unmixing.

Given the good unmixing results of the 12x binning experiment, we now quantify the corresponding three spectral components and compare their compositions with the ground truth phase compositions. These results are shown in Table 6.2. The Brg component exhibits an impressive match to the ground truth Brg composition, with a maximum relative composition error being less than 3.0%. In the case of the Fp component, the minor element Cu shows the highest relative composition error of 16%, with a value of 1.16 at.% in contrast to the ground truth value of 1.00 at.%. For the CaPv component, its minor element Al shows the highest relative composition error of 12%, with a value of 2.20 at.% in contrast to the ground truth value of 2.50 at.%. Besides these, the relative composition errors for other elements in the Fp and the CaPv component are all less than 4.5%. The obtained quantification of components demonstrates an accurate identification and unmixing for the three spatially overlapping and chemically similar phases via PSNMF with a bin size of 12.

Summarizing on this evaluation, in this section, we have studied the effectiveness of PSNMF on a dataset that has an average of 147 X-ray counts per pixel. The ground truth comprises three phases with significant spectral similarity, as indicated by the spectral angle between the Brg-Fp pair (36.1°) and the Brg-CaPv pair (32.0°). Additionally, these phases exhibit a significant spatial overlap. As we saw first, direct application of NMF on the C147 dataset fails to accurately retrieve CaPv, the phase with the smallest proportion. By instead performing

Atomic %	Mg	Si	Al	Ca	Fe	Nd	Sm	U	O	Cu
Brg / GT	18.50	18.20	1.50	1.00	1.00	0.10	0.10	-	60.00	-
Brg / HSF12	18.49	18.10	1.47	1.01	0.99	0.10	0.10	-	59.72	-
Fp / GT	39.00	-	-	-	10.00	-	-	-	50.00	1.00
Fp / HSF12	39.53	-	-	-	10.46	-	-	-	48.84	1.16
CaPv / GT	-	17.50	2.50	16.20	1.00	1.00	1.00	1.00	60.00	-
CaPv / HSF12	-	17.42	2.20	16.57	0.98	0.99	0.96	0.99	59.81	-

Table 6.2: Composition comparison between the ground truth and PSNMF decomposed components through the 12x bin experiment.

PSNMF with the HSF12 dataset generated by 12 by 12 binning, we extract the phase abundance maps and spectra with high accuracy. Overall, binning-based PSNMF is clearly a useful approach for phase unmixing. However, the impact of binning on phase unmixing accuracy is not necessarily monotonic. As for instance shown by the HSF12 vs HSF30, selecting an optimal binning number is crucial to balance the trade-off between SNR improvement and the distinguishability of each phase in relevant pixels, particularly for smaller phases.

Dataset Denosing

Having looked at the use of PSNMF for phase unmixing, now we consider its use for dataset denoising. NMF assumes that the concerned data can be represented as a linear combination of non-negative components. The quality of data reconstruction via NMF hence depends on the accuracy of the decomposed components. As previously discussed, the accuracy of the decomposed components is largely dependent on the noise level of the dataset, with noisier data resulting in less faithful components. Indeed, data reconstruction using unfaithful components has a large chance of containing artifacts. Through the experiments and analyses presented above, we demonstrate that PSNMF results in high quality component spectra and abundance maps. With these, it is possible to reconstruct a high quality dataset with improved SNR.

PCA remains the 'gold standard' of spectrum image denosing technique in the EM community, so it is taken as a comparative reference. Applying PCA to the C147 dataset, the scree plot (Appendix 9) indicates the presence of three major components within the dataset. These are used to reconstruct the dataset. In Figure 6.7, these PCA results are compared to our proposed denoising alternative using PSNMF on the 12x binned dataset. For the comparisons, we present the elemental maps of integrated peak counts of Mg Kα, Al Kα, and Nd Lα to illustrate the major, minor, and trace elements, respectively. It is evident that both PCA and PSNMF denoise the dataset effectively, particularly for the minor and trace elements. However, unlike PSNMF, PCA cannot ensure non-negativity in the reconstructed dataset, resulting in negative counts that cannot be quantified. For example, the elemental

map of Mg Kα exhibits a minimum intensity of negative four counts. Furthermore, we calculate the average map spectral angle for both the PCA reconstructed dataset and PSNMF reconstructed dataset in reference to the ground truth dataset. The spectral angle value for the PSNMF reconstructed dataset is 1.14°, whereas the value for the PCA reconstructed dataset is 2.49°. In addition to the non-negativity advantage, PSNMF therefore demonstrates superior denoising performance compared to PCA for the C147 dataset.

To further assess the effectiveness of PSNMF in denoising the dataset, we selected three small regions of interests (ROIs) located on Fp, CaPv, and Brg, as illustrated in Figure 6.8. Each ROI comprises four pixels. For each of them, Figure 6.8 shows a comparison of the summed spectra between the raw dataset and the PSNMF reconstructed dataset. Minor and trace elements, such as Cu in Fp (1.0 at.%), U in CaPv (1.0 at.%), and Nd and Sm in Brg (0.1 at.% for each) are present as mere counts in the raw spectra, and could not be identified. In contrast, PSNMF successfully denoised the dataset, accurately revealing these signals.

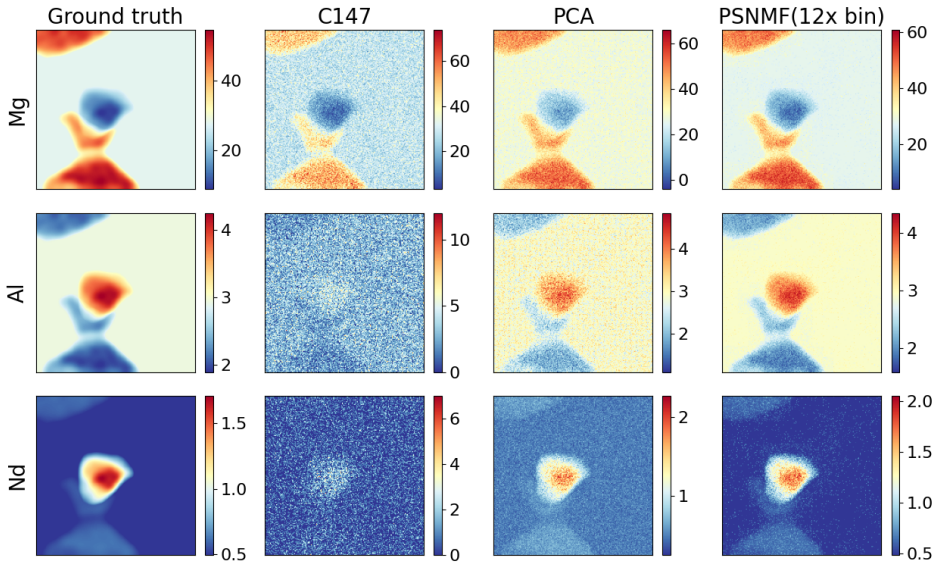

Figure 6.7: Elemental maps of Mg Kα, Al Kα, and Nd Lα for ground truth dataset, C147 dataset, PCA reconstructed dataset, and PSNMF reconstructed dataset through 12x bin experiment. The colorbar scales range from the minimum to the maximum value for each map.

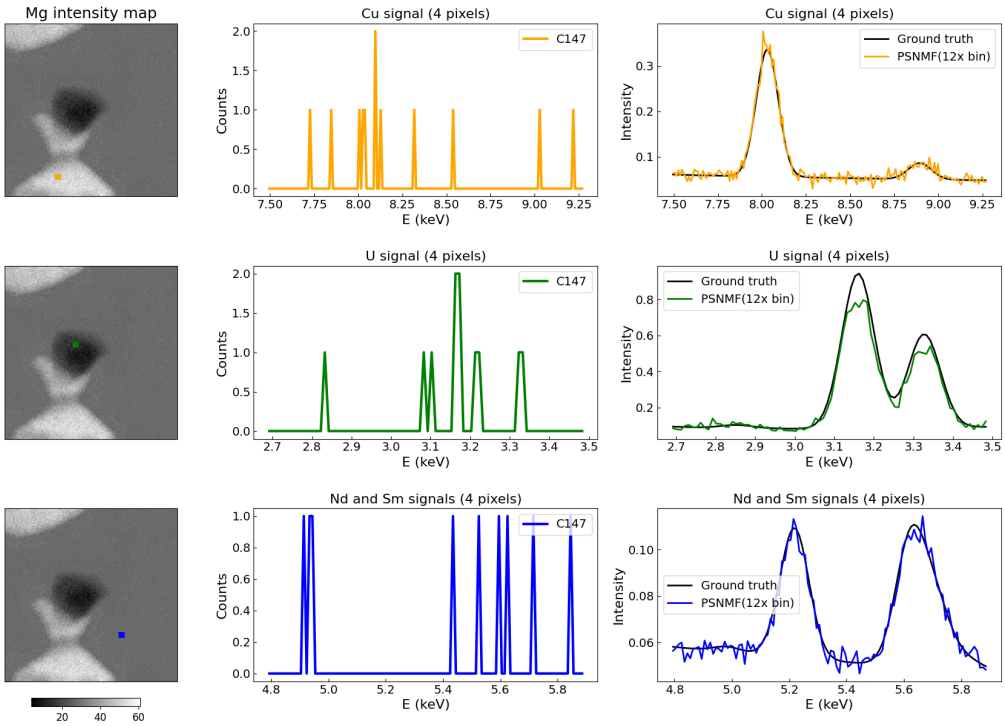

Figure 6.8: First column: Mg intensity maps of integrated peak counts reconstructed by PSNMF through the 12x bin experiment. The orange square indicates the Fp ROI, the green square indicates the CaPv ROI, and the blue square indicates the Brg ROI. Second column: raw spectra of the Cu Kα, U Mα, Nd Lα, and Sm Lα signals from the respective ROIs. Third column: comparison of these signals between the ground truth dataset and PSNMF reconstruction through the 12x bin experiment.

6.4.2 Low SNR Dataset: C15

Overlapped Phase Unmixing

In this section, we extend our evaluation of the PSNMF method by testing its effectiveness on the C15 dataset, which has an extremely low SNR with an average of only 15 X-ray counts per pixel. We first apply NMF directly to the C15 dataset, and present the results in Figure 6.9. Clearly, NMF fails to correctly retrieve any phase due to the high noise level in the dataset. Specifically, the spectral angle of the first component compared with the ground truth spectrum of Brg is 29.7°, and the spectra for the other two components show only some spikes at the energy range of some elements. Furthermore, the component abundance maps do not reflect the distribution of phases in the dataset. These results demonstrate the limitations of the classical NMF algorithm for phase unmixing in the presence of a very high noise level.

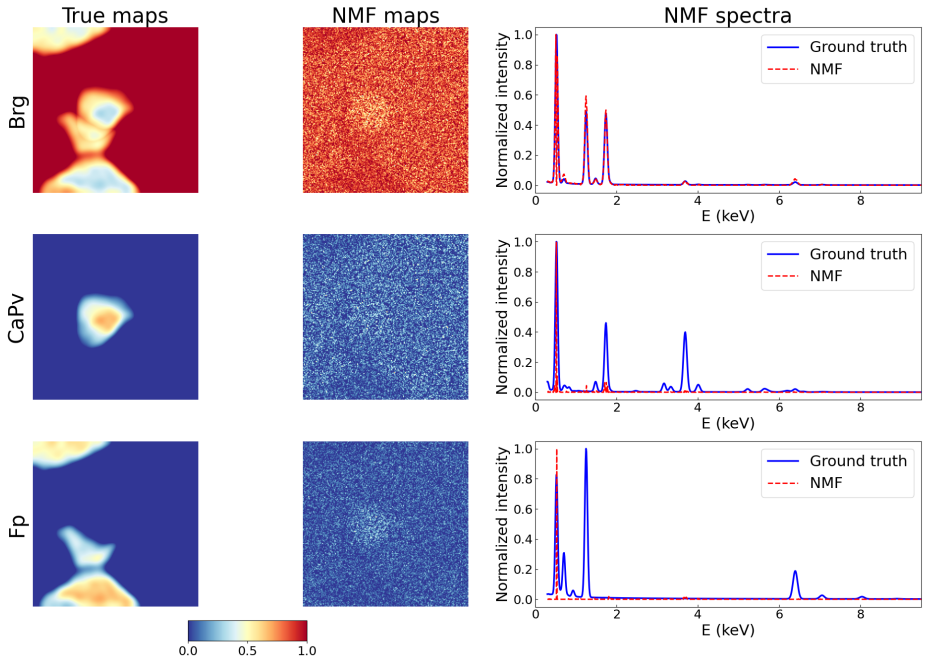

Figure 6.9: Abundance maps and spectra of NMF decomposition compared to ground truths on C15 dataset.

Similar to the previous section, we conduct a series of binning experiments on the C15 dataset and perform PSNMF on each of them. The PSNMF decomposition results for all bin sizes are included in the Appendix 10. The corresponding values of spectral angle and MSE and their averages are plotted in Figure 6.10. As mentioned earlier, the higher noise level within the data makes it more difficult for the decomposition to converge to a global minimum. For the C15 dataset, the decomposition results of 2x bin and 4x bin end up in

different local minima, resulting in incorrect phase extraction and large values of spectral angle and MSE. Only when we increase the bin size to 12, do we start to correctly extract the three phases, with spectral angles of 0.68°, 2.68°, and 5.23°, and MSEs of 0.055, 0.025, and 0.021 when compared with the ground truths of Brg, Fp, and CaPv, respectively. The 15x bin experiment produces similar decomposition results, with spectral angles of 0.64°, 2.72°, and 5.04°, and MSEs of 0.054, 0.025, and 0.021 for the three components, respectively. When further increasing the bin size to 30, the spectral angles of the Brg and Fp components remain stable at 0.65° and 2.65°. However, the spectral angle of the CaPv component increases to 6.89°. As discussed earlier, the increase in the spectral angle of the CaPv component is related to the reduced distinctiveness of the CaPv phase in the relevant binned pixels. Meanwhile, we observe that the MSEs of the three components are slightly improved, with values of 0.048, 0.025, and 0.016. This can be attributed to the fluctuation of local minima during the decomposition of the HSR dataset that was aimed at obtaining abundance maps with recovered high spatial resolution. Here, we believe that a bin size of 15 is optimal for the phase unmixing of the C15 dataset out of the investigated binning numbers. The PSNMF results for the 15x bin experiment are presented in Figure 6.11.

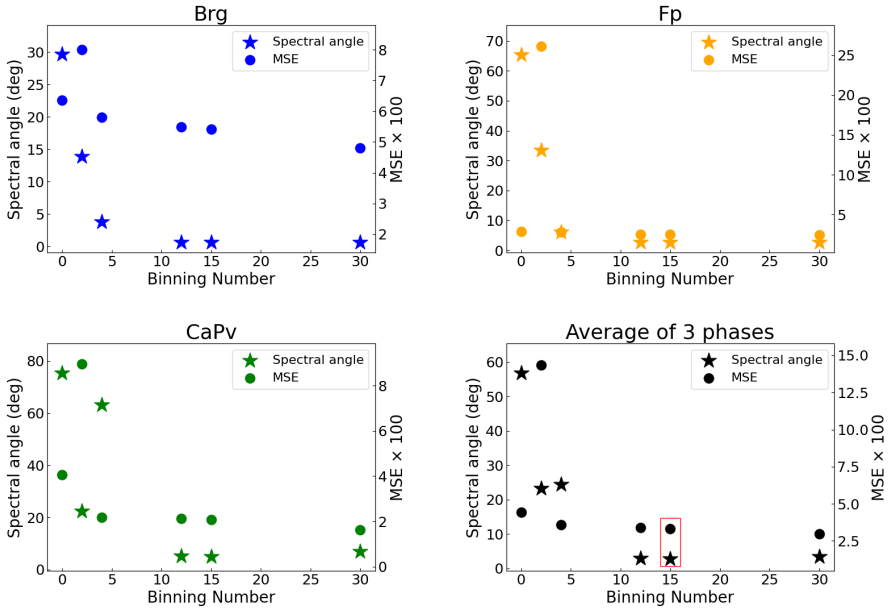

Figure 6.10: Spectral angles and MSEs of Brg, Fp, and CaPv components and their averages with increasing bin size for the C15 dataset.

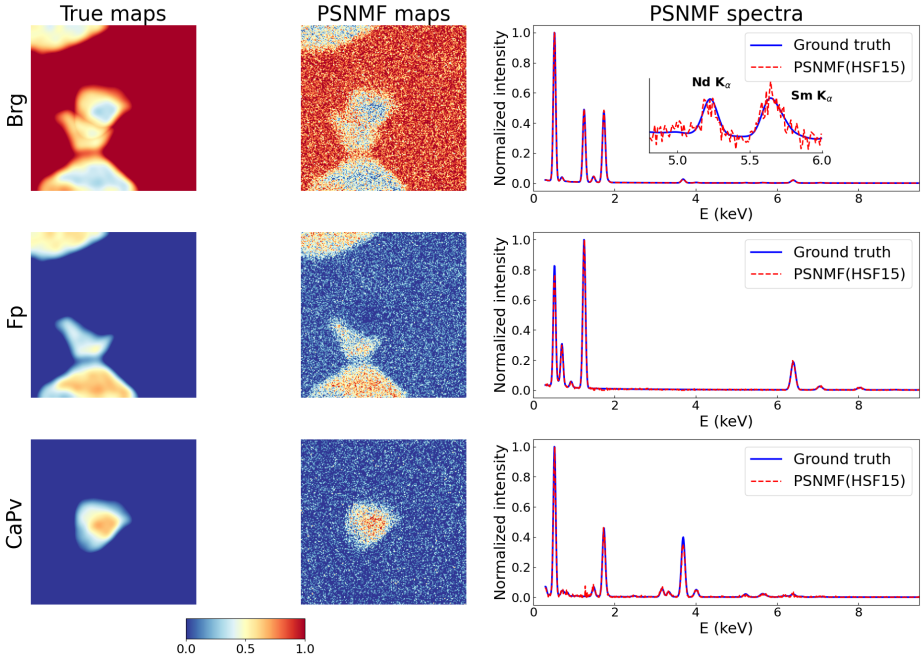

Figure 6.11: Abundance maps and spectra of PSNMF decomposition (15x bin) compared to ground truths on C15 dataset. The inset figure shows a localized magnification of trace elements Nd and Sm in the Brg component, proving accurate phase unmixing in the presence of high noise level.

Next, we quantify the spectral components of the 15x bin experiment, and compare their compositions with the ground truth compositions of phases. These results are summarized in Table 6.3. Once again, we observe that the concentrations of minor and trace elements in the three unmixed phases are more prone to errors. For example, the nominal concentration of Nd in Brg is 0.10 at.%, whereas the extracted Brg component overestimates it by 23%, exhibiting 0.12 at.%. The Cu concentration in the Fp component is also overestimated by 30%, with a nominal value of 1.00 at.% but exhibiting 1.26 at.%. As for the CaPv component, the Sm concentration is underestimated as 0.91 at.% with a nominal value of 1.00 at.%, while the U concentration is overestimated as 1.08 at.% with a nominal value of 1.00 at.%. Besides these, the relative composition errors for the remaining elements in the three unmixed phases are below 5%. Based on the above quantification, we conclude that the PSNMF method remains effective in unmixing spatially overlapping and chemically similar phases in the presence of high noise levels.

Atomic %	Mg	Si	Al	Ca	Fe	Nd	Sm	U	O	Cu
Brg / GT	18.50	18.20	1.50	1.00	1.00	0.10	0.10	-	60.00	-
Brg / HSF15	18.47	18.29	1.43	1.01	0.99	0.10	0.12	-	59.55	-
Fp / GT	39.00	-	-	-	10.00	-	-	-	50.00	1.00
Fp / HSF15	39.65	-	-	-	10.36	-	-	-	48.63	1.26
CaPv / GT	-	17.50	2.50	16.20	1.00	1.00	1.00	1.00	60.00	-
CaPv / HSF15	-	17.43	2.41	15.47	1.05	0.99	0.91	1.08	60.25	-

Table 6.3: Composition comparison between the ground truths and PSNMF decomposed components through the 15x bin experiment.

Dataset Denosing

Having tested the effectiveness of PSNMF for phase unmixing for the C15 dataset, we now evaluate its effect on dataset denoising. We also perform PCA on the C15 dataset, as we did in the analysis of the C147 dataset. The scree plot (included in the Appendix 9) also suggests the existence of three major components within the dataset. These components are subsequently utilized for the reconstruction of the dataset. Meanwhile, we also reconstruct the dataset by using the component spectra and their abundance maps obtained through the PSNMF decomposition of the 15x bin, and the 30x bin experiment. The average map spectral angle for the PCA reconstructed dataset is 8.33°. In contrast, those values of the PSNMF reconstructed dataset from the 15x bin and 30x bin experiments are both lower than that of the PCA one, with values of 6.00° and 6.05°, respectively. This suggests that the proposed PSNMF method has a superior denoising ability compared to the classical PCA method. In Figure 6.12, we further demonstrate the denoising effect of PCA and PSNMF on representative major, minor, and trace elements (i.e., Mg Kα, Al Kα, and Nd Lα). From those elemental maps of integrated peak counts, it is evident that both PCA and PSNMF

can denoise the dataset effectively. However, as previously discussed, PCA cannot ensure non-negativity in the reconstructed dataset. This is reflected in the fact that the minimum intensities of the three elemental maps are all negative in the PCA reconstructed dataset.

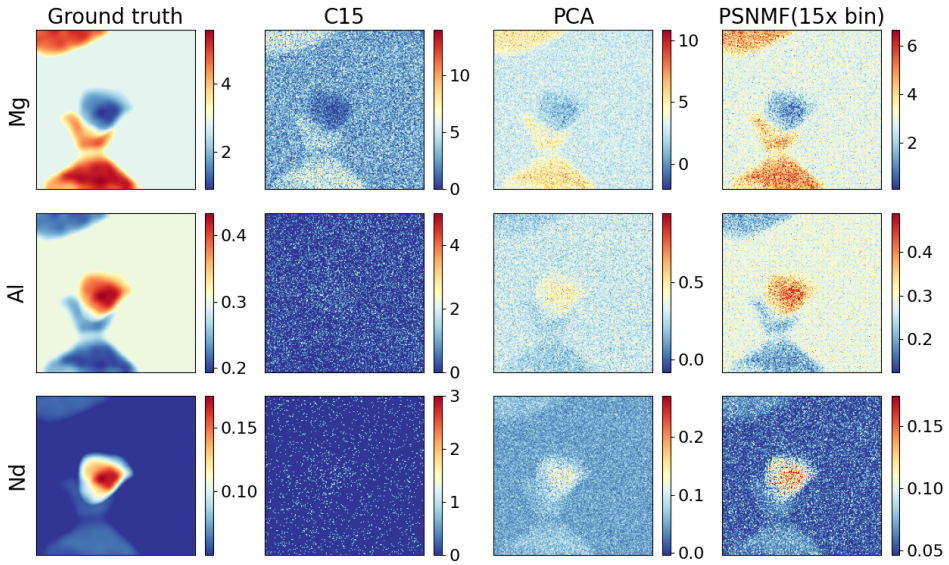

Figure 6.12: Elemental maps of Mg Kα, Al Kα, and Nd Lα for ground truth dataset, C15 dataset, PCA reconstructed dataset, and PSNMF reconstructed dataset through 15x bin experiment. The colorbar scales range from the minimum to the maximum value for each map.

To further validate the effectiveness of PSNMF in improving the quality of the dataset, three small regions of interests (ROIs) located on Fp, CaPv, and Brg were selected, each containing 25 pixels as illustrated in Figure 6.12. Figure 6.13 compares their summed spectra for the raw dataset and the PSNMF reconstructed dataset from the 15x bin experiment. Minor and trace elements, such as Cu in Fp (1.0 at.%), U in CaPv (1.0 at.%), and Nd and Sm in Brg (0.1 at.% for each) are present as mere counts in the raw spectra, and could not be identified. In contrast, the PSNMF reconstruction successfully denoises the dataset and reveals these weak signals. Therefore, by leveraging the non-negativity constraint and the ability of PSNMF to generate high quality component spectra and abundance maps, we are able to detect minor and trace elements even in the presence of extremely low SNR.

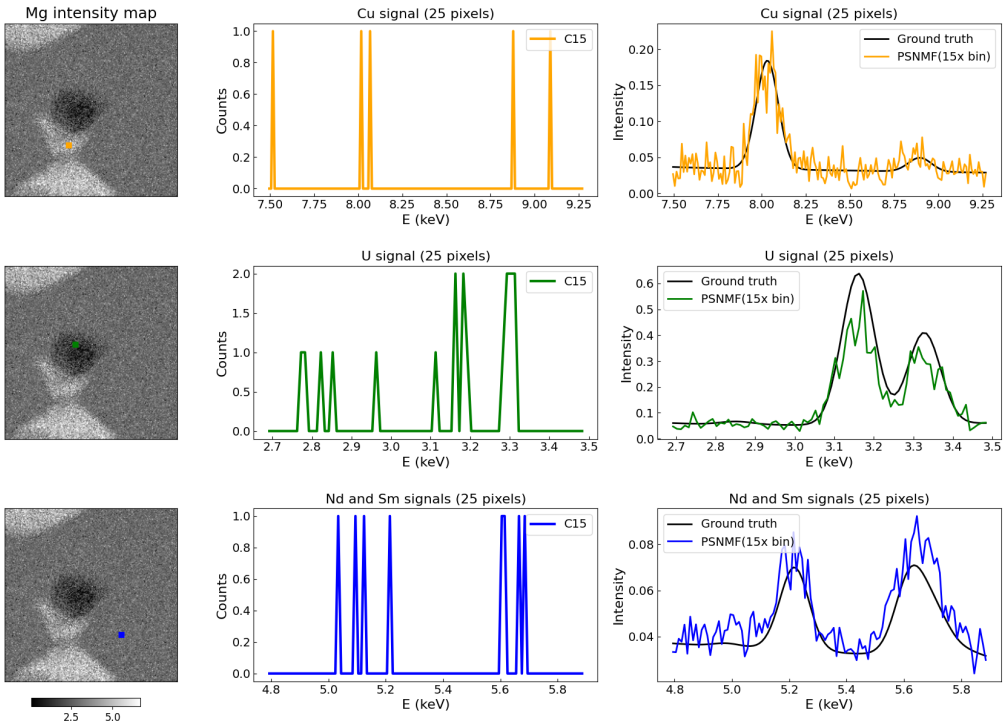

Figure 6.13: First column: Mg intensity maps of integrated peak counts reconstructed by PSNMF through the 15x bin experiment. The orange square indicates the Fp ROI, the green square indicates the CaPv ROI, and the blue square indicates the Brg ROI. Second column: raw spectra of the Cu Kα, U Mα, Nd Lα, and Sm Lα signals from the respective ROIs. Third column: comparison of the ROI signals between the ground truth dataset and PSNMF reconstruction through the 15x bin experiment.

6.5 Application to Experimental Data

6.5.1 Overlapped Phase Unmixing

In this section, we aim at evaluating the effectiveness of the PSNMF method on the experimental STEM-EDXS data, specifically the C120 dataset, following our validation of the PSNMF method on synthetic datasets. The C120 dataset features a spatial size of 512 by 512 and an average of 120 X-ray counts per pixel, therefore closely resembling the counting statistics of the synthetic dataset, C147, which has a medium SNR.

Initially, we apply NMF to decompose the C120 dataset into three components and present the results in Figure 6.14. The Brg and Fp components are revealed with spectral angles of 5.09° and 8.94°, respectively, while the CaPv component remains undetected. Note that the ground truth spectra of the phases utilized here were obtained using our NMF aided method presented in the previous chapter.

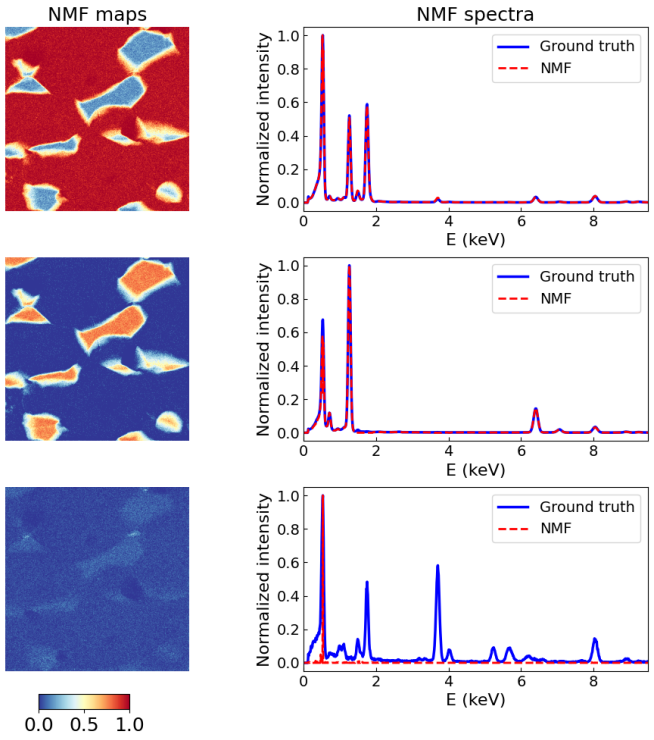

Figure 6.14: Abundance maps and spectra of NMF decomposition of the C120 dataset, and the spectra are compared to 'ground truth' phase spectra obtained with the NMF aided method.

Next, we conduct a series of PSNMF experiments on the C120 dataset with bin sizes of 2, 4, 8, 16, 32, and 64. Since our ground truths provided by the NMF aided method consist

only of phase spectra, we focus on the comparison of spectral angles. Figure 6.15 plots the component spectral angles and their average numbers. Similar to the results observed for the C147 synthetic dataset, increasing the bin size to 4 allows for the correct spectral identification of the three phases, with spectral angles of 0.21°, 1.04°, and 3.93° for Brg, Fp, and CaPv, respectively. The spectral angles decrease further to 0.15°, 0.96°, and 2.64° upon increasing the bin size to 8. The average spectral angle now reaches a value of 1.25° that is the lowest among all tested binning experiments for the C120 dataset. Figure 6.16 presents the full PSNMF results of the 8x bin experiment. As we increase the bin size to 16, 32, and 64, the Fp and Brg component remain accurately unmixed. However, the CaPv component, being the smallest phase, becomes less accurately unmixed with increasing bin size. This is evidenced by the spectral angle values in Figure 6.15 and the decomposed spectra in the Appendix 11.

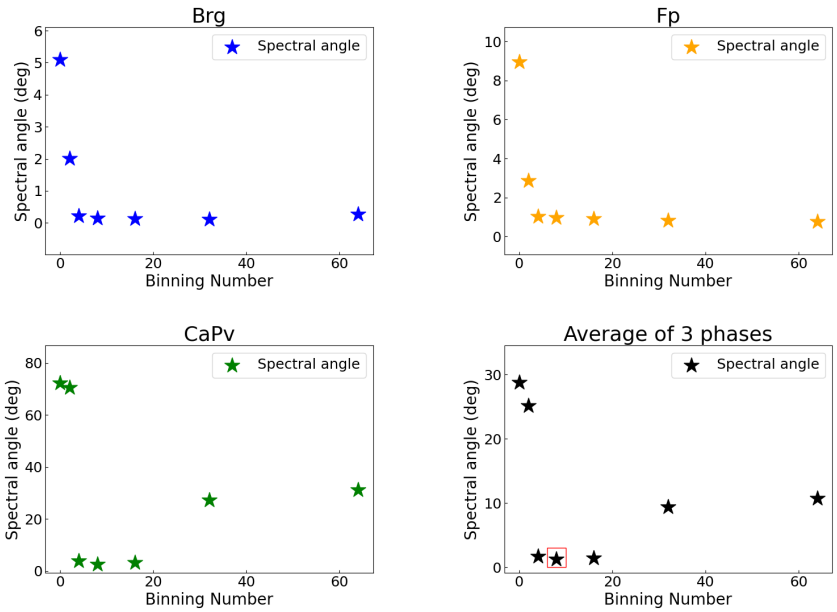

Figure 6.15: Spectral angles of Brg, Fp, and CaPv components and their averages with increasing bin size for the PSNMF decomposition on C120 dataset.

As the 8x bin experiment results in the optimal phase unmixing, we use them to quantify the three spectral components and compare their compositions with the assumed ground truth compositions obtained from the NMF aided method. These results are listed in Table 6.4 and Table 6.5. We find that the PSNMF unmixed Brg reveals trace elements (i.e., Nd and Sm at a concentration level of around 200 ppm) but underestimates them. For Fp and CaPv, the relative composition errors of major elements remain less than 1.3%, and those of minor ones remain below 25%. Overall, our evaluation demonstrates the potential of the PSNMF

method in accurately unmixing the phases on experimental STEM-EDXS data with a medium SNR. While the accuracy of Nd and Sm concentration in Brg may not be as high as that of the other elements, we anticipate that the PSNMF reconstruction will enhance the data quality, enabling us to precisely quantify the trace elements in Brg. The subsequent subsection will delve into this aspect in detail.

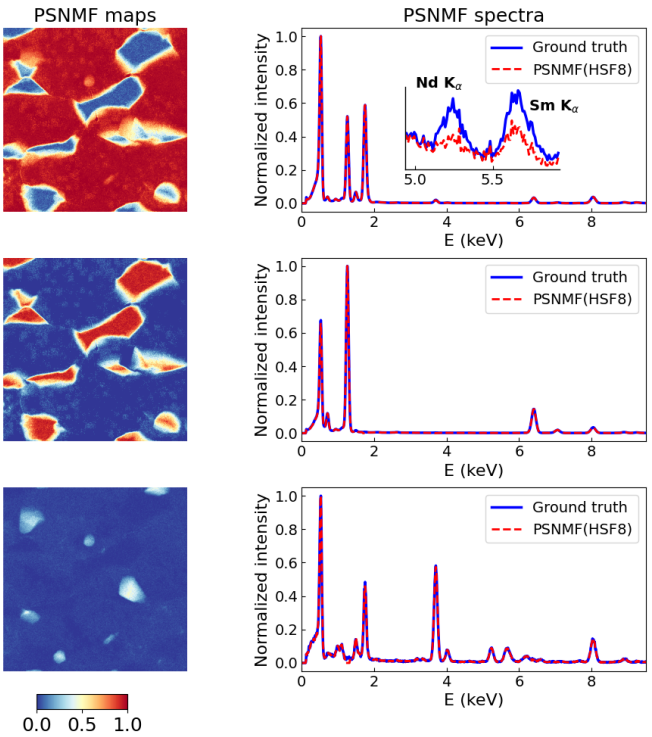

Figure 6.16: Abundance maps and spectra of PSNMF decomposition (8x bin) of the C120 dataset; the spectra are compared to 'ground truth' phase spectra obtained with the NMF aided method. The inset figure shows a localized magnification of trace elements Nd and Sm in the Brg component.

Atomic %	Mg	Si	Al	Ca	Fe	Nd (ppm)	Sm (ppm)	U	O
Brg / NMF aided	17.27	20.04	2.18	0.71	1.54	180	238	-	58.11
Brg / PSNMF (HSF8)	17.26	20.03	2.18	0.61	1.55	66	162	-	58.23

Table 6.4: Composition comparison between the Brg from NMF-aided method (that serves as ground truth) and PSNMF decomposed Brg component through the 8x bin experiment.

Atomic %	Mg	Si	Al	Ca	Fe	Nd	Sm	U	O
Fp / NMF aided	39.53	-	0.59	-	8.23	-	-	-	51.65
Fp / PSNMF (HSF8)	40.05	-	0.43	-	8.25	-	-	-	51.27
CaPv / NMF aided	-	14.93	3.53	21.15	0.53	3.93	3.11	0.40	51.35
CaPv / PSNMF (HSF8)	-	15.12	3.55	21.38	0.43	3.87	3.14	0.30	51.37

Table 6.5: Composition comparison between the Fp and Brg from NMF-aided method (that serve as ground truths) and PSNMF decomposed Fp and Brg components through the 8x bin experiment.

6.5.2 Dataset Denosing for Improved Quantification

Utilizing the three high-quality spectral components and abundance maps obtained from the 8x bin experiment, we then reconstruct the C120 dataset to assess the denoising effect of PSNMF on the experimental dataset. This reconstruction is compared to a PCA reconstructed dataset. The PCA scree plot, depicted in the Appendix 9, highlights three major components within the dataset, as subsequently used for its reconstruction. Figure 6.17 displays the elemental maps of integrated peak counts for Mg Kα, Al Kα, and Nd Mα of the raw, noisy dataset, as well as the datasets reconstructed using both PSNMF and PCA. This comparison proves the denoising capabilities of both techniques, especially for minor and trace elements. Nevertheless, as observed in the synthetic dataset, the PCA reconstructed data here also exhibits negative counts in the Mg and Nd maps, indicating a common artifact of dataset denoising via PCA.

In previous analyses, we detected Nd and Sm within the Brg component from the 8x bin experiment, but were unable to quantify them accurately. In this section, we demonstrate the advantage of PSNMF denoising, which facilitates the accurate quantification of these trace elements incorporated within phases. As indicated by the blue squares in the maps shown in Figure 6.18, we select 3 ROIs situated in the Brg area. Each ROI includes 16 pixels. Figure 6.18 illustrates that the raw spectra do not exhibit any distinct features, while the PSNMF reconstructed data successfully uncovers both Nd and Sm. On the other hand, PCA struggles to consistently and accurately retrieve Nd and Sm. We further quantified the three PSNMF denoised spectra and list their compositions in Table 6.6. The quantifications from the three ROIs and the NMF aided quantification demonstrate consistency. By employing PSNMF, we effectively reconstruct and hence denoise the C120 dataset and so enable accurate trace element quantification, as exemplified by the Nd and Sm in Brg.

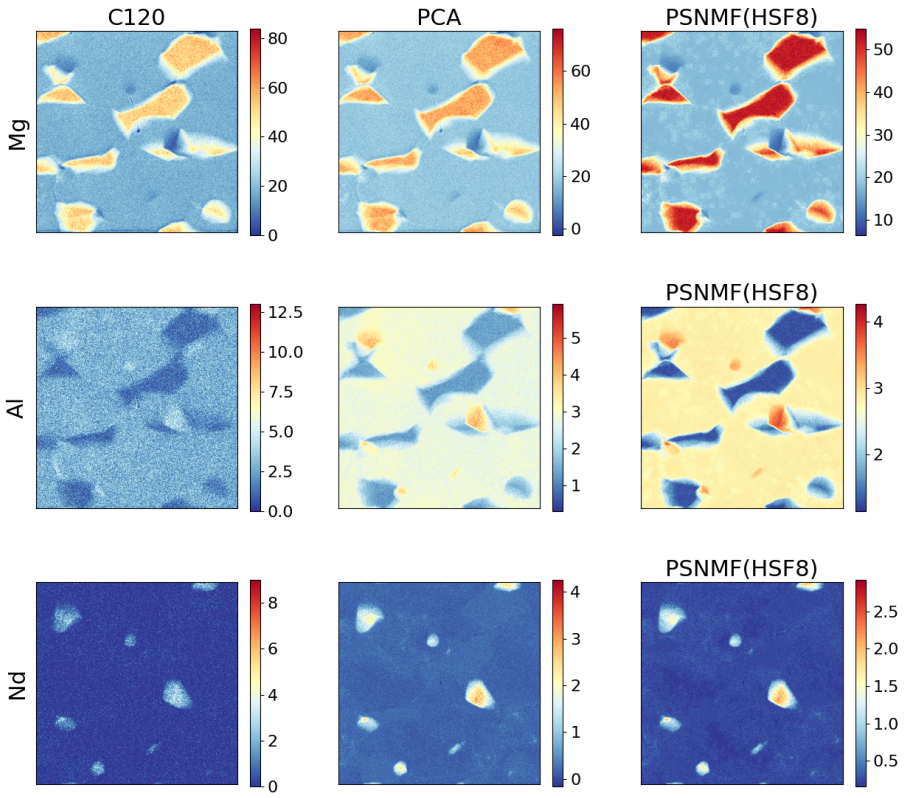

Figure 6.17: Elemental Maps of Mg Kα, Al Kα, and Nd Lα for C120 dataset, PCA reconstructed dataset, and PSNMF reconstructed dataset through 8x bin experiment. The colorbar scales range from the minimum to the maximum value for each map.

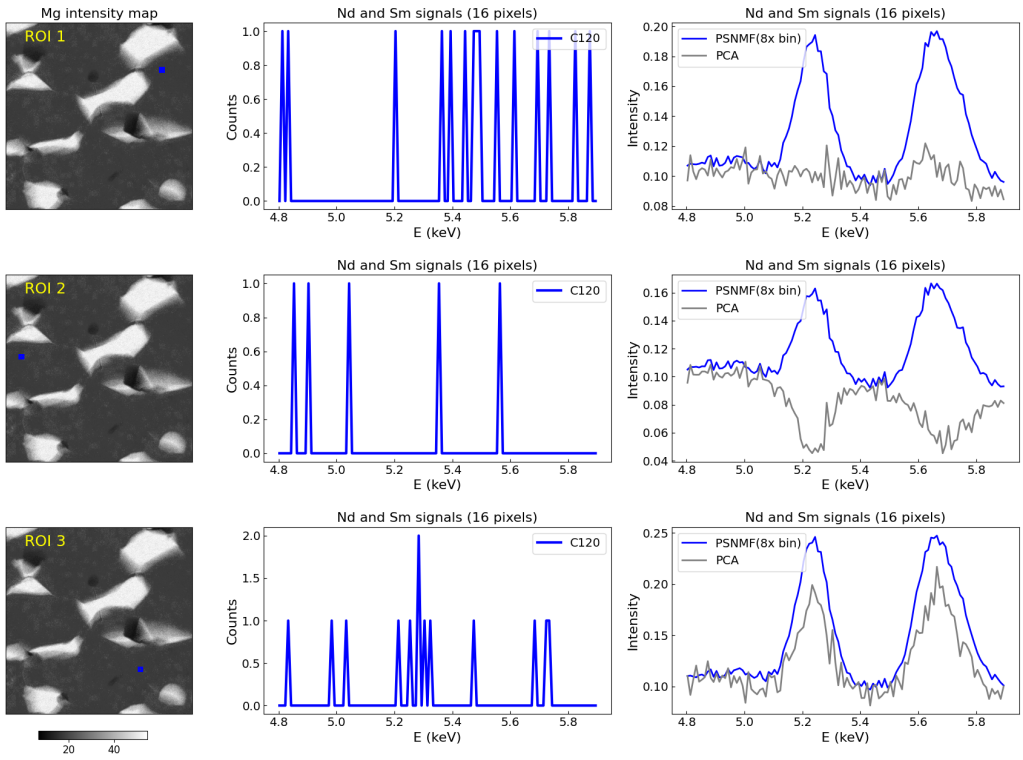

Figure 6.18: First column: Mg intensity maps of integrated peak counts reconstructed by PSNMF through the 8x bin experiment. The blue squares indicate three Brg ROIs. Second column: raw spectra of the Nd Lα, and Sm Lα signals from the respective ROIs. Third column: comparison of these signals between the PCA reconstruction and PSNMF reconstruction through the 8x bin experiment.

Atomic %	Mg	Si	Al	Ca	Fe	Nd (ppm)	Sm (ppm)	U (ppm)	O
Brg/ NMF aided	17.27	20.04	2.18	0.71	1.54	180	238	-	58.11
Brg/ PSNMF (ROI 1)	17.03	20.04	2.21	0.82	1.53	200	231	-	58.17
Brg/ PSNMF (ROI 2)	17.12	20.04	2.20	0.81	1.54	188	215	-	58.12
Brg/ PSNMF (ROI 3)	17.21	20.02	2.22	0.78	1.52	191	227	-	58.00

Table 6.6: Composition comparison between the Brg from NMF aided method and Brg from 16 pixles of PSNMF reconstructed dataset.

6.6 Conclusion

In this chapter, we presented PSNMF, a novel technique for processing STEM-EDXS datasets, which allows simultaneous phase unmixing and denoising. We evaluated the effectiveness of PSNMF on various STEM-EDXS datasets, including synthetic dataset C147 with moderate SNR, synthetic dataset C15 with extremely low SNR, and experimental dataset C120 with medium SNR. All of these datasets comprise three phases, namely Brg, Fp, and CaPv, exhibiting considerable spectral similarity and spatial overlap. We observe that under a sum-to-one constraint the classical NMF technique often fails to retrieve the CaPv phase, which has the smallest proportion. In contrast, by performing a series of binning experiments, PSNMF extracts the phase abundance maps and spectra with high accuracy for the datasets with moderate SNR. Furthermore, PSNMF remains effective in unmixing phases even in the presence of high noise levels. Our results therefore indicate that binning-based PSNMF offers a useful approach for phase unmixing. However, selecting an optimal binning number is crucial to balance the trade-off between SNR improvement and the distinguishability of each phase in relevant pixels with increasing bin size. Our analysis further demonstrates the superior denoising ability of PSNMF in comparison to the classical PCA method. By exploiting the non-negativity constraint and the capacity of PSNMF to generate high quality component spectra and abundance maps, the resulting reconstructed dataset by PSNMF is of high quality. As a result, minor and trace elements can be detected and reliably quantified even in the presence of extremely low SNR. The proposed PSNMF method presents significant potential for wide-ranging applications in the study of materials that are challenging to be chemically characterized by STEM-EDXS, such as those with complex volumetric phase relationships, restricted SNR and beam sensitivity, or vital trace constituents.

7 Correlative EDXS-EELS Analysis via Implicit Neural Representations

In this chapter, we explore the use of implicit neural representations for correlative EDXS-EELS analysis and present some preliminary results. Our experimental data were acquired with the support of the ESTEEM3 (Enabling Science and Technology through European Electron Microscopy) project, and we received valuable assistance from Prof. G. Kothleitner and Dr. D. Knez from Technische Universität Graz. By leveraging the power of emerging neural networks, we are motivated to develop a new approach that can provide a more comprehensive chemical understanding of materials. Although our results are preliminary, they offer promising evidence of the potential of our approach and provide a foundation for future developments in this subject.

7.1 Improved Chemical Analysis via Simultaneously Acquired EDXS and EELS

EDXS and EELS are both useful techniques for the chemical characterization of materials. In this thesis, we present a comprehensive analysis of the strengths and weaknesses of the two techniques in Chapter sections 2.3 and 2.4. EELS is particularly effective for analyzing light elements, such as C and O, whereas EDXS is better suited for analyzing heavier elements. EELS is often complicated by an intense background, while EDXS typically has a low background intensity and a high peak-to-background ratio. When the concentration of the element of interest is low and the elemental ionization edge energy is high, EDXS is preferred because it can more easily separate the signal from the background than EELS. However, it has limitations when it comes to analyzing elements of low atomic number due to the strong absorption of their X-rays. Moreover, when the elemental concentration is too low (e.g., less than 0.1 at.%), the low counting statistics of EDXS limits its ability to accurately detect and quantify the elements of interest.

At their core, there is an implicit link between the the generation of the signal dataset in EELS and EDXS, since they both derive from atomic ionisation. This link raises the prospect of synergistic analyses, in which both signals are recorded, for improved elemental analysis. In Chapter 2.5, a summary of existing methodologies for the synergistic analysis of these two complementary techniques has been provided. The development of high temporal resolution detectors has allowed researchers like Jannis et al. [109, 275] to employ the temporal correlation of the underlying physics behind these two techniques to obtain additional information beyond individual spectra. Meanwhile, recent advancements in electron microscopy have enabled the simultaneous acquisition of EDXS and EELS data in STEM mode [276]. Researchers, including Kothleitner et al. [105] and Varambhia et al. [107], have explored the partial cross-section conversion of EELS and EDXS in order to achieve a more thorough analysis of materials. The former method necessitates the acquisition of accurate thickness measurements, whereas the latter method requires the synthesis of standards. More recently, Thersleff et al. [122] employed a data fusion approach to amalgamate both datasets into a unified dataset based on shared spatial factors. This method aims to expand the spectral dimension and augment the analytical explanatory power of the fused dataset; however, it demands a meticulous selection of a weighting factor for the concatenation of the two datasets and requires repeated assessment of the fused dataset's variance. We were therefore motivated to develop an effective and easy-to-use method for the co-analysis of simultaneously obtained EDXS and EELS datasets. In this chapter, we propose a novel framework for the synergistic analyses by harnessing the potential of neural networks. This approach capitalizes on the powerful descriptive capabilities of neural networks to complement the EDXS dataset with its EELS counterpart.

7.2 The Motivation for Using Neural Networks

In recent years, neural networks have established themselves as a formidable tool for analyzing massive datasets. They can process high-dimensional, diverse, and complex data in an automatic and efficient manner while revealing intricate patterns and relationships within the data. One type of neural network that has gained attention in recent years is the implicit neural representation (INR). INRs facilitate learning and generate continuous representations of data input, such as objects or scenes, without need of explicit geometric or parametric models. Prominent INR methods include SIREN (SInusoidal REpresentation Networks) [277], NeRF (Neural Radiance Fields) [278], and GPT (Generative Pre-trained Transformer) [279–281]. Overall, INR allows deep learning neural networks to efficiently process, encode, and represent information. Under the assumption that EELS contains complementary information compared to its simultanouelsy acquired EDXS counterpart, here I propose that converting EELS data into EDXS data (i.e., EELS-represented EDXS data) via INR should result in an enhanced EDXS dataset compared to the raw EDXS data. This fundamental concept forms the basis of the current chapter.

7.3 Materials and Methodology

7.3.1 Materials and Data Acquisition

In this chapter, we utilize solidus mineral assemblages that are similar to those tested in Chapter 6 of this thesis. These assemblages were synthesized at 88 GPa and were composed of three distinct phases, namely Brg, Fp, and CaPv. In our initial attempt to simultaneously acquire EELS and EDXS data for these phases, we employed a Titan Themis microscope, housed at the CIME (Centre Interdisciplinaire de Microscopie Electronique) at EPFL. This microscope is equipped with a Gatan GIF Quantum ERS spectrometer featuring a charge-coupled device (CCD) detector for EELS data acquisition, and four silicon drift detectors (SDD) for EDXS data acquisition. However, we encountered issues related to the correlated channel noise present in the EELS data obtained using the CCD detector. This noise introduces inherent challenges for data processing algorithms such as PCA. Via the acquisition of preliminary data with a GIF Quantum fitted with a K2 camera in Institut des Matériaux Jean Rouxel of Nantes (IMN), we identified that direct electron detection (DED) sensors, which can count individual electrons, effectively circumvent this problem.

Through the support of the ESTEEM3 project, we successfully acquired both EDXS and EELS data using the ASTEM (Austrian Scanning Transmission Electron Microscope) at Technische Universität Graz. The EELS data was collected using a Gatan GIF Quantum spectrometer with a K2 camera, which employs a DED sensor, This type of sensor is crucial as it guarantees

that the noise can be assumed to be Lorentzian. EDXS data were acquired simultaneously using four SDD X-ray detectors.

We conducted a series of systematic tests to determine an optimal condition for collecting EDXS and EELS data. The goal was to acquire the two types of data with suitable statistics while minimizing sample damage under the single scan mapping constraint that was effectively imposed by the EELS detector. (As compared to the multi-frame mapping used with STEM-EDXS elsewhere in this thesis). We ultimately settled on the following parameters: a high-tension voltage of 300 kV, a beam current of 150 pA, a spot size of 11, a semi-convergence angle of 19.6 mrad and a scan size of 100 by 100 with a pixel size of 3 nm. Each pixel was exposed for 0.05 s, resulting in a total acquisition time of 8 minutes for each spectrum imaging datacube. For EELS acquisition, we utilized a dispersion value of 0.5 ev/ch, an entrance aperture of 5 mm, and a collection angle of 30.74 mrad. Additionally, for good EELS signal-to-background, the chosen regions for sampling had to be thinner than for the EDXS measurement of previous chapters. Given the optimization of conditions for acquiring EELS data in thin regions, the counting statistics of the obtained EDXS data yields an average of only 92 X-ray counts per pixel. The quality and SNR of the EDXS dataset is therefore inferior than the one tested in the previous chapter which has an average of 120 X-ray counts per pixel.

7.3.2 Network Architecture and Implementation

We first need to learn an implicit neural representation that maps the EELS data ($g(x)$) to EDXS data ($f(x)$) at spatial location x and outputs EELS-predicted EDXS data $f'(x)$. To achieve this, I employ a multi-layer perceptron (MLP) architecture. After multiple testing, I developed a neural network whose schematic representation is shown in Figure 7.1. The network consists of three layers, with each layer comprising 128, 128, and 1024 neurons, respectively. The activation functions utilized in the neural network consist of PReLU (parametric rectifier linear units) [282] in the first two layers and Sigmoid [283] in the last layer. The network is trained using backpropagation with the mean squared error (MSE) loss function to minimize the difference between the predicted EDXS spectra $f'(x)$ and the acquired EDXS spectrum $f(x)$.

Prior to feeding the training data to the network, several data preprocessing steps were carried out. We first normalize $g(x)$ and $f(x)$ to [0,1], and then carry out multiple spatial binning with bin sizes of 2, 4, 8, 12, 20, and 24. These binned datasets are contributed into an augmented training dataset. Their increased SNR facilitates the representation learning.

We implement the network in Pytorch [284] and train it on an NVIDIA RTX8000 GPU using

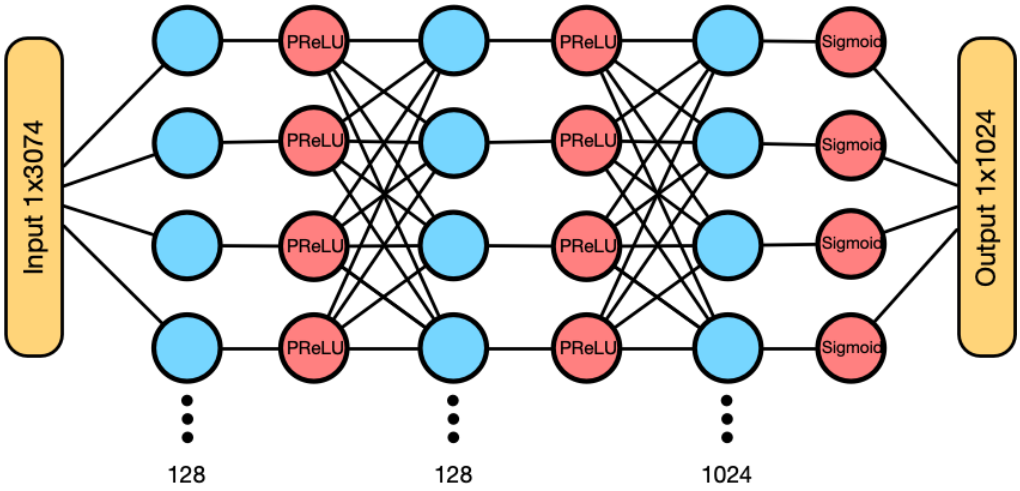

Figure 7.1: Schematic illustration of the neural network architecture used in this work.

the Adam optimizer [196] with a learning rate of 1×10^{-4} and a mini-batch size of 1. The training process contains 10 epochs and each epoch takes less than one minute. The network converges to a good solution after 3.5×10^6 iterations. Finally, the obtained derivative $f'(x)$ is renormalized to ensure that its maximum intensity is equivalent to that of the original function $f(x)$.

7.4 Validation on Simultaneously Acquired EDXS-EELS Dataset

Having established the INR method, it was applied to output the EDXS dataset. In order to demonstrate its effect, here we present the elemental maps integrated from the Si Kα (with the concentration of 17.27 at.%), Fe Kα (with the concentration of 1.54 at.%), Nd Lα and Sm Lα (with the concentration of around 200 ppm) X-ray peaks, as shown in Figure 7.2 (the middle column). These three elements serve as representatives for major, minor, and trace elements, respectively. An observable denoising effect is noted for all the three elements in the neural network reconstructed dataset.

Additionally, a PCA decomposition was performed on the raw EDXS dataset. The screeplot of this decomposition is depicted in Figure 7.3, revealing the presence of three major components within the dataset, which were subsequently utilized to reconstruct the dataset. Figure 7.2 also presents the resulting three elemental maps from the PCA reconstruction. Consistent with the findings of the PCA reconstructed elemental maps in Chapter 6, negative counts were detected in these three maps, implying potentially unfeasible quantification in certain areas. In contrast, the INR method ensures non-negativity for the outputed EDXS dataset, as neither EDXS data nor EELS data involved contain negative signals. Moreover, the

maps from the INR output show distinctively better denoising and sharper spatial features than those from the PCA reconstruction.

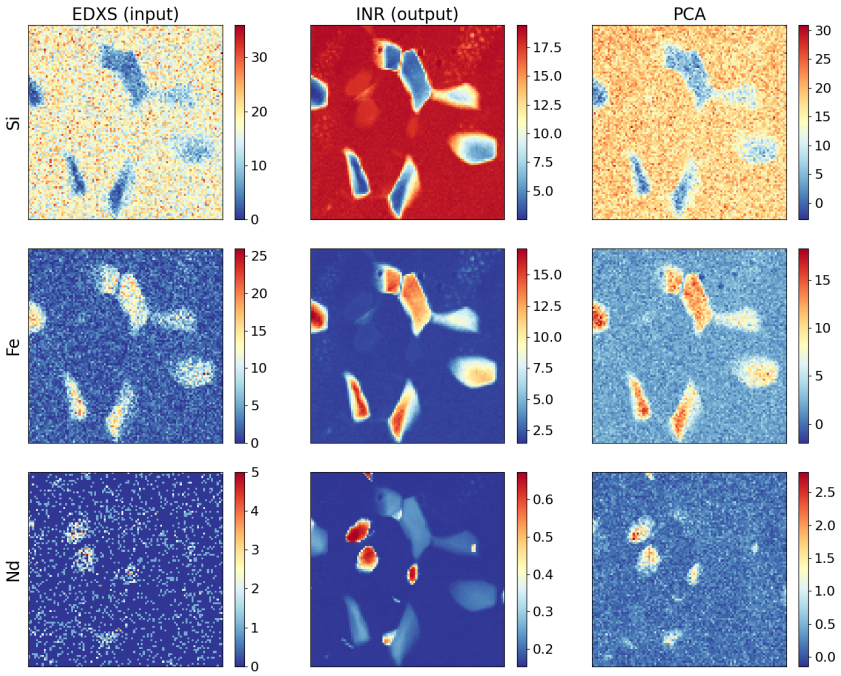

Figure 7.2: Elemental maps of Si Kα, Fe Kα, and Nd Lα for raw EDXS dataset, INR outputed dataset, and PCA reconstructed dataset. The colorbar scales range from the minimum to the maximum value.

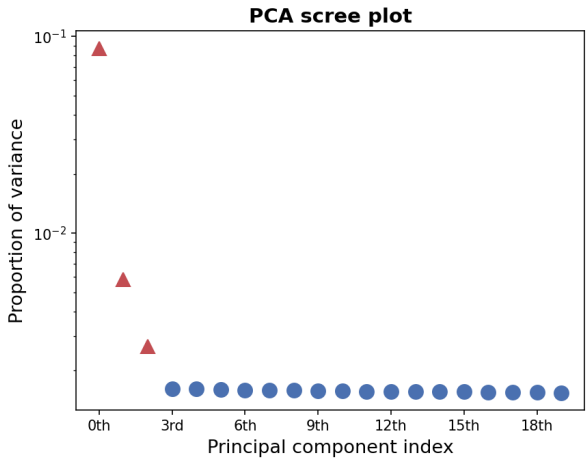

Figure 7.3: The scree plot of PCA decomposition of the EDXS dataset.

To further compare the denoising effects between the PCA reconstruction and the INR method, we select two regions of interest (ROIs), as illustrated in Figure 7.4. The smaller ROI contains 4 pixels, while the larger ROI consists of 16 pixels. It is noted that both methods successfully retrieve the Si Kα peak summing only 4 pixels. In the summed spectra of 16 pixels, the signals of a minor element, Fe Kα peak, are correctly retrieved using both methods. Furthermore, the signals of trace elements, Nd Lα peak and Sm Lα peak, are detected using both methods, while the raw spectra do not display any discernible meaningful signals. Notably, the spectra generated by our method appear noisier than those produced by the PCA reconstruction.

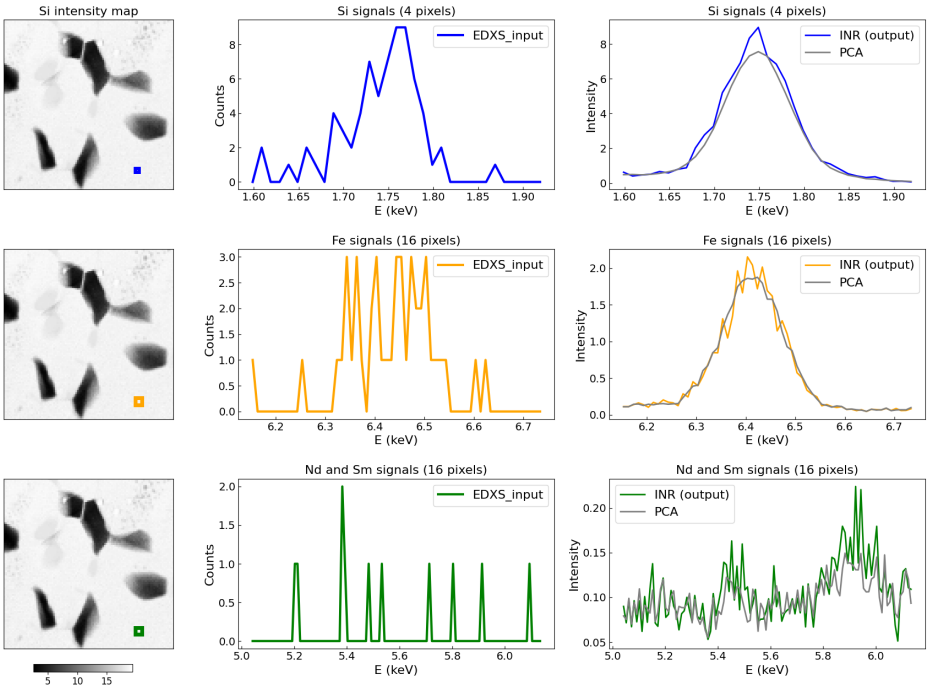

Figure 7.4: First column: Si intensity maps of integrated peak counts reconstructed by our method. The blue square indicates the smaller ROI, and the orange and green squares indicate the larger ROI. Second column: raw spectra of the Si Kα, Fe Kα signals, and Nd Lα and Sm Lα from the respective ROIs. Third column: comparison of these signals between the PCA reconstructed dataset and the INR learned dataset.

7.5 Discussion

The results shown in Figure 7.2 and Figure 7.4 indicate that both INR and PCA are effective in denoising EDXS dataset in both spatial and spectral domains. However, the results also suggest that each method has its strengths in different domains. Specifically, INR performs

better on spatial denoising, while PCA is more effective at spectral denoising. The superior performance of PCA in spectral denoising can be attributed to its ability to analyze the principal components of a signal and remove noise in the frequency domain. In contrast, the strength of neural networks such as INR lies in their ability to learn patterns in training data and use this knowledge to denoise images in space. This preliminary analysis strongly suggests that they are better suited for removing spatial noise.

7.6 Conclusion and Outlook

In this chapter, a novel methodology is proposed that leverages implicit neural representation to establish a linkage between simultaneously acquired EDXS and EELS datasets. It is proved that the synergistic utilization of INR on EELS data with a suitable SNR and EDXS data with poor statistics results in a significant improvement in the quality of the final output EDXS data. We believe that the robust representation between the two modalities of spectroscopic data is rooted in their fundamental physical relationship. Once identified and applied to all concerned data points, such a robust representation can contribute to a global enhancement of the dataset's quality.

Furthermore, investigations are underway to test the proposed methodology's effectiveness when the EELS dataset exhibits poor statistical quality. In such cases, the proposed strategy involves mapping EDXS data to EELS data to improve the latter's quality. In the near future, synthetic EDXS and EELS datasets with various SNRs and composing materials will be simulated to conduct a comprehensive investigation on the potential of INR. Potentially, the methodology can be further improved by combining spectral denosing techniques such as PCA with INR to achieve a superior denoising in both the spatial and spectral domains. Overall, this preliminary study therefore raises a number of promissing prospects for improved elemental analysis using correlative analytical STEM.

8 Conclusions and Perspectives

8.1 Melting Experiments in Lower Mantle Conditions

In conclusion, this study provides insights into the solidification process of the Earth's mantle and the lower mantle mineralogy. The melt pocket's characterization has elucidated the crystallization of bridgmanite from the melt, which may have led to the formation of a Si-enriched lower mantle and thus a Si-depleted upper mantle, consistent with present-day observations. Additionally, our findings suggest that Fe accumulates preferentially in the residual melt, which supports the basal magma ocean theory. Furthermore, the investigation of the partitioning behavior of Fe between solidus ferropericlase and bridgmanite reveals that the Fe content in bridgmanite may contribute to the observed rheological variations in the lower mantle. Subsequent research endeavors should concentrate on exploring the partitioning of trace elements among the liquidus phase, bridgmanite, and the coexisting residual silicate melt. Such investigations could yield crucial geochemical constraints on the magnitude and characteristics of the enigmatic reservoir within the lower mantle.

8.2 Advanced Data Processing for Enhanced STEM-EDXS Analysis

The proposed NMF aided phase analysis methodology presents a promising avenue for overcoming the constraints of traditional phase quantification approaches in the context of complex materials. This method has been effectively employed for the quantification of phases characterized by considerable spatial and spectral overlap, as well as for the detection of trace elements in beam-sensitive mineral assemblages. The method is suitable for analyzing a wide variety of materials that have complex volumetric phase relationships and vital trace constituents.

PSNMF presents a more robust and effective methodology for phase unmixing and de-

noising in STEM-EDXS datasets. Our results demonstrate the effectiveness of PSNMF in accurately unmixing phases, even in the presence of extremely high noise levels. Moreover, PSNMF surpasses the classical PCA method in terms of denoising capabilities and can effectively reconstruct high-quality datasets for accurate trace element quantification. The proposed methodology holds considerable potential for extensive applications in the characterization of materials that pose challenges for chemical characterization via STEM-EDXS. Future research perspectives encompass the development of automated binning methods for optimizing the number of bins, and the extension of the PSNMF approach to alternative spectroscopic data types.

We also underscore the potential of employing implicit neural representations (INR) for correlating simultaneously acquired EDXS and EELS datasets, facilitating improved chemical analysis. The proposed methodology effectively denoises EDXS data within the spatial domain, while PCA proves more effective for spectral denoising. In the near future, synthetic EDXS and EELS datasets with various SNRs and comprising materials will be simulated to investigate the potential of INR comprehensively. Also, a method that combines PCA and INR for superior denoising in both the spatial and spectral domains will be developed.

Appendix

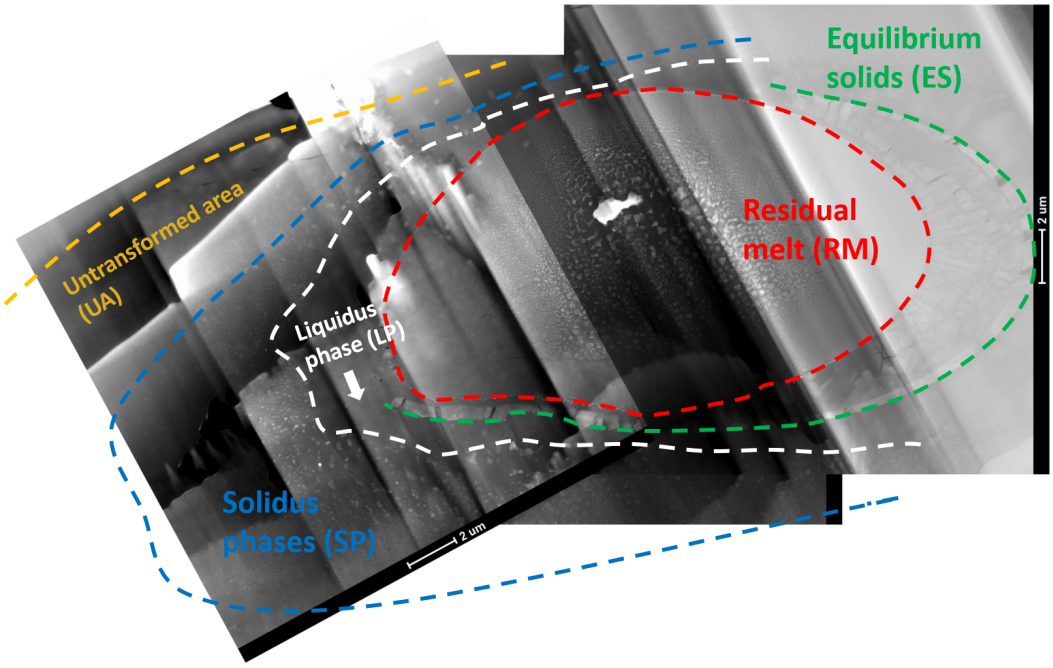

Figure 1: Overview images (HAADF) of the 46 GPa sample.

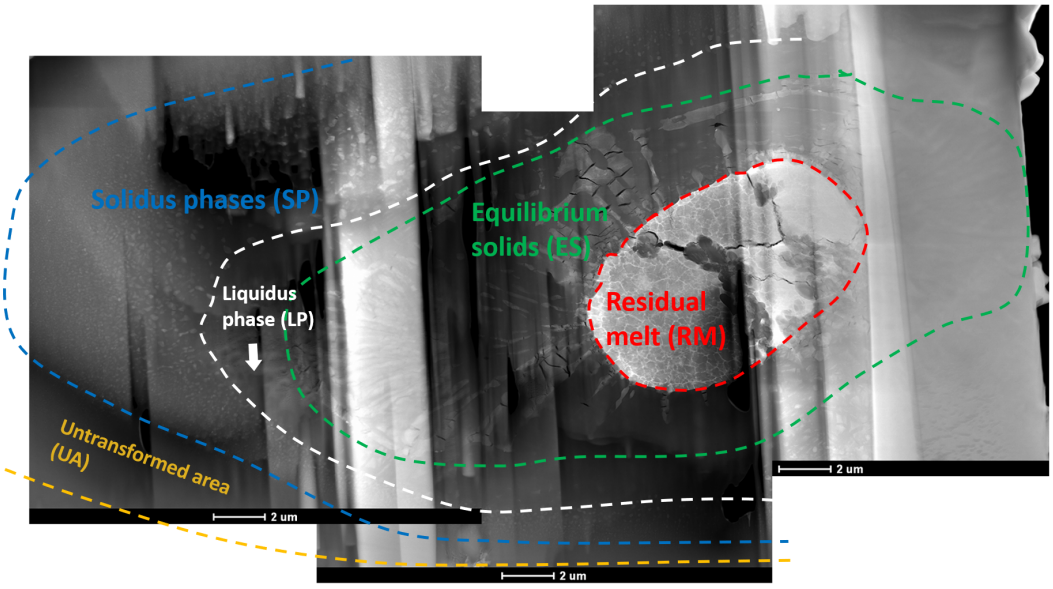

Figure 2: Overview images (HAADF) of the 55 GPa sample.

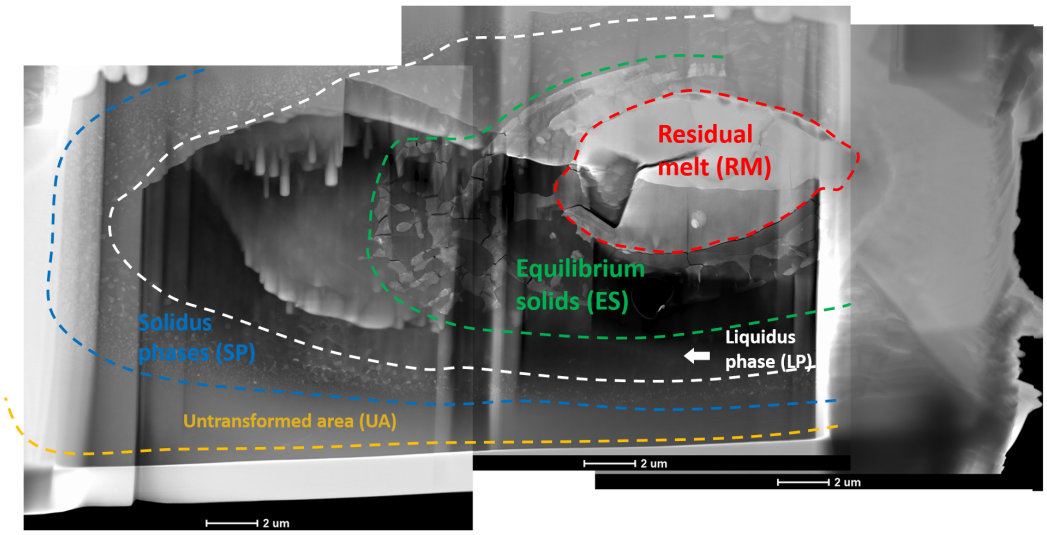

Figure 3: Overview images (HAADF) of the 71 GPa sample.

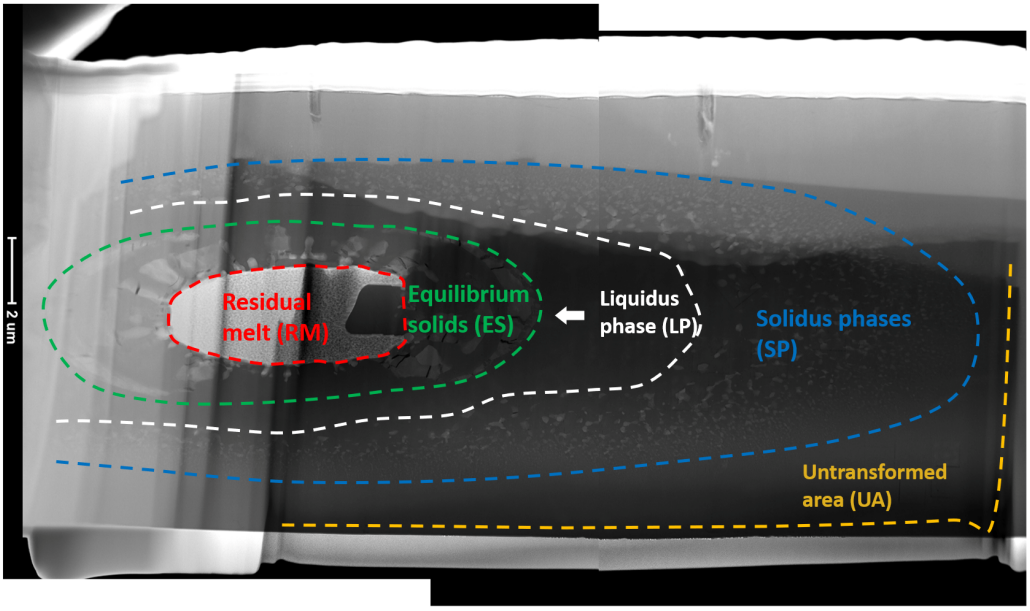

Figure 4: Overview images (HAADF) of the 88 GPa sample.

Sample name: B-C2-46 GPa

Sample overview:

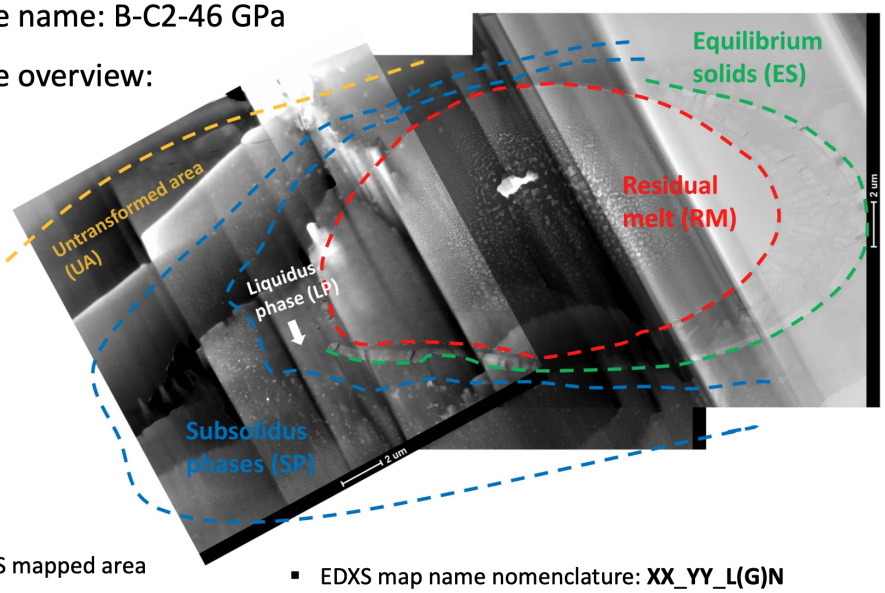

- EDXS mapped area

- EDXS map name nomenclature: **XX_YY_L(G)N**

XX: the pressure at which the sample was synthesized
YY: the area where the map data was collected as well as the interest of research
L: map acquired at a local scale; **G**: map acquired at a global scale
N: the index number of the map in each category

(a)

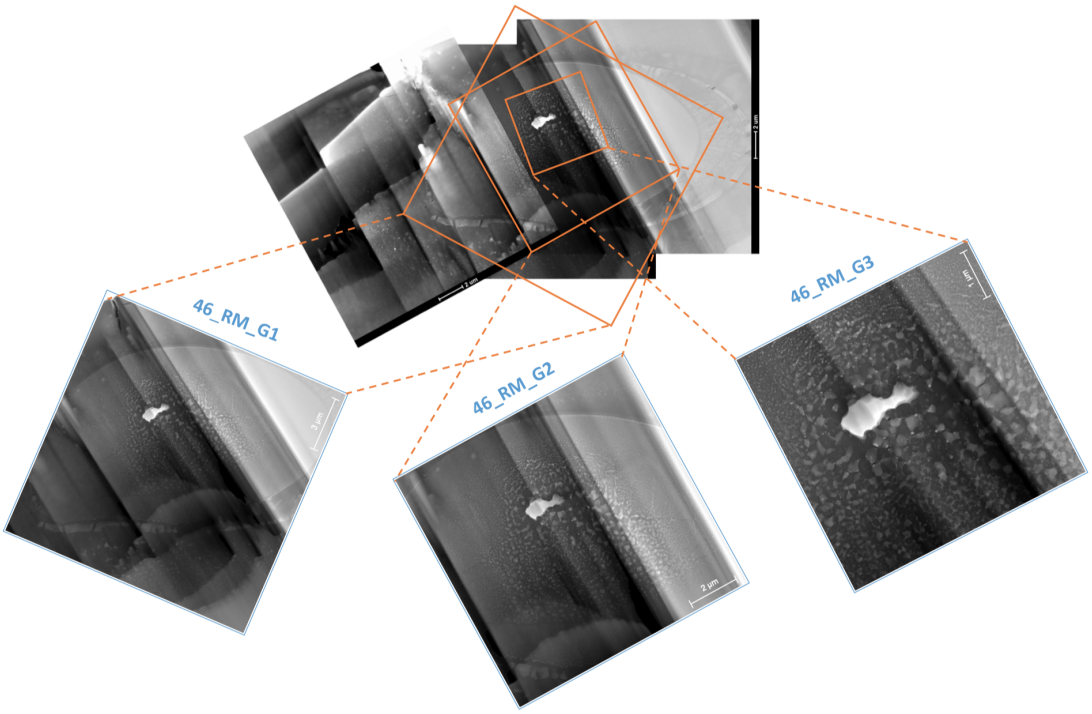

(b)

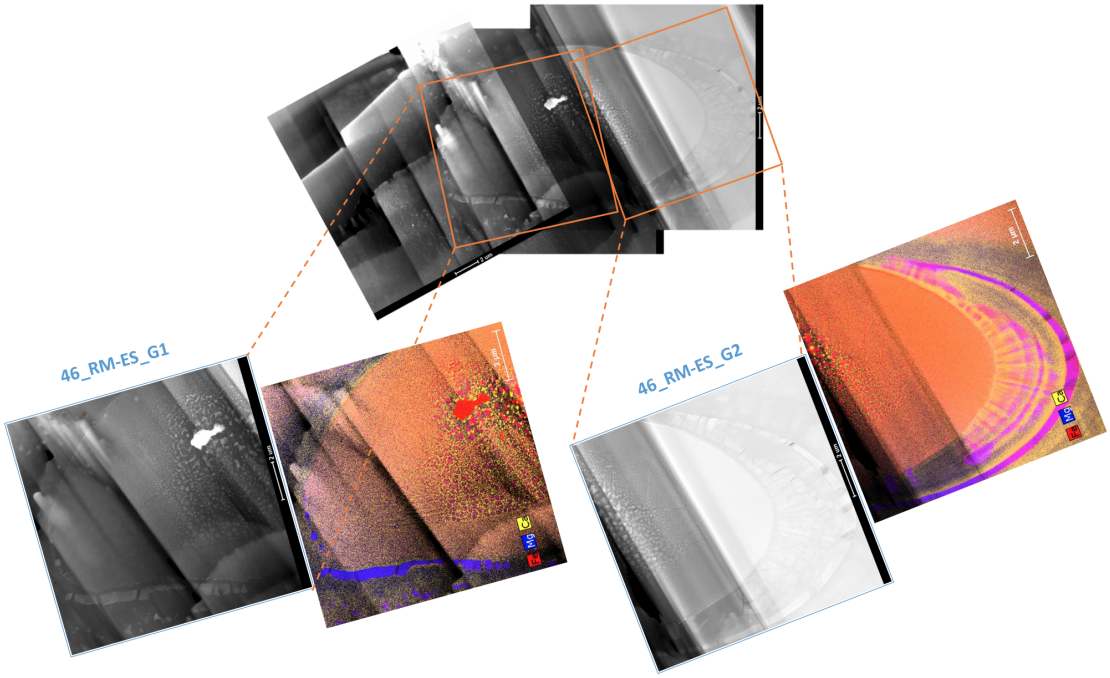

(c)

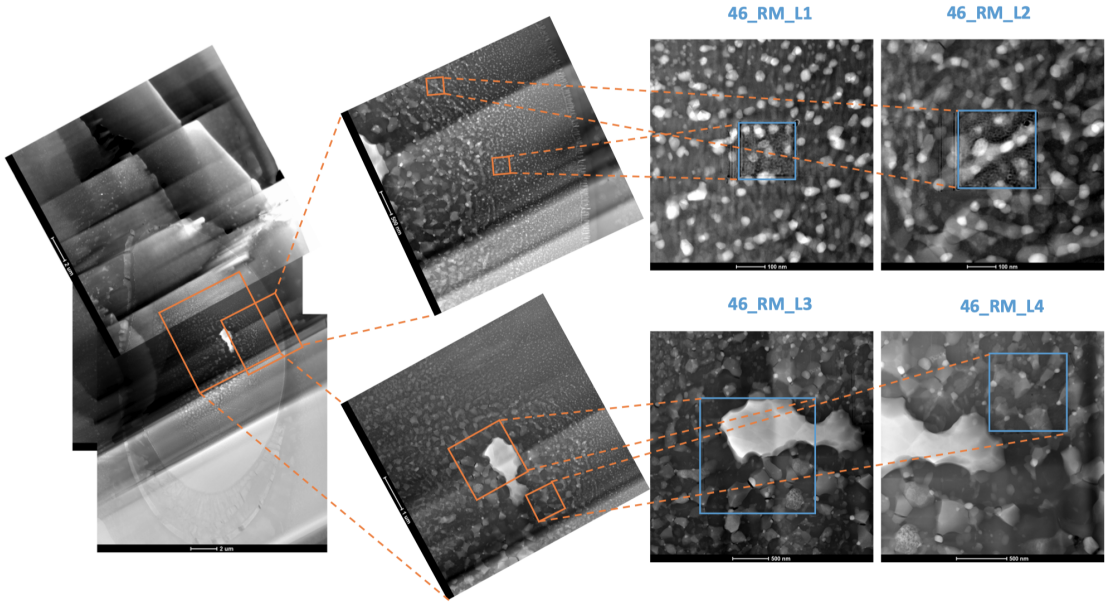

(d)

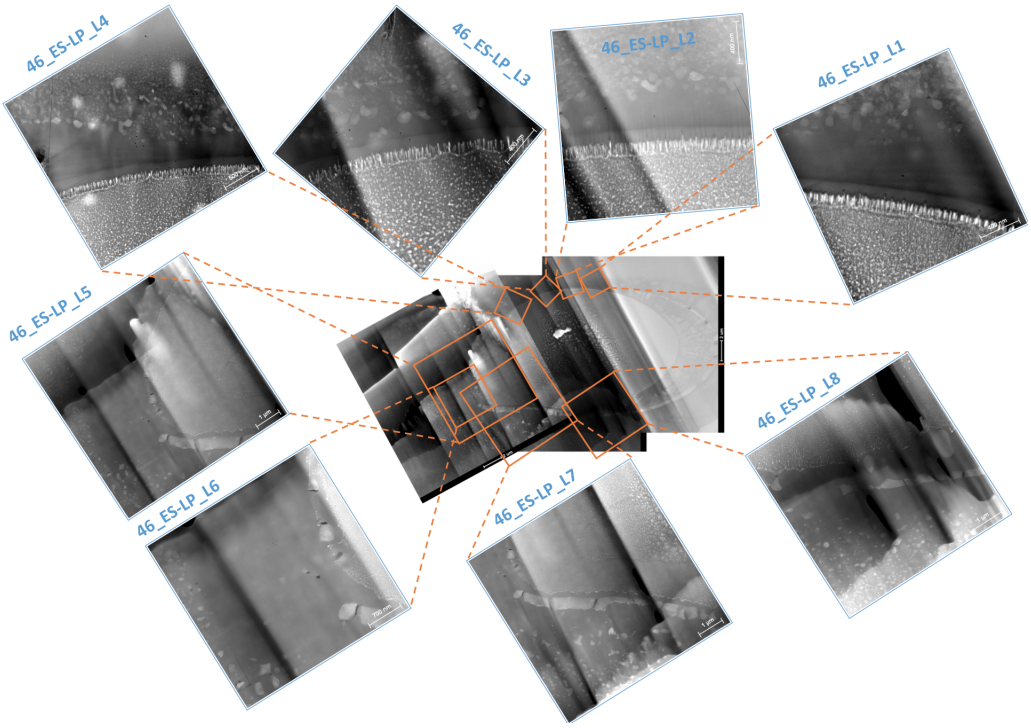
46_ES-LP_L4
46_ES-LP_L3
46_ES-LP_L2
46_ES-LP_L1
46_ES-LP_L5
46_ES-LP_L8
46_ES-LP_L6
46_ES-LP_L7

(e)

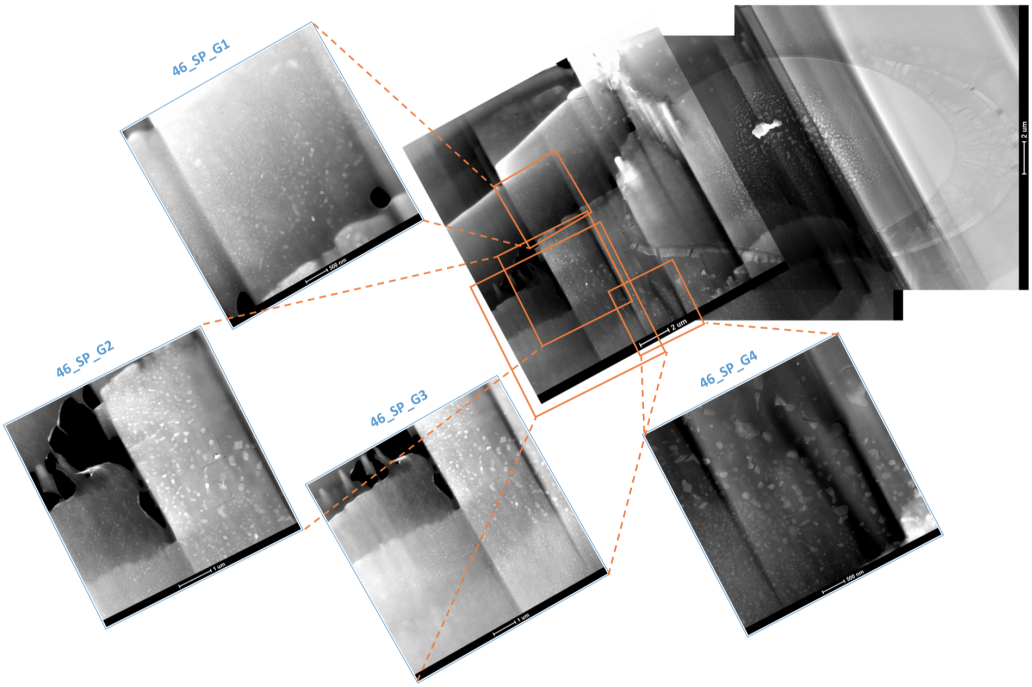
46_SP_G1
46_SP_G2
46_SP_G3
46_SP_G4

(f)

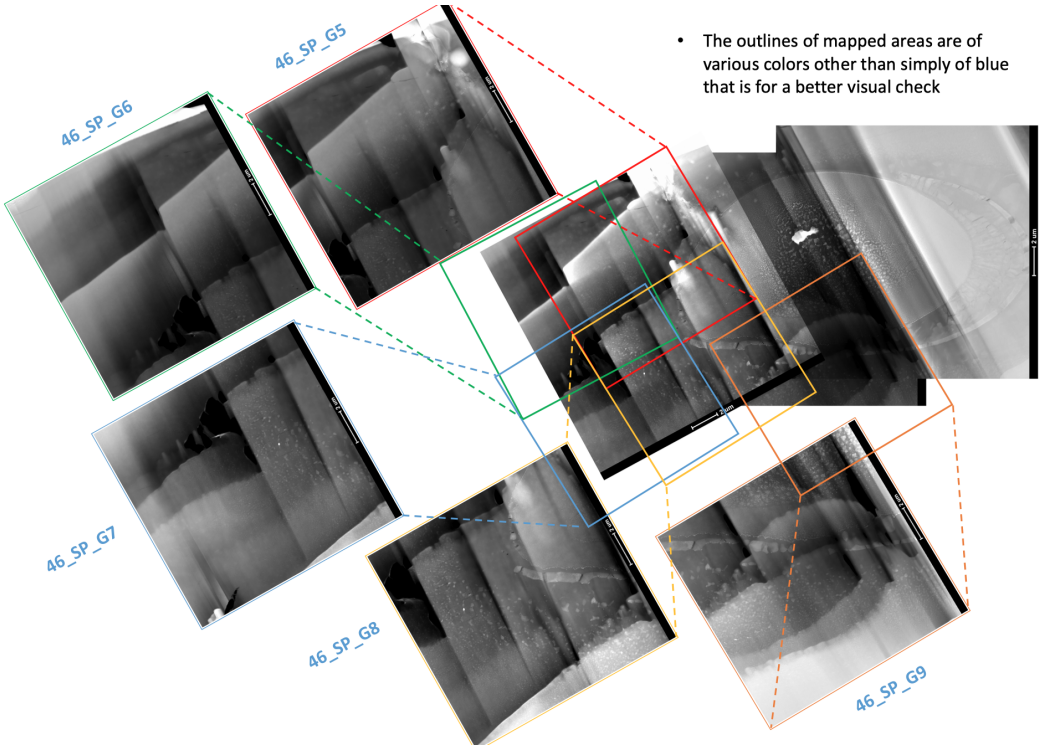
• The outlines of mapped areas are of various colors other than simply of blue that is for a better visual check
46_SP_G5
46_SP_G6
46_SP_G7
46_SP_G8
46_SP_G9

(g)

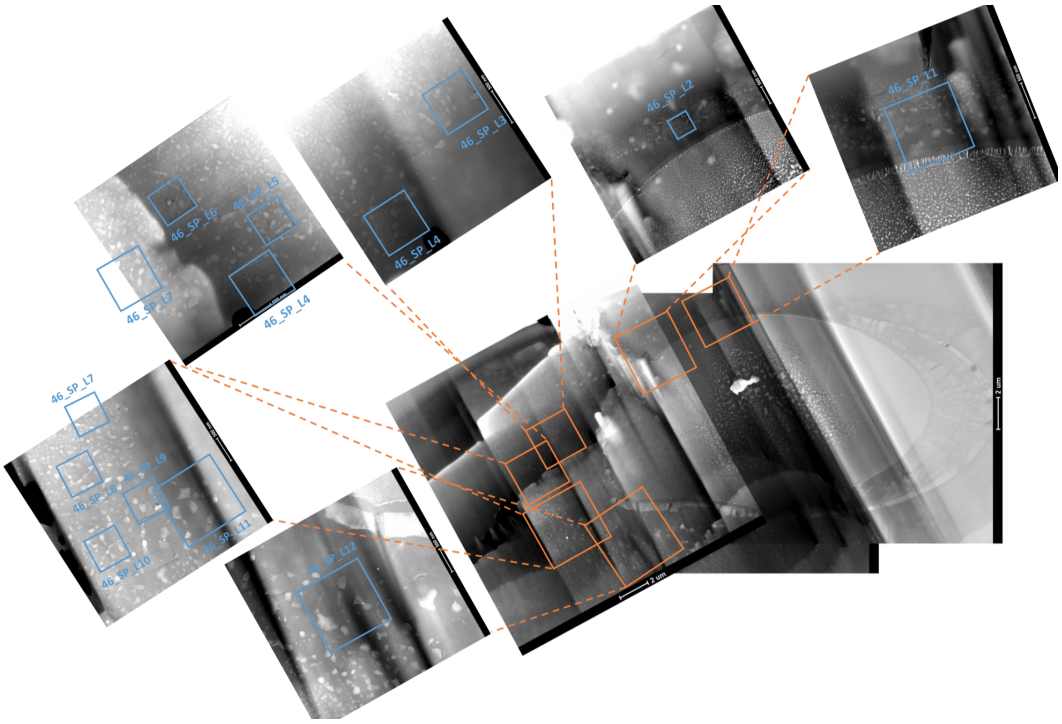
46_SP_L1
46_SP_L2
46_SP_L3
46_SP_L4
46_SP_L5
46_SP_L6
46_SP_L7
46_SP_L8
46_SP_L9
46_SP_L10
46_SP_L11
46_SP_L12

(h)

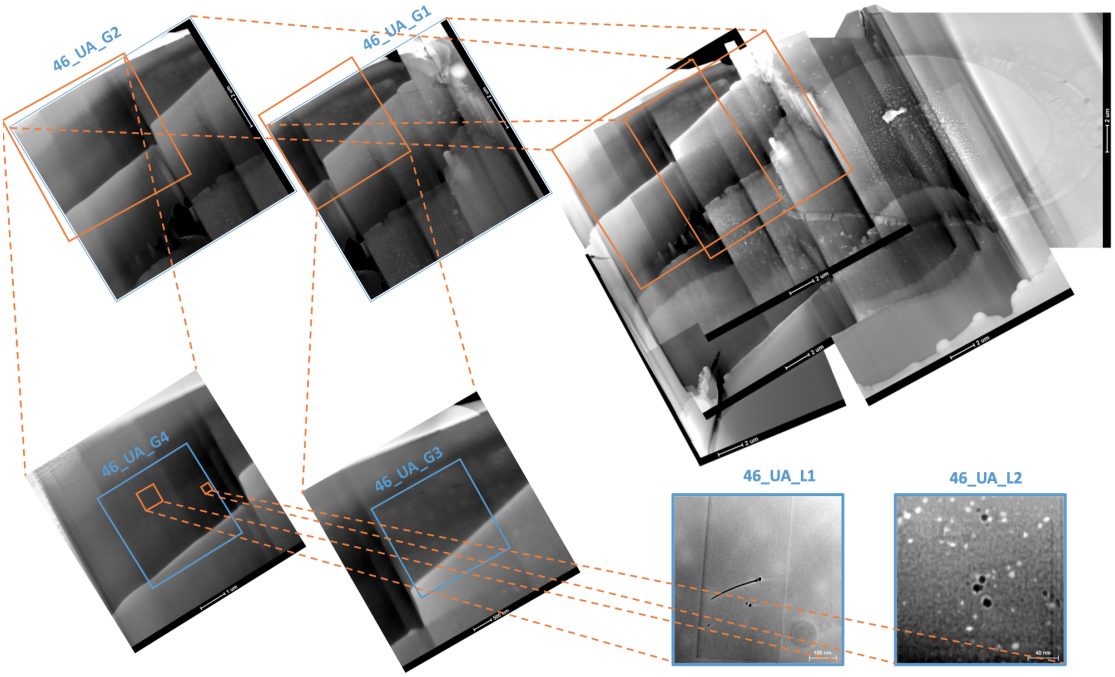

(i)

Figure 5: Scanned STEM-EDXS maps of the 46 GPa sample.

Sample name: C-C5-55 GPa

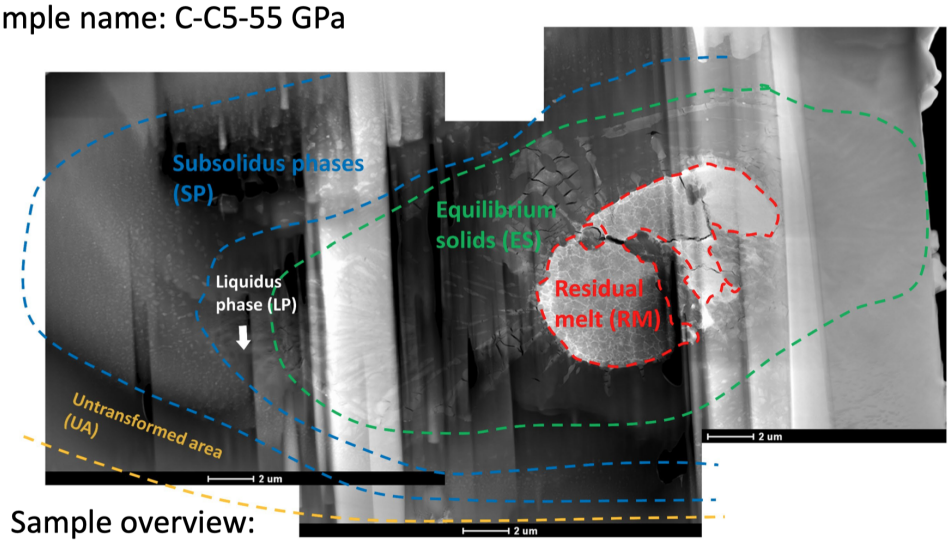

Sample overview:

- EDXS mapped area

- EDXS map name nomenclature: **XX–YY–L(G)N**

XX: the pressure at which the sample was synthesized
YY: the area where the map data was collected as well as the interest of research
L: map acquired at a local scale; **G**: map acquired at a global scale
N: the index number of the map in each category

(a)

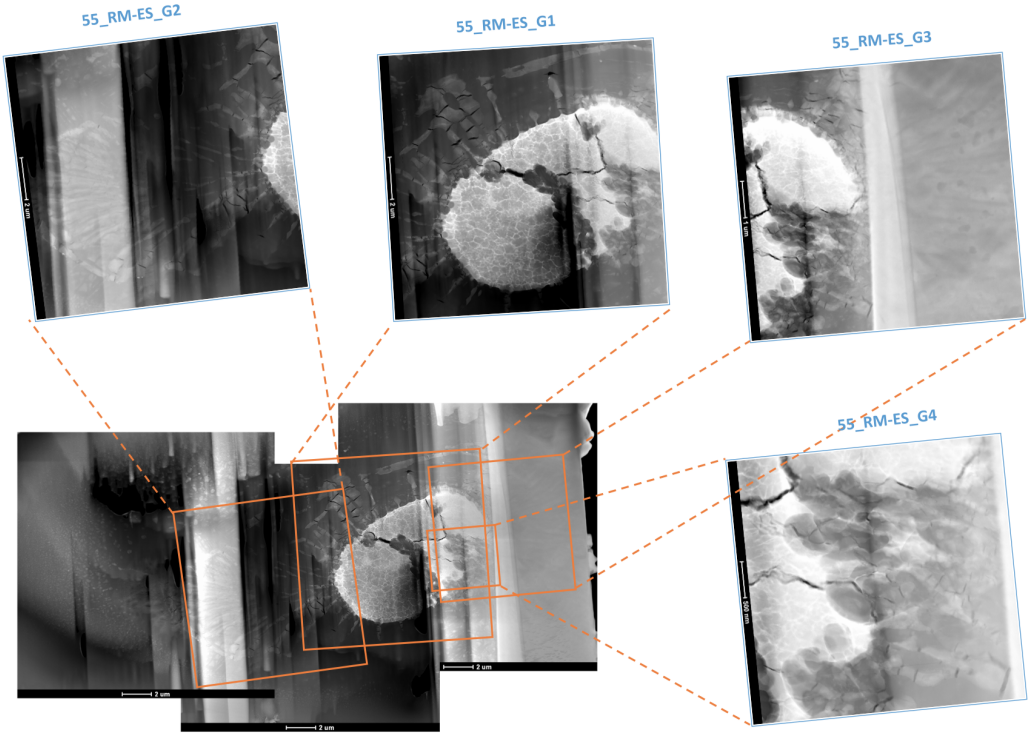

(b)

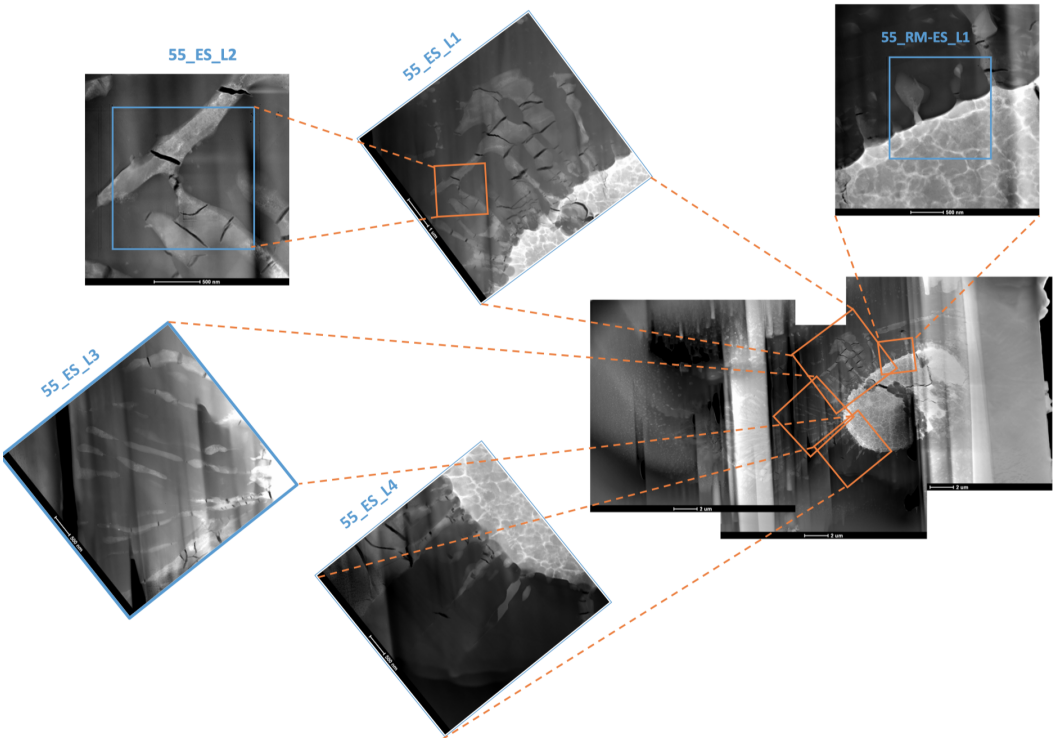
55_ES_L2
55_ES_L1
55_RM-ES_L1
55_ES_L3
55_ES_L4

(c)

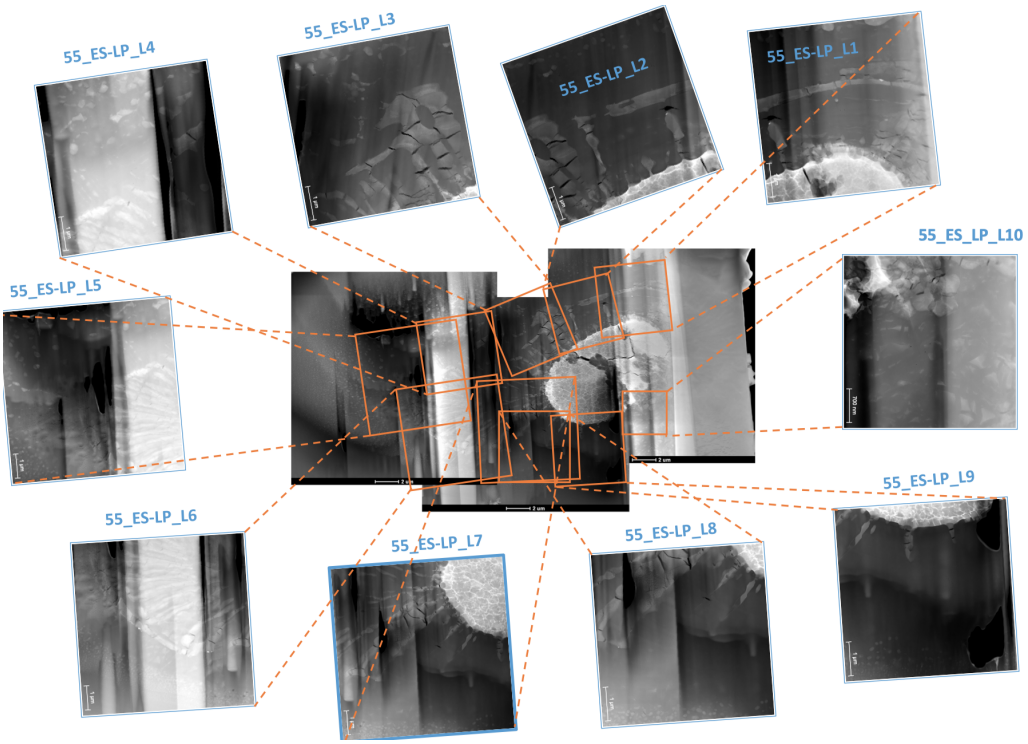
55_ES-LP_L4
55_ES-LP_L3
55_ES-LP_L2
55_ES-LP_L1
55_ES_LP_L10
55_ES-LP_L5
55_ES-LP_L6
55_ES-LP_L7
55_ES-LP_L8
55_ES-LP_L9

(d)

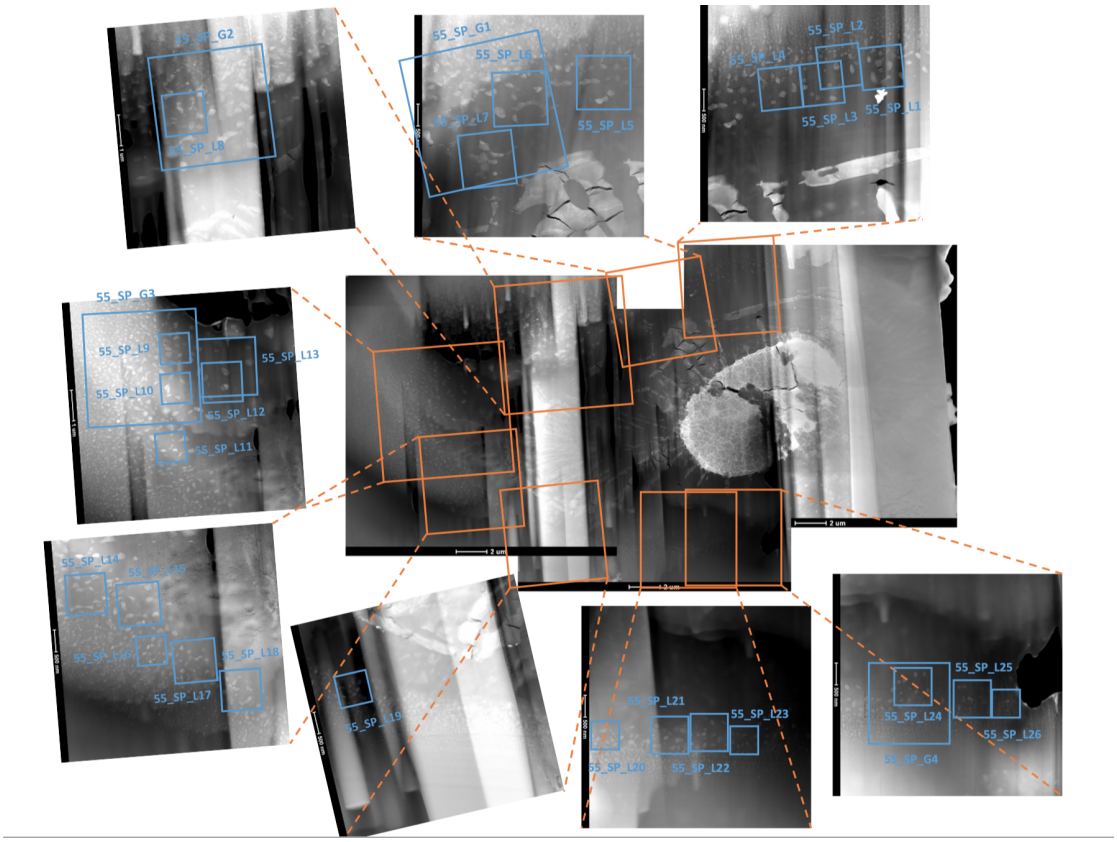
55_SP_G2
55_SP_L8
55_SP_G1
55_SP_L6
55_SP_L7
55_SP_L5
55_SP_L2
55_SP_L4
55_SP_L3
55_SP_L1
55_SP_G3
55_SP_L9
55_SP_L13
55_SP_L10
55_SP_L12
55_SP_L11
55_SP_L14
55_SP_L15
55_SP_L16
55_SP_L18
55_SP_L17
55_SP_L19
55_SP_L21
55_SP_L23
55_SP_L20
55_SP_L22
55_SP_L25
55_SP_L24
55_SP_L26
55_SP_G4

(e)

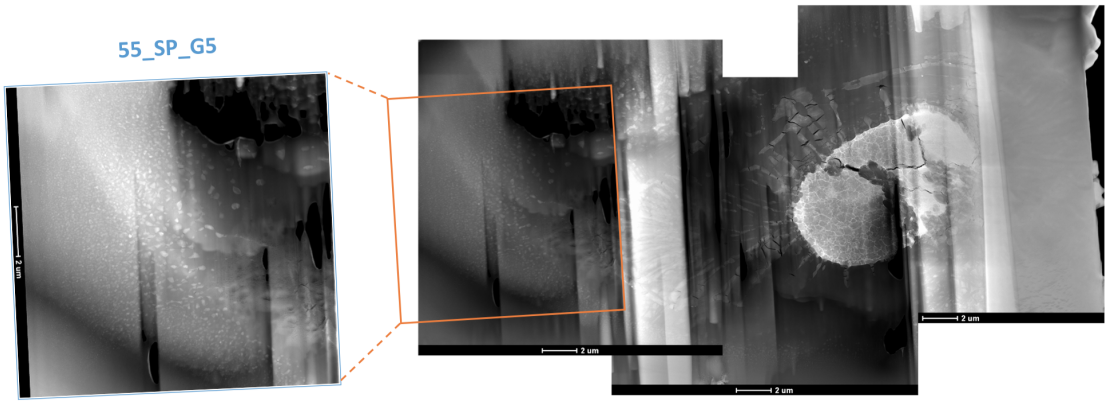
55_SP_G5

(f)

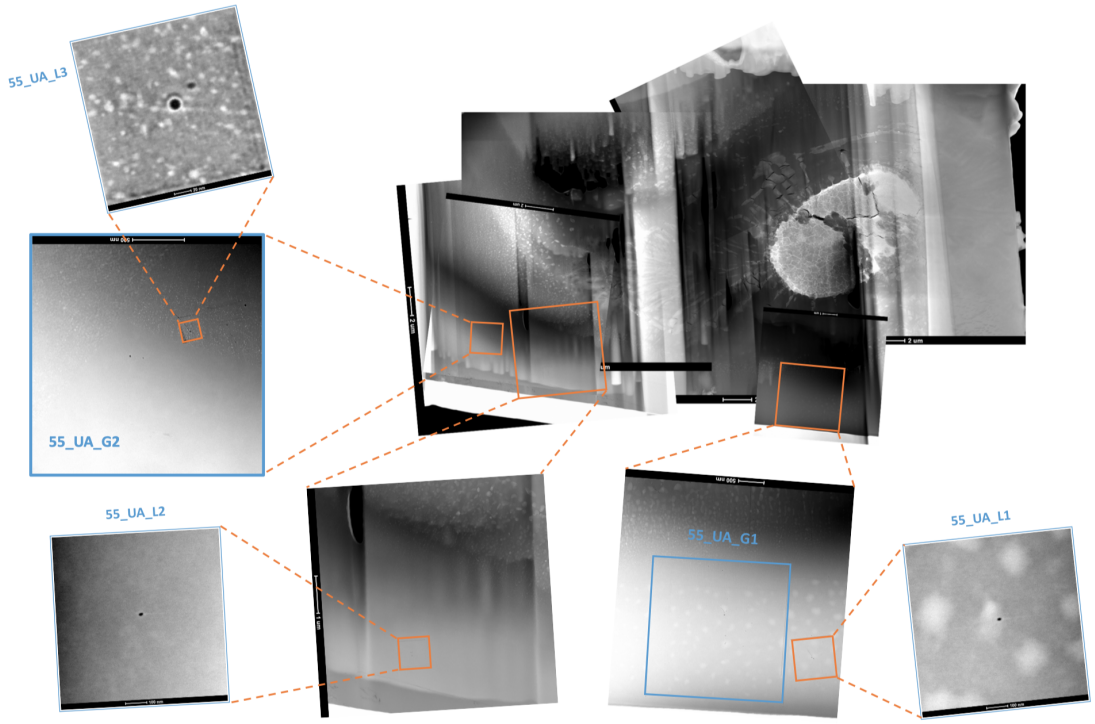

(g)

Figure 6: Scanned STEM-EDXS maps of the 55 GPa sample.

Sample name: C-C4-88 GPa

Sample overview:

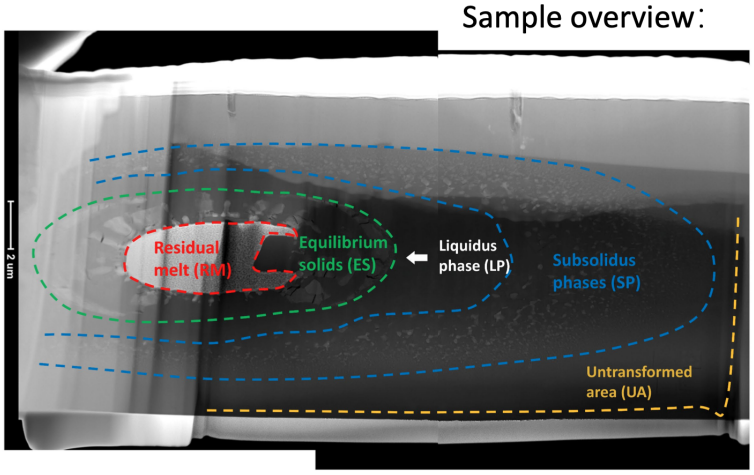

- EDXS mapped area

- EDXS map name nomenclature: **XX–YY–L(G)N**

XX: the pressure at which the sample was synthesized
YY: the area where the map data was collected as well as the interest of research
L: map acquired at a local scale; **G**: map acquired at a global scale
N: the index number of the map in each category

(a)

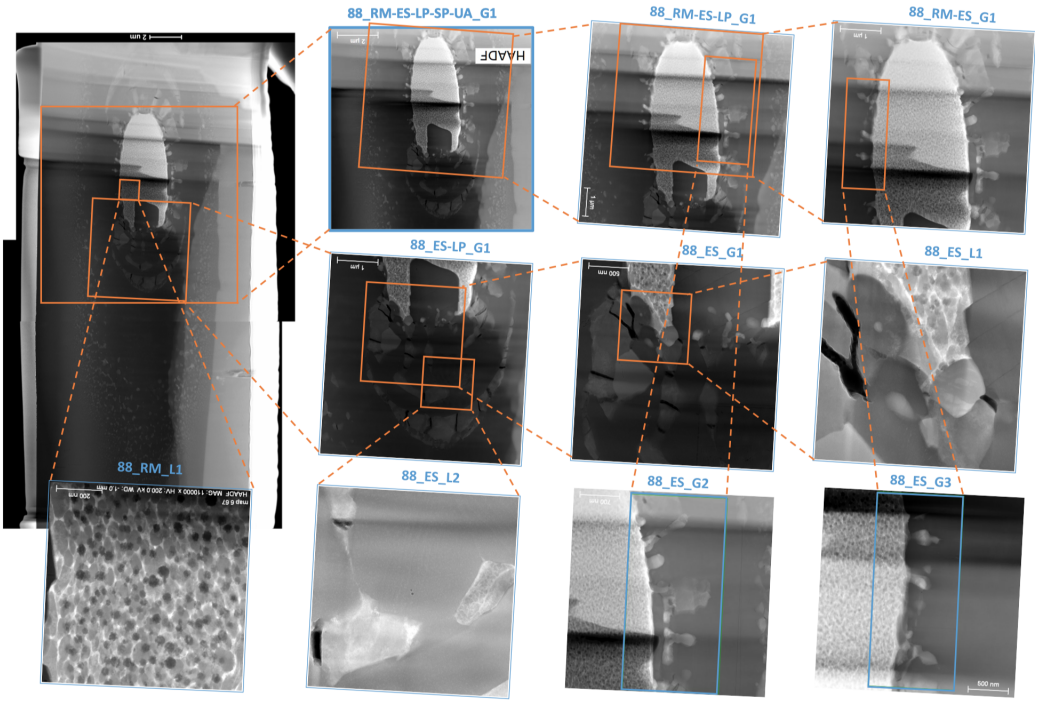

(b)

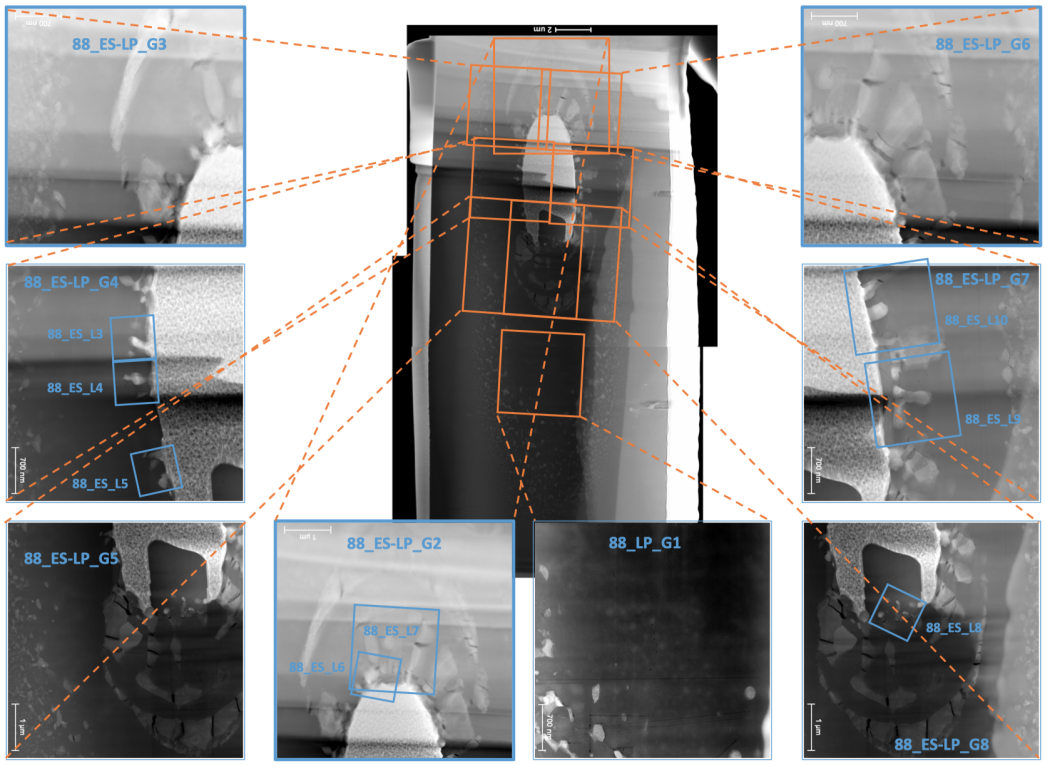
88_ES-LP_G3
88_ES-LP_G6
88_ES-LP_G4
88_ES_L3
88_ES_L4
88_ES_L5
88_ES-LP_G7
88_ES_L10
88_ES_L9
88_ES-LP_G5
88_ES-LP_G2
88_ES_L7
88_ES_L6
88_LP_G1
88_ES_L8
88_ES-LP_G8

(c)

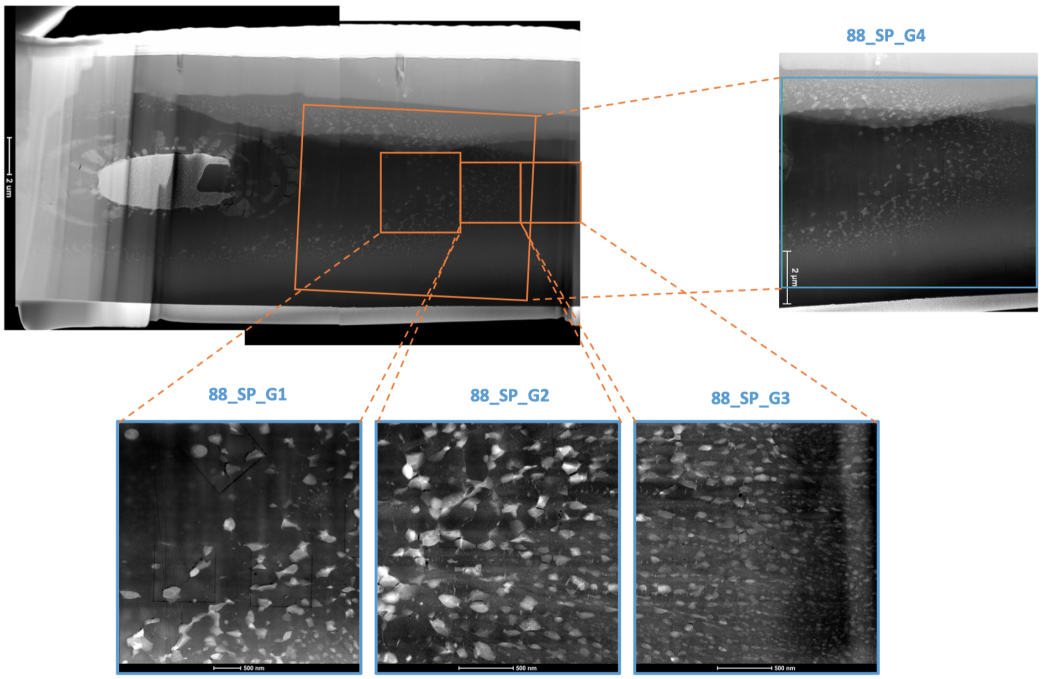
88_SP_G4
88_SP_G1
88_SP_G2
88_SP_G3

(d)

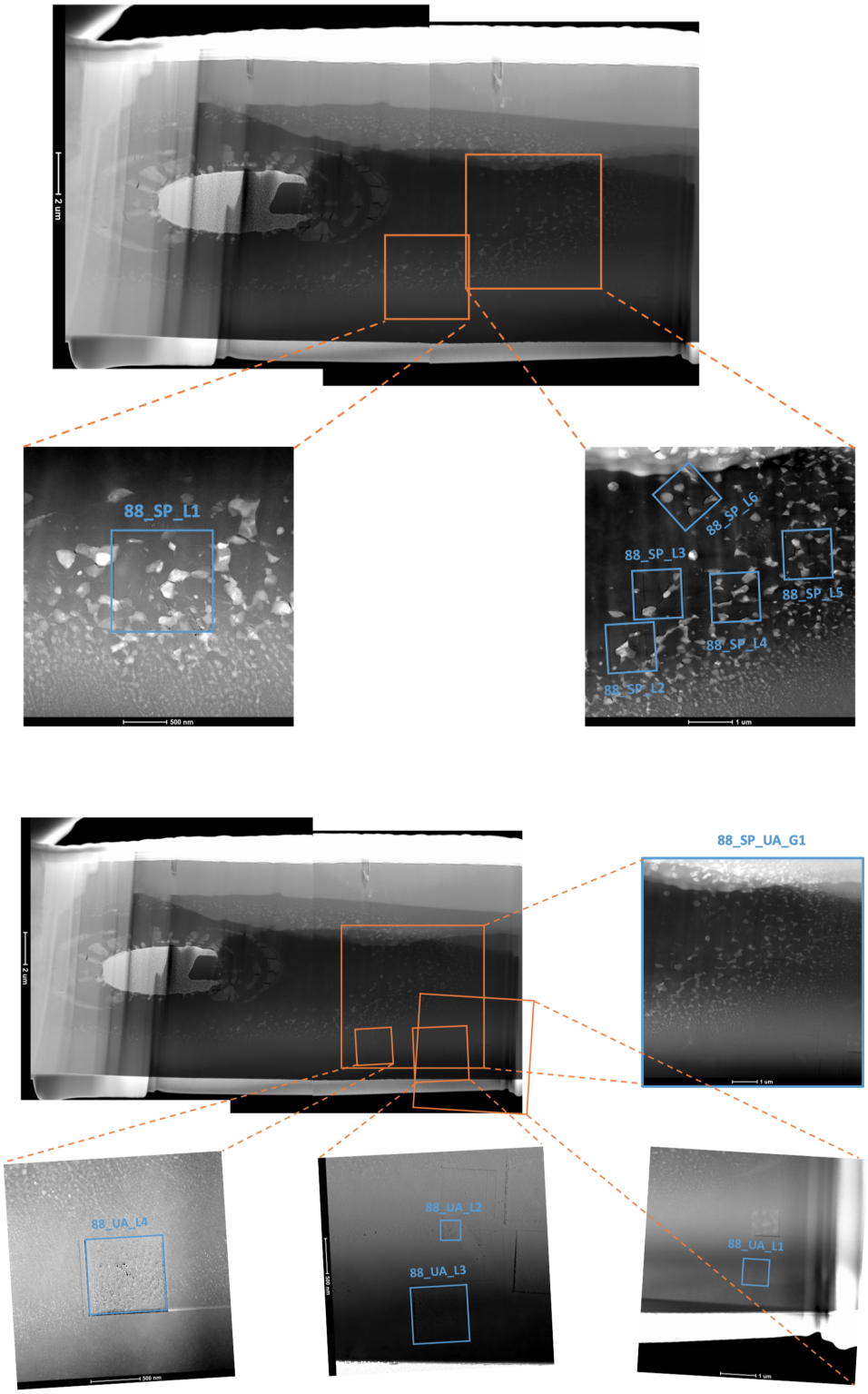

(e)

Figure 7: Scanned STEM-EDXS maps of the 88 GPa sample.

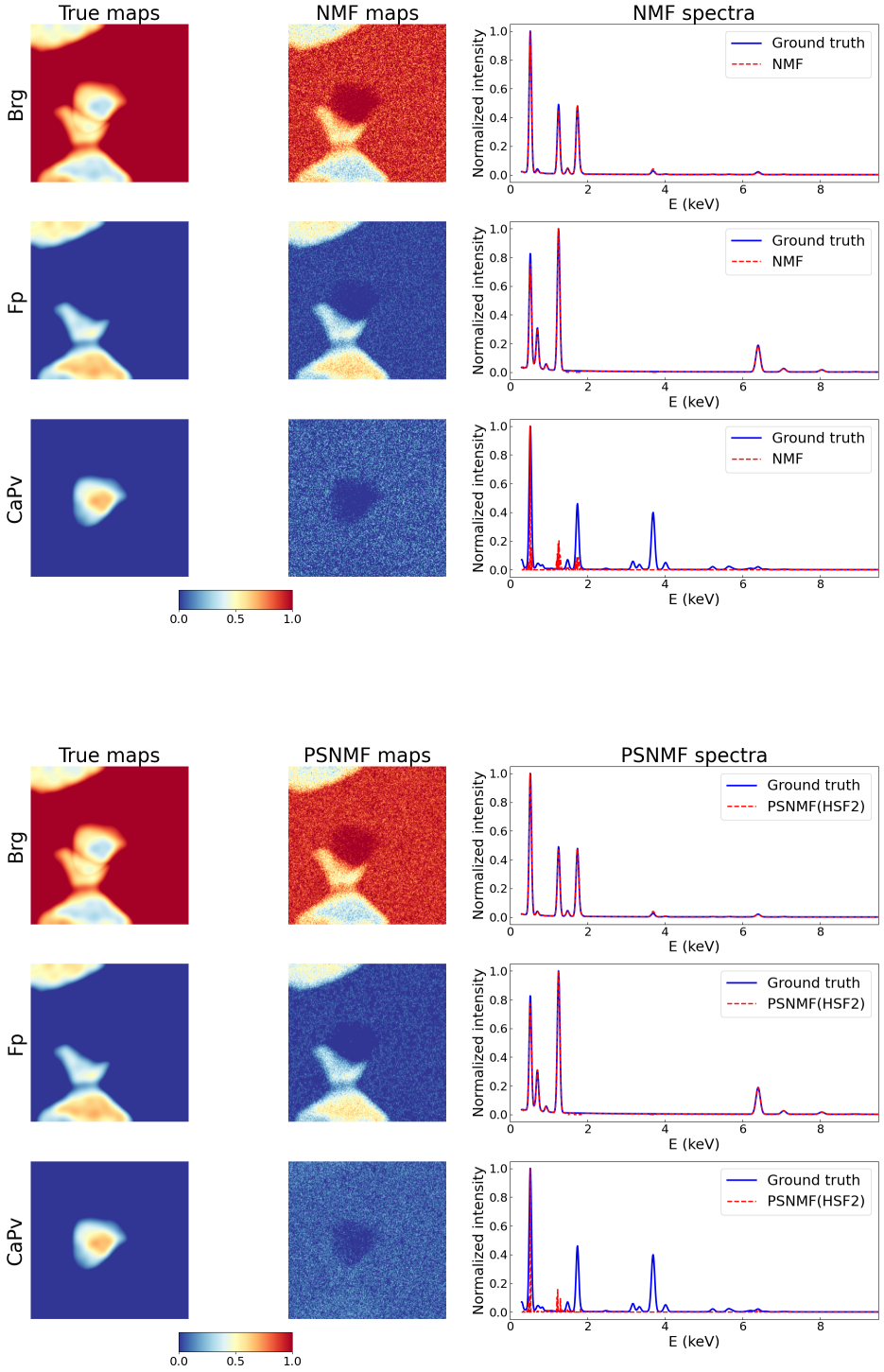

Figure 8: NMF and PSNMF decomposition results of the C147 dataset.

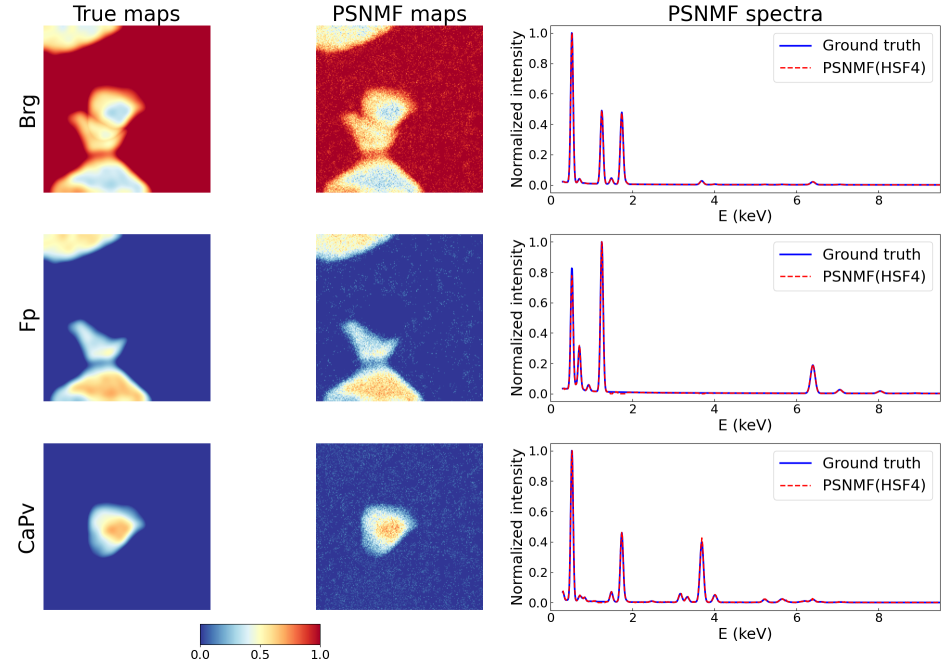

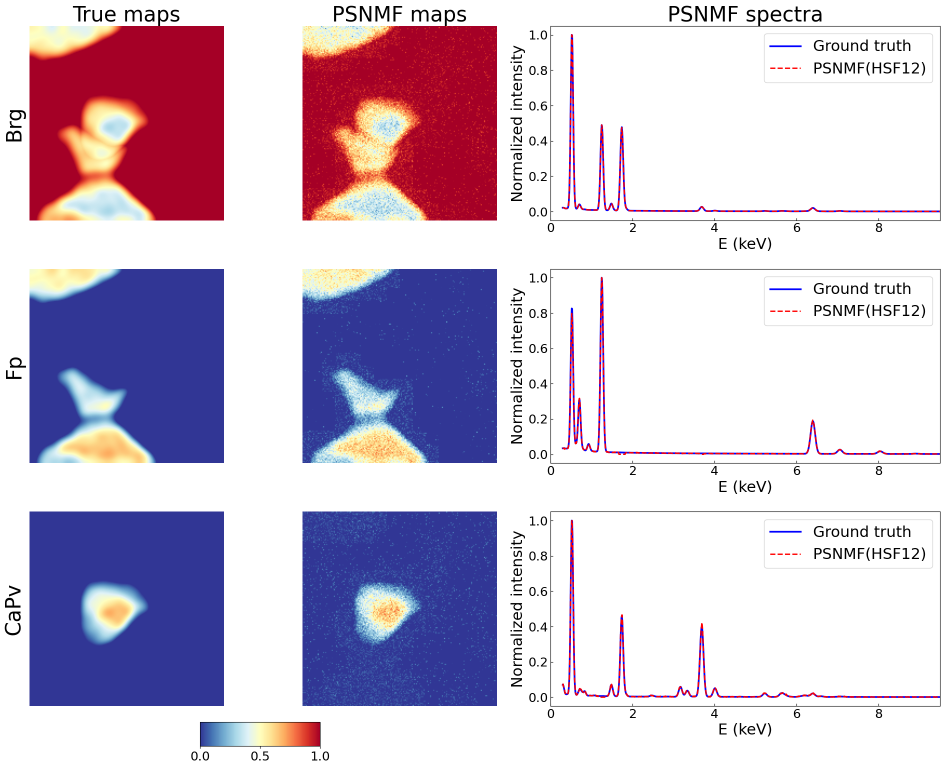

Figure 8: NMF and PSNMF decomposition results of the C147 dataset (continued).

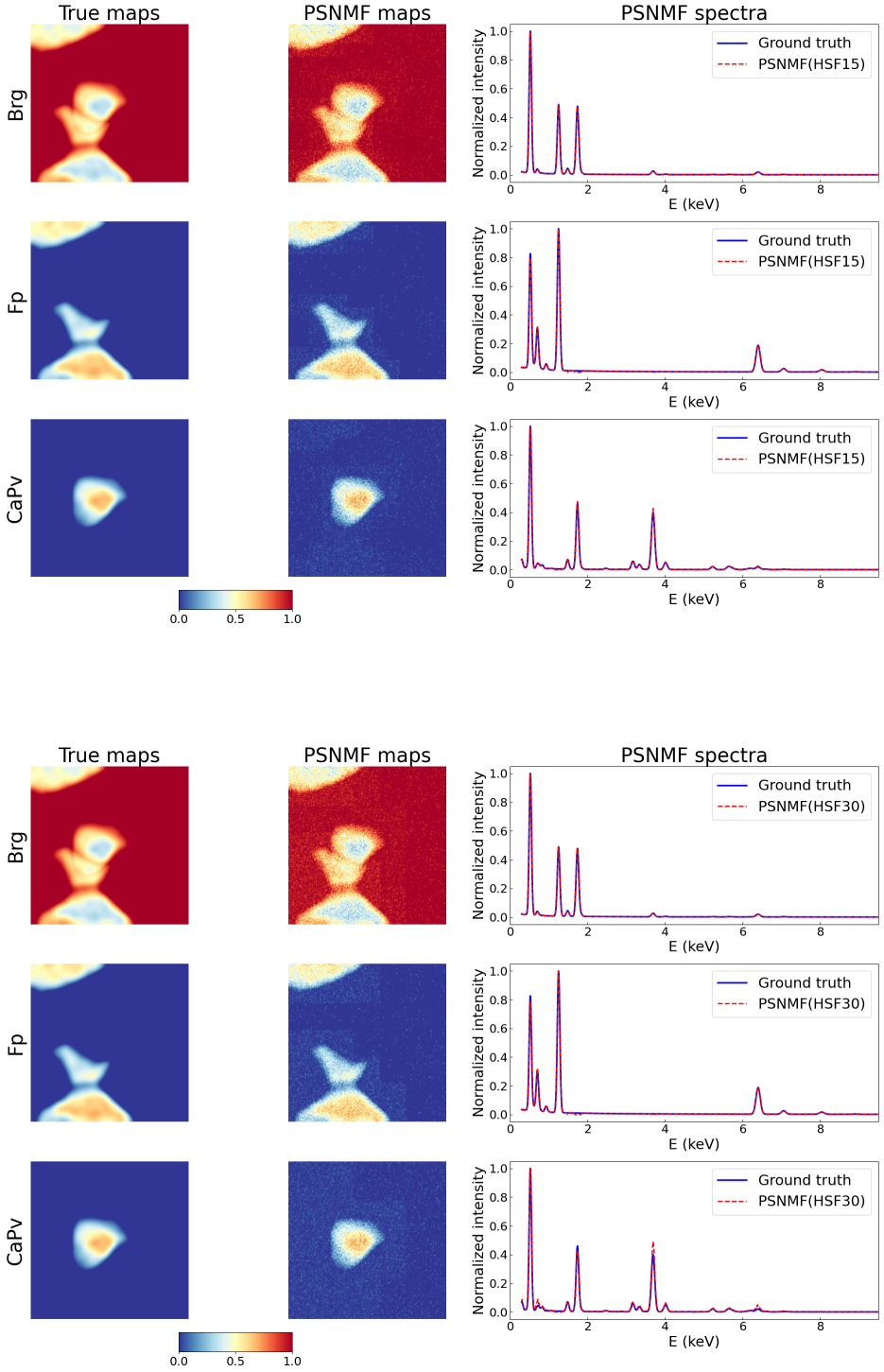

Figure 8: NMF and PSNMF decomposition results of the C147 dataset (continued).

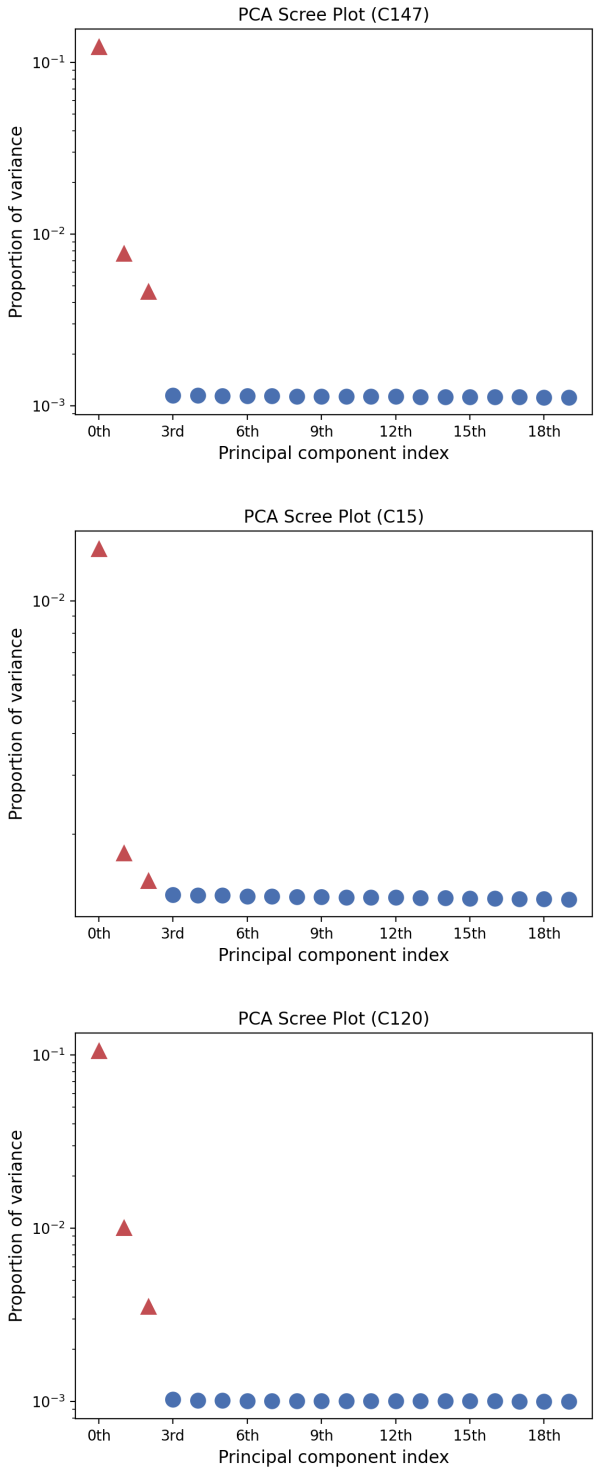

Figure 9: The scree plots of PCA decomposition of the C147, C15, and C120 dataset, respectively.

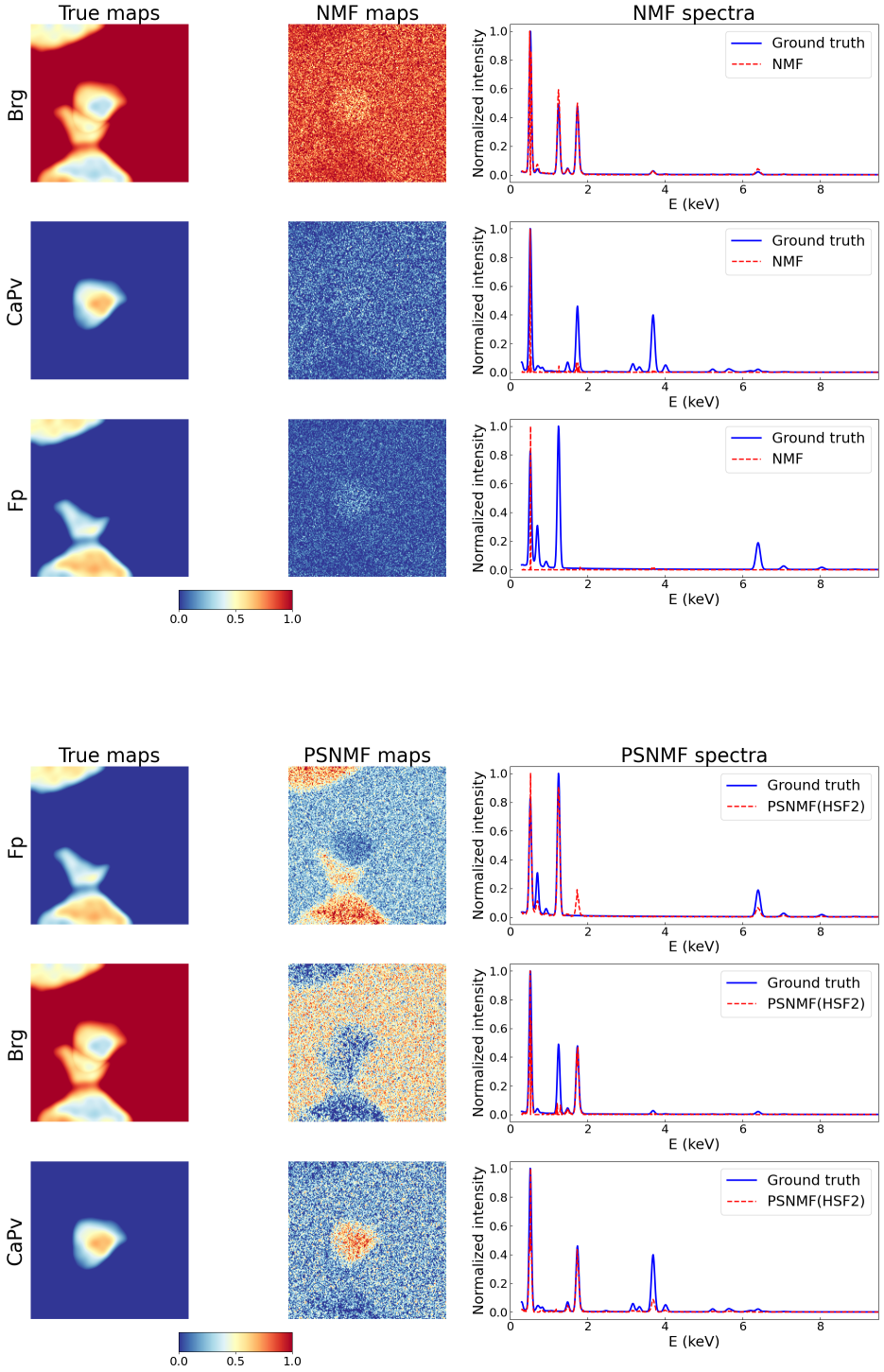

Figure 10: NMF and PSNMF decomposition results of the C15 dataset.

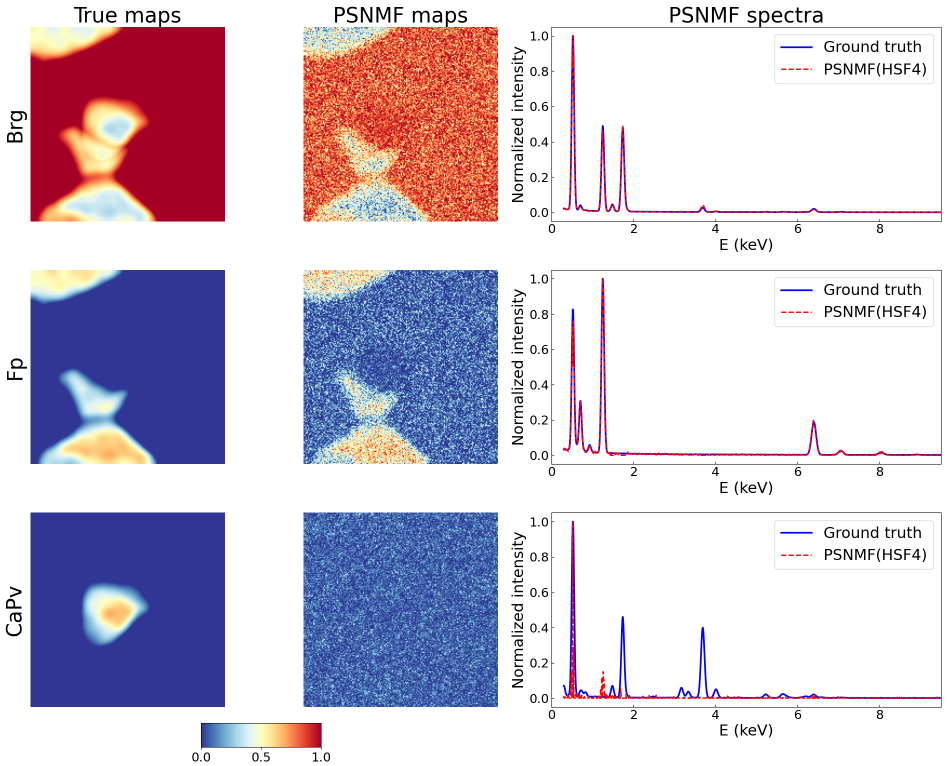

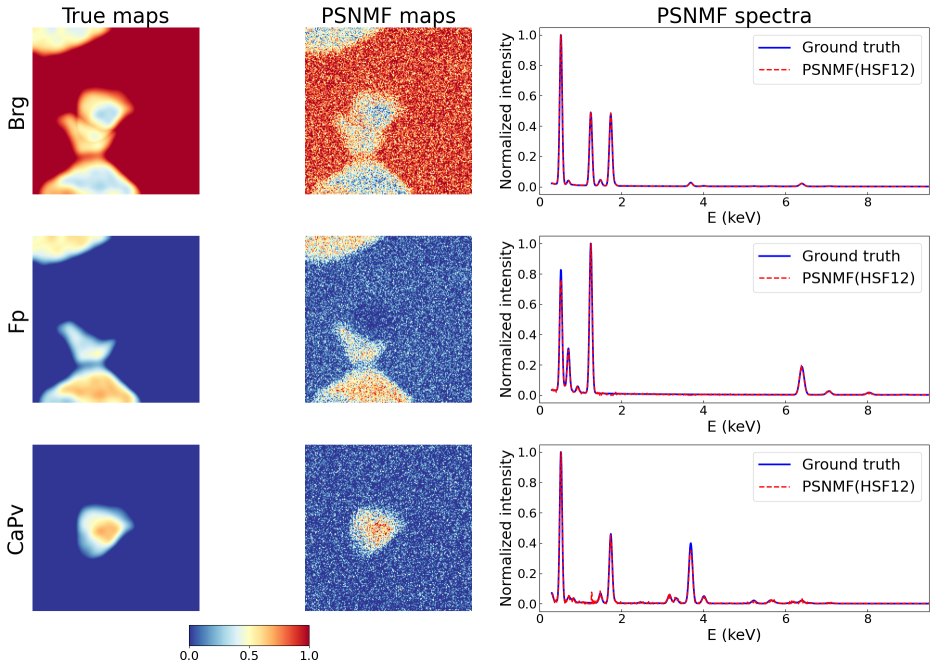

Figure 10: NMF and PSNMF decomposition results of the C15 dataset (continued).

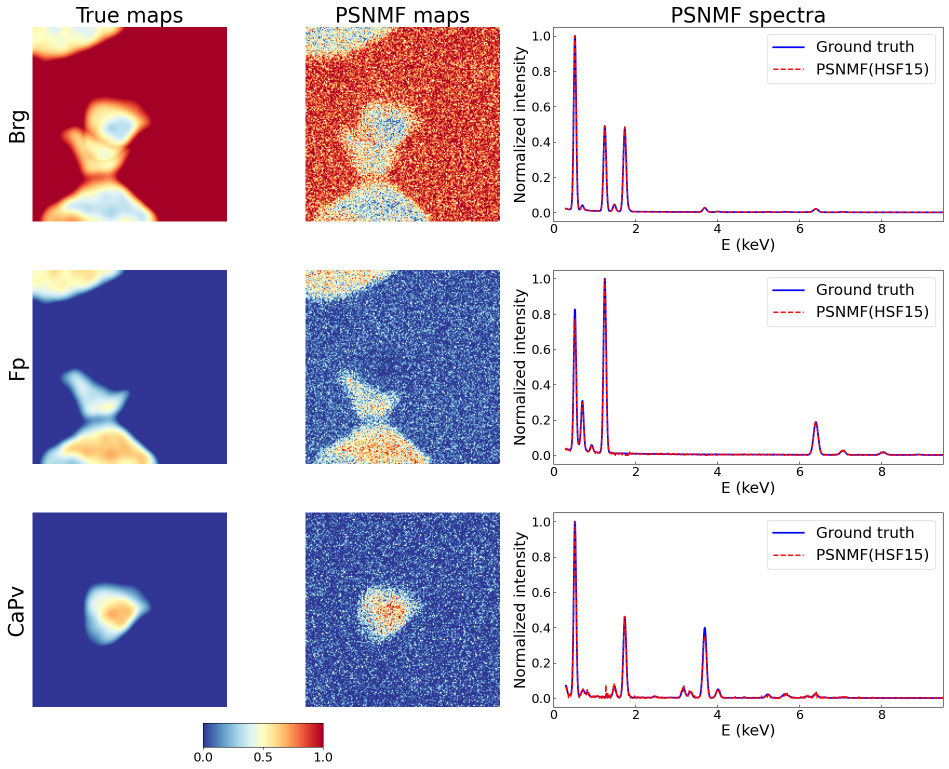

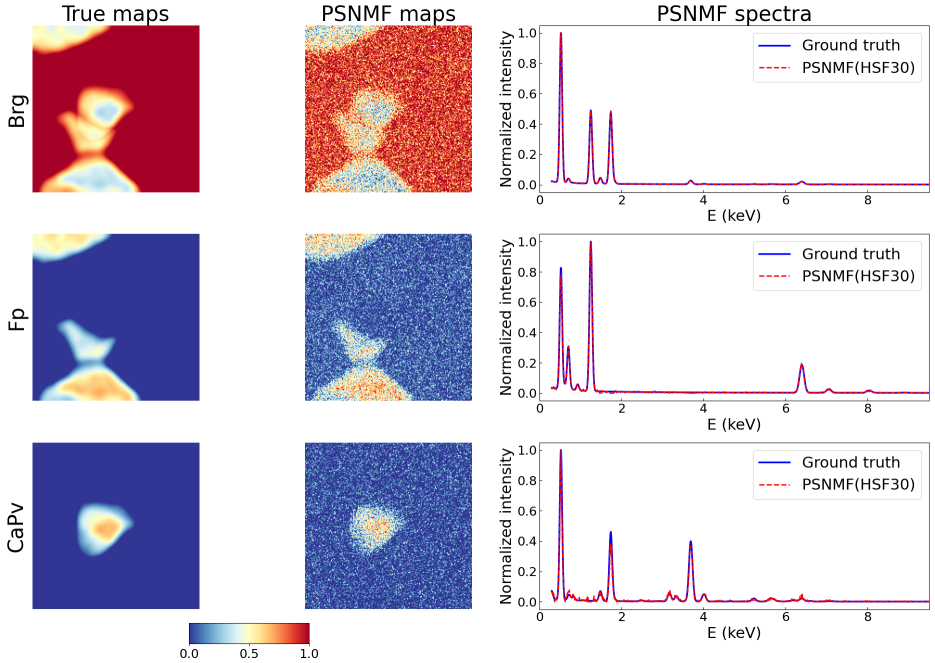

Figure 10: NMF and PSNMF decomposition results of the C15 dataset (continued).

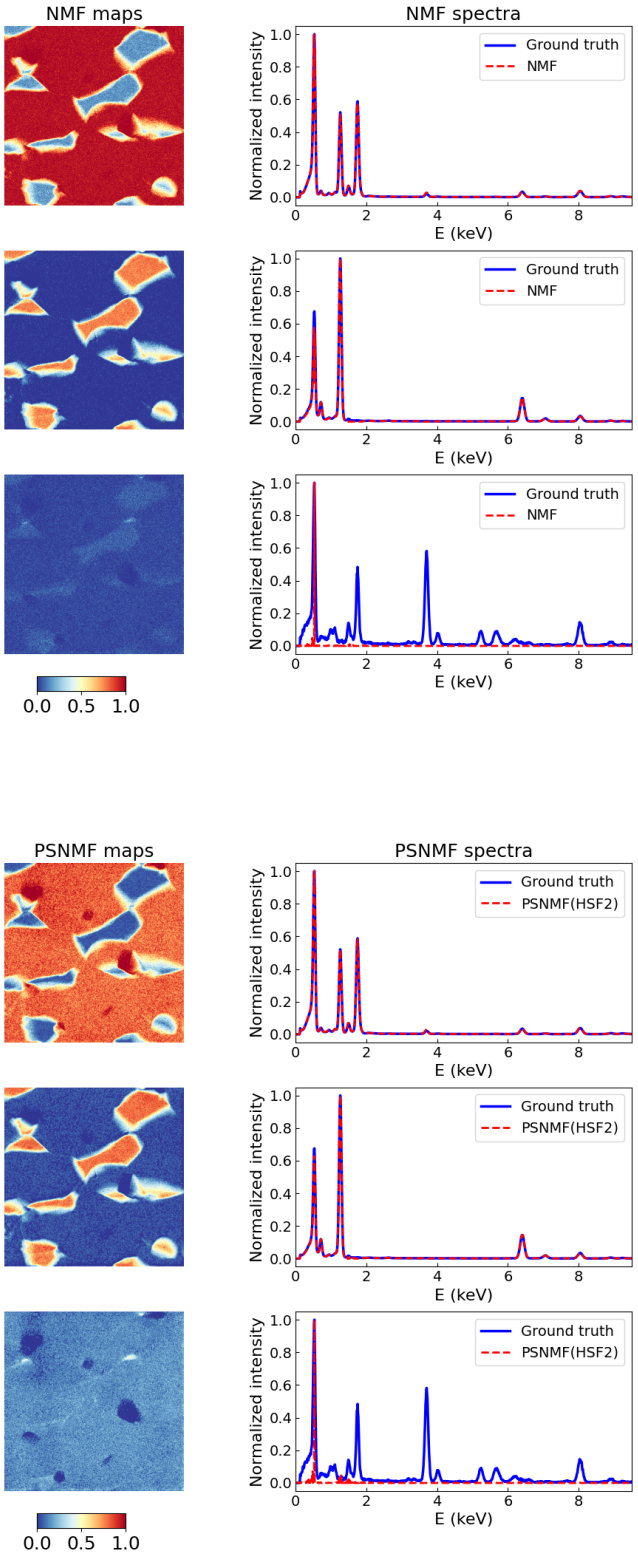

Figure 11: NMF and PSNMF decomposition results of the C120 dataset.

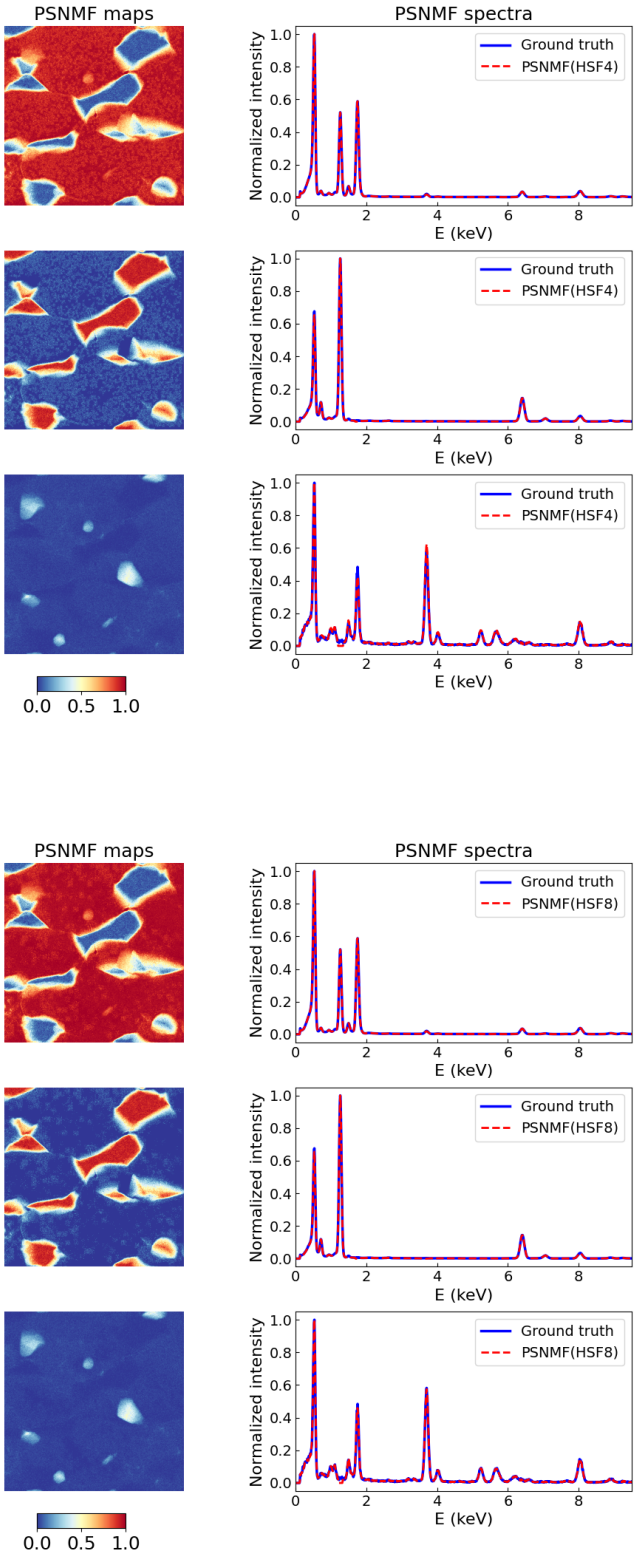

Figure 11: NMF and PSNMF decomposition results of the C120 dataset (continued).

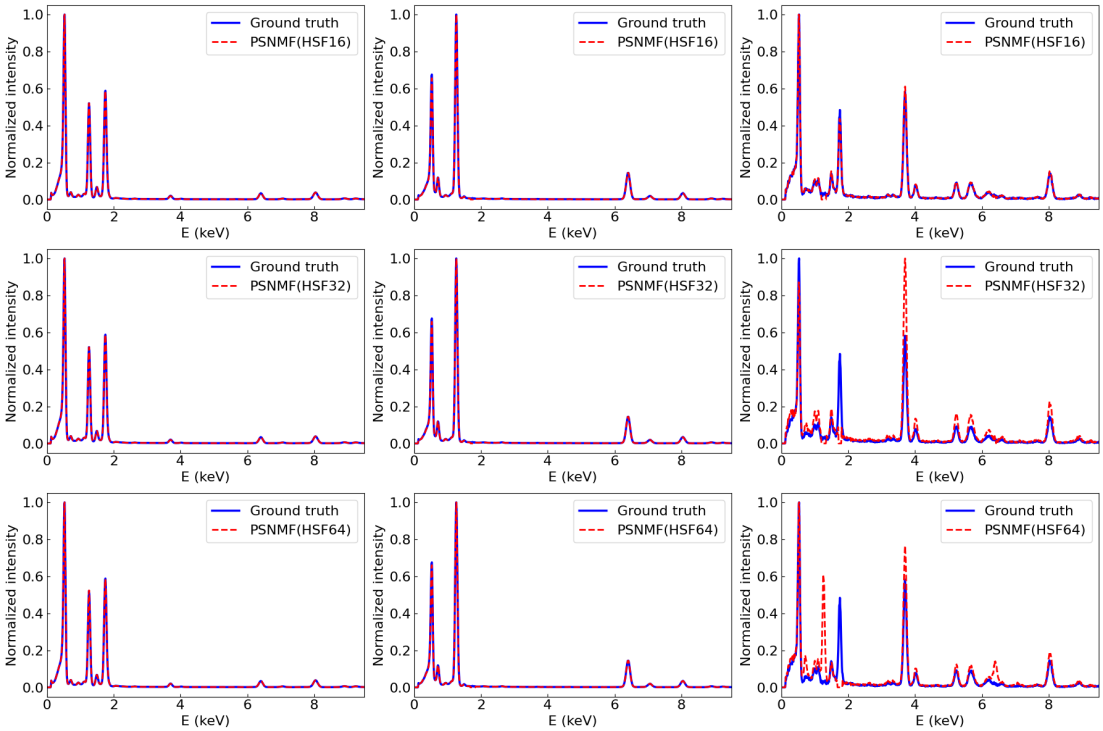

Figure 11: NMF and PSNMF decomposition results of the C120 dataset (continued).

Bibliography

(1) Walter, M.; Nakamura, E.; Trønnes, R.; Frost, D. *Geochimica et Cosmochimica Acta* **2004**, *68*, 4267–4284.

(2) Corgne, A.; Wood, B. J. *Physics of the Earth and Planetary Interiors* **2004**, *143*, 407–419.

(3) Labrosse, S.; Hernlund, J.; Coltice, N. *Nature* **2007**, *450*, 866–869.

(4) Wetherill, G. W. *Annual Review of Earth and Planetary Sciences* **1990**, *18*, 205–256.

(5) Dziewonski, A. M.; Anderson, D. L. *Physics of the earth and planetary interiors* **1981**, *25*, 297–356.

(6) Piet, H. M. *Chemical Characterisation of Deep Earth Reservoirs*; tech. rep.; EPFL, 2016.

(7) Dziewonski, A. M.; Lekic, V.; Romanowicz, B. A. *Earth and Planetary Science Letters* **2010**, *299*, 69–79.

(8) Garnero, E. J.; McNamara, A. K. *Science* **2008**, *320*, 626–628.

(9) Den Tex, E. *Tectonophysics* **1969**, *7*, 457–488.

(10) Nicolas, A.; Boudier, F. *Special papers-Geological Society of America* **2003**, 137–152.

(11) Bonatti, E.; Emiliani, C.; Ferrara, G.; Honnorez, J.; Rydell, H. *Marine Geology* **1974**, *16*, 83–102.

(12) McDonough, W. F.; Sun, S.-S. *Chemical geology* **1995**, *120*, 223–253.

(13) Kerr, R. A. *Science* **1993**, *261*, 1391–1391.

(14) Allegre, C. J.; Poirier, J.-P.; Humler, E.; Hofmann, A. W. *Earth and Planetary Science Letters* **1995**, *134*, 515–526.

(15) Dye, S.; Huang, Y.; Lekic, V.; McDonough, W.; Šrámek, O. *Physics Procedia* **2015**, *61*, 310–318.

(16) Wood, B. J.; Walter, M. J.; Wade, J. *Nature* **2006**, *441*, 825–833.

(17) Lodders, K. *The Astrophysical Journal* **2003**, *591*, 1220.

(18) ST O'NEILL, H. *The Earth's mantle: Composition, structure, and evolution* **1998**, 3–126.

(19) Tateno, S.; Hirose, K.; Ohishi, Y.; Tatsumi, Y. *Science* **2010**, *330*, 359–361.

(20) Oganov, A. R.; Ono, S. *Nature* **2004**, *430*, 445–448.

(21) Helffrich, G. R.; Wood, B. J. *Nature* **2001**, *412*, 501–507.

(22) Ringwood, A. *Journal of Geophysical Research* **1962**, *67*, 857–867.

(23) Ringwood, A. E. *MacGraw-Hill* **1975**, *618*.

(24) Sun, S.-S. *Geochimica et Cosmochimica Acta* **1982**, *46*, 179–192.

(25) Irifune, T. *Island Arc* **1993**, *2*, 55–71.

(26) Frost, D. J.; Langenhorst, F. *Earth and Planetary Science Letters* **2002**, *199*, 227–241.

(27) Corgne, A.; Liebske, C.; Wood, B. J.; Rubie, D. C.; Frost, D. J. *Geochimica et Cosmochimica Acta* **2005**, *69*, 485–496.

(28) Stixrude, L.; Lithgow-Bertelloni, C.; Kiefer, B.; Fumagalli, P. *Physical Review B* **2007**, *75*, 024108.

(29) Garnero, E. J.; McNamara, A. K.; Shim, S.-H. *Nature Geoscience* **2016**, *9*, 481–489.

(30) Davies, D. R.; Goes, S.; Davies, J. H.; Schuberth, B.; Bunge, H.-P.; Ritsema, J. *Earth and Planetary Science Letters* **2012**, *353*, 253–269.

(31) Davies, D.; Goes, S.; Lau, H. *The Earth's heterogeneous mantle* **2015**, 441–477.

(32) Huang, C.; Leng, W.; Wu, Z. *Journal of Geophysical Research: Solid Earth* **2020**, *125*, e2019JB018262.

(33) French, S. W.; Romanowicz, B. *Nature* **2015**, *525*, 95–99.

(34) Garnero, E. J.; Helmberger, D. V. *Geophysical Research Letters* **1996**, *23*, 977–980.

(35) Rost, S.; Garnero, E. J.; Stefan, W. *Journal of Geophysical Research: Solid Earth* **2010**, *115*.

(36) Wicks, J.; Jackson, J.; Sturhahn, W. *Geophysical Research Letters* **2010**, *37*.

(37) Wicks, J. K.; Jackson, J. M.; Sturhahn, W.; Zhang, D. *Geophysical Research Letters* **2017**, *44*, 2148–2158.

(38) Buffett, B. A.; Garnero, E. J.; Jeanloz, R. *Science* **2000**, *290*, 1338–1342.

(39) Williams, Q.; Garnero, E. J. *Science* **1996**, *273*, 1528–1530.

(40) Yuan, K.; Romanowicz, B. *Science* **2017**, *357*, 393–397.

(41) Andrault, D.; Pesce, G.; Bouhifd, M. A.; Bolfan-Casanova, N.; Hénot, J.-M.; Mezouar, M. *Science* **2014**, *344*, 892–895.

(42) Liu, J.; Li, J.; Hrubiak, R.; Smith, J. S. *Proceedings of the National Academy of Sciences* **2016**, *113*, 5547–5551.

(43) Yu, S.; Garnero, E. J. *Geochemistry, Geophysics, Geosystems* **2018**, *19*, 396–414.

(44) Tonks, W. B.; Melosh, H. J. *Journal of Geophysical Research: Planets* **1993**, *98*, 5319–5333.

(45) Liebske, C. Mantle-Melting at High Pressure: Experimental Constraints on Magma Ocean Differentiation, Ph.D. Thesis, 2005.

(46) Albarede, F.; Blichert-Toft, J.; Vervoort, J. D.; Gleason, J. D.; Rosing, M. *Nature* **2000**, *404*, 488–490.

(47) Caro, G.; Bourdon, B.; Birck, J.-L.; Moorbath, S. *Nature* **2003**, *423*, 428–432.

(48) Knoll, M.; Ruska, E. *Zeitschrift für physik* **1932**, *78*, 318–339.

(49) Pennycook, S. J. *Ultramicroscopy* **2017**, *180*, 22–33.

(50) Pennycook, S. J.; Li, C.; Li, M.; Tang, C.; Okunishi, E.; Varela, M.; Kim, Y.-M.; Jang, J. H. *Journal of Analytical Science and Technology* **2018**, *9*, 1–14.

(51) Zachman, M. J.; Hachtel, J. A.; Idrobo, J. C.; Chi, M. *Angewandte Chemie International Edition* **2020**, *59*, 1384–1396.

(52) Rayleigh, L. *The London, Edinburgh, and Dublin Philosophical Magazine and Journal of Science* **1879**, *8*, 261–274.

(53) Egerton, R. F., *Electron energy-loss spectroscopy in the electron microscope*; Springer Science & Business Media: 2011.

(54) Carter, C. B.; Williams, D. B., *Transmission electron microscopy: Diffraction, imaging, and spectrometry*; Springer: 2016.

(55) Wang, C.; Spendelow, J. S. *Current Opinion in Electrochemistry* **2021**, *28*, 100715.

(56) Fan, Y.; Girard, A.; Waals, M.; Salzemann, C.; Courty, A. *ACS Applied Nano Materials* **2023**.

(57) Jiang, J.; Zhou, X. L.; Lv, H. G.; Yu, H. Q.; Yu, Y. *Advanced Functional Materials* **2022**, 2212160.

(58) Reimer, L., *Transmission electron microscopy: physics of image formation and microanalysis*; Springer: 2013; Vol. 36.

(59) Kramers, H. A. *The London, Edinburgh, and Dublin Philosophical Magazine and Journal of Science* **1923**, *46*, 836–871.

(60) Philibert, J. *X-ray Optics and X-ray Microanalysis* **1963**, 379–392.

(61) Myers, B.; McIlwrath, K.; Wu, J.; Li, S.; Inada, H.; Dravid, V. *Microscopy and Microanalysis* **2010**, *16*, 942–943.

(62) Kotula, P. G.; Michael, J. R.; Rohde, M. *Results from two four-channel Si-drift detectors on an SEM: Conventional and annular geometries.* Tech. rep.; Sandia National Lab.(SNL-NM), Albuquerque, NM (United States), 2008.

(63) Zaluzec, N. J. *Microscopy Today* **2009**, *17*, 56–59.

(64) Von Harrach, H.; Dona, P.; Freitag, B.; Soltau, H.; Niculae, A.; Rohde, M. *Microscopy and Microanalysis* **2009**, *15*, 208–209.

(65) Zaluzec, N. *Microscopy and Microanalysis* **2021**, *27*, 2070–2074.

(66) Slater, T. J. A. Three dimensional chemical analysis of nanoparticles using energy dispersive X-ray spectroscopy, Ph.D. Thesis, University of Manchester, 2015.

(67) Kotula, P.; Brewer, L.; Michael, J.; Giannuzzi, L. *Microscopy and Microanalysis* **2007**, *13*, 1324–1325.

(68) Yaguchi, T.; Konno, M.; Kamino, T.; Watanabe, M. *Ultramicroscopy* **2008**, *108*, 1603–1615.

(69) Lepinay, K.; Lorut, F.; Pantel, R.; Epicier, T. *Micron* **2013**, *47*, 43–49.

(70) Goris, B.; Roelandts, T.; Batenburg, K. J.; Mezerji, H. H.; Bals, S. *Ultramicroscopy* **2013**, *127*, 40–47.

(71) Yeoh, C. S.; Rossouw, D.; Saghi, Z.; Burdet, P.; Leary, R. K.; Midgley, P. A. *Microscopy and Microanalysis* **2015**, *21*, 759–764.

(72) Cliff, G.; Lorimer, G. W. *Journal of Microscopy* **1975**, *103*, 203–207.

(73) Williams, D.; Goldstein, J. In *Electron Probe Quantitation*; Springer: 1991, pp 371–398.

(74) Sheridan, P. J. *Journal of electron microscopy technique* **1989**, *11*, 41–61.

(75) Watanabe, M.; Horita, Z.; Nemoto, M. *Ultramicroscopy* **1996**, *65*, 187–198.

(76) Watanabe, M.; Williams, D. *Journal of microscopy* **2006**, *221*, 89–109.

(77) Egerton, R. F. *Reports on Progress in Physics* **2008**, *72*, 016502.

(78) MacArthur, K.; Pennycook, T.; Okunishi, E.; D'Alfonso, A.; Lugg, N.; Allen, L.; Nellist, P., et al. *Ultramicroscopy* **2013**, *133*, 109–119.

(79) MacArthur, K. E.; Slater, T. J.; Haigh, S. J.; Ozkaya, D.; Nellist, P. D.; Lozano-Perez, S. *Microscopy and Microanalysis* **2016**, *22*, 71–81.

(80) Martinez, G.; Jones, L.; De Backer, A.; Béché, A.; Verbeeck, J.; Van Aert, S.; Nellist, P. *Ultramicroscopy* **2015**, *159*, 46–58.

(81) Hofer, F. *Microscopy Microanalysis Microstructures* **1991**, *2*, 215–230.

(82) Pennycook, S. J.; Nellist, P. D., *Scanning transmission electron microscopy: imaging and analysis*; Springer Science & Business Media: 2011.

(83) Chen, Z.; Weyland, M.; Sang, X.; Xu, W.; Dycus, J.; LeBeau, J.; d'Alfonso, A.; Allen, L.; Findlay, S. *Ultramicroscopy* **2016**, *168*, 7–16.

(84) Findlay, S.; Chen, Z.; Weyland, M.; Sang, X.; Xu, W.; Dycus, J.; LeBeau, J.; Allen, L. *Microscopy and Microanalysis* **2017**, *23*, 388–389.

(85) Besa, P. T. Development of novel eels methods to unveil nanoparticle properties, Ph.D. Thesis, Universitat de Barcelona, 2019.

(86) Park, J.; Heo, S.; Chung, J.-G.; Kim, H.; Lee, H.; Kim, K.; Park, G.-S. *Ultramicroscopy* **2009**, *109*, 1183–1188.

(87) Ouyang, F.; Batson, P.; Isaacson, M. *Physical Review B* **1992**, *46*, 15421.

(88) Nelayah, J.; Kociak, M.; Stéphan, O.; García de Abajo, F. J.; Tencé, M.; Henrard, L.; Taverna, D.; Pastoriza-Santos, I.; Liz-Marzán, L. M.; Colliex, C. *Nature Physics* **2007**, *3*, 348–353.

(89) Krivanek, O. L.; Lovejoy, T. C.; Dellby, N.; Aoki, T.; Carpenter, R.; Rez, P.; Soignard, E.; Zhu, J.; Batson, P. E.; Lagos, M. J., et al. *Nature* **2014**, *514*, 209–212.

(90) Wang, Z.; Yin, J.; Jiang, Y. *Micron* **2000**, *31*, 571–580.

(91) Colliex, C.; Manoubi, T.; Ortiz, C. *Physical Review B* **1991**, *44*, 11402.

(92) Scott, J.; Thomas, P.; MacKenzie, M.; McFadzean, S.; Wilbrink, J.; Craven, A.; Nicholson, W. *Ultramicroscopy* **2008**, *108*, 1586–1594.

(93) Gubbens, A.; Barfels, M.; Trevor, C.; Twesten, R.; Mooney, P.; Thomas, P.; Menon, N.; Kraus, B.; Mao, C.; McGinn, B. *Ultramicroscopy* **2010**, *110*, 962–970.

(94) Craven, A.; Wilson, J.; Nicholson, W. *Ultramicroscopy* **2002**, *92*, 165–180.

(95) Craven, A.; MacKenzie, M.; McFadzean, S. In *EMC 2008 14th European Microscopy Congress 1–5 September 2008, Aachen, Germany*, 2008, pp 363–364.

(96) Johnson, D.; Spence, J. H. *Journal of Physics D: Applied Physics* **1974**, *7*, 771.

(97) Egerton, R. *Ultramicroscopy* **1978**, *3*, 243–251.

(98) Held, J. T.; Yun, H.; Mkhoyan, K. A. *Ultramicroscopy* **2020**, *210*, 112919.

(99) Steele, J.; Titchmarsh, J.; Chapman, J.; Paterson, J. *Ultramicroscopy* **1985**, *17*, 273–276.

(100) Shuman, H.; Somlyo, A. *Ultramicroscopy* **1987**, *21*, 23–32.

(101) Leapman, R.; Swyt, C. *Ultramicroscopy* **1988**, *26*, 393–403.

(102) Verbeeck, J.; Van Aert, S. *Ultramicroscopy* **2004**, *101*, 207–224.

(103) Verbeeck, J.; Van Aert, S.; Bertoni, G. *Ultramicroscopy* **2006**, *106*, 976–980.

(104) Verbeeck, J.; Bertoni, G. *Microchimica Acta* **2008**, *161*, 439–443.

(105) Kothleitner, G.; Grogger, W.; Dienstleder, M.; Hofer, F. *Microscopy and Microanalysis* **2014**, *20*, 678–686.

(106) Varambhia, A. M. Quantitative structural and compositional studies of catalyst nanoparticles using imaging and spectroscopy in STEM, Ph.D. Thesis, University of Oxford, 2018.

(107) Varambhia, A.; Jones, L.; London, A.; Ozkaya, D.; Nellist, P. D.; Lozano-Perez, S. *Micron* **2018**, *113*, 69–82.

(108) Kruit, P.; Shuman, H.; Somlyo, A. *Ultramicroscopy* **1984**, *13*, 205–213.

(109) Jannis, D.; Müller-Caspary, K.; Béché, A.; Oelsner, A.; Verbeeck, J. *Applied physics letters* **2019**, *114*, 143101.

(110) Arnold, L.; Baumann, R.; Chambit, E.; Filliger, M.; Fuchs, C.; Kieber, C.; Klein, D.; Medina, P.; Parisel, C.; Richer, M., et al. *IEEE Transactions on Nuclear Science* **2006**, *53*, 723–728.

(111) Papp, T.; Maxwell, J. *Nuclear Instruments and Methods in Physics Research Section A: Accelerators, Spectrometers, Detectors and Associated Equipment* **2010**, *619*, 89–93.

(112) Oelsner, A.; Schmidt, O.; Schicketanz, M.; Klais, M.; Schönhense, G.; Mergel, V.; Jagutzki, O.; Schmidt-Böcking, H. *Review of Scientific Instruments* **2001**, *72*, 3968–3974.

(113) Müller-Caspary, K.; Oelsner, A.; Potapov, P. *Applied Physics Letters* **2015**, *107*, 072110.

(114) Akiba, K.; Artuso, M.; Badman, R.; Borgia, A.; Bates, R.; Bayer, F.; Van Beuzekom, M.; Buytaert, J.; Cabruja, E.; Campbell, M., et al. *Nuclear Instruments and Methods in Physics Research Section A: Accelerators, Spectrometers, Detectors and Associated Equipment* **2012**, *661*, 31–49.

(115) Ballabriga, R.; Campbell, M.; Llopart, X. *Nuclear Instruments and Methods in Physics Research Section A: Accelerators, Spectrometers, Detectors and Associated Equipment* **2018**, *878*, 10–23.

(116) Cocchi, M., *Data fusion methodology and applications*; Elsevier: 2019.

(117) Khaleghi, B.; Khamis, A.; Karray, F. O.; Razavi, S. N. *Information fusion* **2013**, *14*, 28–44.

(118) Castanedo, F. *The scientific world journal* **2013**, *2013*.

(119) Lahat, D.; Adali, T.; Jutten, C. *Proceedings of the IEEE* **2015**, *103*, 1449–1477.

(120) Spiegelberg, J. Signal processing tools for electron microscopy, Ph.D. Thesis, Acta Universitatis Upsaliensis, 2018.

(121) Braidy, N.; Gosselin, R. *Scientific reports* **2019**, *9*, 1–8.

(122) Thersleff, T.; Budnyk, S.; Drangai, L.; Slabon, A. *Ultramicroscopy* **2020**, *219*, 113116.

(123) Smilde, A. K.; Westerhuis, J. A.; De Jong, S. *Journal of Chemometrics: A Journal of the Chemometrics Society* **2003**, *17*, 323–337.

(124) Naik, G. R.; Wang, W., *Blind Source Separation: Advances in Theory, Algorithms and Applications*; Springer: 2014.

(125) Thersleff, T.; Tai, C.-W. *arXiv preprint arXiv:2203.11044* **2022**.

(126) Samuel, A. L. *IBM Journal of research and development* **1959**, *3*, 210–229.

(127) Alpaydin, E., *Introduction to machine learning*; MIT press: 2020.

(128) Jeerige, A.; Bein, D.; Verma, A. In *2019 IEEE 9th Annual Computing and Communication Workshop and Conference (CCWC)*, 2019, pp 0366–0371.

(129) Kiran, B. R.; Sobh, I.; Talpaert, V.; Mannion, P.; Al Sallab, A. A.; Yogamani, S.; Pérez, P. *IEEE Transactions on Intelligent Transportation Systems* **2021**, *23*, 4909–4926.

(130) James, G.; Witten, D.; Hastie, T.; Tibshirani, R., *An introduction to statistical learning*; Springer: 2013; Vol. 112.

(131) Montgomery, D. C.; Peck, E. A.; Vining, G. G., *Introduction to linear regression analysis*; John Wiley & Sons: 2021.

(132) Kleinbaum, D. G.; Dietz, K.; Gail, M.; Klein, M.; Klein, M., *Logistic regression*; Springer: 2002.

(133) Jolliffe, I. T.; Cadima, J. *Philosophical Transactions of the Royal Society A: Mathematical, Physical and Engineering Sciences* **2016**, *374*, 20150202.

(134) Hearst, M. A.; Dumais, S. T.; Osuna, E.; Platt, J.; Scholkopf, B. *IEEE Intelligent Systems and their applications* **1998**, *13*, 18–28.

(135) Kanungo, T.; Mount, D. M.; Netanyahu, N. S.; Piatko, C. D.; Silverman, R.; Wu, A. Y. *IEEE transactions on pattern analysis and machine intelligence* **2002**, *24*, 881–892.

(136) LeCun, Y.; Bengio, Y.; Hinton, G. *Nature* **2015**, *521*, 436–444.

(137) Krizhevsky, A.; Sutskever, I.; Hinton, G. E. *Communications of the ACM* **2017**, *60*, 84–90.

(138) Liang, M.; Hu, X. In *Proceedings of the IEEE conference on computer vision and pattern recognition*, 2015, pp 3367–3375.

(139) Goodfellow, I.; Pouget-Abadie, J.; Mirza, M.; Xu, B.; Warde-Farley, D.; Ozair, S.; Courville, A.; Bengio, Y. *Communications of the ACM* **2020**, *63*, 139–144.

(140) Hinton, G. E.; Salakhutdinov, R. R. *Science* **2006**, *313*, 504–507.

(141) Silver, D.; Huang, A.; Maddison, C. J.; Guez, A.; Sifre, L.; Van Den Driessche, G.; Schrittwieser, J.; Antonoglou, I.; Panneershelvam, V.; Lanctot, M., et al. *Nature* **2016**, *529*, 484–489.

(142) Esteva, A.; Kuprel, B.; Novoa, R. A.; Ko, J.; Swetter, S. M.; Blau, H. M.; Thrun, S. *Nature* **2017**, *542*, 115–118.

(143) Senior, A. W.; Evans, R.; Jumper, J.; Kirkpatrick, J.; Sifre, L.; Green, T.; Qin, C.; Žídek, A.; Nelson, A. W.; Bridgland, A., et al. *Nature* **2020**, *577*, 706–710.

(144) Sanchez-Lengeling, B.; Aspuru-Guzik, A. *Science* **2018**, *361*, 360–365.

(145) Pearson, K. *The London, Edinburgh, and Dublin philosophical magazine and journal of science* **1901**, *2*, 559–572.

(146) Titchmarsh, J. *Ultramicroscopy* **1999**, *78*, 241–250.

(147) Bosman, M.; Watanabe, M.; Alexander, D.; Keast, V. *Ultramicroscopy* **2006**, *106*, 1024–1032.

(148) Lozano-Perez, S. In *Journal of Physics: Conference Series*, 2008; Vol. 126, p 012040.

(149) Keenan, M. R.; Kotula, P. G. *Surface and Interface Analysis: An International Journal devoted to the development and application of techniques for the analysis of surfaces, interfaces and thin films* **2004**, *36*, 203–212.

(150) Yankovich, A. B.; Zhang, C.; Oh, A.; Slater, T. J.; Azough, F.; Freer, R.; Haigh, S. J.; Willett, R.; Voyles, P. M. *Nanotechnology* **2016**, *27*, 364001.

(151) Haberfehlner, G.; Hoefler, S. F.; Rath, T.; Trimmel, G.; Kothleitner, G.; Hofer, F. *Micron* **2021**, *140*, 102981.

(152) Cueva, P.; Hovden, R.; Mundy, J. A.; Xin, H. L.; Muller, D. A. *Microscopy and Microanalysis* **2012**, *18*, 667–675.

(153) Parish, C. M.; Brewer, L. N. *Microscopy and Microanalysis* **2010**, *16*, 259–272.

(154) Kotula, P. G.; Keenan, M. R.; Michael, J. R. *Microscopy and Microanalysis* **2003**, *9*, 1–17.

(155) Spiegelberg, J.; Rusz, J. *Ultramicroscopy* **2017**, *172*, 40–46.

(156) Lichtert, S.; Verbeeck, J. *Ultramicroscopy* **2013**, *125*, 35–42.

(157) Potapov, P. *Ultramicroscopy* **2016**, *160*, 197–212.

(158) Keenan, M. R. *Surface and Interface Analysis: An International Journal devoted to the development and application of techniques for the analysis of surfaces, interfaces and thin films* **2009**, *41*, 79–87.

(159) Lucas, G.; Burdet, P.; Cantoni, M.; Hébert, C. *Micron* **2013**, *52*, 49–56.

(160) Comon, P. *Signal processing* **1994**, *36*, 287–314.

(161) Comon, P.; Jutten, C., *Handbook of Blind Source Separation: Independent component analysis and applications*; Academic press: 2010.

(162) Makino, S.; Araki, S.; Mukai, R.; Sawada, H. In *2004 IEEE International Symposium on Circuits and Systems*, 2004; Vol. 5, pp 668–671.

(163) Cichocki, A.; Douglas, S. C.; Amari, S.-i. *Neurocomputing* **1998**, *22*, 113–129.

(164) Hyvarinen, A.; Sasaki, H.; Turner, R. In *The 22nd International Conference on Artificial Intelligence and Statistics*, 2019, pp 859–868.

(165) Bach, F. R.; Jordan, M. I. *Journal of machine learning research* **2002**, *3*, 1–48.

(166) Bonnet, N. *Micron* **2004**, *35*, 635–653.

(167) Nuzillard, D.; Bonnet, N. In *Independent Component Analysis and Blind Signal Separation: Fifth International Conference, ICA 2004, Granada, Spain, September 22-24, 2004. Proceedings 5*, 2004, pp 1150–1157.

(168) De la Peña, F.; Ostasevicius, T.; Fauske, V. T.; Burdet, P.; Jokubauskas, P.; Nord, M.; Sarahan, M.; Prestat, E.; Johnstone, D. N.; Taillon, J., et al. *Microscopy and Microanalysis* **2017**, *23*, 214–215.

(169) Li, G.; Rivarola, F. W. R.; Davis, N. J.; Bai, S.; Jellicoe, T. C.; de la Peña, F.; Hou, S.; Ducati, C.; Gao, F.; Friend, R. H., et al. *Advanced materials* **2016**, *28*, 3528–3534.

(170) Sanchez, A.; Beltran, A.; Beanland, R.; Ben, T.; Gass, M.; de la Pena, F.; Walls, M.; Taboada, A.; Ripalda, J.; Molina, S. *Nanotechnology* **2010**, *21*, 145606.

(171) Genç, A.; Patarroyo, J.; Sancho-Parramon, J.; Arenal, R.; Duchamp, M.; Gonzalez, E. E.; Henrard, L.; Bastús, N. G.; Dunin-Borkowski, R. E.; Puntes, V. F., et al. *ACS photonics* **2016**, *3*, 770–779.

(172) De la Peña, F.; Berger, M.-H.; Hochepied, J.-F.; Dynys, F.; Stephan, O.; Walls, M. *Ultramicroscopy* **2011**, *111*, 169–176.

(173) Rossouw, D.; Burdet, P.; de la Peña, F.; Ducati, C.; Knappett, B. R.; Wheatley, A. E.; Midgley, P. A. *Nano letters* **2015**, *15*, 2716–2720.

(174) Rossouw, D.; Krakow, R.; Saghi, Z.; Yeoh, C. S.; Burdet, P.; Leary, R. K.; De La Pena, F.; Ducati, C.; Rae, C. M.; Midgley, P. A. *Acta Materialia* **2016**, *107*, 229–238.

(175) Lee, D. D.; Seung, H. S. *Nature* **1999**, *401*, 788–791.

(176) Jany, B.; Janas, A.; Krok, F. *Nano letters* **2017**, *17*, 6520–6525.

(177) Teng, C.; Gauvin, R. *Scanning* **2020**, *2020*.

(178) Nicoletti, O.; de La Peña, F.; Leary, R. K.; Holland, D. J.; Ducati, C.; Midgley, P. A. *Nature* **2013**, *502*, 80–84.

(179) Kong, D.; Ding, C.; Huang, H. In *Proceedings of the 20th ACM international conference on Information and knowledge management*, 2011, pp 673–682.

(180) Jia, S.; Qian, Y. *IEEE Transactions on Geoscience and Remote Sensing* **2008**, *47*, 161–173.

(181) Shiga, M.; Tatsumi, K.; Muto, S.; Tsuda, K.; Yamamoto, Y.; Mori, T.; Tanji, T. *Ultramicroscopy* **2016**, *170*, 43–59.

(182) Miao, L.; Qi, H. *IEEE Transactions on Geoscience and Remote Sensing* **2007**, *45*, 765–777.

(183) Zhang, D.; Zhou, Z. H.; Chen, S. In *PRICAI 2006: Trends in Artificial Intelligence: 9th Pacific Rim International Conference on Artificial Intelligence*, 2006, pp 404–412.

(184) Févotte, C.; Dobigeon, N. *IEEE Transactions on Image Processing* **2015**, *24*, 4810–4819.

(185) Wiersma, S.; Just, T.; Heinrich, M. *International Journal of Housing Markets and Analysis* **2022**, *15*, 548–578.

(186) Anjna, E.; Kaur, E. R. *International Journal of Advanced Research in Computer Science* **2017**, *8*, 36–39.

(187) Michaels, G. S.; Carr, D. B.; Askenazi, M.; Fuhrman, S.; Wen, X.; Somogyi, R. In *Pacific symposium on biocomputing*, 1998; Vol. 3, pp 42–53.

(188) Eisen, M. B.; Spellman, P. T.; Brown, P. O.; Botstein, D. *Proceedings of the National Academy of Sciences* **1998**, *95*, 14863–14868.

(189) Murtagh, F.; Contreras, P. *Wiley Interdisciplinary Reviews: Data Mining and Knowledge Discovery* **2012**, *2*, 86–97.

(190) Cai, R. F.; Chang, M. T.; Lo, S. C.; Chen, C. C. *New Journal of Physics* **2020**, *22*, 033029.

(191) Blanco-Portals, J.; Torruella, P.; Baiutti, F.; Anelli, S.; Torrell, M.; Tarancón, A.; Peiró, F.; Estradé, S. *Ultramicroscopy* **2022**, *232*, 113403.

(192) Blanco-Portals, J.; Peiró, F.; Estradé, S. *Microscopy and Microanalysis* **2022**, *28*, 109–122.

(193) Bishop, C. M.; Nasrabadi, N. M., *Pattern recognition and machine learning*; 4; Springer: 2006; Vol. 4.

(194) Kullback, S.; Leibler, R. A. *The annals of mathematical statistics* **1951**, *22*, 79–86.

(195) Bottou, L. *Neural Networks: Tricks of the Trade: Second Edition* **2012**, 421–436.

(196) Kingma, D. P.; Ba, J. *arXiv preprint arXiv:1412.6980* **2014**.

(197) Hinton, G.; Deng, L.; Yu, D.; Dahl, G. E.; Mohamed, A.-r.; Jaitly, N.; Senior, A.; Vanhoucke, V.; Nguyen, P.; Sainath, T. N., et al. *IEEE Signal processing magazine* **2012**, *29*, 82–97.

(198) Ma, J.; Sheridan, R. P.; Liaw, A.; Dahl, G. E.; Svetnik, V. *Journal of chemical information and modeling* **2015**, *55*, 263–274.

(199) Xiong, H. Y.; Alipanahi, B.; Lee, L. J.; Bretschneider, H.; Merico, D.; Yuen, R. K.; Hua, Y.; Gueroussov, S.; Najafabadi, H. S.; Hughes, T. R., et al. *Science* **2015**, *347*, 1254806.

(200) Xu, W.; LeBeau, J. M. *Ultramicroscopy* **2018**, *188*, 59–69.

(201) Aguiar, J.; Gong, M. L.; Unocic, R.; Tasdizen, T.; Miller, B. *Science advances* **2019**, *5*, eaaw1949.

(202) Oxley, M. P.; Yin, J.; Borodinov, N.; Somnath, S.; Ziatdinov, M.; Lupini, A. R.; Jesse, S.; Vasudevan, R. K.; Kalinin, S. V. *Machine Learning: Science and Technology* **2020**, *1*, 04LT01.

(203) Zhang, C.; Feng, J.; DaCosta, L. R.; Voyles, P. M. *Ultramicroscopy* **2020**, *210*, 112921.

(204) Cherukara, M. J.; Nashed, Y. S.; Harder, R. J. *Scientific reports* **2018**, *8*, 16520.

(205) Cherukara, M. J.; Zhou, T.; Nashed, Y.; Enfedaque, P.; Hexemer, A.; Harder, R. J.; Holt, M. V. *Applied Physics Letters* **2020**, *117*, 044103.

(206) Wang, F.; Eljarrat, A.; Müller, J.; Henninen, T. R.; Erni, R.; Koch, C. T. *Scientific reports* **2020**, *10*, 1–11.

(207) Wang, F.; Henninen, T. R.; Keller, D.; Erni, R. *Applied Microscopy* **2020**, *50*, 1–9.

(208) Ede, J. M.; Beanland, R. *Ultramicroscopy* **2019**, *202*, 18–25.

(209) Ede, J. M.; Beanland, R. *Scientific reports* **2020**, *10*, 8332.

(210) Lee, C.-H.; Khan, A.; Luo, D.; Santos, T. P.; Shi, C.; Janicek, B. E.; Kang, S.; Zhu, W.; Sobh, N. A.; Schleife, A., et al. *Nano letters* **2020**, *20*, 3369–3377.

(211) Maksov, A.; Dyck, O.; Wang, K.; Xiao, K.; Geohegan, D. B.; Sumpter, B. G.; Vasudevan, R. K.; Jesse, S.; Kalinin, S. V.; Ziatdinov, M. *npj Computational Materials* **2019**, *5*, 12.

(212) Ziatdinov, M.; Dyck, O.; Maksov, A.; Li, X.; Sang, X.; Xiao, K.; Unocic, R. R.; Vasudevan, R.; Jesse, S.; Kalinin, S. V. *ACS nano* **2017**, *11*, 12742–12752.

(213) Ziatdinov, M.; Dyck, O.; Li, X.; Sumpter, B. G.; Jesse, S.; Vasudevan, R. K.; Kalinin, S. V. *Science advances* **2019**, *5*, eaaw8989.

(214) Chatzidakis, M.; Botton, G. *Scientific reports* **2019**, *9*, 1–10.

(215) Skorikov, A.; Heyvaert, W.; Albecht, W.; Pelt, D. M.; Bals, S. *Nanoscale* **2021**, *13*, 12242–12249.

(216) Han, Y.; Jang, J.; Cha, E.; Lee, J.; Chung, H.; Jeong, M.; Kim, T.-G.; Chae, B. G.; Kim, H. G.; Jun, S., et al. *Nature Machine Intelligence* **2021**, *3*, 267–274.

(217) Yang, X.; De Andrade, V.; Scullin, W.; Dyer, E. L.; Kasthuri, N.; De Carlo, F.; Gürsoy, D. *Scientific reports* **2018**, *8*, 1–13.

(218) Morbidelli, A.; Lunine, J. I.; Obrien, D. P.; Raymond, S. N.; Walsh, K. J. *arXiv preprint arXiv:1208.4694* **2012**.

(219) Bowen, N. *The Journal of Geology* **1912**, *20*, 457–468.

(220) Solomatov, V. S.; Stevenson, D. J. *Journal of Geophysical Research: Planets* **1993**, *98*, 5391–5406.

(221) Boukaré, C.-E.; Ricard, Y.; Fiquet, G. *Journal of Geophysical Research: Solid Earth* **2015**, *120*, 6085–6101.

(222) Liebske, C.; Corgne, A.; Frost, D. J.; Rubie, D. C.; Wood, B. J. *Contributions to Mineralogy and Petrology* **2005**, *149*, 113–128.

(223) Liebske, C.; Frost, D. J. *Earth and Planetary Science Letters* **2012**, *345*, 159–170.

(224) Badro, J.; Brodholt, J. P.; Piet, H.; Siebert, J.; Ryerson, F. J. *Proceedings of the National Academy of Sciences* **2015**, *112*, 12310–12314.

(225) Ito, E.; Schubert, G.; Romanowicz, B.; Dziewonski, A. *Treatise on geophysics* **2007**, *2*, 197–230.

(226) Ohtani, E.; Nagata, Y.; Suzuki, A.; Kato, T. *Chemical Geology* **1995**, *120*, 207–221.

(227) Jagoutz, E.; Palme, H.; Baddenhausen, H.; Blum, K.; Cendales, M.; Dreibus, G.; Spettel, B.; Lorenz, V.; Wänke, H. In *Lunar and Planetary Science Conference Proceedings*, 1979; Vol. 10, pp 2031–2050.

(228) Agee, C. B.; Walker, D. *Earth and planetary science letters* **1988**, *90*, 144–156.

(229) Martinez, I.; Wang, Y.; Guyot, F.; Liebermann, R. C.; Doukhan, J.-C. *Journal of Geophysical Research: Solid Earth* **1997**, *102*, 5265–5280.

(230) Irifune, T.; Shinmei, T.; McCammon, C. A.; Miyajima, N.; Rubie, D. C.; Frost, D. J. *Science* **2010**, *327*, 193–195.

(231) Sinmyo, R.; Hirose, K. *Physics and Chemistry of Minerals* **2013**, *40*, 107–113.

(232) Kobayashi, Y.; Kondo, T.; Ohtani, E.; Hirao, N.; Miyajima, N.; Yagi, T.; Nagase, T.; Kikegawa, T. *Geophysical Research Letters* **2005**, *32*.

(233) Sakai, T.; Ohtani, E.; Terasaki, H.; Sawada, N.; Kobayashi, Y.; Miyahara, M.; Nishijima, M.; Hirao, N.; Ohishi, Y.; Kikegawa, T. *American Mineralogist* **2009**, *94*, 921–925.

(234) Forte, A. M.; Mitrovica, J. X. *Nature* **2001**, *410*, 1049–1056.

(235) Zhao, Y.-H.; Zimmerman, M. E.; Kohlstedt, D. L. *Earth and Planetary Science Letters* **2009**, *287*, 229–240.

(236) Tommaseo, C. E.; Devine, J.; Merkel, S.; Speziale, S.; Wenk, H.-R. *Physics and chemistry of minerals* **2006**, *33*, 84–97.

(237) Tamarova, A. P.; Marchenko, E. I.; Bobrov, A. V.; Eremin, N. N.; Zinov' eva, N. G.; Irifune, T.; Hirata, T.; Makino, Y. *Minerals* **2020**, *10*, 262.

(238) Popel, A. J.; Spurgeon, S. R.; Matthews, B.; Olszta, M. J.; Tan, B. T.; Gouder, T.; Eloirdi, R.; Buck, E. C.; Farnan, I. *ACS applied materials & interfaces* **2020**, *12*, 39781–39786.

(239) Spurgeon, S. R.; Chambers, S. A.; Richland, W., et al. *Reference Module in Chemistry, Molecular Sciences and Chemical Engineering* **2017**, 1–11.

(240) Roncal-Herrero, T.; Harrington, J.; Zeb, A.; Milne, S. J.; Brown, A. P. *Acta Materialia* **2018**, *158*, 422–429.

(241) Mao, K. S.; Gerczak, T. J.; Harp, J. M.; McKinney, C. S.; Lach, T. G.; Karakoc, O.; Nelson, A. T.; Terrani, K. A.; Parish, C. M.; Edmondson, P. D. *Communications Materials* **2022**, *3*, 21.

(242) Libera, M. R.; Egerton, R. F. *Polymer Reviews* **2010**, *50*, 321–339.

(243) Parent, L. R.; Gnanasekaran, K.; Korpanty, J.; Gianneschi, N. C. *ACS Macro Letters* **2020**, *10*, 14–38.

(244) Zhu, Y.; Ciston, J.; Zheng, B.; Miao, X.; Czarnik, C.; Pan, Y.; Sougrat, R.; Lai, Z.; Hsiung, C.-E.; Yao, K., et al. *Nature materials* **2017**, *16*, 532–536.

(245) Zhang, D.; Zhu, Y.; Liu, L.; Ying, X.; Hsiung, C.-E.; Sougrat, R.; Li, K.; Han, Y. *Science* **2018**, *359*, 675–679.

(246) Susi, T.; Kotakoski, J.; Arenal, R.; Kurasch, S.; Jiang, H.; Skakalova, V.; Stephan, O.; Krasheninnikov, A. V.; Kauppinen, E. I.; Kaiser, U., et al. *ACS nano* **2012**, *6*, 8837–8846.

(247) Garcia, A.; Raya, A. M.; Mariscal, M. M.; Esparza, R.; Herrera, M.; Molina, S. I.; Scavello, G.; Galindo, P. L.; Jose-Yacaman, M.; Ponce, A. *Ultramicroscopy* **2014**, *146*, 33–38.

(248) Moreira, M.; Hillenkamp, M.; Divitini, G.; Tizei, L. H.; Ducati, C.; Cotta, M. A.; Rodrigues, V.; Ugarte, D. *Microscopy and Microanalysis* **2022**, *28*, 338–349.

(249) Potapov, P.; Lubk, A. *Advanced structural and chemical imaging* **2019**, *5*, 1–21.

(250) Nakamura, M.; Tsuya, K. *Powder Metallurgy* **1979**, *22*, 179–186.

(251) Marín, D.; Gañán, P.; Tercjak, A.; Castro, C.; Builes, D. H. *Journal of Applied Polymer Science* **2021**, *138*, 51308.

(252) Mistry, A. N.; Smith, K.; Mukherjee, P. P. *ACS applied materials & interfaces* **2018**, *10*, 6317–6326.

(253) Liu, D.; Shadike, Z.; Lin, R.; Qian, K.; Li, H.; Li, K.; Wang, S.; Yu, Q.; Liu, M.; Ganapathy, S., et al. *Advanced Materials* **2019**, *31*, 1806620.

(254) Wang, X.; Zhong, Y.; Zhai, T.; Guo, Y.; Chen, S.; Ma, Y.; Yao, J.; Bando, Y.; Golberg, D. *Journal of Materials Chemistry* **2011**, *21*, 17680–17687.

(255) Khezami, L.; Alwqyan, T.; Bououdina, M.; Al-Najar, B.; Shaikh, M.; Modwi, A.; Taha, K. K. *Journal of Materials Science: Materials in Electronics* **2019**, *30*, 9683–9694.

(256) Hirose, K.; Sinmyo, R.; Hernlund, J. *Science* **2017**, *358*, 734–738.

(257) Teurtrie, A.; Perraudin, N.; Holvoet, T.; Chen, H.; Alexander, D. T.; Obozinski, G.; Hébert, C. *Ultramicroscopy* **2023**, 113719.

(258) Wilbur, S. Factors Determining Sensitivity in ICP-MS Spectroscopy Online, https://www.spectroscopyonline.com/view/factors-determining-sensitivity-icp-ms (accessed 01/25/2023).

(259) Wu, S.; Yang, M.; Yang, Y.; Xie, L.; Huang, C.; Wang, H.; Yang, J. *International Journal of Mass Spectrometry* **2020**, *456*, 116394.

(260) Kannan, R.; Ievlev, A.; Laanait, N.; Ziatdinov, M. A.; Vasudevan, R. K.; Jesse, S.; Kalinin, S. V. *Advanced Structural and Chemical Imaging* **2018**, *4*, 1–20.

(261) Rother, C.; Kolmogorov, V.; Blake, A. *ACM transactions on graphics (TOG)* **2004**, *23*, 309–314.

(262) Raju, P. D. R.; Neelima, G. *International Journal of Computer Science Engineering and Technology* **2012**, *2*, 776–779.

(263) Muthukrishnan, R.; Radha, M. *International Journal of Computer Science & Information Technology* **2011**, *3*, 259.

(264) Ramesh, N.; Tasdizen, T. In *Computer Vision for Microscopy Image Analysis*; Elsevier: 2021, pp 43–71.

(265) Boykov, Y.; O. Veksler, Y.; Zabih, R. *IEEE Transactions on pattern analysis and machine intelligence* **2001**, *23*, 1222–1239.

(266) Boykov, Y.; Kolmogorov, V. *IEEE transactions on pattern analysis and machine intelligence* **2004**, *26*, 1124–1137.

(267) Heinz, D. C. et al. *IEEE transactions on geoscience and remote sensing* **2001**, *39*, 529–545.

(268) Ernst, T.; Berman, T.; Buscaglia, J.; Eckert-Lumsdon, T.; Hanlon, C.; Olsson, K.; Palenik, C.; Ryland, S.; Trejos, T.; Valadez, M., et al. *X-Ray Spectrometry* **2014**, *43*, 13–21.

(269) Keith, L. H.; Crummett, W.; Deegan, J.; Libby, R. A.; Taylor, J. K.; Wentler, G. *Analytical chemistry* **1983**, *55*, 2210–2218.

(270) Long, G. L.; Winefordner, J. D. *Analytical chemistry* **1983**, *55*, 712A–724A.

(271) Vivone, G.; Alparone, L.; Chanussot, J.; Dalla Mura, M.; Garzelli, A.; Licciardi, G. A.; Restaino, R.; Wald, L. *IEEE Transactions on Geoscience and Remote Sensing* **2014**, *53*, 2565–2586.

(272) Borodinov, N.; Banerjee, P.; Cho, S. H.; Milliron, D. J.; Ovchinnikova, O. S.; Vasudevan, R. K.; Hachtel, J. A. *The Journal of Chemical Physics* **2021**, *154*, 014202.

(273) Díaz, A.; Steele, D. *arXiv preprint arXiv:2106.02213* **2021**.

(274) Loncan, L.; De Almeida, L. B.; Bioucas-Dias, J. M.; Briottet, X.; Chanussot, J.; Dobigeon, N.; Fabre, S.; Liao, W.; Licciardi, G. A.; Simoes, M., et al. *IEEE Geoscience and remote sensing magazine* **2015**, *3*, 27–46.

(275) Jannis, D.; Müller-Caspary, K.; Béché, A.; Verbeeck, J. *Applied Sciences* **2021**, *11*, 9058.

(276) Kothleitner, G. *Microscopy and Microanalysis* **2012**, *18*, 972–973.

(277) Sitzmann, V.; Martel, J.; Bergman, A.; Lindell, D.; Wetzstein, G. *Advances in Neural Information Processing Systems* **2020**, *33*, 7462–7473.

(278) Mildenhall, B.; Srinivasan, P. P.; Tancik, M.; Barron, J. T.; Ramamoorthi, R.; Ng, R. In *Computer Vision–ECCV 2020: 16th European Conference, Glasgow, UK, August 23–28, 2020, Proceedings, Part I*, 2020, pp 405–421.

(279) Radford, A.; Narasimhan, K.; Salimans, T.; Sutskever, I., et al. **2018**.

(280) Radford, A.; Wu, J.; Child, R.; Luan, D.; Amodei, D.; Sutskever, I., et al. *OpenAI blog* **2019**, *1*, 9.

(281) Brown, T.; Mann, B.; Ryder, N.; Subbiah, M.; Kaplan, J. D.; Dhariwal, P.; Neelakantan, A.; Shyam, P.; Sastry, G.; Askell, A., et al. *Advances in neural information processing systems* **2020**, *33*, 1877–1901.

(282) Jin, X.; Xu, C.; Feng, J.; Wei, Y.; Xiong, J.; Yan, S. In *Proceedings of the AAAI Conference on Artificial Intelligence*, 2016; Vol. 30.

(283) Lau, M. M.; Lim, K. H. In *2018 IEEE-EMBS Conference on Biomedical Engineering and Sciences (IECBES)*, 2018, pp 686–690.

(284) Paszke, A.; Gross, S.; Massa, F.; Lerer, A.; Bradbury, J.; Chanan, G.; Killeen, T.; Lin, Z.; Gimelshein, N.; Antiga, L., et al. *Advances in neural information processing systems* **2019**, *32*.

Hui Chen

Ecole Polytechnique Fédérale de Lausanne
Electron Spectrometry and Microscopy Laboratory
E-mail: hui.chen@epfl.ch
Phone: +41 (0)77 974 83 41

EDUCATION

Ph.D. in Materials Science and Engineering
Ecole Polytechnique Fédérale de Lausanne, Lausanne, Switzerland
Sept. 2017 – Feb. 2023

M.Sc. in Physical Chemistry
Shanghai Institute of Ceramics, Chinese Academy of Sciences, Shanghai, China
Sept. 2014 – Jun. 2017
University of Science and Technology of China, Hefei, China
Sept. 2014 – Jul. 2015

B. Eng. in Materials Science and Engineering
Dept. Material Sci. & Eng. Wuhan University of Technology, Wuhan, China
Sept. 2010 – Jul. 2014

RESEARCH EXPERIENCE

Sept. 2017 – Feb. 2023 Doctoral Assistant
Electron Spectrometry and Microscopy Laboratory
Ecole Polytechnique Fédérale de Lausanne

- **Thesis title:** New tools for phase segmentation and denoising of analytical STEM data for enhanced chemical sensitivity, applied to Earth mantle research

  Supervisor: Prof. Cécile Hébert

Sept. 2015 – Jun. 2017 Graduate Research Assistant
Key Laboratory of Inorganic Functional Materials and Devices
Shanghai Institute of Ceramics, Chinese Academy of Sciences

- **Master thesis title**: Microstructural and compositional design for enhanced pyroelectricity and ferroelectricity of strontium barium niobate-based ceramics

  Supervisor: Prof. Genshui Wang

Apr. 2012 – May. 2014 Undergraduate Research Assistant
State Key Laboratory of Advanced Technology for Materials Synthesis and Processing, Wuhan University of Technology

- **Bachelor thesis title:** The influence of chiral molecules modified graphene oxide on Amyloid formation

Advisors: Prof. Taolei Sun & Prof. Guangyan Qing

PROFESSIONAL SKILLS

Experimental techniques: Functional oxide ceramics solid-state synthesis

Analytical techniques: (Scanning) Transmission electron microscopy ((S)TEM), X-ray energy dispersive spectrometry (EDXS), Electron energy-loss spectrometry (EELS), Electrical properties measurement (ferroelectricy, pyroelectricity, dielectricity)

Professional software and programming languages: Python, Mathematica, Gatan DigitalMicrograph, Velox, Esprit, TIA, ImageJ Fiji

PUBLICATIONS

1. **Hui Chen,** Cécile Hébert, et al. Non-negative Matrix Factorization-Aided Phase Unmixing and Trace Element Quantification of STEM-EDXS Data (prepared to submit)

2. Adrien Teurtrie, Nathanael Perraudin, Thomas Holvoet, **Hui Chen,** et al. espm: A Python library for the simulation of STEM-EDXS datasets, ***Ultramicroscopy*** 249 (2023) 113719

3. **Hui Chen,** Genshui Wang, et al. $Ca_xSr_{0.3-x}Ba_{0.7}Nb_2O_6$ Lead-free Pyroelectric Ceramics with High Depoling Temperature, ***Journal of Alloys and Compounds*** 695 (2017) 2723-2729

4. **Hui Chen,** Genshui Wang, et al. Induced Anisotropic Behavior and Enhanced Electrical Properties on Hot-pressed Strontium Barium Niobate Ceramics, ***Ceramics International*** 43 (2017) 3610-3615

5. Guangyan Qing, Shilong Zhao, **Hui Chen,** et al, Chiral Effect at Protein/Graphene Interface: A Bioinspired Perspective to Understand Amyloid Formation, ***Journal of the American Chemical Society***. 136 (30), 10736 (2014)

6. Genshui Wang, **Hui Chen** and Shaobo Guo. ***Chinese Patent***, No. 201610738896.2.

CONFERENCE PRESENTATIONS

1. **Hui Chen,** Farhang Nabiei, James Badro, Duncan T.L. Alexander and Cécile Hébert. STEM EDS/EELS for Phase Analysis of Deep-Mantle Rock Assemblages Supported by Machine Learning**,** ***Microscopy & Microanalysis, Portland, American, Aug. 2019*** (poster presentation)

2. **Hui Chen,** Farhang Nabiei, James Badro, Duncan T.L. Alexander and Cécile Hébert. STEM EDS/EELS for Deep-Mantle Rock Assemblages Analyses Assisted by Machine Learning,

Microscopy Conference, Berlin, Germany, Sept. 2019 (poster presentation, Best Poster Award in section: Material Science (MS) 7)

3. **Hui Chen,** Farhang Nabiei, James Badro, Duncan T.L. Alexander and Cécile Hébert. Machine Learning on STEM-EDS Data for Quantifying Overlapping Deep-mantle Rock Assemblages**,** ***Microscopy & Microanalysis, Virtual Conference, Aug. 2020*** (oral presentation)

4. **Hui Chen,** Farhang Nabiei, James Badro, Duncan T.L. Alexander and Cécile Hébert. Machine Learning on STEM-EDS Data for Quantifying Trace Elements in Bridgmanite, ***Microscopy Conference, Virtual Conference, Aug. 2021*** (oral presentation)

5. **Hui Chen,** James Badro, Duncan T.L. Alexander and Cécile Hébert. Unmixing Mineral Phases, Improving Quantification: Use Machine Learning to Understand Deep-mantle with STEM-EDS Data***, Microscopy & Microanalysis, Portland, American, Aug. 2022*** (oral presentation)

6. **Hui Chen,** Duncan T.L. Alexander and Cécile Hébert. Machine Learning for Unmixing Overlapping Phases with Low SNR STEM-EDXS Data, ***Microscopy Conference, Darmstadt, Germany, Feb. 2023*** (poster presentation)

MENTORING EXPERIENCE

- **Master semester project co-supervisor**

Jialiang Fan (2019 Spring)

Project title: Transmission electron microscopy microstructural investigation of TiAl-based alloy

- **Master semester project co-supervisor**

Thomas Holvoet (2019 Fall)

Project title: Dictionary learning for material structure estimation in transmission electron microscopy

- **Master semester project supervisor**

Quentin Chaboche (2020 Fall)

Project title: Investigation of quantification uncertainty, determination of sensitivity of STEM-EDXS technique and inference for an optimal experiment design